1971

The influence of inlet velocity distribution on the flow through a plane curved diffuser

Chester Joseph Blechinger
Iowa State University

The influence of inlet velocity distribution on the flow through a plane curved diffuser

by

Chester Joseph Blechinger

A Dissertation Submitted to the
Graduate Faculty in Partial Fulfillment of
The Requirements for the Degree of
DOCTOR OF PHILOSOPHY

Major Subjects: Mechanical Engineering
Engineering Mechanics

Approved:

Signature was redacted for privacy.

In Charge of Major Work

Signature was redacted for privacy.

Heads of Major Departments

Signature was redacted for privacy.

Dean of Graduate College

Iowa State University
Ames, Iowa

1971

TABLE OF CONTENTS

NOMENCLATURE[1]

A	passage cross-section area	in^2
AR	passage cross-section area ratio, exit/inlet	dimensionless
AS	diffuser aspect ratio, diffuser height/diffuser width	dimensionless
b	diffuser height	in
B	passage blockage factor (eq. 100)	dimensionless
C_1, C_2, C_3	coefficient in second order equation (Equation 91)	
dA	element of area	in^2
dt	increment of time	sec
dx	element of axial distance	in
D_h	hydraulic diameter	in
E_b	bridge voltage,	volts
$\bar{F}$	force vector	lb_f
Δh	Pitot-static differential pressure pressure	inches of water
h_1, h_2, h_3	transformation coefficients in x_1, x_2, x_3 directions respectively	
H	boundary-layer shape factor	dimensionless
i	current through sensor	amperes
k	constant in cosine law for hot wires (Equation 81)	dimensionless
$\bar{n}$	outward normal	
N	diffuser centerline length	in

[1]Nomenclature not in this list are defined and used locally within the text.

P	wall static pressure	lb_f/ft^2
P_t	total pressure	lb_f/ft^2
Q	magnitude of velocity vector	ft/sec
Q_{ℓ}	centerline velocity	ft/sec
r	radius from diffuser centerline	in
R_c	radius of curvature of curved diffuser meanline	in
R_{oh}	overheating ratio	dimensionless
R_t	total resistance	ohms
$u,v,w,$	velocity components along axis x, y, and z respectively	ft/sec
V	velocity vector with components u, v, w	ft/sec
W	diffuser width in the plane of the curve	in
x	cartesian coordinate in streamwise direction	ft
x_1, x_2, x_3	curvilinear coordinates in tangential, principal normal and binormal direction respectively	ft
y	cartesian coordinate parallel to end walls	ft
z	cartesian coordinate orthogonal to x and y coordinates	ft
α	fluid skewing angle	degrees
β	local diffuser turning angle	degrees
β_{max}	maximum diffuser turning angle	degrees
δ	boundary-layer thickness	in
δ^*	boundary-layer displacement thickness	in

η	diffuser effectiveness	dimensionless
θ	boundary-layer momentum thickness	in.
μ	absolute viscosity	lb_f-sec/ft^2
ν	kinematic viscosity	ft^2/sec
ρ	fluid density	lb_m/ft^3
τ_0	shear stress at the wall	lb_f/ft^2
ϕ	angle between the principal normal and the normal to the Bernoulli surface	degrees
ψ	stream function	ft^2/sec
$\overline{\Omega}$	vorticity vector with components Ω_x, Ω_y, Ω_z in x, y, z directions respectively	sec^{-1}

INTRODUCTION

The importance of diffusers has long been recognized not only in the field of turbomachinery but also in other areas involving internal flows, for example, wind tunnels, forced air ventilating and air conditioning systems, fluid flow systems of power plants, both nuclear and conventional, and fluidic devices.

The diffusion process (conversion of velocity of the fluid to pressure) is particularly important, for example, downstream of a gas turbine compressor since work done on the fluid in the compressor can result in significant fluid velocities. This diffusion process has significant influence on the efficiency of the overall compression process, which is an essential part of the gas turbine cycle. Analytical prediction of this diffusion process is desirable since it helps minimize the cost of development.

Presently, satisfactory analytical diffuser performance prediction methods are available only for simple straight[1] two-dimensional and axisymmetric diffusers with very little inlet blockage. Though useful, the above methods are not satisfactory for predicting performance of the diffusion that

[1]Throughout this dissertation, reference is made to straight and curved diffusers. The terms straight and curved refer to the shape of the meanline.

takes place in curved passages, such as usually exist in practice. Experimental evidence suggests that the flow is three-dimensional in a number of such curved passages (see for example Sprenger (1959), Fox and Kline (1962)). However, detailed measurements of the magnitude and the direction of the velocity vector at the exit of a plane curved diffuser was not found in the literature.

Cascade flows studied experimentally by Lakshminarayana and Horlock (1967) and Soderberg (1958) with a simulated inlet velocity profile suggest that the exit flows are three-dimensional even in the core (uniform stagnation pressure region). Related three-dimensional inviscid flows have recently been studied by Hawthorne (1967) and Lakshminarayana and Horlock (1967) among others. Although an inviscid rotational flow analysis provides insight into the physics of curved diffuser flow, the real flow will probably not be understood and modeled satisfactorily until more is known about the nature of the inviscid core and the surrounding boundary layer (see Hawthorne and Novak (1970)) that exists in such configurations.

The purpose of the research described in this dissertation is to increase our present understanding of the influence of inlet blockage on the flow through a plane curved diffuser.

The main objectives of the study were:

1) to investigate the influence of inlet blockage on the effectiveness of a plane curved diffuser, and

2) to investigate the extent of the three dimensional flows in the core and the surrounding boundary layer at the exit, thus filling a void in the curved diffuser literature.

RELATED-RESEARCH REVIEW

Diffuser Research

Introduction

As stated by Cockrell and Markland (1963), a paper published by G. N. Patterson (1937) served as a useful design guide for industrial diffusers for nearly a quarter of a century. However, with increased demands on diffuser performance in terms of lower losses and larger flow velocities, the need for a more thorough understanding of diffuser flow became apparent. Although it had been known for many years (see for example Prandtl and Tietjens (1934)) that there were significantly different diffuser flow regimes, the variables associated with defining these regimes remained obscure.

Straight diffusers

Under the direction of Professor S. J. Kline a group at Stanford University attempted to more precisely define diffuser flow regimes by testing straight two-dimensional diffusers having high aspect ratios. This research centered around an adjustable water-flow-visualization test rig (see Fox and Kline (1962)). It was obviously necessary to define a meaningful set of "symptoms" to be associated with the different diffuser flow regimes in order to present useful experimental results. These symptoms were used to delineate distinct flow

regimes as shown in Figure 1.

Line a-a indicates when first appreciable stall operation could be expected, first appreciable stall being defined as the stall condition involving separated flow over about 20% of the diffuser height.

Line b-b indicates when transition from three-dimensional transitory stall flow to fully developed stall flow could be expected. Transitory stall flow is very erratic, and gross fluctuations of the entire flow field pattern are present. Fully developed stall is characterized by flow in downstream direction on one diverging wall with the flow over the entire length of the opposite wall reversed.

Line c-c denotes when transition from fully developed stall flow to jet flow could be expected with divergence angle increase. In the jet flow regime the flow separates from both walls and proceeds through the diffuser like a free jet in the absence of the diffuser walls.

Line d-d shows when transition from the jet flow regime to fully developed stall flow could be expected with divergence angle decrease. The region between line c-c and line d-d indicates a hysteresis effect.

It can be seen in Figure 1 that the divergence angle and normalized length determine the flow regime. The results of this flow regime study are important for engineering purposes since the overall performance of the diffuser and the

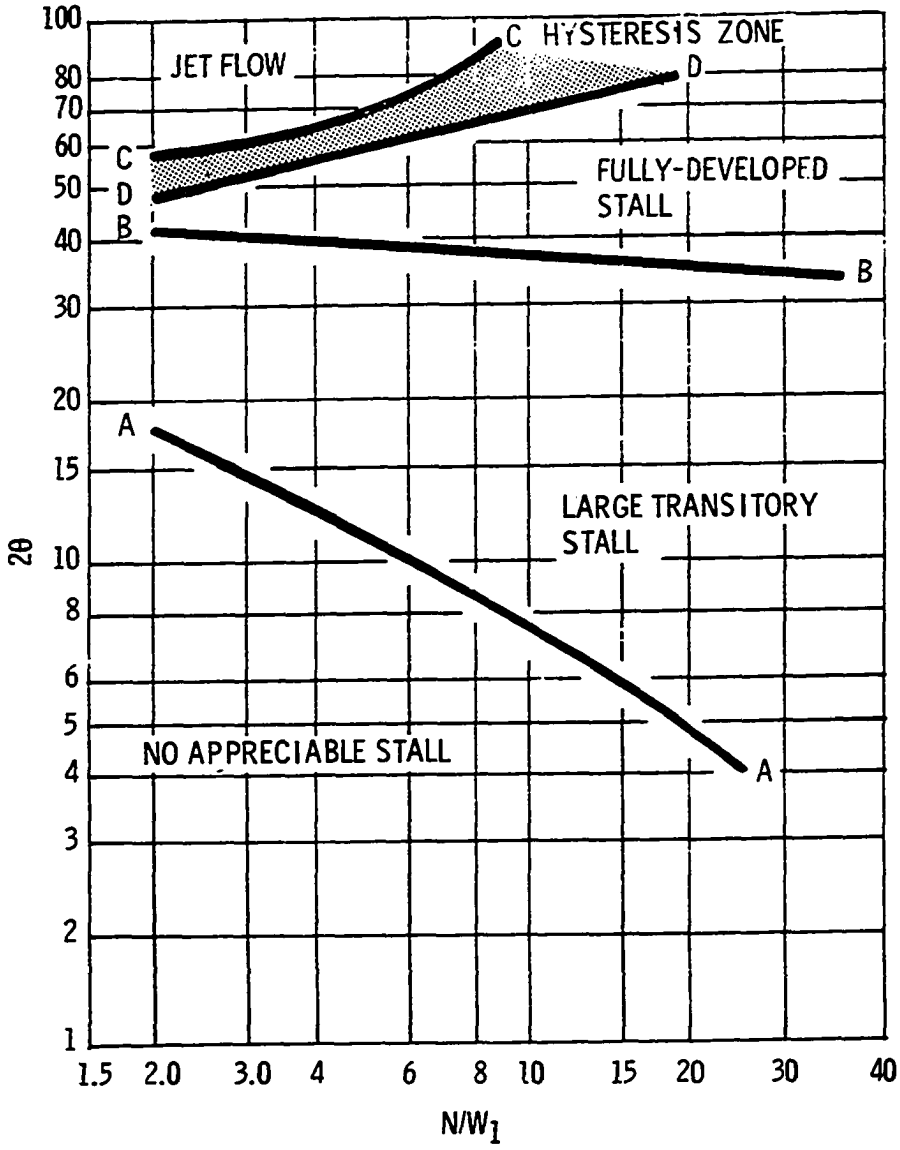

Figure 1. Flow regimes for straight diffusers, Fox and Kline (1962)

nature of the flow through the diffuser are quite strongly related to the flow regime in which a given diffuser performs. The performance of a diffuser is summarized with a parameter called the effectiveness, defined as the ratio of actual static pressure increase across the diffuser to the ideal static pressure rise,

$$\eta = \frac{P_2 - P_1}{P_2' - P_1} \qquad (1)$$

where

η = diffuser effectiveness

P_2, P_2' = actual exit static pressure and ideal exit static pressure respectively

P_1 = inlet static pressure

Utilizing the variables determining the flow regimes namely, the divergence angle and the normalized length, it has been possible to establish the performance characteristics of plane straight diffusers for fixed inlet blockage values. Such performance maps were determined by Reneau et al. (1967) and a typical performance map is shown in Figure 2. These performance maps serve as a good design guide for straight diffusers.

The knowledge provided by the flow regime map also serves the important purpose of indicating what kind of analytical models might be used to predict diffuser

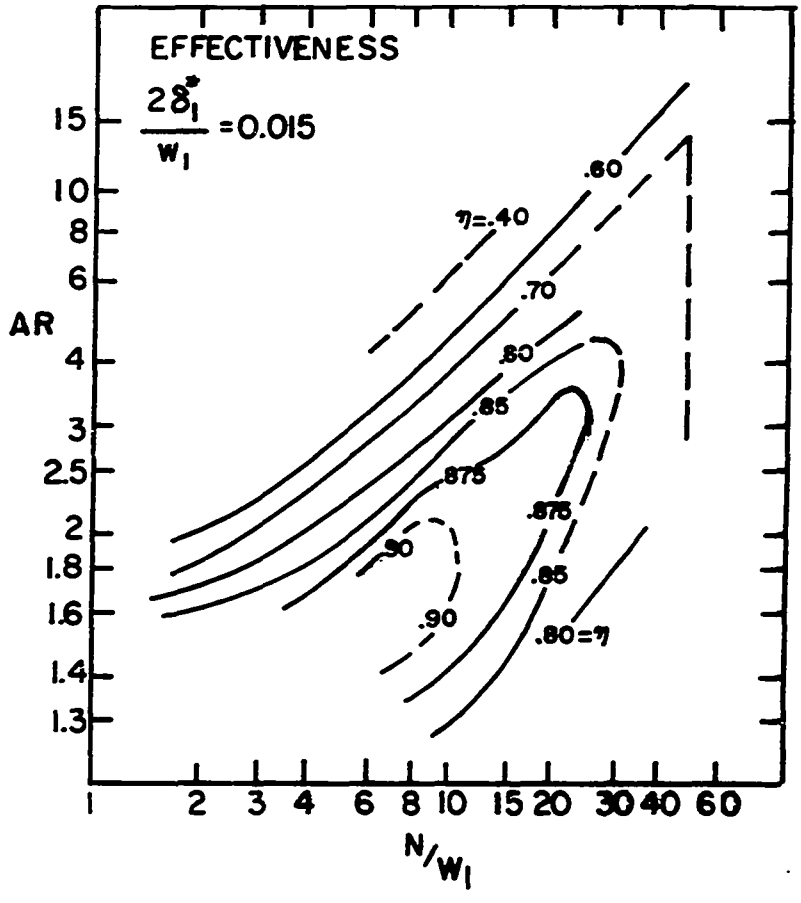

Figure 2. Performance map for straight diffusers, Reneau et al. (1967)

performance. For example, the no appreciable stall regime generally consists of "well behaved" flow made up of a core surrounded by boundary layers on the walls. A model patterned in this fashion has been applied by Schlichting and Gersten (1961) and Reneau and Johnston (1967) to straight, rotationally symmetric and straight two-dimensional diffusers respectively.

A review of Schlichting and Gersten's (1961) approach for the calculation of the flow in rotationally symmetric diffusers with the aid of boundary layer theory will be useful for understanding the basic principles involved in such an application.

The flow is considered steady, incompressible and rotationally symmetric with the nomenclature and geometry as presented in Figure 3. The momentum equation can be written in general form as follows:

$$\int_{\tau} \frac{\partial}{\partial t} (\rho \bar{V}) d\tau + \int_{A} \bar{V} \rho \bar{V} \cdot \bar{n} dA = \Sigma \bar{F} \qquad (2a)$$

where

$d\tau$ = element of volume

dA = element of area

$\bar{F}$ = force vector

Equation 2a can be applied to the element dx of Figure 3 by writing it in terms of the mean velocity u, thus

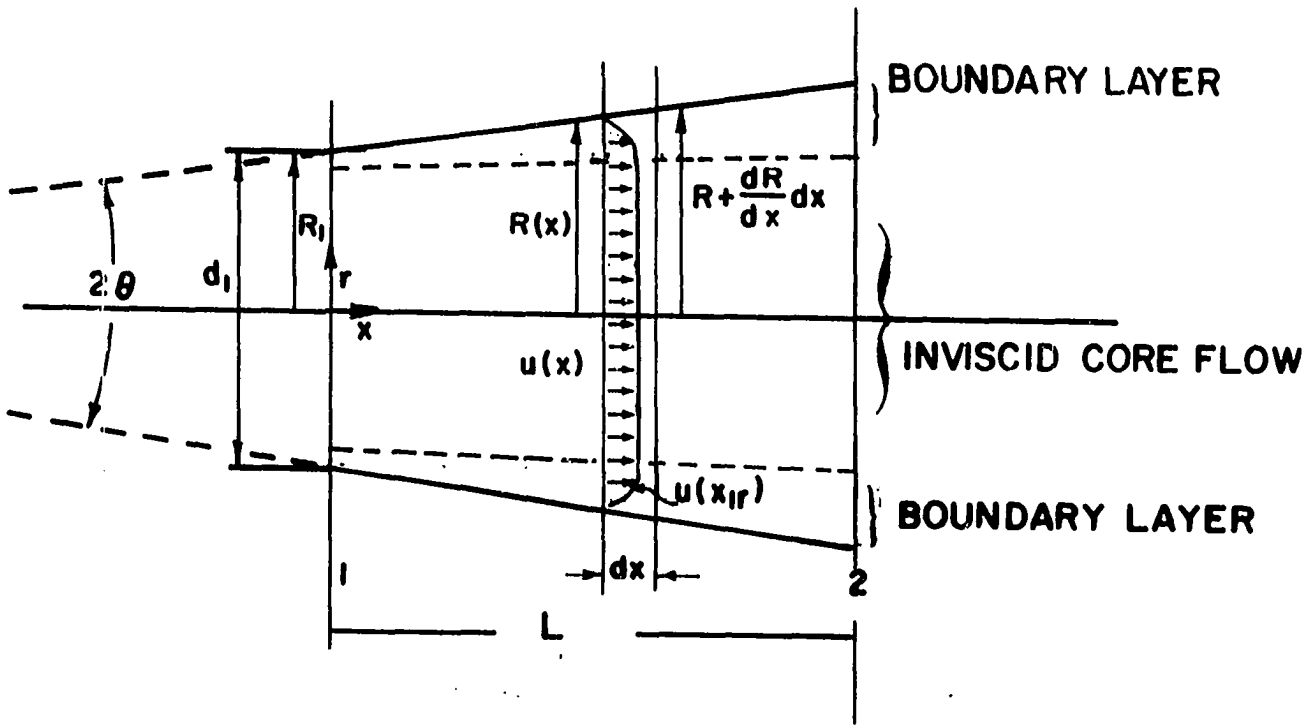

Figure 3. Boundary layer development model and nomenclature

$$-2\pi\rho \int_0^R u^2 r\, dr + 2\pi\rho \int_0^{R + \frac{dR}{dx} dx} (u + \frac{du}{dx} dx)^2 r\, dr$$

$$= \pi R^2 \frac{dP}{dx} dx - \tau_0\, 2\pi\, R dx \qquad (2b)$$

Expanding Equation (2b) yields

$$-2\pi\rho \int_0^R u^2\, rdr + 2\pi\rho \int_0^{R + \frac{dR}{dx} dx} [u^2 + 2u \frac{du}{dx} dx + (\frac{du}{dx} dx)^2] rdr$$

$$= -\pi R^2 \frac{dP}{dx} dx - \tau_0\, 2\pi\, R dx \qquad (3)$$

Note that $\frac{dR}{dx} << 1$, so that it is of second order compared to R. Neglecting higher order terms,

$$2\int_0^R u \frac{du}{dx} dx\, rdr = - \frac{R^2}{2\rho} \frac{dP}{dx} dx - \frac{\tau_0 R}{\rho}$$

or

$$\int_0^R \frac{du^2}{dx} rdr = - \frac{R^2}{2\rho} \frac{dP}{dx} dx - \frac{\tau_0 R}{\rho} \qquad (4)$$

But u(R) = 0, then by Leibnitz rule the equation becomes

$$\frac{d}{dx} \int_0^R u^2\, rdr = - \frac{R^2}{2\rho} \frac{dP}{dx} - \frac{R\tau_0}{\rho} \qquad (5)$$

The left side can be written as

$$\int_0^R u^2\, r dr = U^2 R\left[\frac{R}{2} - \int_0^R \left(1 - \frac{u}{U}\right)\frac{r}{R}\, dr - \int_0^2 \frac{u}{U}\left(1 - \frac{u}{U}\right)\frac{r}{R}\, dr\right]$$

where U(x) is the velocity in the core.

A rotationally symmetric displacement thickness

$$\delta^* = \int_0^R \left(1 - \frac{u}{U}\right)\frac{r}{R}\, dr \tag{6}$$

and momentum thickness

$$\theta = \int_0^R \frac{u}{U}\left(1 - \frac{u}{U}\right)\frac{r}{R}\, dr \tag{7}$$

can be defined. Recalling also that within the core

$$P + \frac{\rho}{2} U^2 = \text{constant.}$$

The momentum theorem gives the result

$$\frac{d}{dx}\left[\frac{U^2R^2}{2} - U^2R^2\delta^* - U^2R\theta\right] = \frac{1}{2} R^2 U \frac{dU}{dx} - \frac{R\tau_0}{\rho} \tag{8}$$

The continuity equation is

$$\frac{d}{dx}\int_0^R ur\, dr = \frac{d}{dx}(\bar{u} R^2) = 0 \tag{9}$$

where

$$\bar{u} = \frac{1}{R^2}\int_0^R ur\, dr$$

Using the displacement thickness one obtains

$$\frac{d}{dx}\left(\frac{UR^2}{2} - UR\delta^*\right) = 0 \tag{10}$$

Substituting the above equation in Equation 8, the momentum equation gives

$$\frac{d}{dx}(U^2 R\theta) + R\delta^* U \frac{dU}{dx} = \frac{R\tau_0}{\rho} \tag{11}$$

If

$$\frac{\delta^*}{\theta} \equiv H \tag{12}$$

then

$$U^2 \frac{d}{dx}(R\theta) + R\theta(H+2)\, U \frac{dU}{dx} = \frac{R\tau_0}{\rho} \tag{13}$$

This relationship is much like the boundary layer equation on a flat plate. In order to solve the above equation for boundary-layer momentum thickness growth a knowledge of the distribution of core velocity U, boundary layer shape factor H, and surface shear stress in the streamwise direction is required. The shear stress has been experimentally correlated for flat plate flow by Ludwieg and Tillman (1949) (see also Schlichting (1968)) and can be approximated well by the formula

$$\frac{\tau_0}{\rho U^2} = 0.123 \cdot 10^{-0.678H} \left(\frac{U\theta}{\nu}\right)^{-0.268} \tag{14}$$

But U and θ are not known. The method of Truckenbrodt (1955) gives an approximate expression for θ

$$\frac{\theta(x)}{R} = \frac{\left[\left(\frac{\theta_1}{R_1}\right)^{5/4} + \frac{0.037^{5/4}}{(U_1 R_1/\ )^{1/4}} \int_0^{x/R_1} \left(\frac{u}{U_1}\right)^{3.5} d\left(\frac{x}{R_1}\right)\right]^{4/5}}{\left(\frac{U}{U_1}\right)^3 \left(\frac{R}{R_1}\right)} \qquad (15)$$

where

U_1 = initial velocity in the core

R_1 = initial radius R

θ_1 = initial momentum thickness θ

The displacement thickness, δ^* can be calculated from the following

$$L = \frac{\xi_1}{\xi} L_1 + \ln \frac{u}{U_1} + \frac{1}{\xi} \int_{\xi_1}^{\xi} (b - \ln \frac{u}{U_1})\, d\xi \qquad (16)$$

where

$$b = 0.07 \log \frac{u\theta}{\nu} - 0.23 \qquad (17)$$

$$\xi = \left(\frac{U}{U_1}\right)^3 \frac{R}{R_1} \frac{\theta}{R_1} \qquad (18)$$

and H = H(L) see Figure 4.

The iteration procedure is begun with entrance boundary layer conditions. Then a displacement thickness is estimated at some downstream distance, dx, away from the entrance. The continuity Equation (10) is used to calculate the velocity in the core. Truckenbrodt's (1955) Equations (15 and 16) can be used to calculate the momentum thickness θ, and the shape factor H. The shear stress is found from Equation 14.

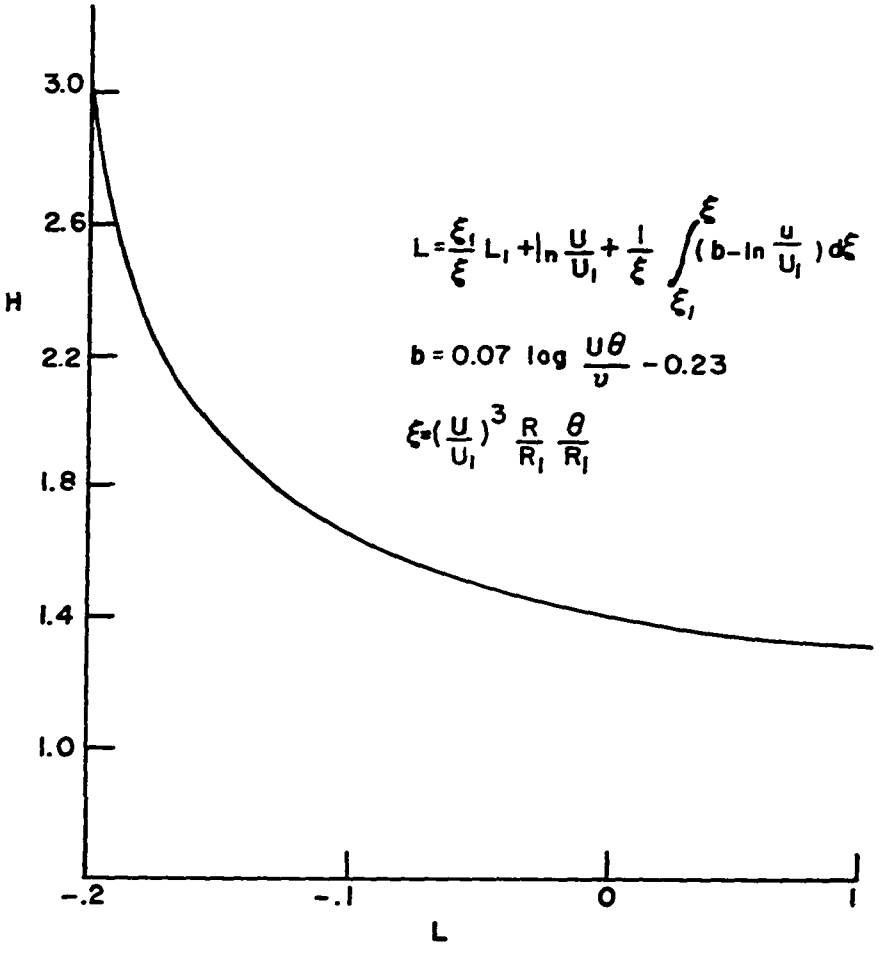

Figure 4. Shape factor correlation, Truckenbrodt (1955)

One must iterate until convergence takes place, then continue onto the next step. The digital computer can readily be used for this purpose.

Summarizing, it is observed that the flow regimes for straight wall diffusers are well defined in terms of the divergence angle (or area ratio) and the normalized length N/W_1. The performance, in terms of the effectiveness, can be obtained from performance maps such as those generated by Reneau et al. (1967). Analytical performance predictions can be made in the no appreciable stall regime using a model consisting of an inviscid core with boundary layer on the walls, as formulated by Schlichting and Gersten (1961) and Reneau and Johnston (1967). There are to date, no satisfactory performance prediction methods valid for the transitory flow regime, the fully developed stall, nor for the jet flow regime.

Curved diffusers

Although curved diffusers are as common as straight diffusers, if not more so, the technology associated with curved diffuser flow is not as advanced as that for straight diffusers.

Flow regimes were established by Fox and Kline (1962) for high aspect ratio curved diffusers each with a circular-arc meanline and linear cross-sectional-area progression. The flow regimes of these curved diffusers depend not only on the

divergence angle (or area ratio) and the normalized length, but also on the diffuser turning angle. Figure 5 shows lines of first appreciable stall for various diffuser turning angles.

A systematic study of curved diffuser performance comparable to that conducted by Reneau et al. (1967) for straight diffusers has not yet been reported in the open literature. However, some important studies of curved wall diffusers were carried out by Sprenger (1959) and Sagi and Johnston (1967) and some performance data were reported by them.

Sprenger (1959) established experimentally that the performance of a curved diffuser with elliptical cross-section depends on the inlet boundary layer thickness, the magnitude of the flow turning angle and the aspect ratio. The aspect ratio is defined as the dimension normal to the plane of the bend divided by the width contained in the plane. According to Sprenger (1959) diffuser effectiveness tends to decrease with increasing inlet boundary layer thickness and flow turning angle, but tends to increase with increase in the aspect ratio. Sprenger's Pitot tube did not permit him to measure the angle of the velocity vector at the exit plane and thus it was possible to get only approximate value of the magnitude of the velocity vector at the exit plane. Since skewing of the boundary layers on the top and bottom walls probably occurred (see for example Francis (1965) and Smith

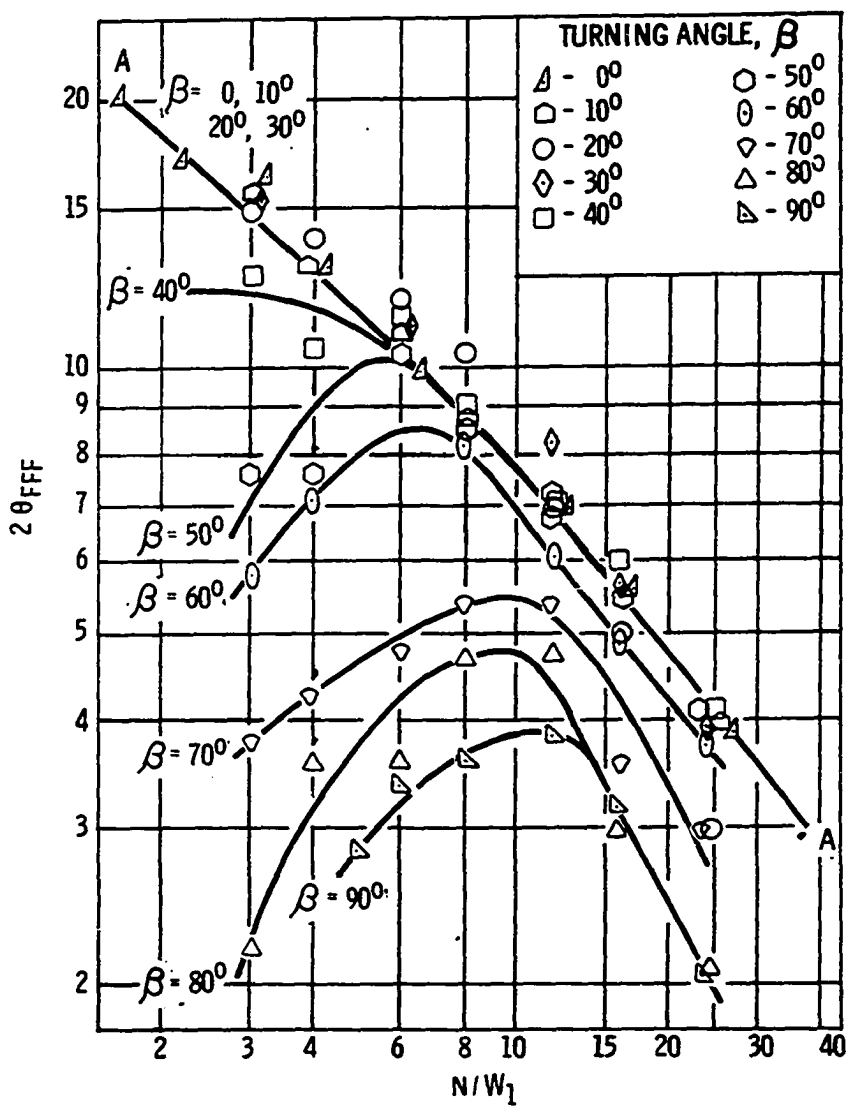

Figure 5. Lines of first appreciable stall for curved two-dimensional diffusers, Fox and Kline (1962)

(1970)) it is unlikely that the exit velocity vector was normal everywhere to the exit plane. Thus Sprenger's study only provides overall effectiveness information.

Sagi and Johnston (1967) made an effort to determine if the effectiveness of a curved circular arc wall diffuser could be raised by appropriately contouring the walls. The approach was based on the nature of the velocity distribution that exists on the inner wall of straight and circular arc curves diffusers as shown in Figure 6. In straight diffusers ($\beta = 0$), the inner wall velocity decreases rapidly in the first portion of the diffuser ($0 < S_{in}/L_{in} < a$), but not so rapidly as the exit is approached. However, curved diffusers with large turning angle (upper curve in Figure 6) exhibit light velocity gradients, possibly even a velocity increase, on the inner wall for $0 < S_{in}/L_{in} < a$, which is then followed by high velocity gradients toward the exit of the diffuser, that is for $S_{in}/L_{in} > a$. Sagi and Johnston (1967) stated that these light negative and/or positive velocity gradients close to the entrance permitted the boundary layer momentum thickness to grow before the adverse pressure gradient is applied. They also noted that adverse pressure gradients are larger, in circular arc curved diffusers than in straight diffusers for $S_{in}/L_{in} > a$.

Theoretical work by Reneau and Johnston (1967) shows that the momentum thickness growth rate increases with the

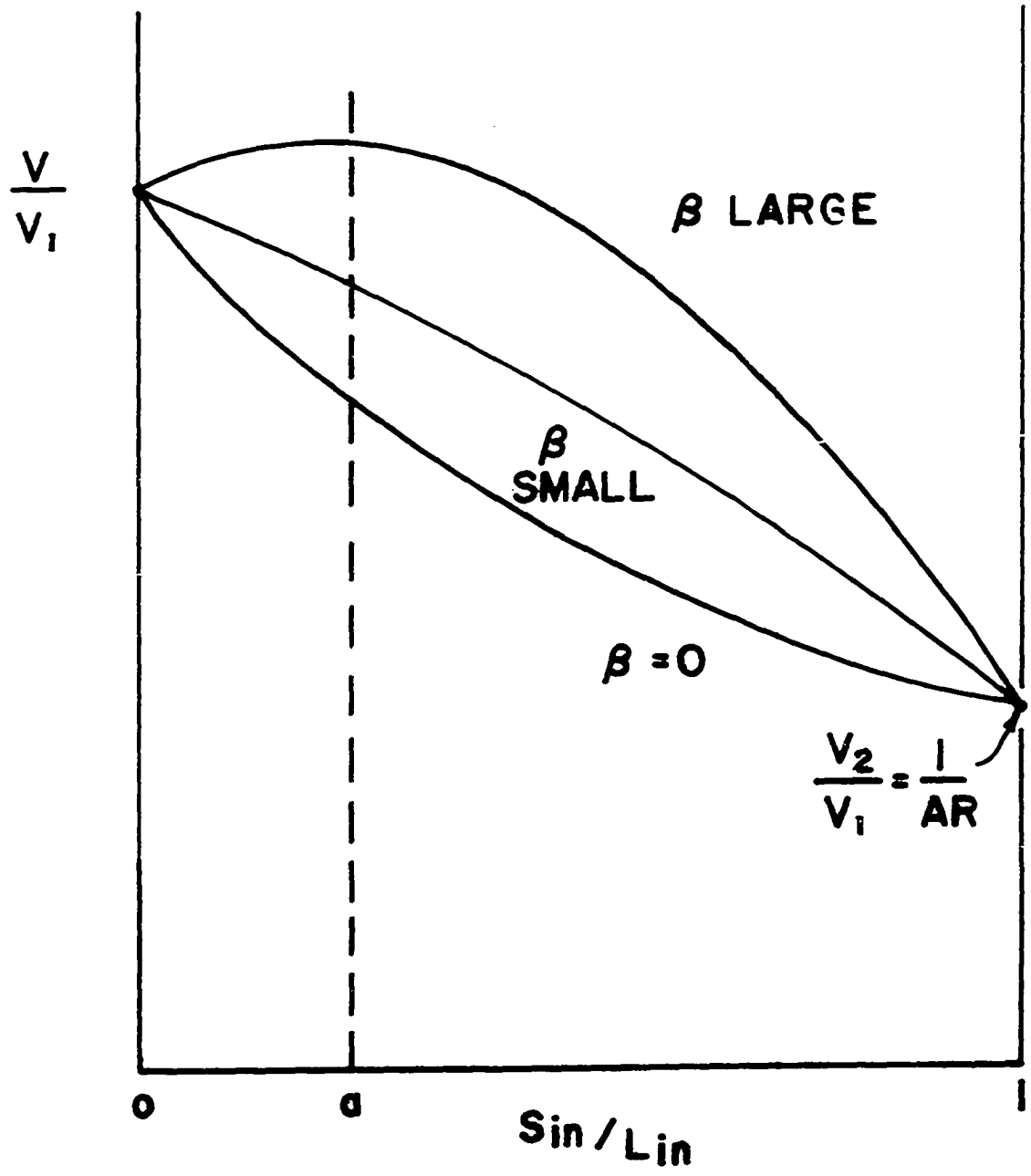

Figure 6. Qualitative variation of the inner wall velocity distribution for fixed area ratio and length, Sagi and Johnston (1967)

momentum thicknesses as shown by the equation

$$\frac{d\theta}{dx} = \frac{\theta}{w_1}\left(\frac{2+H}{2}\right)\left(\frac{w_1}{\frac{1}{2}\rho U^2}\frac{dp}{dx}\right) + \frac{\tau_0}{\rho U^2} \qquad (19)$$

Thus for best performance, the largest pressure gradient should be applied when the boundary layer is thin. The same conclusion was reached by Stratford (1959) and Schubauer and Spangenberg (1960) for external flows (flows over a wing).

Experimental evidence confirming validity of this analysis for curved wall internal flow was provided by Carlson et al. (1967). If the largest pressure gradient is applied initially, followed by a decrease towards the exit, the diffuser will have convex outward (bell shaped) geometry. Carlson et al. (1967) compared the bell shaped diffuser effectiveness to that of straight and trumpet shaped diffuser. The more desirable bell shaped geometry tested by Carlson et al. (1967) is shown in Figure 7, together with the straight and trumpet shaped ones.

Acting on these results, Sagi and Johnston (1965) suggested that the walls of curved wall diffusers should be contoured to provide high pressure gradient near the entrance to obtain improved curved diffuser performance. The contouring of the walls provided reduced inner wall loading and increased the outer wall loading near the entrance. With the above concept they were able to improve the performance

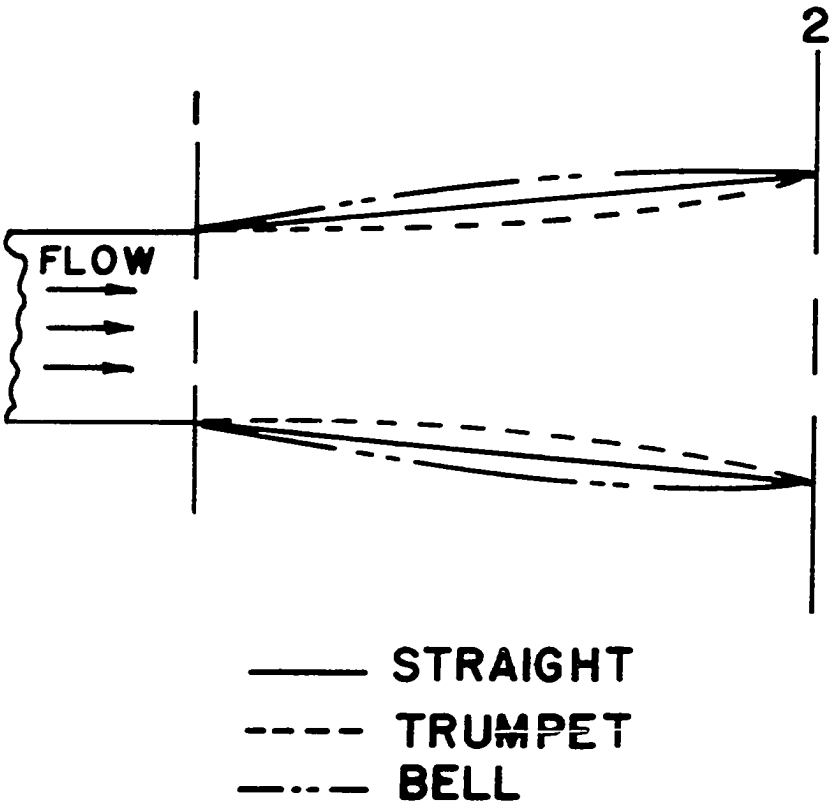

Figure 7. Schematic of diffuser contours, Carlson, et al. (1967)

of curved diffusers. An idea of the required change in the geometry, the resulting wall velocity distribution and magnitude of improvement of the effectiveness is indicated in Figures 8a, 8b and 9 respectively.

The data taken by Sagi and Johnston (1967) were limited since no detailed outlet velocity vector information was taken. However, the inlet conditions were well documented.

During the discussion of curved diffuser performance, Sagi and Johnston (1967) indicated that two other phenomena contribute to the difference in the performance between the straight and the curved diffuser. One of these is the influence of secondary flow. Secondary flows were observed in all of the circular-arc-center-line diffusers they tested which had a turning angle greater than 40° (Fox and Kline (1962)). Sagi and Johnston (1967) assumed secondary flows are partially responsible for the low first-stall limits of curved diffusers with turning angles greater than 40°.

The other phenomenon discussed by Sagi and Johnston (1967) was the curvature effect on the turbulent mixing near the channel wall. Referring to the data of Wattendorf (1935) and Eskinazi and Yeh (1956), they stated that near the inner wall (suction surface) of a curved diffuser the momentum exchange between the inner and outer boundary layer regions is less, while near the outer wall (pressure surface) there is more momentum exchange. This observation is consistent

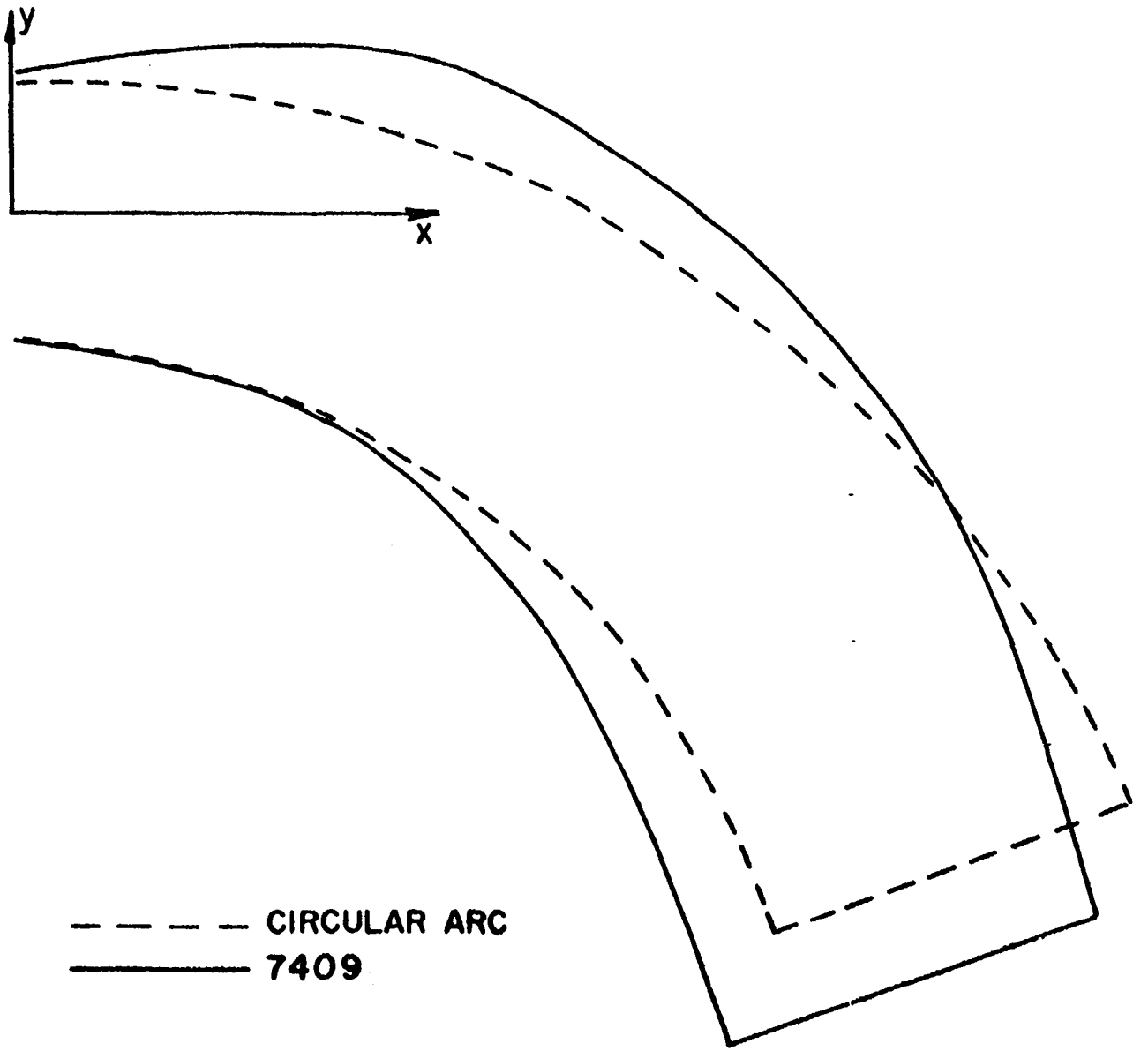

Figure 8a. Comparison of a circular arc diffuser and diffuser with modified wall contour, Sagi et al. (1967)

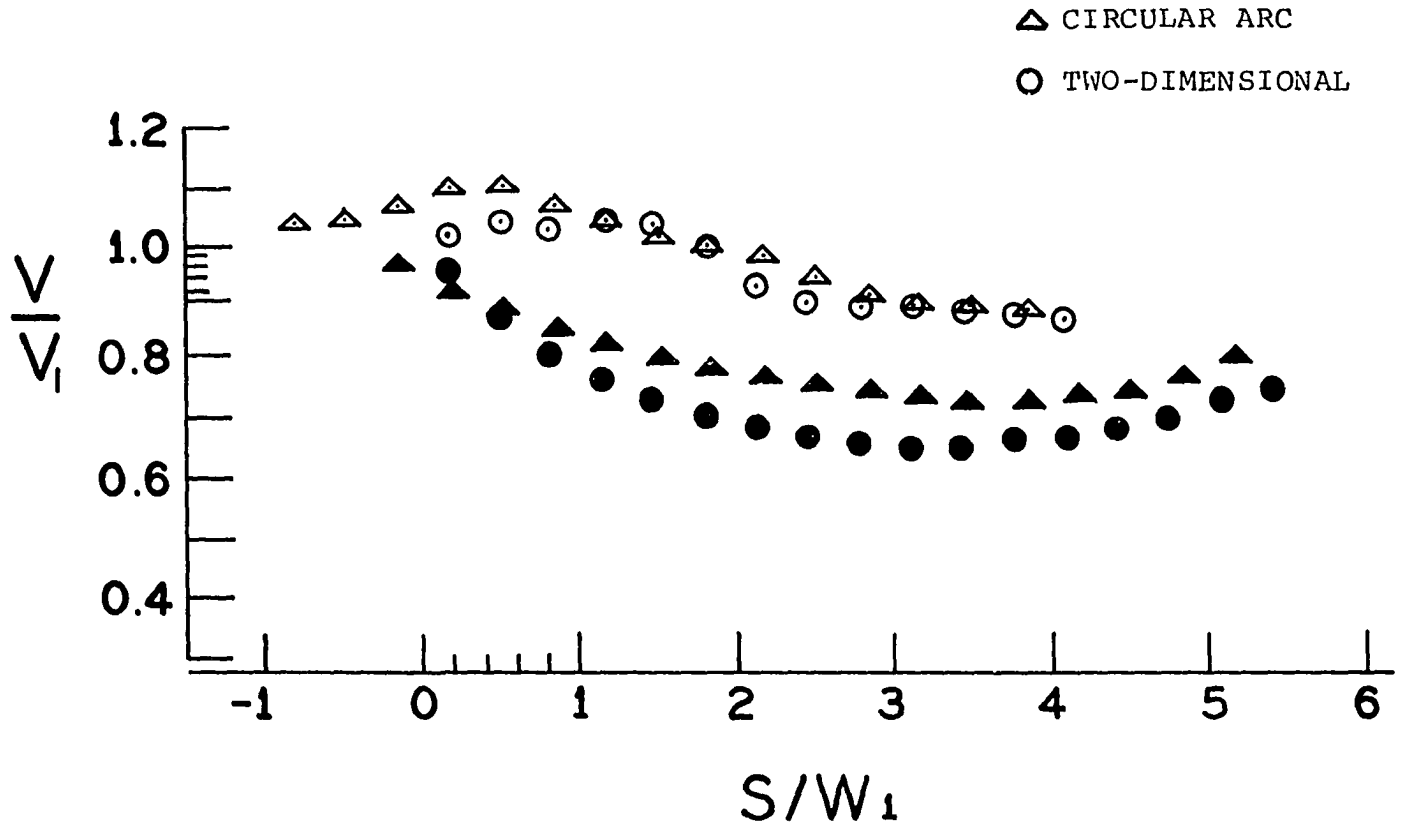

Figure 8b. Measured wall velocity distribution on a circular arc and a two-dimensional diffuser, Sagi et al. (1965)

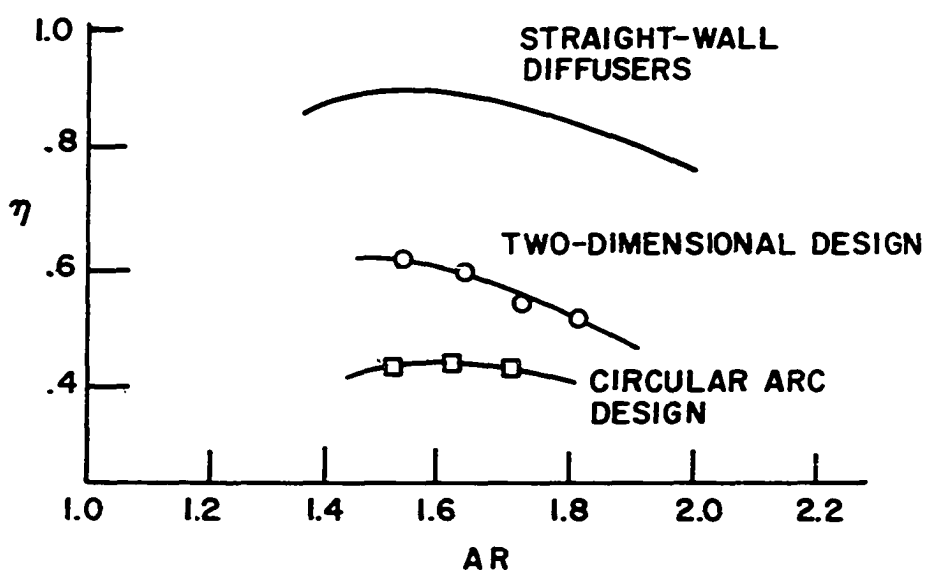

Figure 9. Effectiveness comparison of a circular arc and a two dimensional diffuser $\beta=70$, Sagi et al. (1965)

with a stability criteria due to Rayleigh (1916) which is: a stratification of angular momentum about an axis is stable if and only if it increases monotomically outward. On the pressure surface of a curved diffuser the angular momentum per unit mass decreases as one proceeds from the core towards the wall, thus, the flow is unstable causing greater interchange of fluid in the boundary layer and greater turbulence. The boundary layer on the outer wall can therefore withstand a greater pressure gradient. Conversely, the inner wall has less interchange of fluid and thus cannot withstand as great a loading as the outer wall.

Summarizing, the research of Sprenger (1959) and Sagi and Johnston (1967) suggest that curved diffuser effectiveness is significantly dependent on variables such as the inlet boundary layer, aspect ratio, flow turning angle and wall contour. Since the nature of the flow within a curved diffuser is not yet well understood it is difficult to say which of the associated flow phenomena are most important in influencing performance. A careful study of the secondary flow and three dimensional boundary layers in a curved diffuser would probably aid in developing a satisfactory model of the entire diffuser flow field.

Secondary Flows

Introduction

It is useful to define the term "secondary flow" in order to help eliminate ambiguity. A component of the velocity vector that is in a plane normal to the meanline (centerline) of the flow passage is considered to be a component which contributes to secondary flow. The primary component u is parallel to the meanline (centerline) of a passage while v and w are the secondary flow components.

The presence of secondary flows has been known for a long time, Bazin (1865). However, it has only recently been recognized that there are several distinct types of secondary flows. In the discussion that follows, each type of secondary flow will be discussed in relation to its cause. Theoretical as well as experimental evidence will be included in the discussion.

Streamline curvature induced secondary flow

Perhaps the most important of the secondary flows are those which are related to the streamline curvature. Squire and Winter (1951) showed that secondary flows could exist in a curved channel through which an inviscid fluid is flowing, provided the velocity distribution at the inlet was non-uniform. In other words, secondary flows can exist downstream of the entrance to a curved channel in which a

rotational inviscid fluid is flowing. The assumption of zero viscosity implies that the vorticity is conserved, thus, analyses of this type are sometimes known as "frozen vorticity analyses."

A schematic of the inlet velocity distribution and the resulting secondary flows under discussion is shown in Figure 10. The general theory applicable to this type of flow has been presented by Hawthorne (1951) for flow that is:

1. steady
2. inviscid
3. incompressible
4. void of body forces.

The vorticity vector, $\bar{\Omega}$, is obtained by taking the curl of the velocity vector, $\bar{V}$,

$$\bar{\Omega} = \bar{\nabla} \times \bar{V} \tag{20}$$

The vorticity vector can be resolved in a streamwise (tangential) and a normal component,

$$\frac{\Omega_x}{Q} \bar{V} = \left(\frac{\bar{\Omega} \cdot \bar{V}}{\bar{V} \cdot \bar{V}}\right) \bar{V} \qquad \text{streamwise component} \tag{21}$$

and

$$\frac{(\bar{V} \times \bar{\Omega}) \times \bar{V}}{\bar{V} \cdot \bar{V}} \qquad \text{component normal to streamline} \tag{22}$$

where

Ω_x = magnitude of streamwise vorticity

Q = magnitude of the velocity vector $\bar{V}$

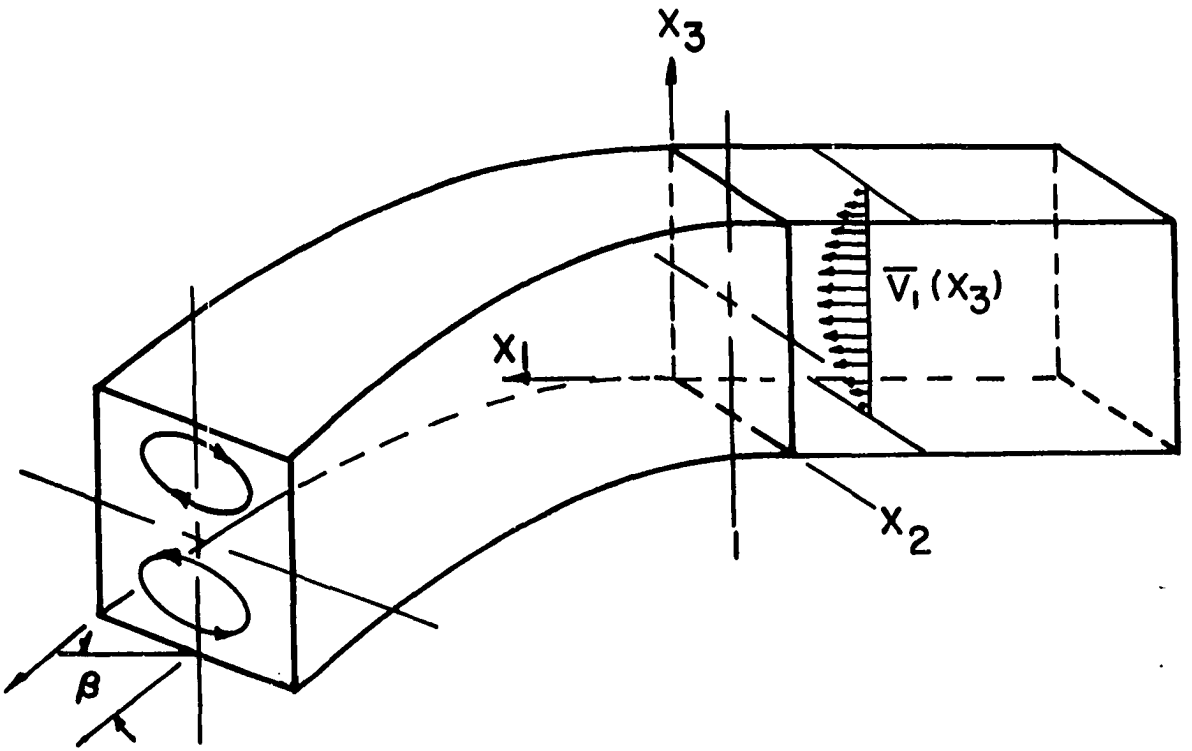

Figure 10. Schematic of secondary flow due to streamline curvature

Recall that the divergence of the curl of a vector is zero,

$$\overline{\nabla} \cdot (\overline{\nabla} \times \overline{V}) = \overline{\nabla} \cdot \overline{\Omega} = 0. \tag{23}$$

Writing the vorticity vector, $\overline{\Omega}$, in terms of its streamwise and normal components using Equations 21 and 22 yields

$$\overline{\nabla}\left(\frac{\overset{\Omega}{x}}{Q} \overline{V}\right) - \overline{\nabla} \cdot \left(\frac{\overline{V} \times (\overline{V} \times \overline{\Omega})}{\overline{V} \cdot \overline{V}}\right) = 0 \tag{24}$$

Performing the required operation one obtains

$$\frac{\overset{\Omega}{x}}{Q}(\overline{\nabla} \cdot \overline{V}) + \overline{\nabla} \cdot \overline{\nabla}\left(\frac{\overset{\Omega}{x}}{Q}\right) - \overline{\nabla} \times (\overline{V} \times \overline{\Omega}) \cdot \overline{\nabla}\left(\frac{1}{\overline{V} \cdot \overline{V}}\right) - \frac{1}{Q^2} \overline{\nabla} \cdot (\overline{V} \times (\overline{V} \times \overline{\Omega})) = 0 \tag{25}$$

Noting the identities

$$\overline{\nabla} \cdot (\overline{V} \times (\overline{V} \times \overline{\Omega})) \equiv (\overline{V} \times \overline{\Omega}) \cdot \overline{\nabla}\ \overline{V} - \overline{V} \cdot \overline{\nabla} \times (\overline{V} \times \overline{\Omega})$$

$$\overline{\nabla}(\overline{V} \cdot \overline{V}) \equiv 2(\overline{V} \cdot \overline{\nabla})\overline{V} + 2\overline{V} \times (\overline{\nabla} \times \overline{V})$$

and with the assumptions above

$$\overline{V} \times \overline{\Omega} = \overline{\nabla}\left(\frac{P}{\rho} + \frac{1}{2} Q^2\right) = \overline{\nabla}\left(\frac{P_T}{\rho}\right)$$

The continuity equation for an incompressible fluid is

$$\overline{\nabla} \cdot \overline{V} = 0$$

The resulting equation becomes

$$\overline{\nabla} \cdot \overline{\nabla}\left(\frac{\overset{\Omega}{x}}{Q}\right) = \frac{-\overline{V} \times (\overline{V} \times \overline{\Omega}) \cdot 2(\overline{V} \cdot \overline{\nabla})\overline{V}}{Q^4} \tag{26}$$

Inspection of the left hand side of Equation 26 reveals that it is proportional to the velocity vector and the change of the secondary flow along the streamline. On the right hand side of the equation is a triple product of the velocity vector, a vector $(\overline{V}\times\overline{\Omega})$ and the vector $2(\overline{V}\cdot\overline{\nabla})\overline{V}$. The velocity vector is, of course, along the streamline, the vector $(\overline{V}\times\overline{\Omega})$ is normal to the Bernoulli surface containing the streamline, and also the velocity vector. The Bernoulli surface is defined as a surface which is characterized by a constant value of the stagnation pressure, that is, a surface of constant $P + \frac{1}{2}\rho Q^2$. The vector $(\overline{V}\cdot\overline{\nabla})\overline{V}$ is recognized as the convective acceleration and can be resolved into streamwise and normal (principal normal) components. The component of acceleration along the principal normal is $\frac{Q^2}{R}$. ϕ is defined as the angle between the principal normal and vector $(\overline{V}\times\overline{\Omega})$, normal to the Bernoulli surface (Figure 11). The only component of acceleration entering into the right hand side triple product of Equation 26 is $(\text{Sin } \phi)\frac{Q^2}{R}$, the other component is coplanar and therefore zero. Thus,

$$\overline{V}\cdot\overline{\nabla}\left(\frac{\Omega_x}{Q}\right) = -2Q\left|\overline{\nabla}\left(\frac{P_T}{\rho}\right)\right|\frac{\sin\phi}{Q^2R} \tag{27}$$

Integration along the streamline yields

$$\left(\frac{\Omega_x}{Q}\right)_2 - \left(\frac{\Omega_x}{Q}\right)_1 = -2\int_1^2 \frac{1}{Q^2}\left|\overline{\nabla}\left(\frac{P_T}{\rho}\right)\right|\frac{\sin\phi}{R}\,ds \tag{28}$$

where ds is an element of arc measured along the streamline, 1 and 2 are upstream and downstream stations respectively.

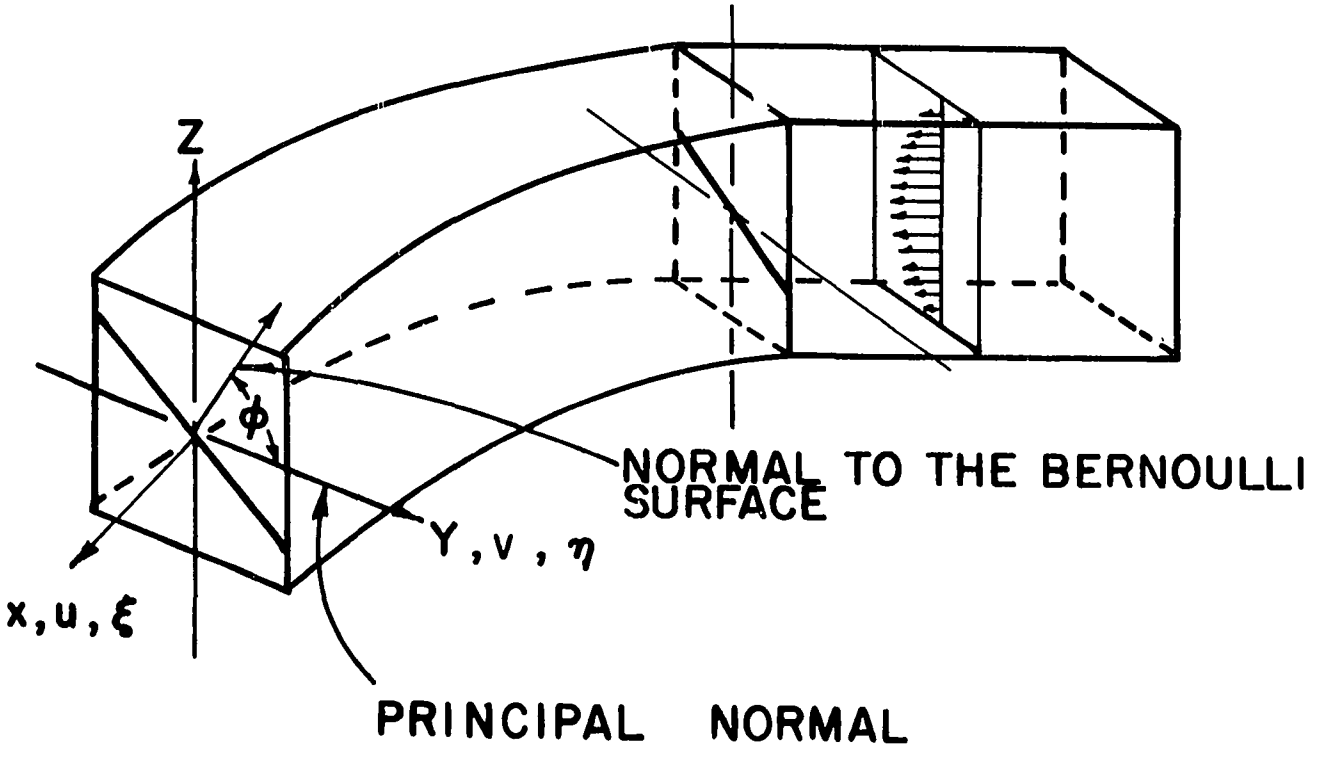

Figure 11. Model showing normal to Bernoulli surface

By definition

$$\frac{1}{R} = \frac{d\theta}{ds}$$

where

R = the radius of curvature

$d\theta$= the angle between tangents to the streamline at points arc length, ds apart

Thus, Equation 28 may be written

$$\left(\frac{\Omega_x}{Q}\right)_2 - \left(\frac{\Omega_x}{Q}\right)_1 = -2\int_1^2 \frac{1}{Q^2}\left|\overline{\nabla}\left(\frac{P_T}{\rho}\right)\right|\sin\phi\, d\theta \qquad (29)$$

If the vorticity in the streamwise direction is zero at station 1, $\phi = 90°$ and constant, and q changes little along the streamline, then Equation 29 can be integrated to yield

$$\left(\frac{\Omega_x}{Q}\right)_2 - \left(\frac{\Omega_x}{Q}\right)_1 = -2\,\frac{Q}{Q^2}\,\Omega_y\,\varepsilon \qquad (30)$$

where

$\Omega_y = \frac{\partial v}{\partial z}$ (Figure 10)

ε = flow turning angle in radians

Note that

$$Q\Omega_y = \overline{\nabla}\left(\frac{P_T}{\rho}\right) = \overline{\nabla}\left(\frac{P}{\rho} + \frac{1}{2}Q^2\right) = (\overline{V}\cdot\overline{\nabla})\overline{V}$$

and

$$\overline{V} = \overline{V}(z)$$

It is important to recognize here that secondary flow depends on inlet velocity distribution, that is on $\frac{\partial \overline{V}}{\partial z}$, and on the flow

turning angle ε. That these variables influence the actual performance of curved diffuser was mentioned previously.

An alternate approach to the analysis of secondary flow has been published by Puzyrewski (1964). The flow was considered to be:

1. steady
2. inviscid
3. barotropic
4. void of body forces

If the continuity and Helmholtz vortex theorem are applied to a vortex tube (a material tube), at times t_1 and t_2 respectively, the result is

$$\rho_1 \delta \ell_1 A_1 = \rho_2 \delta \ell_2 A_2 \qquad \text{Continuity} \qquad (31)$$

$$\bar{\Omega}_1 A_1 = \bar{\Omega}_2 A_2 \qquad \text{Helmholtz theorem} \qquad (32)$$

where

$\bar{\Omega}$ = vorticity vector

ρ = density

$\delta \ell$= an element length of the vortex tube

A = vortex tube cross sectional area perpendicular to $\bar{\Omega}$

The above two equations may be solved for the vorticity at t_2,

$$\bar{\Omega}_2 = \frac{\rho_2}{\rho_1} \bar{\Omega}_1 \frac{\delta \ell_2}{\delta \ell_1} \qquad (33)$$

Projecting in the streamwise direction results in the streamwise vorticity

$$\Omega_{x2} = \frac{\rho_2}{\rho_1} \bar{\Omega}_1 \frac{\delta \ell_2}{\delta \ell_1} \cos \varepsilon_2 \tag{34}$$

where

ε_2 is the angle between the vorticity vector and the streamwise direction (tangent to the streamline).

It can be seen from Figure 12 that

$$\delta \ell_2 \cos \varepsilon_2 = \Delta S_2 \simeq S - S' + \Delta S_1 \tag{35}$$

Dividing by $\delta \ell_1$, and considering the limit as $\delta \ell_1 \to 0$ the result is:

$$\frac{\delta \ell_2}{\delta \ell_1} \cos \varepsilon_2 = \lim_{\delta \ell_1 \to 0} \frac{\Delta S_2}{\delta \ell_1} = \frac{\delta}{\delta \ell_1} \int_1^2 u dt + \cos \varepsilon_1 \tag{36}$$

Then the secondary vorticity is

$$\Omega_{x2} = \frac{\rho_2}{\rho_1} (\bar{\Omega}_1 \frac{\delta}{\delta \ell_1} \int_1^2 u dt + \Omega_{x1} \tag{37}$$

And the change in the secondary vorticity is

$$\Omega_{x2} - \Omega_{x1} = \frac{\rho_2}{\rho_1} \bar{\Omega}_1 \frac{\delta}{\delta \ell_1} \int_1^2 u dt + \Omega_{x1} (\frac{\rho_2}{\rho_1} - 1) \tag{38}$$

If one assumes a potential velocity field as a first approximation, at a given plane z_a, Figure 13, it is possible to calculate the quantity

$$\phi \simeq \frac{\Delta S_2}{\Delta \ell_1} = \frac{\delta}{\delta \ell_1} \int_1^2 u dt$$

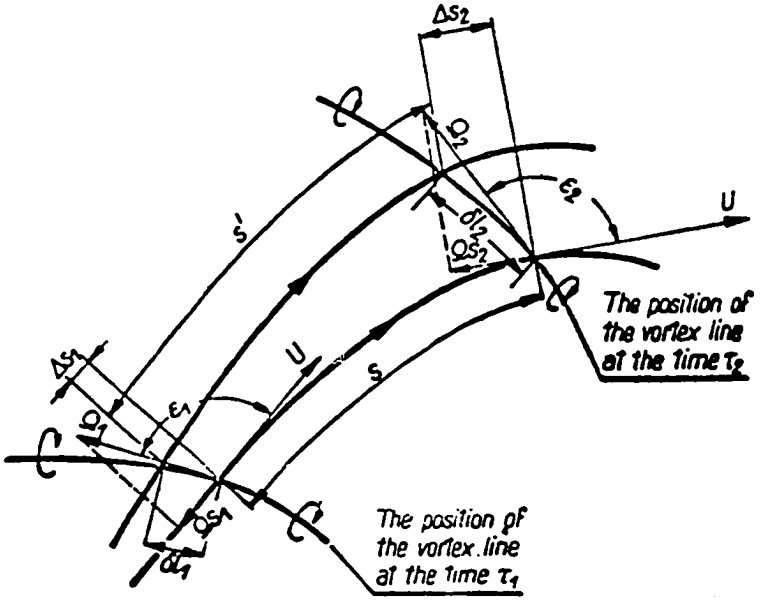

Figure 12. Puzyrewski's (1964) model

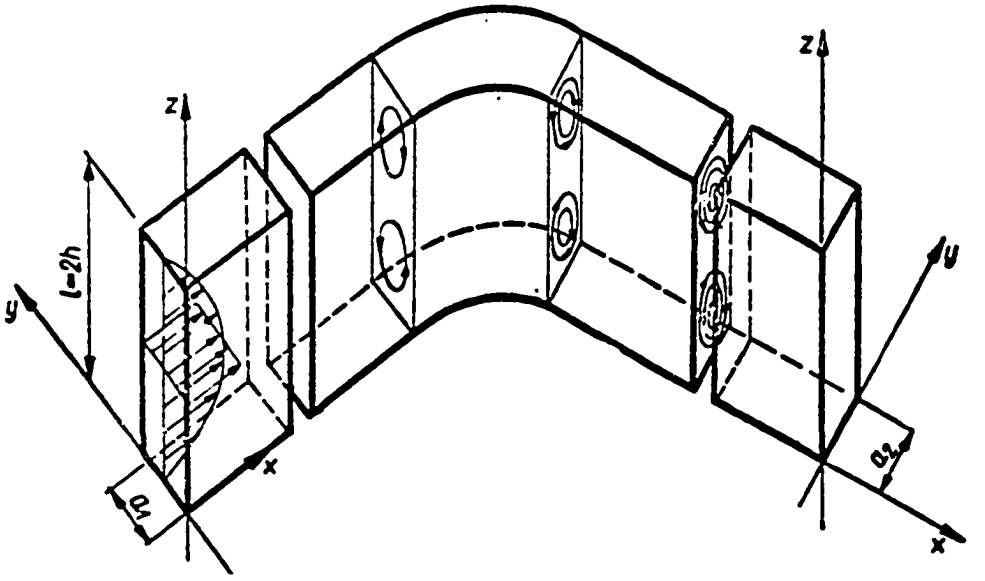

Figure 13. Secondary flow development, Puzyrewski (1964)

(if $\Omega_{x1} = 0$)

By using the finite difference method, so that:

$$\Omega_{x2} = \frac{\rho_2}{\rho_1} \bar{\Omega}_1 \phi \tag{39}$$

A physical feeling for the means by which secondary flow is generated may be obtained by considering the particles in a given vortex line, for a fixed value of z. A potential flow solution shows that the particles close to the inner (suction) wall travel faster than particles in the vicinity of the outer (pressure) wall. Because of this, two things happen. The vortex line is stretched increasing vorticity and the angle between the vortex line and the streamline becomes obtuse yielding a component of vorticity along the streamline, thus, secondary flow results (see Figure 14). The magnitude of the secondary flow is related, of course, to the difference in the velocity between the inner and outer walls. If the difference in velocities is reduced, less secondary flow will be generated.

It is believed that Sagi and Johnston's (1967) method of improving curved diffuser performance in effect reduces secondary flow by reducing the difference in velocities by proper wall contouring as shown in Figure 8b.

Several additional mathematical analyses of secondary flows in cascades were executed by Gomi (1967), Horlock et al.

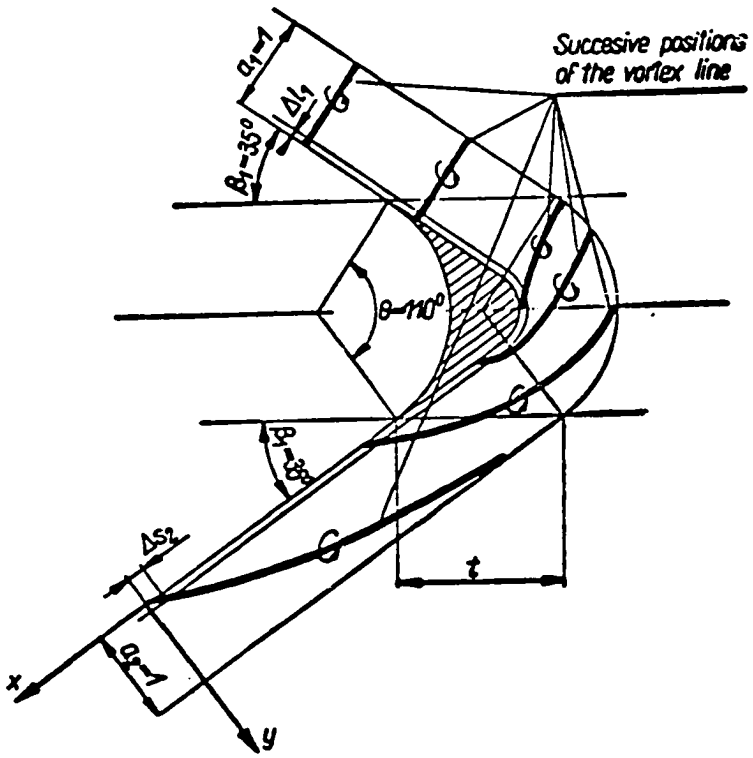

Figure 14. Vortex line positions, Puzyrewski (1964)

(1966), Masuda and Otsuka (1966), Smith (1955), Lakshminarayana and Horlock (1967), Belik (1968) and Loos (1953). Some of these, Lakshminarayana and Horlock (1967) and Belik (1968), for example, consider the problem simply as channel flow. Such analysis are also applicable to the flow in a plane curved diffuser.

Lakshminarayana and Horlock (1967) and Soderberg (1958) attempted to determine the magnitude and direction of the secondary flows that might exist at the end walls of a cascade. The end walls are the horizontal surfaces in Figure 15, which correspond to the top and bottom walls of the diffuser tested by the author. They simulated the inlet velocity distribution with a midspan wake. Soderberg (1958) observed the maximum skewing angle midway between the blades. He also reported an average skewing angle which he obtained by integrating across the blade spacing. The form of these curves was the same. It is not clear how Lakshminarayana and Horlock (1967) calculated the average skewing angle.

It is pertinent to note that they observed an average skewing of the velocity vector toward the suction wall (overturning) for the flow very close to the end wall and an average skewing away from the suction wall (underturning) at some distance further out, but still within the boundary layer. Further, the uniform core flow exhibited

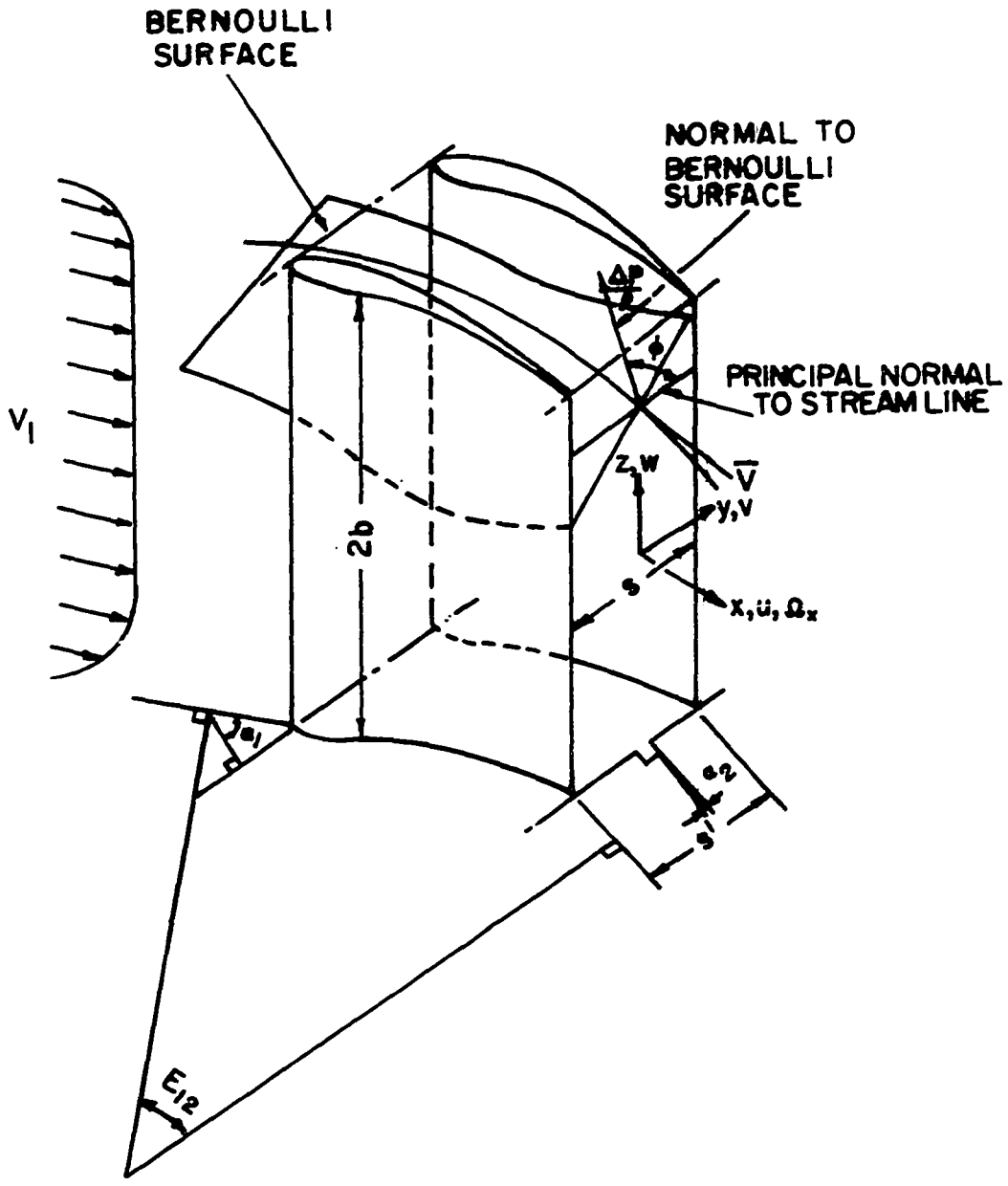

Figure 15. Lakshminarayana and Horlock's (1967) simulated cascade flow

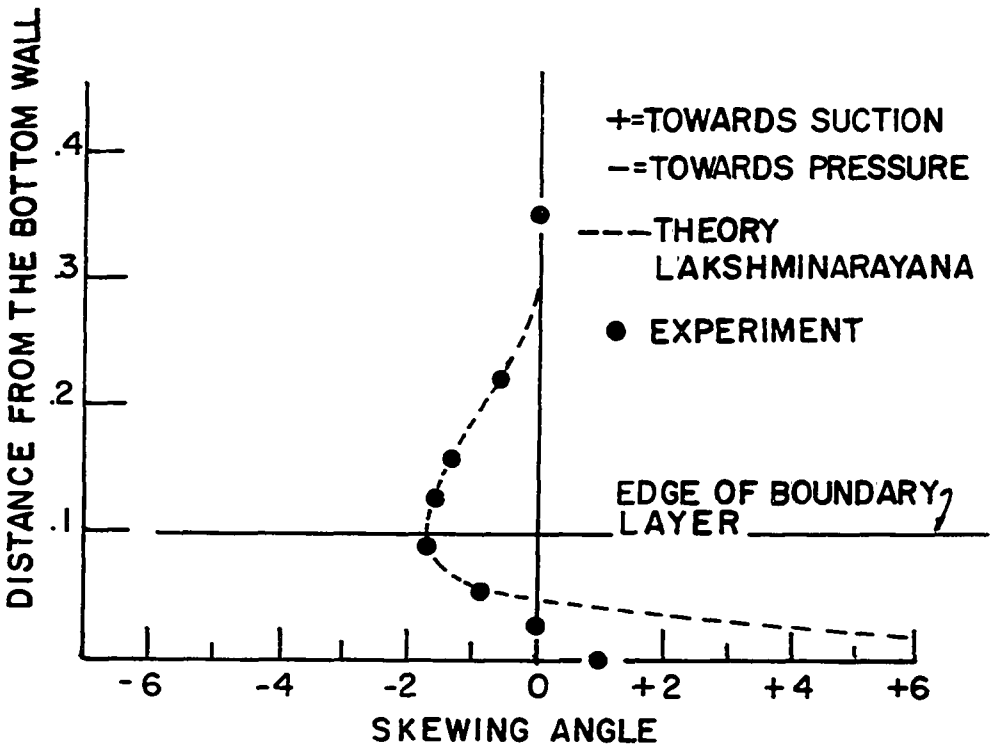

Figure 16. Lakshminarayana and Horlock's (1967) results from simulated cascade flow

an average skewing toward the pressure wall which diminished as the passage centerline was approached. These skewing trends are summarized in Figure 16.

Turbulence induced secondary flow

Secondary flows that are related to turbulence were originally observed in channels with corners and thus attributed for a long time to the flow in the corner itself. On the basis of the theoretical and experimental evidence available, it seems as if the cause of these secondary flows is turbulence. A schematic of the type of secondary flow under discussion is shown in Figure 17. The magnitude of secondary flow due to turbulence has been estimated by Pletcher (1962) to be in the order of 2% of the primary flow.

The mechanism governing the secondary flow induced by turbulence is not fully understood at this time. There are, however, at least two analyses that shed light on the nature of the phenomenon.

The analysis of Einstein and Li (1958) is based on the general vorticity transport equation written in the axial direction

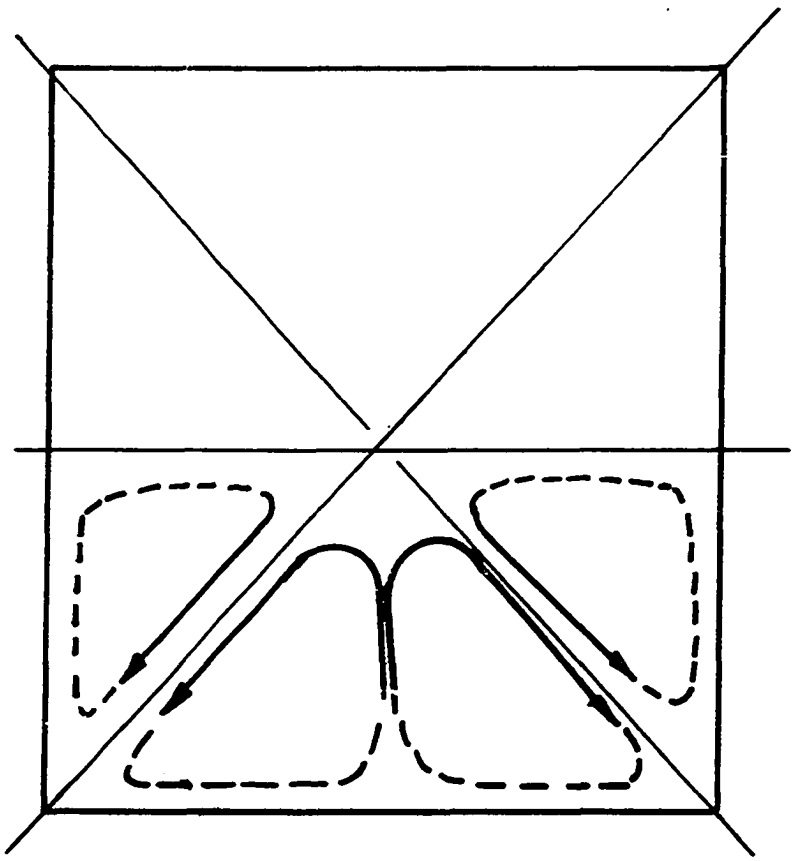

Figure 17. Schematic of secondary flow into the corner

$$\frac{D}{Dt}\,\Omega_x = \Omega_x \frac{\partial U}{\partial x} + \Omega_y \frac{\partial U}{\partial y} + \Omega_z \frac{\partial U}{\partial z} + \nu\nabla^2\,\Omega_x$$

$$+ \frac{\partial^2}{\partial x \partial z}\,(\overline{u'v'}) + \frac{\partial^2}{\partial y \partial z}\,(\overline{v'^2}) + \frac{\partial^2}{\partial z^2}\,(\overline{v'w'})$$

$$- \frac{\partial^2}{\partial x \partial y}\,(\overline{u'w'}) - \frac{\partial^2}{\partial y^2}\,(\overline{v'w'}) - \frac{\partial^2}{\partial y \partial z}\,(\overline{w'^2}) \qquad (41)$$

Einstein and Li (1958) attempted to answer the question, "Under what conditions will secondary flow in the axial direction be generated if the initial secondary vorticity was zero?" The flow was assumed to be:

1. straight and uniform;

2. with initial vorticity zero.

The first assumption, reduces the total derivative of the axial vorticity to the time derivative,

$$\frac{\partial \Omega_x}{\partial t} + U \frac{\partial \Omega_x}{\partial x} + V \frac{\partial \Omega_x}{\partial y} + W \frac{\partial \Omega_x}{\partial z} = \frac{\partial \Omega_x}{\partial t} \qquad (41)$$

since

$$\frac{\partial}{\partial x} = 0, \quad V = 0 = W.$$

The derivatives in the axial direction are zero, then the fifth and the eighth terms on the right side of Equation 41 become zero. The second assumption eliminates the Laplacian of the vorticity, the simplified equation being,

$$\frac{\partial \Omega_x}{\partial t} = \frac{\partial^2}{\partial y \partial z} (\overline{v'^2} - \overline{w'^2}) - \frac{\partial^2}{\partial y^2} (\overline{v'w'}) + \frac{\partial^2}{\partial z^2} (\overline{v'w'}) \quad . \quad (42)$$

The remaining terms on the right hand side are only turbulent terms. In view of this fact, Einstein and Li (1958) concluded that this type of secondary flow could not exist in laminar flow or in isotropic turbulent flow.

It was shown later by Brundrett and Baines, (1964) that the term $\overline{v'w'}$ is exceedingly small and cannot account for the generation of axial vorticity. The remaining equation

is therefore

$$\frac{\partial}{\partial t}\,\Omega_x \simeq \frac{\partial^2}{\partial y \partial z}\,(\overline{v'^2} - \overline{w'^2}) \tag{43}$$

At this time the data is not sufficiently accurate nor plentiful to verify this relationship.

Hinze (1967) proposed that secondary flow should be analyzed utilizing the mechanical turbulent energy equation,

$$\frac{d}{dt}\,(\frac{\overline{u_i u_i}}{2}) + \frac{\partial}{\partial x_i}\,\overline{u_i(\frac{p}{\rho} + \frac{u_i u_i}{2})} = -\overline{u_i u_j}\,\frac{\partial \bar{U}_j}{\partial x_i} +$$

$$\frac{\partial}{\partial x_i}\,[\nu\, u_j(\frac{\partial u_j}{\partial x_i} + \frac{\partial u_i}{\partial x_j})] - \nu(\frac{\partial u_i}{\partial x_j} + \frac{\partial u_j}{\partial x_i})\,\frac{\partial u_j}{\partial x_i} \tag{44}$$

where the terms represent the following:

I kinetic energy of turbulence

II convective diffusion by turbulence of total turbulent energy

III production of turbulent energy (Energy transferred from mean motion through turbulent shear stresses)

IV work done per unit mass and time by the viscous shear stresses of the turbulent motion

V dissipation per unit mass by turbulent motion.

If the flow is assumed to be:

1. steady
2. homogeneous in the x_1 direction
3. with derivatives in x_1 direction negligible

the equation becomes

$$\bar{U}_2 \frac{\partial}{\partial x_2}\left(\frac{\overline{u_i u_i}}{2}\right) + \bar{U}_3 \frac{\partial}{\partial x_3}\left(\frac{\overline{u_i u_i}}{2}\right) + \frac{\partial}{\partial x_2}\overline{u_2\left(\frac{u_i u_i}{2} + \frac{p}{\rho}\right)}$$

$$+ \frac{\partial}{\partial x_3}\overline{u_3\left(\frac{u_i u_i}{2} + \frac{p}{\rho}\right)} = -\overline{u_2 u_1}\frac{\partial \bar{U}_1}{\partial x_2} - \overline{u_3 u_1}\frac{\partial \bar{U}_1}{\partial x_3}$$

$$+ \frac{\partial}{\partial x^2}\overline{\left[u_i\, \nu\left(\frac{\partial u_i}{\partial x_2} + \frac{\partial u_2}{\partial x_i}\right)\right]} + \frac{\partial}{\partial x_3}\overline{\left[u_i\, \nu\left(\frac{\partial u_i}{\partial x_3} + \frac{\partial u_3}{\partial x_i}\right)\right]} - \varepsilon \tag{45}$$

where ε = viscous dissipation

Hinze states that the viscous work terms are only important <u>very</u> close to a wall. Laufer's (1954) measurements show that the third and fourth terms on left hand side (convective diffusion terms) are negligible except near the center region of a circular pipe.

The equation thus simplifies to:

$$\bar{U}_2 \frac{\partial}{\partial x_2}\left(\frac{\overline{u_i u_i}}{2}\right) + \bar{U}_3 \frac{\partial}{\partial x_3}\left(\frac{\overline{u_i u_i}}{2}\right) =$$

$$- \overline{u_2 u_1}\frac{\partial \bar{U}_1}{\partial x_2} - \overline{u_3 u_1}\frac{\partial \bar{U}_1}{\partial x_3} - \varepsilon \tag{46}$$

which can be interpreted to mean

TRANSPORT OF TURBULENT ENERGY = PRODUCTION + DISSIPATION (47)

Based on the above result Hinze (1967) proposed the following rule:

IF PRODUCTION OF TURBULENT ENERGY IS MUCH GREATER (smaller) THAN THE VISCOUS DISSIPATION, THERE MUST BE A TRANSPORT OF TURBULENCE - POOR FLUID INTO (away from) THIS REGION AND A TRANSPORT OF TURBULENCE - RICH FLUID AWAY FROM (into) THE REGION.

Based on the analysis due to Hinze (1967) it can be concluded that such flow may exist in regions far away from the corner. Hinze presented experimental evidence confirming this statement. An example of such secondary flow is presented in Figure 18. This theory might also explain the reason for the secondary flow into the wake behind an obstacle such as a sphere (Figure 19). Since the production of turbulence is known to be high in the wake, it follows from Equation 47 that the flow should be into the wake.

Miscellaneous secondary flows

There are several other types of secondary flows that should be mentioned in this review. Moffatt (1964) has analyzed the viscous corner eddies and shows that their size and intensity decrease exponentially as the vertex of the corner is approached, (Figure 20).

Acoustically induced eddies have been studied both theoretically and experimentally by Hribar and Purdy (1969). The magnitude of the acoustically induced eddies depends on the strength of the acoustic field and the velocity through the duct.

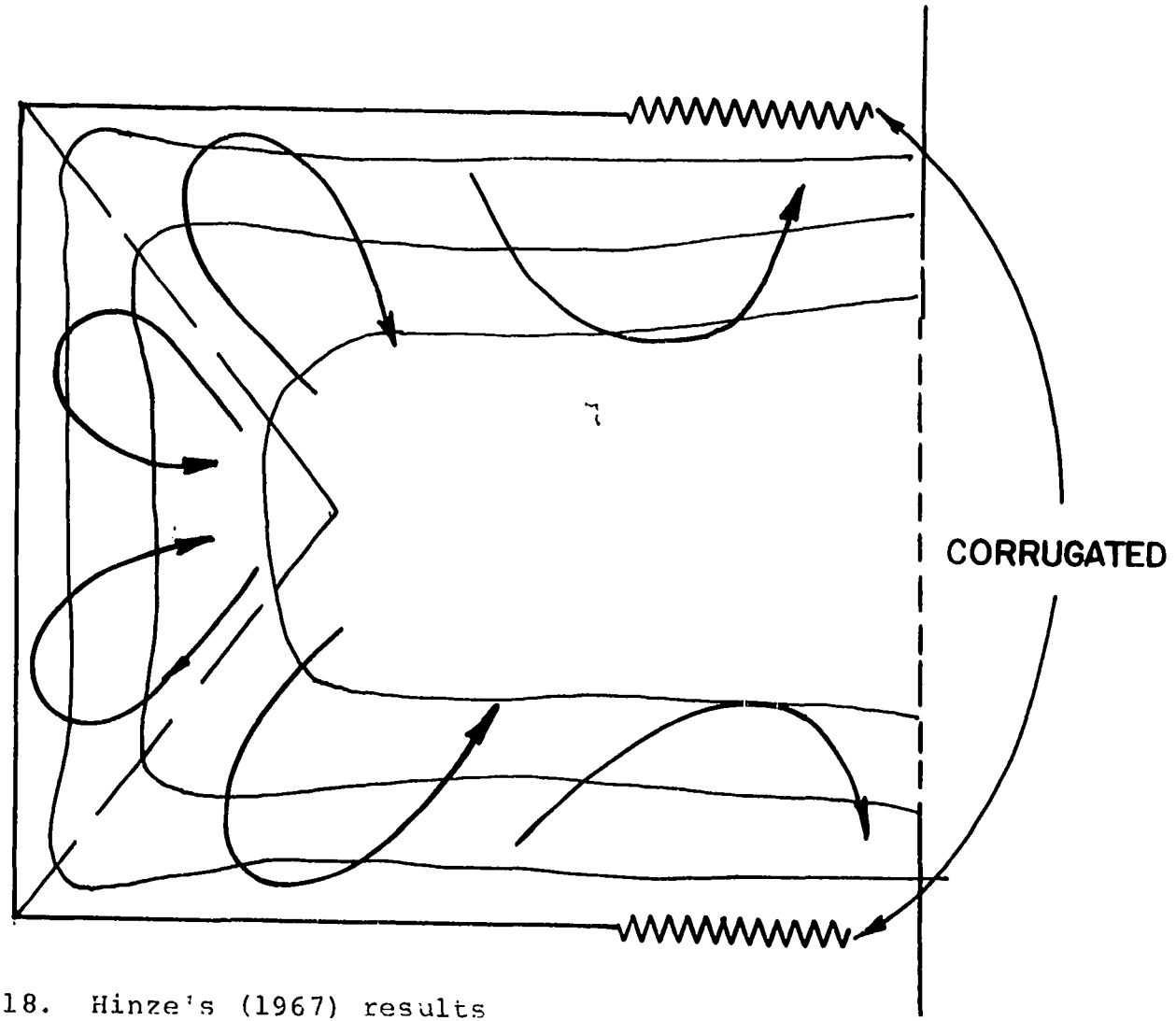

Figure 18. Hinze's (1967) results

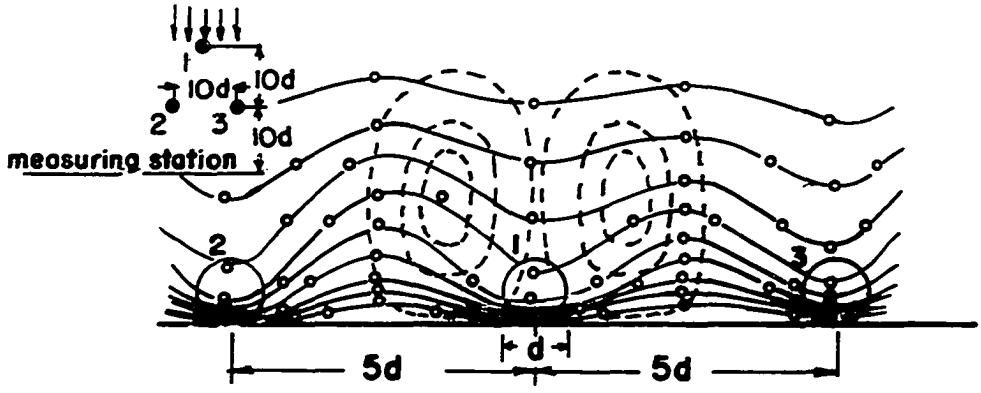

Figure 19. Schlichting's (1968) wake secondary flow

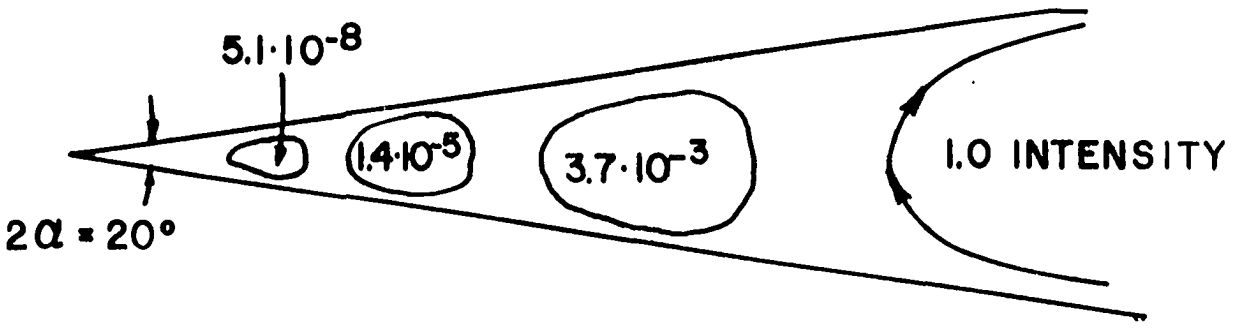

Figure 20. Viscous eddies studied by Moffatt (1964)

Heat transfer induced eddies have been known for some time. This class of flows is referred to as Benard flows (see Chandrasekhar (1962)).

The whole class of boundary layer vortices such as Görtler vortices plays an important role in boundary layer studies (see Görtler (1955)).

Although these miscellaneous types of secondary flows are important, they are considered to be of lesser influence than the secondary flows due to streamline curvature and turbulence.

Three-Dimensional Boundary Layers

Introduction

It has been shown experimentally by Francis and Pierce (1967) that the boundary layer flow along the top and bottom walls (sometimes known as end walls) of a curved passage is three-dimensional. Smith (1970) observed that the end wall boundary layers in a curved diffuser were three-dimensional. In an effort to obtain a better understanding of the boundary layers in a curved diffuser, it is useful to examine some three-dimensional boundary layer models.

As in two-dimensional boundary layer theory, three-dimensional boundary layer analyses can be based on the momentum integral equations. Francis and Pierce (1967) give the momentum integral equations as

$$\frac{1}{h_1}\frac{\partial\theta_{11}}{\partial x_1} + \frac{1}{h_1 U}(2\theta_{11}+\delta_1^*)\frac{\partial U}{\partial x_1} + \frac{1}{h_1 h_2}(2\theta_{12}+\delta_2^*)\frac{\partial h_1}{\partial x_2}$$

$$+ \frac{1}{h_1 h_2}(\theta_{11}-\theta_{22})\frac{\partial h_2}{\partial x_1} + \frac{1}{h_2 U}(2\theta_{12}+\delta_2^*)\frac{\partial U}{\partial x_2}$$

$$+ \frac{1}{h_2}\frac{\partial\theta_{12}}{\partial x_2} = \frac{\tau_{0x_2}}{\rho U^2} \qquad (49)$$

$$\frac{1}{h_2}\frac{\partial\theta_{22}}{\partial x_2} + \frac{2}{h_2 U}\theta_{22}\frac{\partial U}{\partial x_2} + \frac{2}{h_1 h_2}(\theta_{12}+\delta_2^*)\frac{\partial h_2}{\partial x_1}$$

$$+ \frac{1}{h_1 h_2}\frac{\partial h_1}{\partial x_2}(\theta_{22}-\delta_1^*-\theta_{11}) + \frac{2}{h_1 U}(\theta_{12}+\delta_2^*)\frac{\partial U}{\partial x_1}$$

$$+ \frac{1}{h_1}\frac{\partial}{\partial x_1}(\theta_{12}+\delta_2^*) = \frac{\tau_{0x_2}}{\rho U^2} \qquad (50)$$

where

h_1, h_2 = transformation coefficients in x_1, x_2 direction respectively

U = free stream velocity

x_1 = streamwise curvilinear coordinate

x_2 = curvilinear coordinate in the cross flow direction, normal to x_1

η = curvilinear coordinate normal to wall

u, v, w = velocity components in boundary layer in the x_1, x_2, η direction respectively

$$\delta_1^* = \frac{1}{U}\int_0^{\delta} (U-u)\,d\eta \tag{51}$$

$$= \delta\int_0^1 (1 - \frac{u}{U})\,d(\frac{\eta}{\delta})$$

= streamwise displacement thickness

$$\delta_2^* = \frac{1}{U}\int_0^{\delta} (0-v)\,d\eta \tag{52}$$

$$= \delta\int_0^1 (- \frac{v}{U})\,d(\frac{\eta}{\delta})$$

= cross flow displacement thickness

$$\theta_{11} = \frac{1}{U^2}\int_0^{\delta} (U-u)\,u\,d\eta \tag{53}$$

$$= \delta\int_0^1 (1 - \frac{u}{U})\frac{u}{U}\,d(\frac{\eta}{\delta})$$

= streamwise momentum thickness

$$\theta_{12} = \frac{1}{U^2}\int_0^{\delta} (U-u)\,v\,d\eta \tag{54}$$

$$= \delta\int_0^1 (1 - \frac{u}{U})\,(\frac{v}{U})\,d(\frac{\eta}{\delta})$$

= cross flow interaction momentum thickness

$$\theta_{22} = \frac{1}{U^2}\int_0^{\delta} (- v)\,v\,d\eta \tag{55}$$

$$= \delta\int_0^1 (- \frac{v}{U})\,(\frac{v}{U})\,d(\frac{\eta}{\delta})$$

= cross flow momentum thickness

$$\theta_{21} = \frac{1}{U^2}\int_0^{\delta} (0-v)\,u\,d\eta \qquad (56)$$

$$= \delta\int_0^1 (-\frac{v}{U})(\frac{u}{U})\,d(\frac{\eta}{\delta})$$

$$= \text{cross flow interaction momentum thickness}$$

$\tau_{0_{x_1}}, \tau_{0_{x_2}}$ = wall shear components in direction x_1, x_2 respectively

Equations 49 and 50 involve a total of seven unknown quantities, the shear stresses $\tau_{0_{x_1}}$, $\tau_{0_{x_2}}$ and the boundary layer thicknesses δ_1^*, δ_2^*, θ_{11}, θ_{12}, θ_{22}. A solution cannot be obtained, of course, until five other auxiliary equations are formulated to yield seven equations and seven unknowns. The significant features of the auxiliary equations can be summarized in terms of the associated velocity models. These velocity models may be grouped into four main types, as suggested by Smith (1970), namely, polynomial, wake, triangular, and hybrid. The basic features of each type follows.

Polynomial

Prandtl (1946) suggested the first polynomial model for the streamwise and crossflow velocity components. He stated that the velocity profiles can be written in terms of power laws whose independent parameters would be a function of the boundary layer thickness, normal distance from the wall, and the shape factors. The crossflow velocity was proportional

to angle between the wall shear stress direction and the free stream velocity direction.

In mathematical form Prandtl's relationship is

$$\frac{u}{U} = \phi\left(\frac{\eta}{\delta_1}, K, \lambda\right) \tag{57}$$

$$\frac{w}{U} = \varepsilon\, \psi\left(\frac{\eta}{\delta_1}, K, \lambda\right) \tag{58}$$

where

λ is a parameter which is a function of the longitudinal acceleration

K is a parameter which is a function of the convergence or divergence of the potential core

$\varepsilon = \tan \alpha_w$

α_w = angle between U and wall shear vector

Francis (1965) pointed out that Prandtl's model represented his experimental data with modest success. Mager (1952), Cooke (1961), Eichelbrenner and Peube (1966), and Smith (1968) presented modifications of the Prandtl's polynomial model.

Law of the wake

The law of the wake for two-dimensional turbulent boundary layers has been extended by Coles (1956) to represent three-dimensional boundary layers. The velocity vector was resolved into a component in the shear stress direction and one in the pressure gradient direction as follows:

$$\bar{q} = (\bar{q}_{ss}+\bar{q}_{v}) = \bar{q}^{*}[\frac{1}{K_1} \ln(nq^{*}/v)+K_2]+$$

$$\frac{\Pi}{K_1} (x_1,x_2)\ \bar{q}^{*}\ v(\frac{\eta}{\delta}) \qquad (59)$$

where

q^{*} = friction velocity vector

K_1 = universal constant, 0.41

K_2 = universal constant, 5.0

$\Pi(K_1,K_2)$ = tensor profile parameter (depends on two space coordinates)

$v(\frac{\eta}{\delta})$= wake function

$\bar{q}_{ss}$ = total velocity component in the shear stress direction

$\bar{q}_{v}$ = total velocity component in the wake direction

This model has not been tested fully to date.

Triangular

Johnston (1957) observed that his three-dimensional boundary layer data, as well as those of Gruschwitz (1935) and Kuethe et al. (1949), exhibited a characteristic triangular shape on plots of the type shown in Figure 21. In mathematically modeling this flow, Johnston (1957) considered two distinct regions of crossflow. One region includes the crossflow velocity components from the wall up to the edge of the sublayer. The equation describing the crossflow in the inner region is

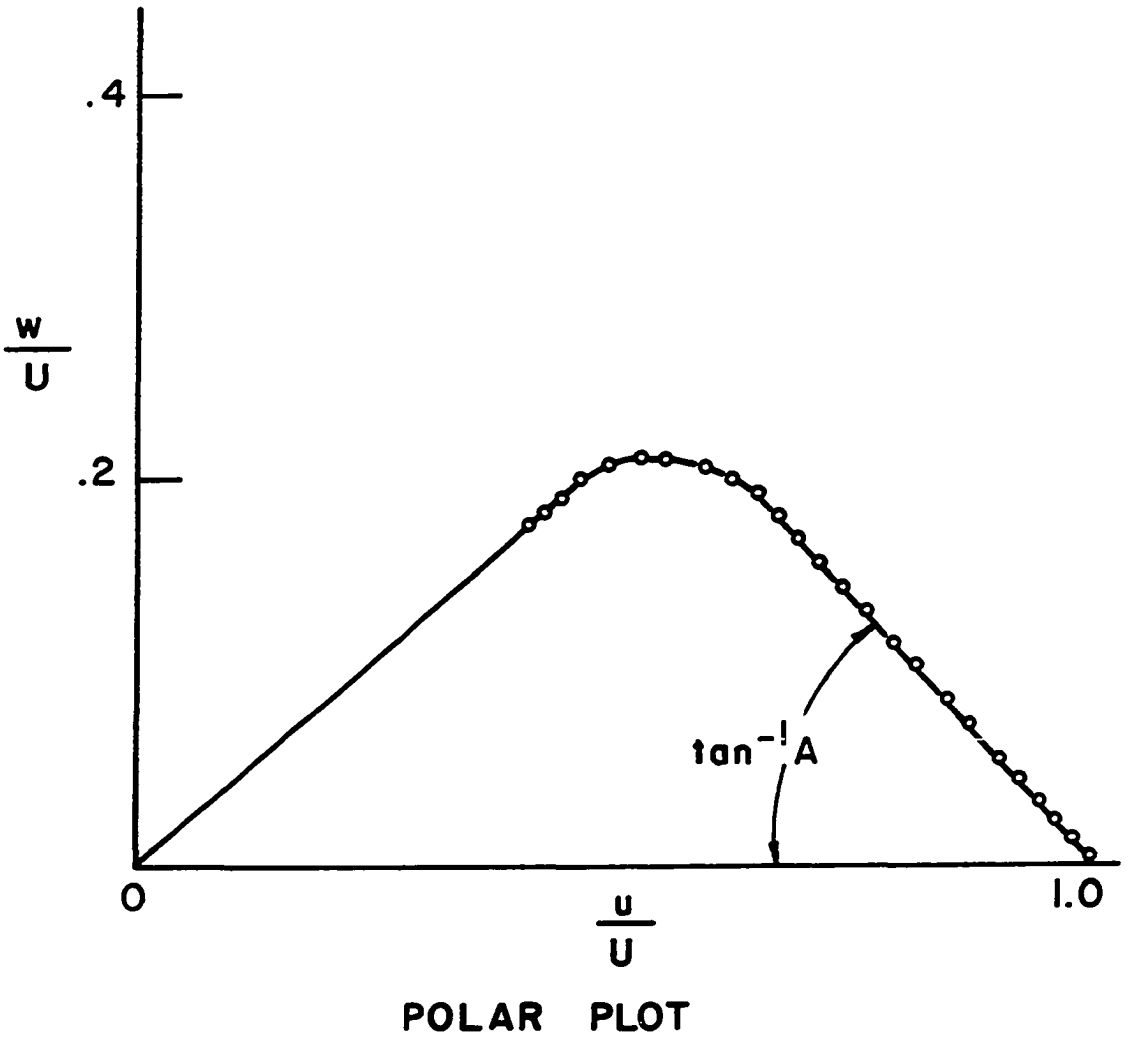

Figure 21. Schematic of a triangular plot

$$\frac{v}{U} = \varepsilon\left(\frac{u}{U}\right)$$

where

ε = tangent of the angle between the free stream direction and the limiting streamline direction

The outer region extends from the vertex of the triangle layer outward. It is described by

$$\frac{v}{U} = A\left(1 - \frac{u}{U}\right) \tag{60}$$

where

$$\frac{\varepsilon}{A} = 0.1\ [(1+\varepsilon^2)^{1/4}\ /\sqrt{C_{f_x}}] - 1.0 \tag{61}$$

$$A = 2U^2 \int_0^{\alpha} \frac{d\alpha}{U^2} \tag{62}$$

C_{f_x} = skin friction in the free stream direction

α = flow turning angle of core

Experimental data of Hornung and Joubert (1963) and Francis and Pierce (1967) contradict Johnston's (1957) statement that the vertex of the polar plot triangle corresponds to the edge of the sublayer. The relationship between α as given by Equation 62 and $\tan^{-1} A$ of the polar plot (Figure 21) using Hornung and Joubert's (1963) data was poor. There is some doubt concerning the usefulness of Johnston's (1957) model.

Hybrid

Perry and Joubert (1965) also subdivided the boundary layer into an inner and an outer section. The inner profile was represented as

$$\frac{U_R}{q^*} = \frac{1}{K} \ln(\eta q^*/\nu) + A \tag{63}$$

and the outer by

$$\frac{\bar{Q}-\bar{q}}{q^*} = \frac{(\bar{U}_\infty - u)}{q_\infty} \bar{\Pi}'(x_1, x_2) \tag{64}$$

where

$\bar{Q}$ = free stream velocity vector

q = boundary layer velocity vector

q^*= shear velocity

U_r= length of arc at the apex of the velocity polar plot

A = parameter infuenced by surface roughness

$\bar{U}_\infty$ = upstream free stream velocity

u = upstream two-dimensional boundary layer velocity

$\bar{\Pi}'(x_1, x_2)$ = a vector depending on free stream flow conditions

This model has been tested (Joubert et al. (1967)) with a variety of data and has evolved into an improved model consisting of three regions. The inner region is influenced by the local wall shear stress, the fluid density, kinematic viscosity and the normal distance from the wall, thus:

$$\frac{U_R}{q^*} = \frac{1}{K} \ln(\eta q^*/\nu) + A - \frac{\Delta u_2}{q^*} \left(\frac{kq^*}{\nu}\right)$$

The intermediate region is represented by

$$\frac{U_R}{q^*} = C\left(\frac{1}{\rho} \frac{dp}{d\xi} \frac{\eta}{(q^*)^2}\right)^{1/2} + \frac{\Delta u_1}{q^*} \left(\frac{[q^*]^3}{\nu} / \frac{1}{\rho} \frac{dp}{d\xi}\right)$$

$$- \frac{\Delta u_2}{q^*}(kq^*/\nu)$$

Finally, the outer region follows:

$$\frac{\bar{Q}-\bar{q}}{q^*} = \frac{(U_\infty - u)}{q^*_\infty} \bar{\Pi}'(\xi,\zeta)$$

Where

U_r = length of arc at the apex of a velocity polar plot

A = parameter influenced by surface roughness

U_∞ = upstream two-dimensional free stream velocity

$\Pi'(\xi,\zeta)$ = a vector dependent on free stream flow conditions

Δu_1 = slip velocity at the wall

Δu_2 = slip velocity function, depends on roughness

k = roughness scale

C = universal constant

There was insufficient data for a thorough test of this model.

Summary

It seems that existing three-dimensional boundary layer models are seldom adequate even for the data upon which they are based and it appears as if a better understanding of

the three-dimensional flow phenomenon is required.

Summary

An examination of the existing means that might be used for determining the performance of a plane curved diffuser has indicated that a more thorough understanding of the flow physics involved is probably a prerequisite to the proposal of any truly useful method. The data collected during the present experiment provides both boundary layer and core flow information at the inlet and exit cross sections of a plane curved diffuser.

EXPERIMENTAL APPARATUS

The experimental equipment utilized in this research program consists of four major elements. The first is the diffuser test section, that is, the actual section under investigation. The second is the development section immediately upstream of the test section. The third and fourth are respectively the air supply and instrumentation sections. Each will now be described in detail.

Diffuser Test Section

It was considered important to design a test geometry that would provide useful information both for further analytical analysis and also for practical design purposes. Thus, it was decided to design a diffuser that would lie in the unstalled flow regime as determined by Fox and Kline (1962) and indicated in Figure 5. To help insure that the test diffuser would not stall, the same design concept used by Fox and Kline (1962), namely, the selection of a circular arc meanline with a linear cross-section area increase distributed along the meanline, was used. The final design had an exit over inlet area ratio (AR) of 1.2, a meanline length normalized by the inlet width (N/W_1) of 3.0, a meanline turning angle of 45° and an inlet aspect ratio (AS) of 1.0.

This geometry places the diffuser operating point, in the "well behaved" region as indicated in Figure 22 which shows the lines of first appreciable stall (Fox and Kline (1962)) as replotted in more general coordinates by Blechinger (1966). A plan view sketch of the test diffuser is shown in Figure 23.

The diffuser was essentially a modified version of the test equipment designed, built and used by Smith (1970) in a three-dimensional boundary layer study. One of the important modifications to the original test section was the construction of a well defined diffuser exit plane. The original rig had curved top and bottom walls which extended some distance beyond the sidewalls (Figure 24). It has been pointed out by Sovran and Klomp (1967) among others that a diffuser "tailpipe" can have a significant effect on its performance.

The bottom piece of the diffuser was fabricated from three-quarter inch thick plywood on which was glued a one-sixteenth inch thick piece of Plexiglas cut to the same shape as the plywood. By painting the side adjacent to the plywood black prior to joining the two pieces together, a reflective surface was provided. The reflective surface made location of the probe with respect to the wall precise when the probe image was viewed with a Gaertner microscope.

The sidewalls were fabricated entirely from Plexiglas sheets. The basic piece was a sheet of Plexiglas one-sixteenth inch thick, five inches high and approximately 38

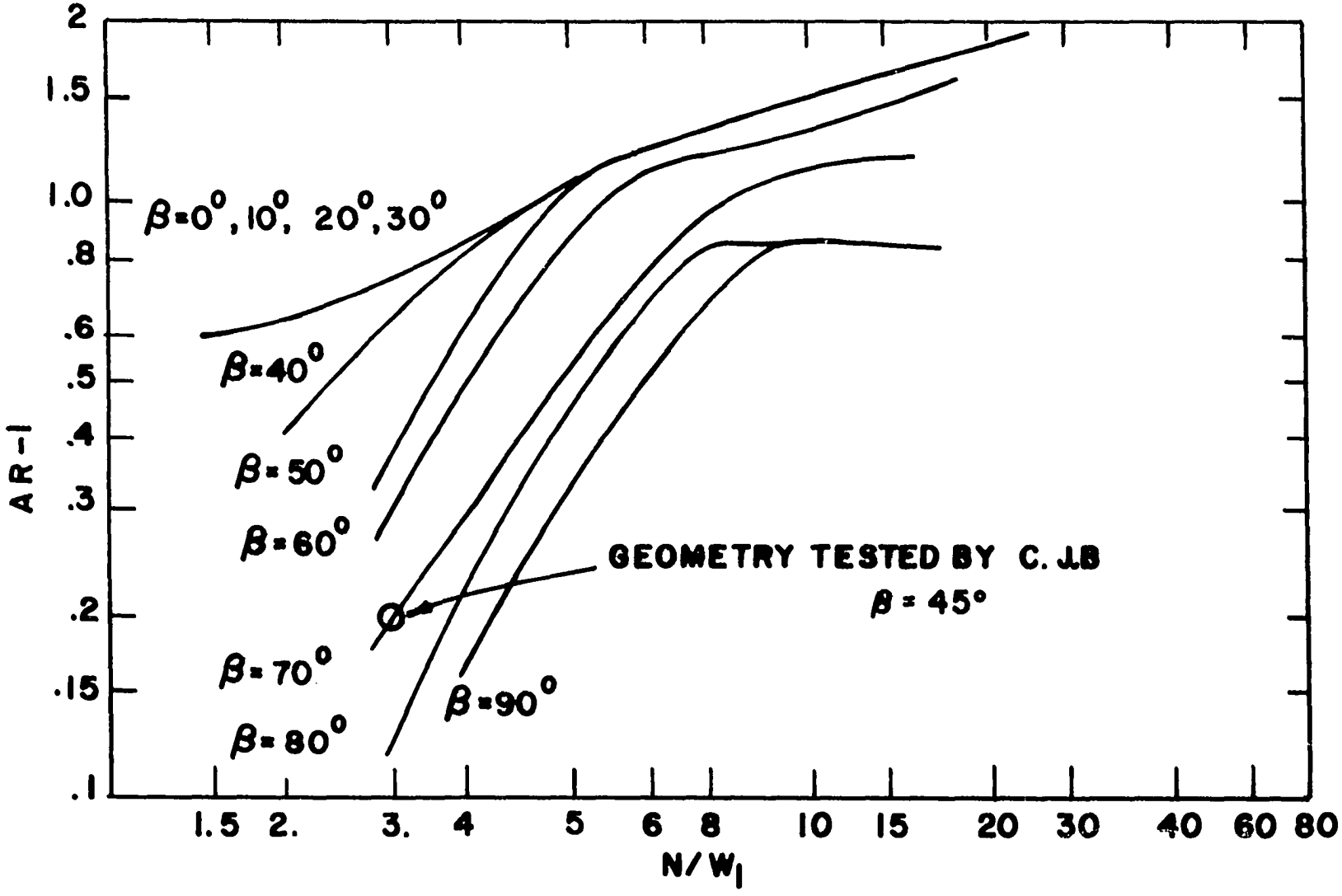

Figure 22. Line of first appreciable stall (Blechinger, 1966)

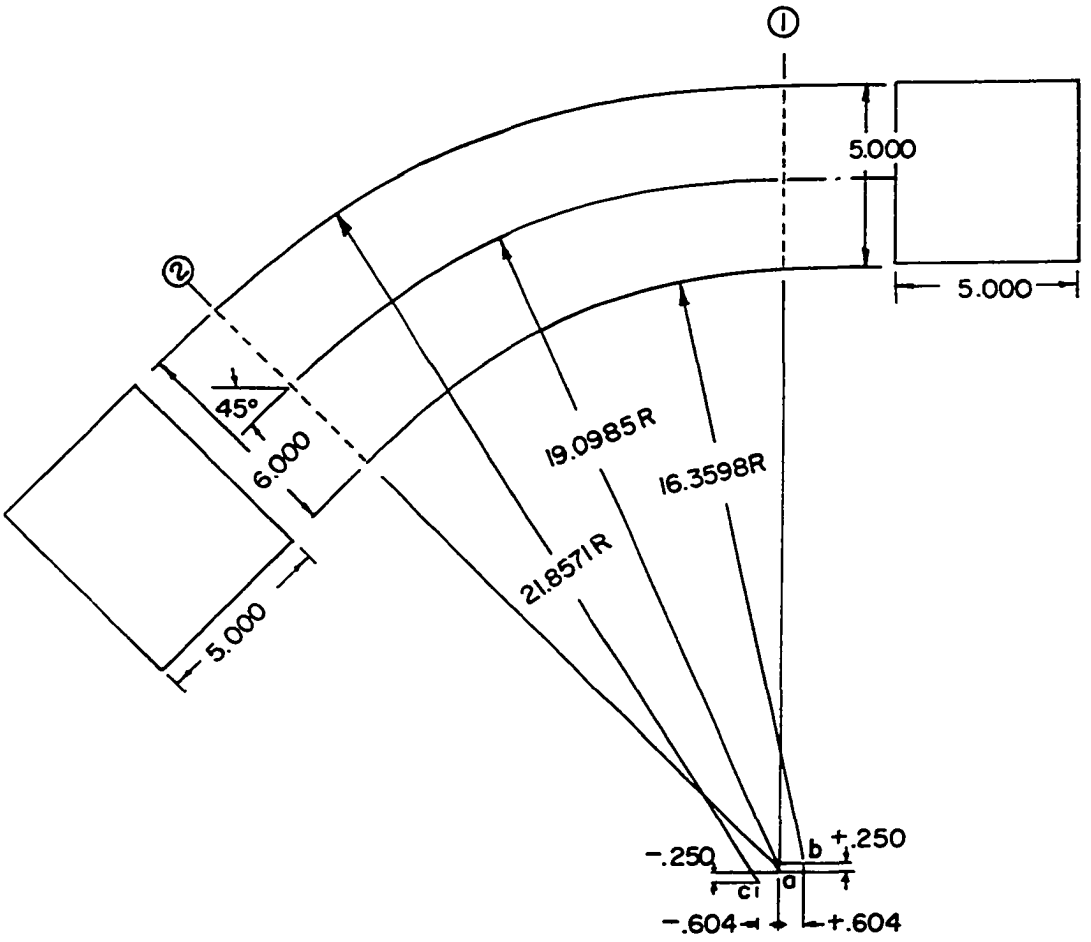

Figure 23. Schematic of author's diffuser geometry

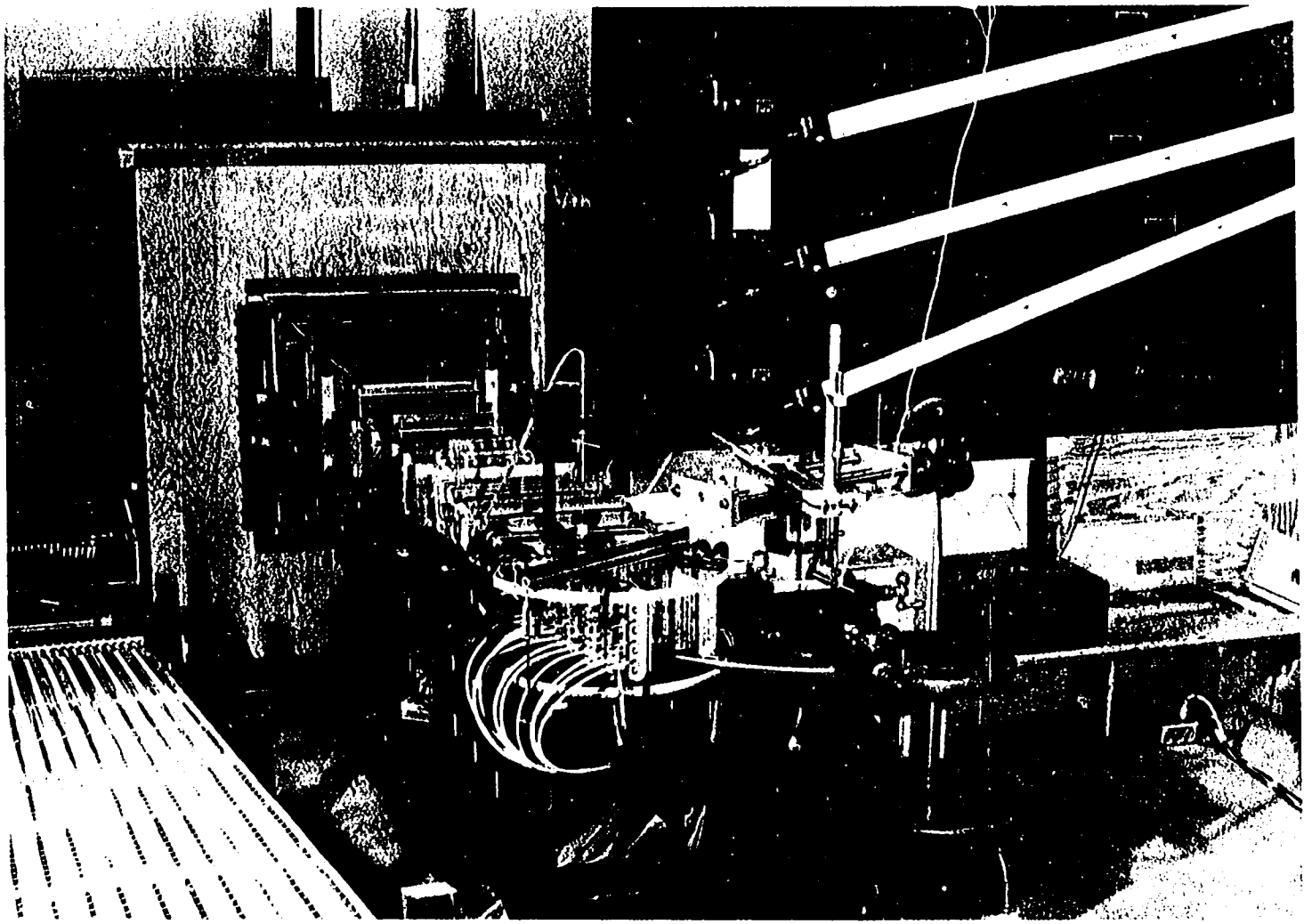

Figure 24. Test apparatus used by Smith (1970)

inches long. The outer wall was slightly longer than the inner wall, however, the construction of the two walls was the same. Each piece was reinforced with spaced vertical stiffeners each with a one-half inch square cross-section. These stiffeners were bonded with methyl ethyl keotane to the one-sixteenth inch piece at two inch intervals. The height of the stiffeners was reduced sufficiently to allow steel templates to slide in horizontally between the stiffener and the top and bottom walls, which were perpendicular to the one-sixteenth inch sidewalls. The steel templates were machined to the desired curved wall contour shapes and utilized in the test section assembly to help maintain proper sidewall curvature and support. The templates were 0.125 inch thick and 0.50 inch wide, with extensions for clamping purposes. They were held in place by template retainers which were fastened to the stiffeners by means of brass screws. Many of the construction details can be seen in Figure 25.

Two sets of static pressure taps were installed in the vertical walls of the diffuser. The first set was located in a plane perpendicular to the diffuser centerline, one hydraulic diameter upstream of the throat. It was utilized to measure the static pressure at the inlet of the diffuser. These taps consisted of four holes, each having a diameter of 0.040 inches, located on each sidewall one and one-fourth inches apart. The second set of sidewall static taps was located in

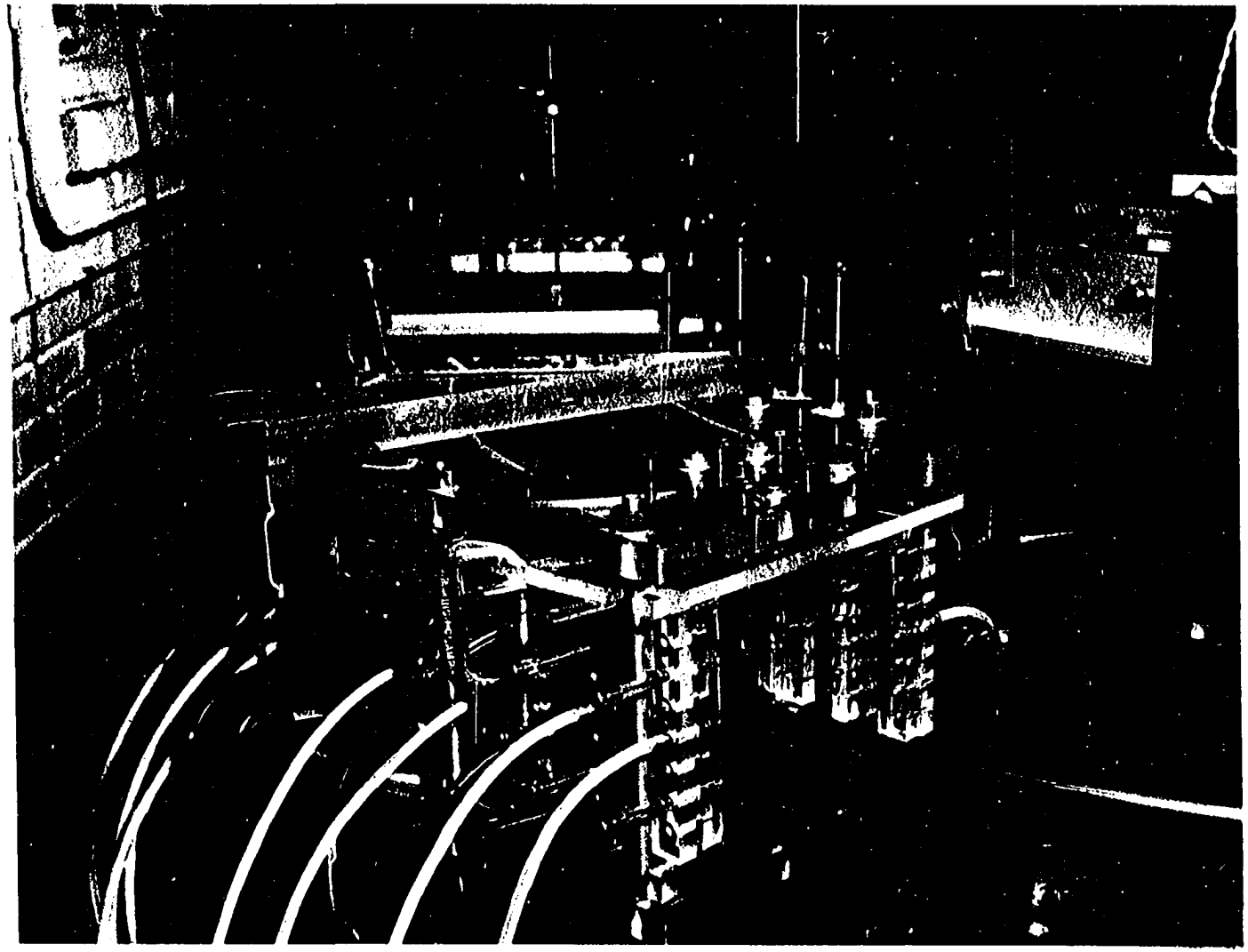

Figure 25. Photograph of test apparatus

a horizontal plane midway between the top and bottom walls of the diffuser. These static pressure taps were spaced two inches apart along the length of each curved sidewall and were used to measure the static pressure distribution along the walls.

The top of the diffuser was made of three-quarter inch thick Plexiglas cut to the same shape as the bottom.

Development Sections

The testing was performed in two series. The first involved a small amount of inlet blockage generated by means of a square constant cross-section area development section with a length of only five and one-half hydraulic diameters. This development section was constructed from one-sixteenth inch Plexiglas reinforced with three-quarter inch Plexiglas joined to the diffuser as seen in Figure 26. The second series of tests was conducted with a larger amount of inlet blockage generated by a longer development section, consisting of the first development section together with an additional development section. The combined length was 24.9 hydraulic diameters. The additional development section was constructed from one-quarter inch thick aluminum sidewalls five inches high and three-quarter inch thick Plexiglas top and bottom walls, bolted together with one-quarter inch diameter steel bolts spaced six inches apart as shown in Figure 27.

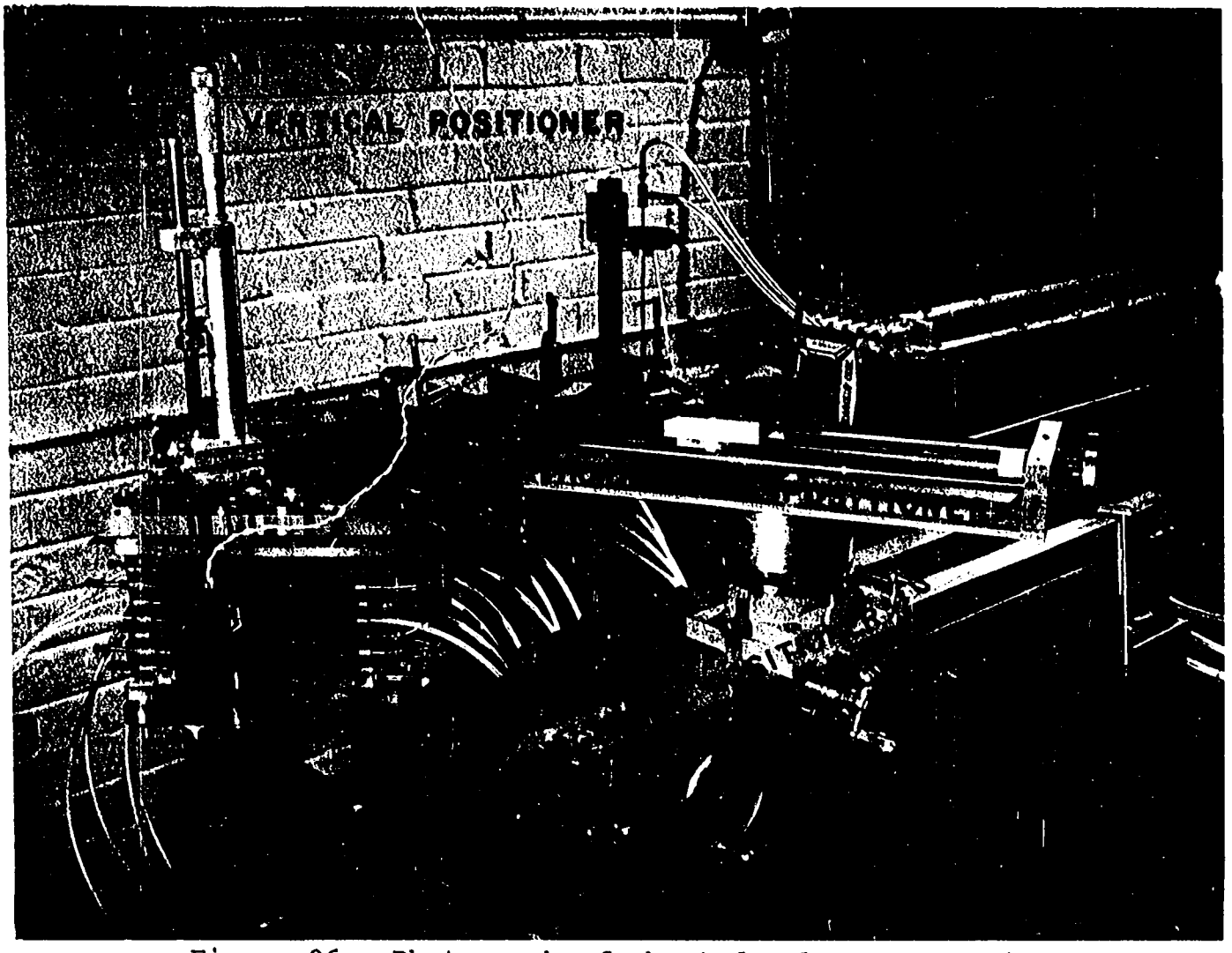

Figure 26. Photograph of short development section

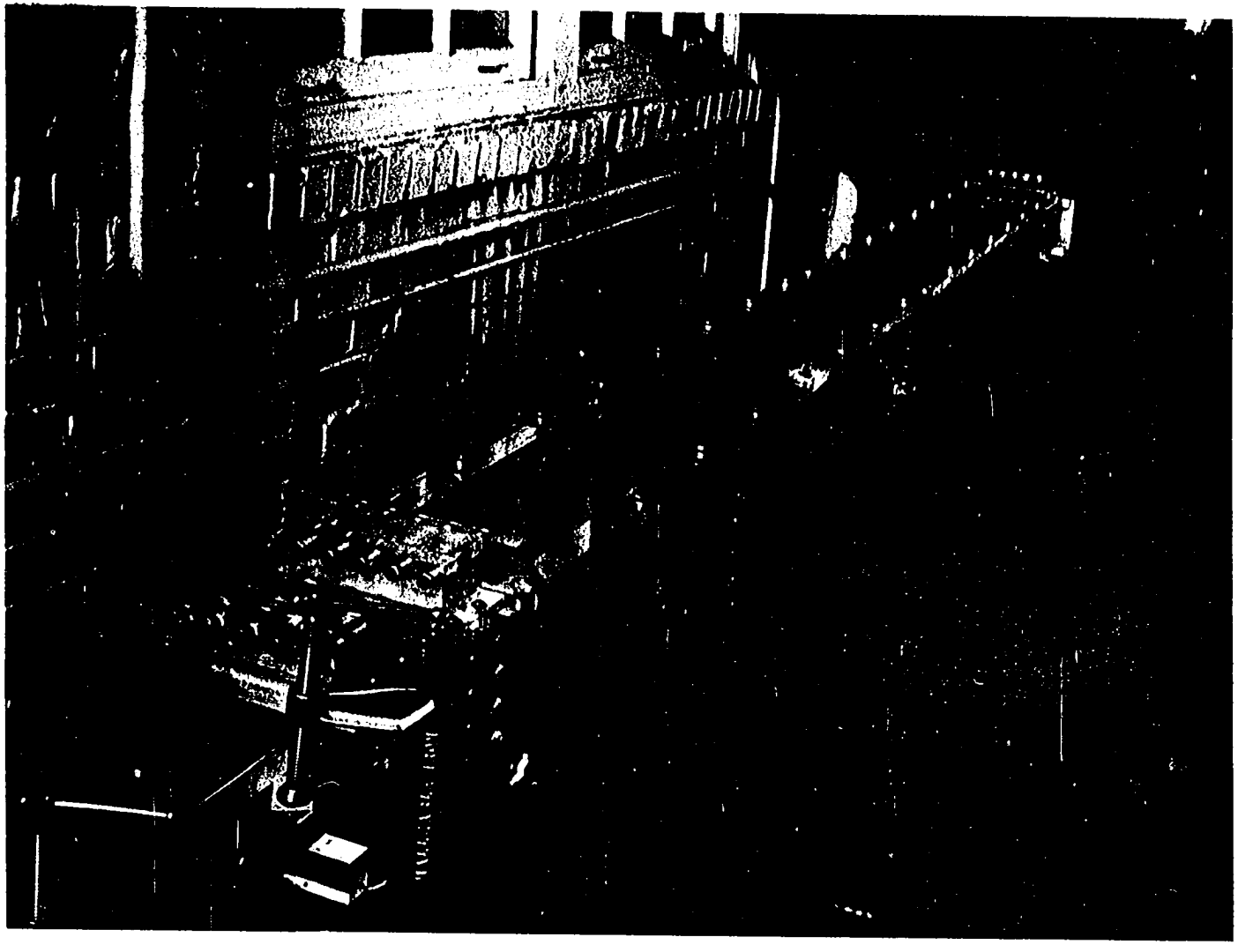

Figure 27. Photograph of long development section

The surface roughness of both the aluminum and the Plexiglas surfaces was less than 20×10^{-6} inches as verified with a Bendix type QB profilometer. There is little doubt that the surface was hydraulically smooth since the laminar sublayer was estimated to be about 2×10^{-3} inches during the tests. The joints were sealed with synthetic resin manufactured by Synkoloid Company of Atlanta, Georgia (trade name Spackling Paste). This synthetic resin was sanded and rubbed with fine steel wool to produce smooth joints. Some joints were sealed with rubber cement as suggested by Smith (1970). The complete assembly was checked for leaks and smooth joints, then cleaned and polished with Plexiglas anti-static polishing and cleaning fluid prior to testing.

Air Supply Section

A schematic of the air flow path upstream of the development section is shown in Figures 28 and 29. The intake opening was approximately fifty-two square feet in area and included a fiberglass filter. Thirty-inch nominal diameter light weight spiral-weld steel piping about forty feet long guided the air from the intake system to the blower. A twelve inch diameter light weight spiral-weld steel pipe was installed between the blower intake ducting and the blower outlet ducting for bypass purposes. A Keystone resilient seated wafer type butterfly valve was incorporated in the

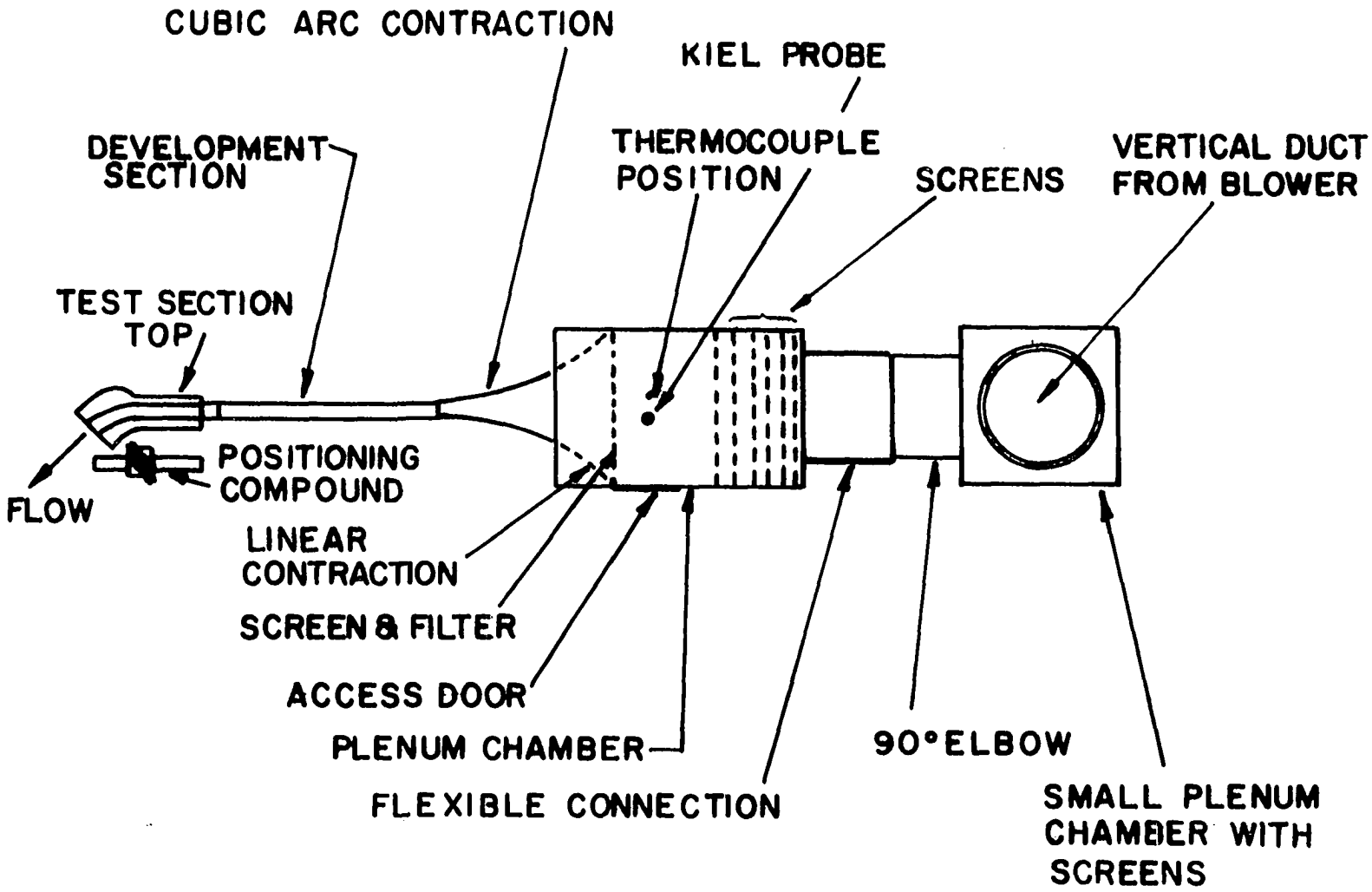

Figure 28. Schematic of flow path

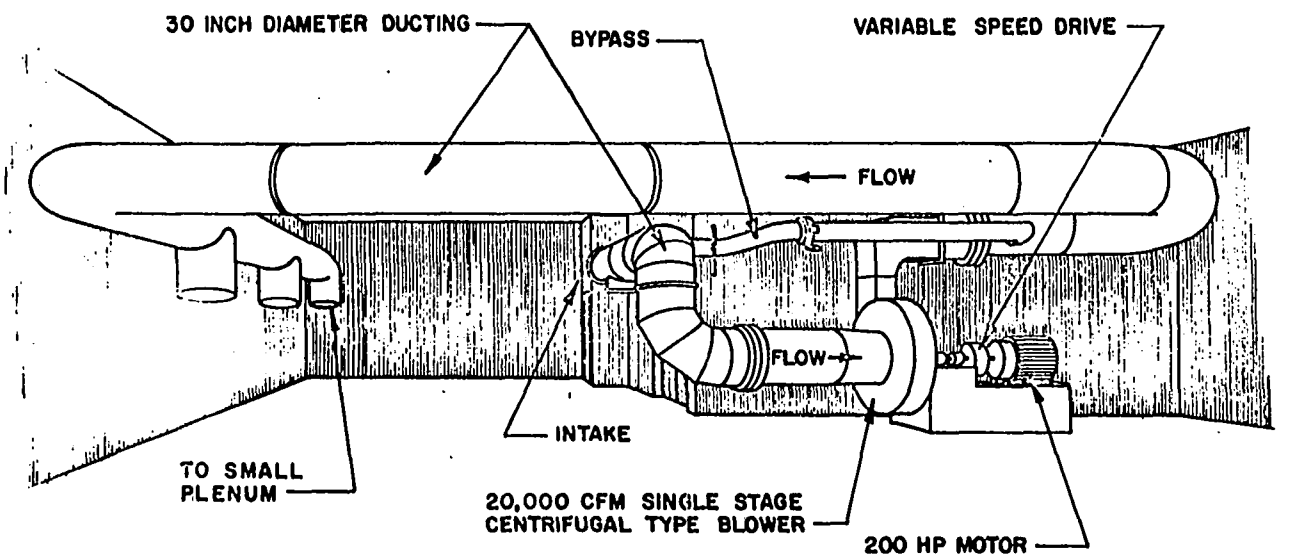

Figure 29. Schematic of test facility

bypass duct and proved to be a useful way to correct for blower motor drift during the experiments.

A Buffalo Forge Company Type CB pressure blower, size 75-5 moved the air. It was driven by a Louis Allis Pacemaker Motor Model 19278 M1M48, rated at 200 HP at 1780 RPM through an Adjustable-Speed-Magnetic Drive Unit (Ampli-Speed) manufactured by Electric Machinery Company, Minneapolis, Minnesota. The electric power was supplied at 460 volt 3 phase.

The complete blower assembly described above is shown in Figure 30. This unit can deliver 20,000 CFM at 40 inches of water static pressure at the design speed of 1770 RPM. Only a fraction of the air flow delivered by the blower was used in the test rig, the remainder being exhausted to the atmosphere.

The air leaving the blower passed through approximately 60 feet of 30-inch diameter pipe before passing through a 3 ft. x 3 ft. plenum chamber constructed out of three-quarter inch plywood. The small plenum chamber included a fiberglass filter and six rows of screens all placed in series. The screens were made from 0.019-inch diameter wire and each had an open area of 72%. This set of screens reduced the flow system velocity fluctuations considerably. From the small plenum chamber the flow proceeded through an elbow and a flexible connection between this elbow and the 4 ft. x 4.5 ft. plenum chamber. This connection isolated the vibrations of

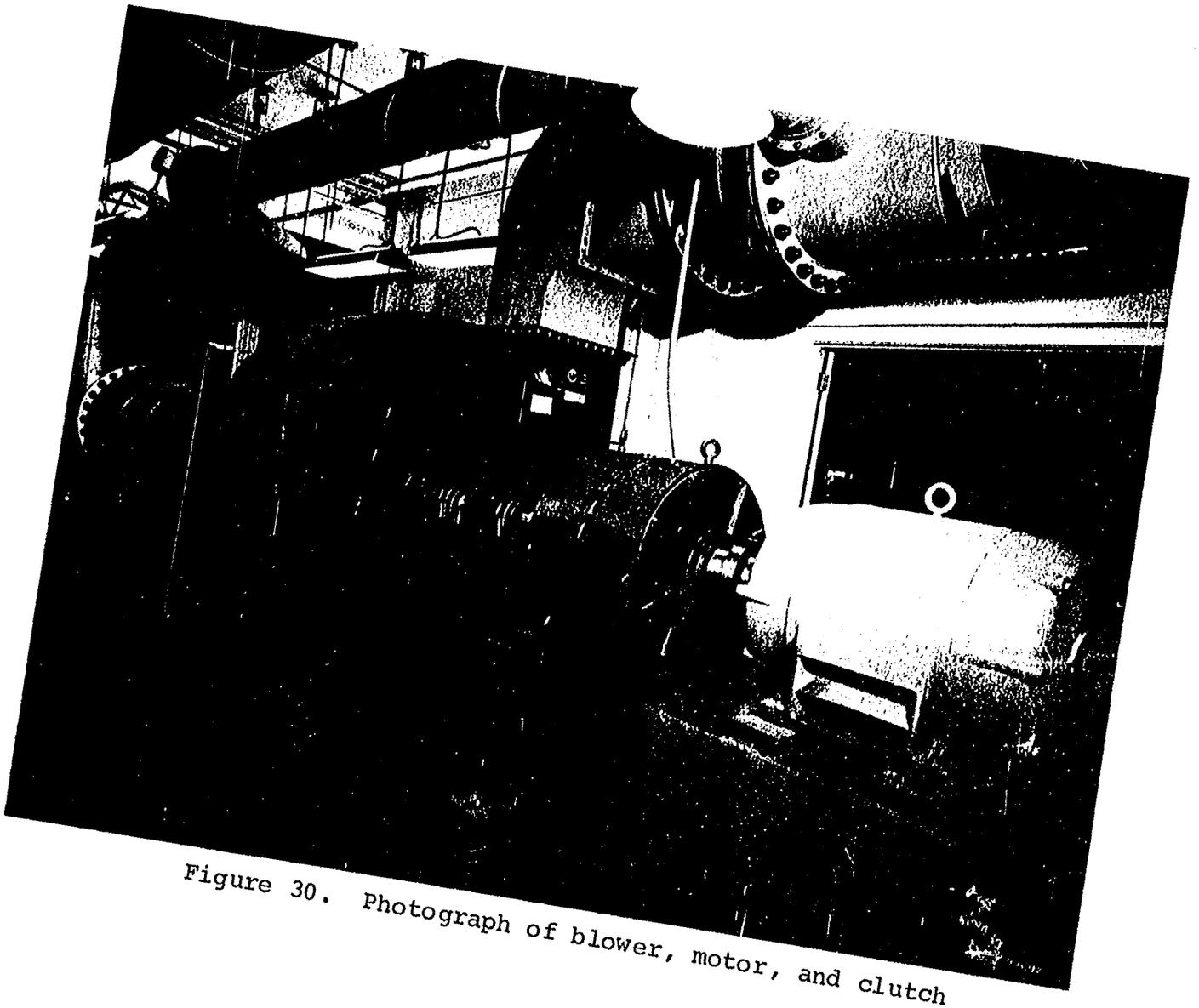

Figure 30. Photograph of blower, motor, and clutch

the piping suspended from the ceiling, from the remaining portion of the test section, which rested on the floor.

The plenum chamber was equipped with seven screens and a fiberglass filter placed in series, each with an open area of approximately 69%. This is well above the 57% minimum open area recommended by Bradshaw (1967). A fiberglass filter was placed over the screen furthest downstream. A Kiel probe and a copper-constantan thermocouple were installed in the plenum chamber top (Figure 28) to provide reference stagnation temperature and pressure measurements. The straight wall plywood contraction section following the plenum chamber had an area reduction of 5.3:1. It was then followed by a Plexiglas contraction having cubic arc walls designed as recommended by Rouse and Hassan (1949). The overall plenum to throat cross-section area contraction ratio was more than 100:1.

Instrumentation

The instrumentation used in the research program consisted of three basic groups, the velocity measuring group, the pressure measuring group and the temperature measuring group.

The velocity measuring group included two Thermo-Systems Model 1010A constant temperature hot wire anemometer systems, assorted hot-wire probes, two Disa Type 55D30 digital voltmeters, Brüel and Kjaer type 2417 random noise voltmeter,

a Brüel and Kjaer type 2107 frequency analyzer, a Thermo-Systems Model 1015B Correlator, and a Tektronix type 502A dual beam oscilloscope. A block diagram and a photograph of this instrumentation group is shown in Figures 31 and 32 respectively. This instrumentation group provided not only the magnitude, but also the direction of the local mean velocity vector and local turbulence intensity.

During the course of this investigation two different kinds of hot wire probes were used. A single wire probe Model 55F14, of the gold plated series manufactured by Disa Electronic A/S, Herlev, Denmark was used in the diffuser throat where angle measurements were not required (Figure 33a). The sensor of this probe has a length of three millimeters (0.120 inch) and a diameter of five microns (0.0002 inch). The sensing element is a platinum plated tungsten filament which is gold plated on the ends, leaving a sensing element length of 1.25 millimeters. The other probe, utilized at the exit plane of the diffuser, was a two wire "V" probe designed by Smith (1970) and manufactured by Thermo-Systems Inc., Minneapolis, Minnesota. Thermo-Systems has assigned model number 1242D to this probe. The majority of the data taken with this probe was acquired with a platinum-iridium sensor, having a length of 0.050 inch and a diameter of 0.0002 inch (Figure 33a). The sensors were coplanar and intersected at an angle of 90° thus forming a "V" (see Figure 33b). A

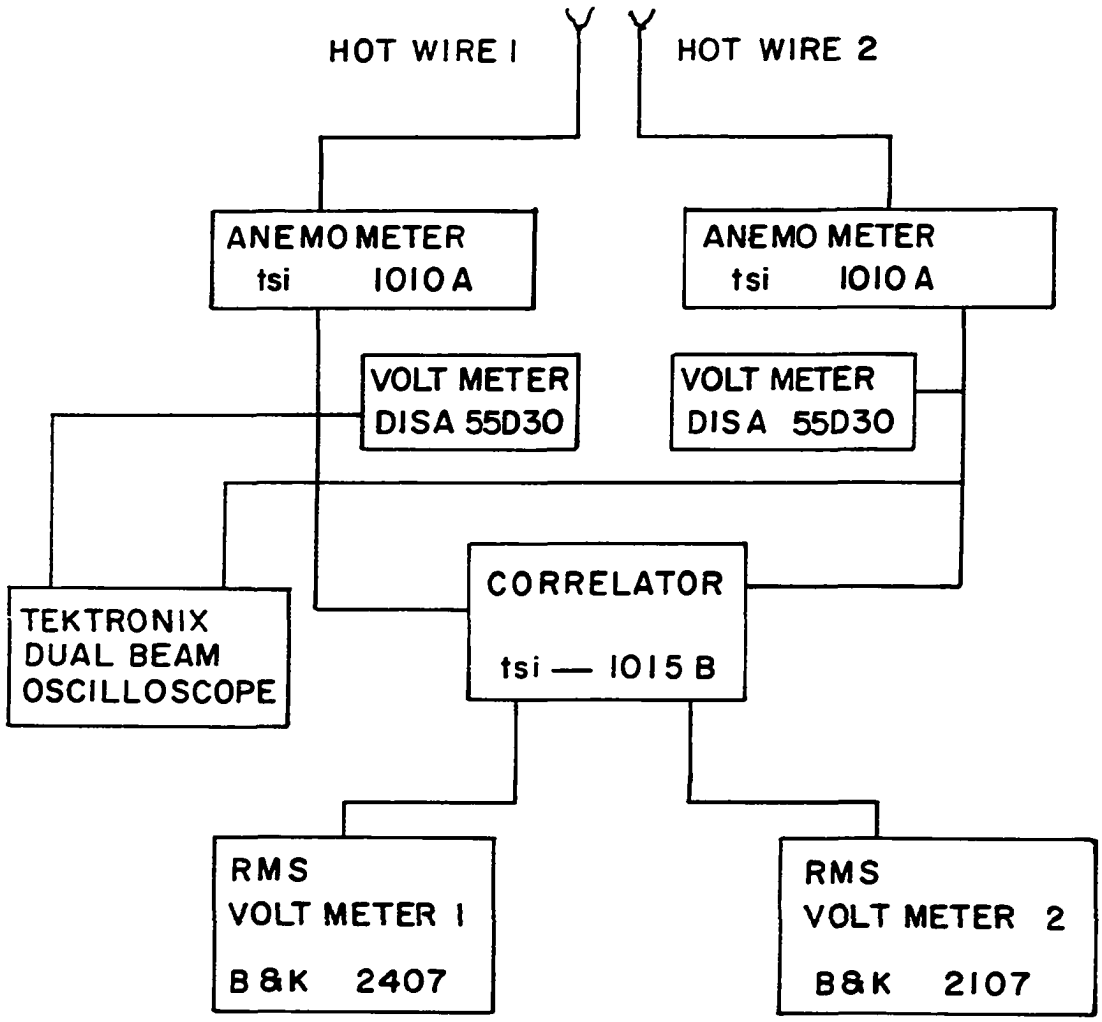

Figure 31. Schematic of instrumentation

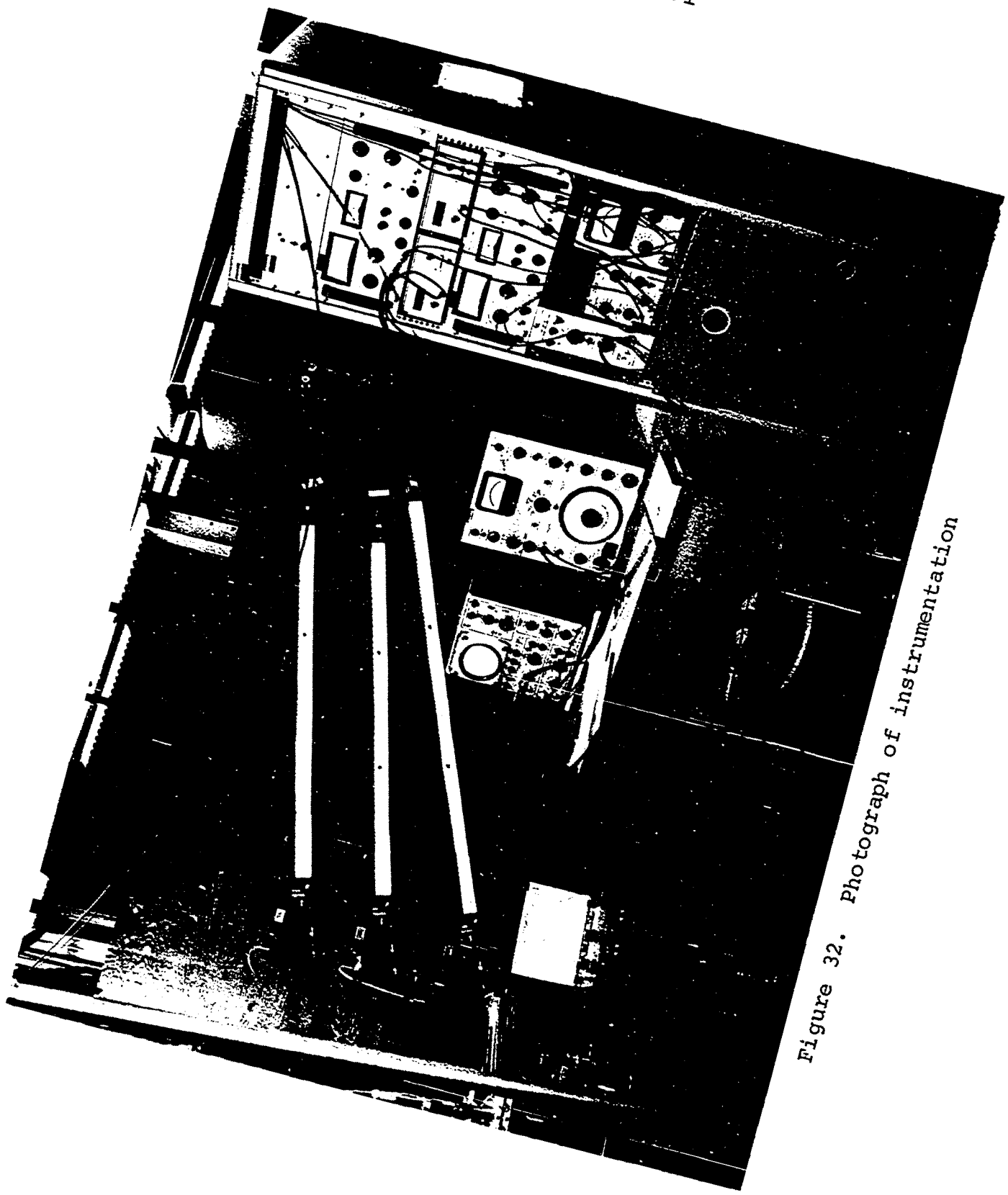

Figure 32. Photograph of instrumentation

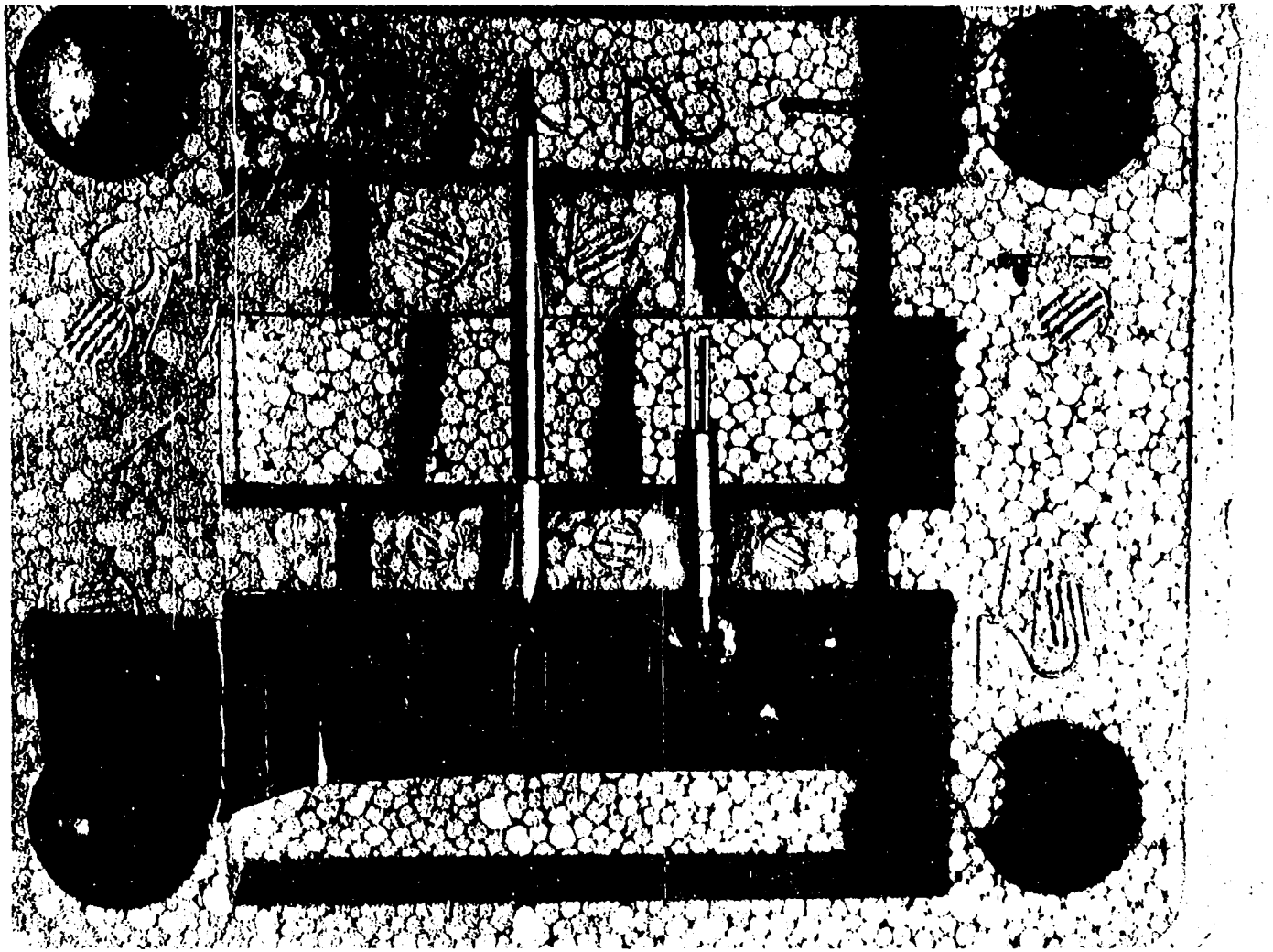

Figure 33a. Photograph of hot wires

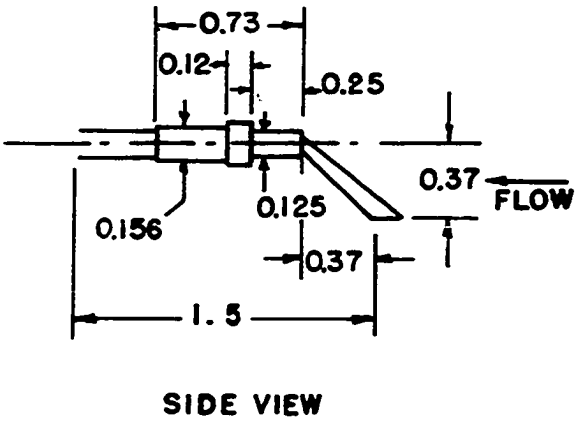

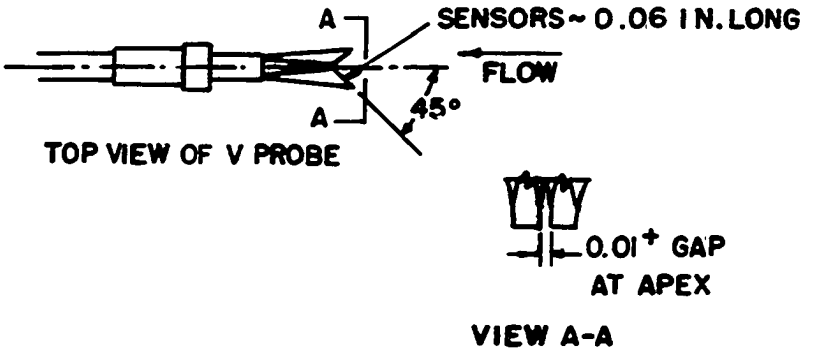

Figure 33b. Hot wire probe drawing, Smith (1970)
(length units are inches)

few runs were made with the "V" probe equipped with a hot film sensor. This sensor consisted of a platinum film sensing material which was deposited on a glass rod. The whole sensing element was subsequently coated with quartz. The length of the hot film sensor was 0.050 inch and the diameter 0.001 inch. The actual sensing element length was 0.020 inch. This was accomplished by plating the ends with gold. This sensing element was abandoned in favor of the platinum-iridium sensing element because it was mechanically weak and less accurate.

Both the Disa Model 55F14 and the Thermo-Systems Model 1242D probes were placed in their respective probe supports which were then attached to the arm of the positioning compound. This positioning compound was designed for vertical, horizontal and tangential traversing (see Figure 26). The probe exhibited some vibration in its operating position when subjected to a free stream air velocity approximately 150 ft/sec. The peak to peak amplitude of these vibrations was 0.014 inch. The mean voltage readings of the probe vibrating as above was identical to the readings observed when the probe was manually restrained from vibrating. A Pitot-static tube was used together with a Meriam inclined manometer to measure the reference velocity.

The pressure measuring group consisted of a mercury in glass barometer, two Meriam inclined manometers and

bank of twenty-four inclined manometers. The barometer was used to measure barometric pressure, the two Meriam inclined manometers measured reference static pressure and plenum chamber total pressure. The inclined manometer bank was used to measure sidewall static pressures in the diffuser (Figure 34).

The air stream temperature was measured with a copper-constantan thermocouple together with a Leeds and Northrup No. 8686 potentiometer. All other reference temperature measurements were made with mercury in glass thermometers.

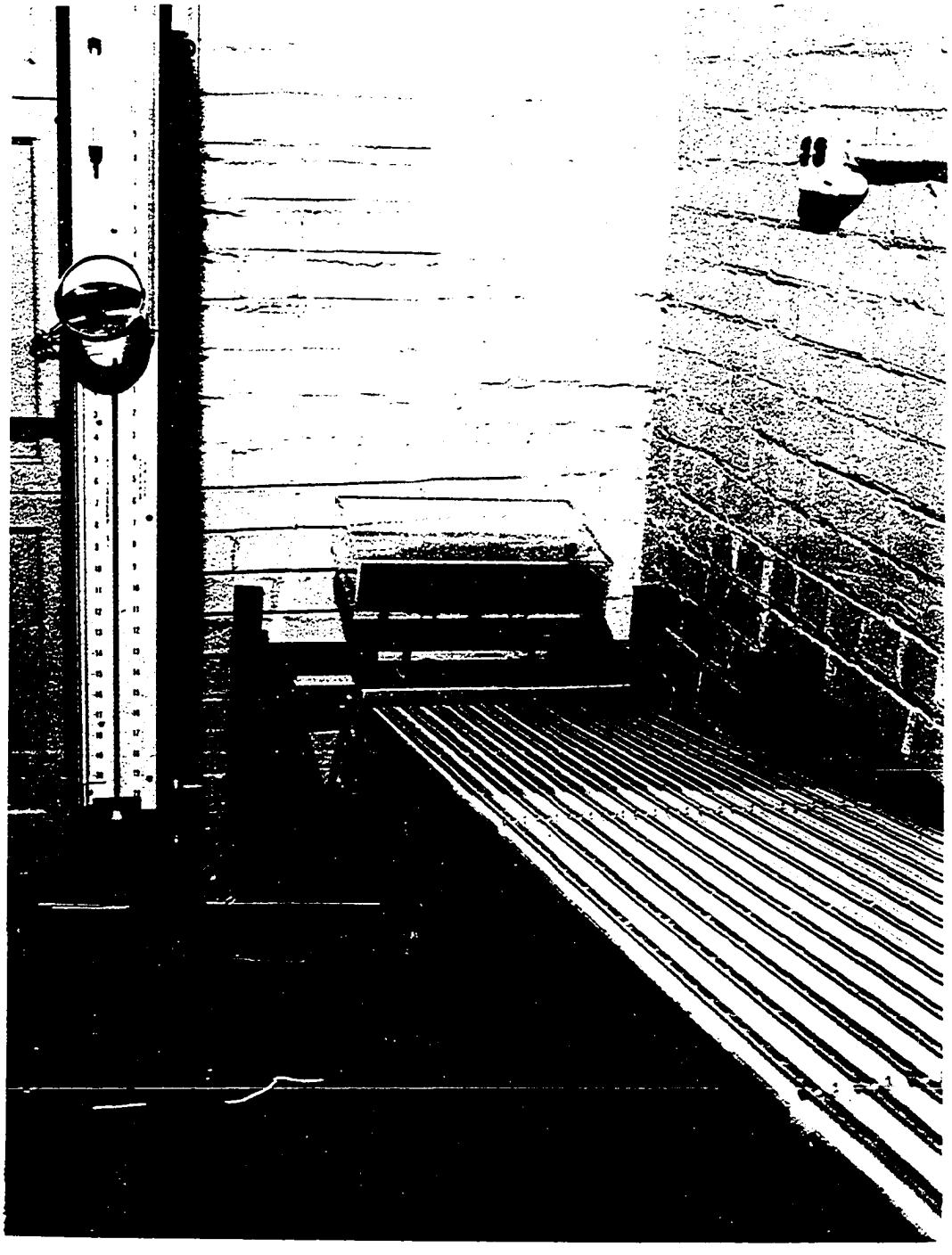

Figure 34. Photograph of manometers

EXPERIMENTAL PROCEDURE

Instrumentation Calibration

Data collection could not commence until the instrumentation was calibrated, the probe positioned and the air supply system brought into proper working order. The process of calibration of instrumentation included calibration of all manometers and the hot wire sensor. The manometers were calibrated against a "standard" which was considered to be a Meriam "Micromanometer" Model 34FB2. The following procedure was employed. Identical pressure was initially applied to both the standard and an inclined manometer. The inclined manometer was adjusted so that it registered the same pressure as the standard. The pressure was then released and the zero setting was noted. If the inclined manometer did not return to zero, it was set to zero and the process was repeated.

The inclined manometer used for the static pressure measurement along the wall had twenty-four tubes each of which had to be individually calibrated. The same pressure was applied to all of the inclined tubes and the standard. The readings of both instruments were then recorded. Six different magnitudes of pressure were used to provide sufficient range. The actual value of subsequent test readings were determined by interpolation using a Lagrangian polynomial of degree two relevant to three successive points

(see for instance, Scarborough (1962) or Froberg (1969)).

The calibration of the hot wire was an elaborate and time consuming task performed by means of a calibration tunnel (Figure 35) consisting of an ASME nozzle having a circular cross section 1.00 inch in diameter at the throat. This nozzle produced a uniform velocity profile vertical air jet. The source of air was a regulated compressed air supply. The throat of the nozzle had a flange which served as the horizontal reference plane. When a hot wire was calibrated for magnitude, the wire was first aligned parallel to the horizontal reference, then calibrated. Positioning was accomplished by aligning the horizontal reference line of the Gaertner microscope parallel to the horizontal reference, then aligning the hot wire parallel to the hair lines in the microscope. The calibration was completed by varying the velocity of the jet by means of a valve and recording both the voltage reading and the Pitot-static pressure reading.

When a hot-wire was calibrated for both magnitude and direction, the probe alignment procedure was more complicated. Since the velocity of the air jet decreases as the distance from the throat increases, it was necessary to keep the hot wires of the "V" probe at nearly the same distance from the throat of the nozzle for all yaw angles of the wire with respect to the air jet axis. In order to accomplish this

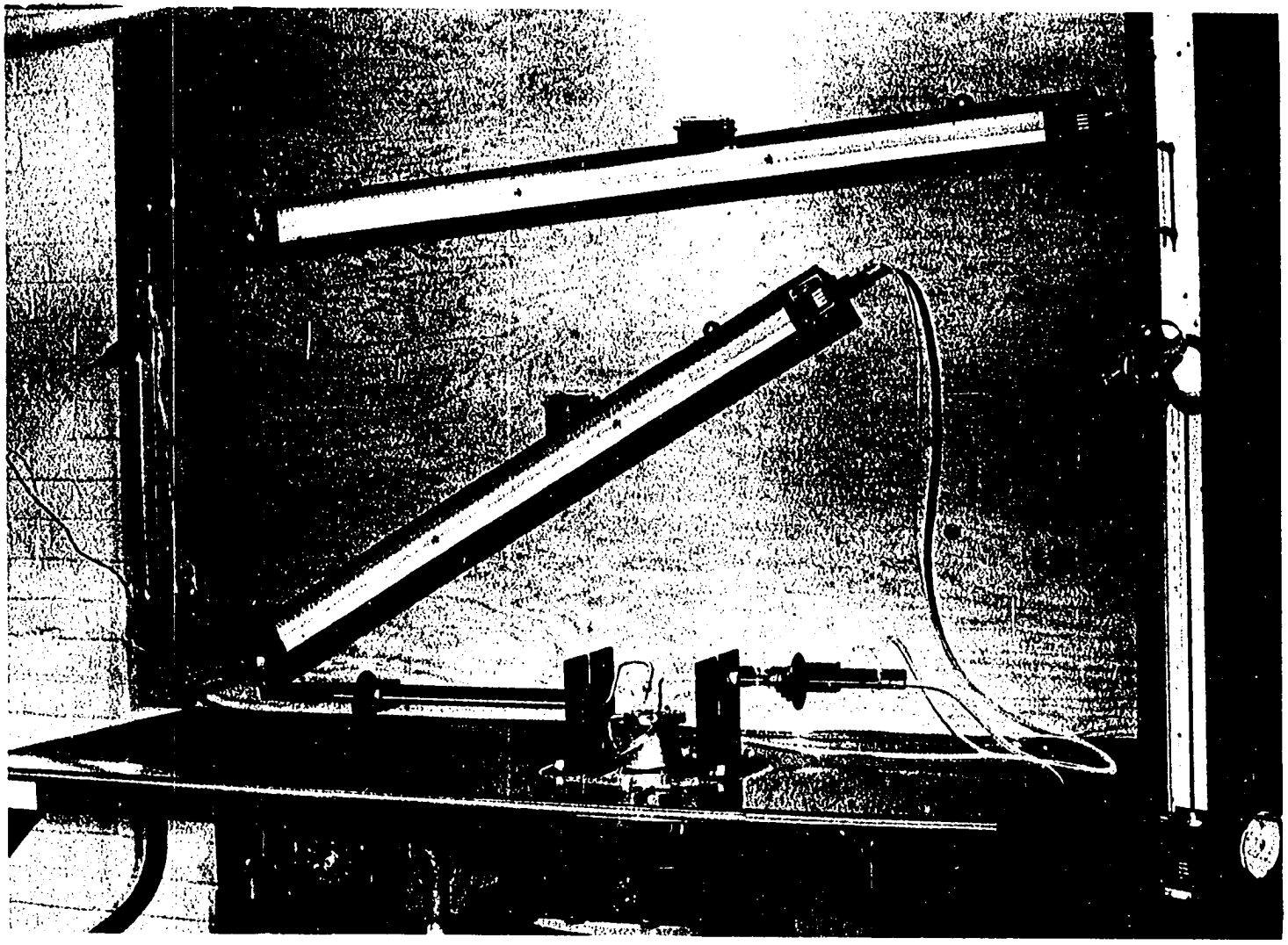

Figure 35. Photograph of calibration tunnel

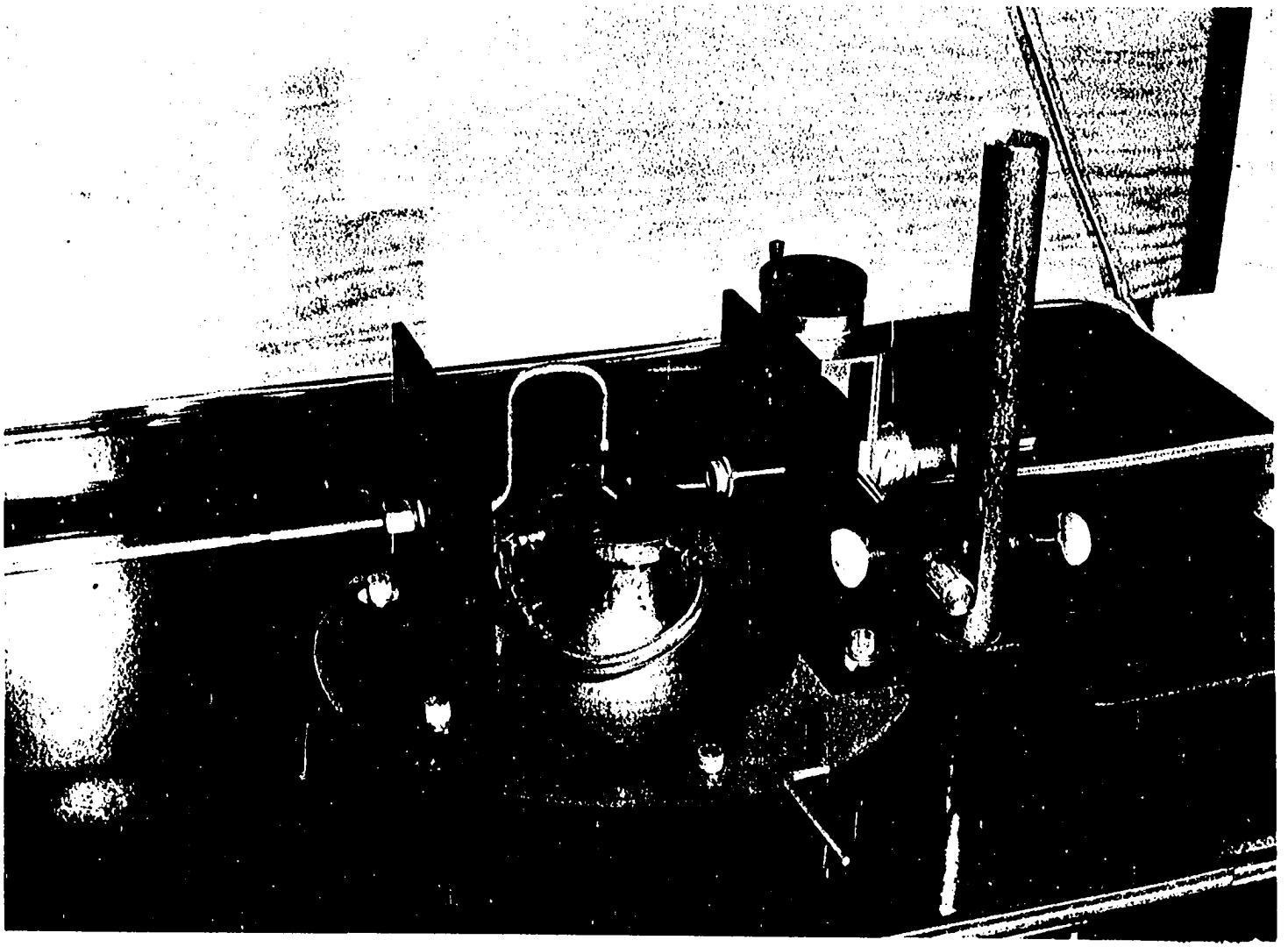

Figure 35. Photograph of calibration tunnel, Smith (1970)

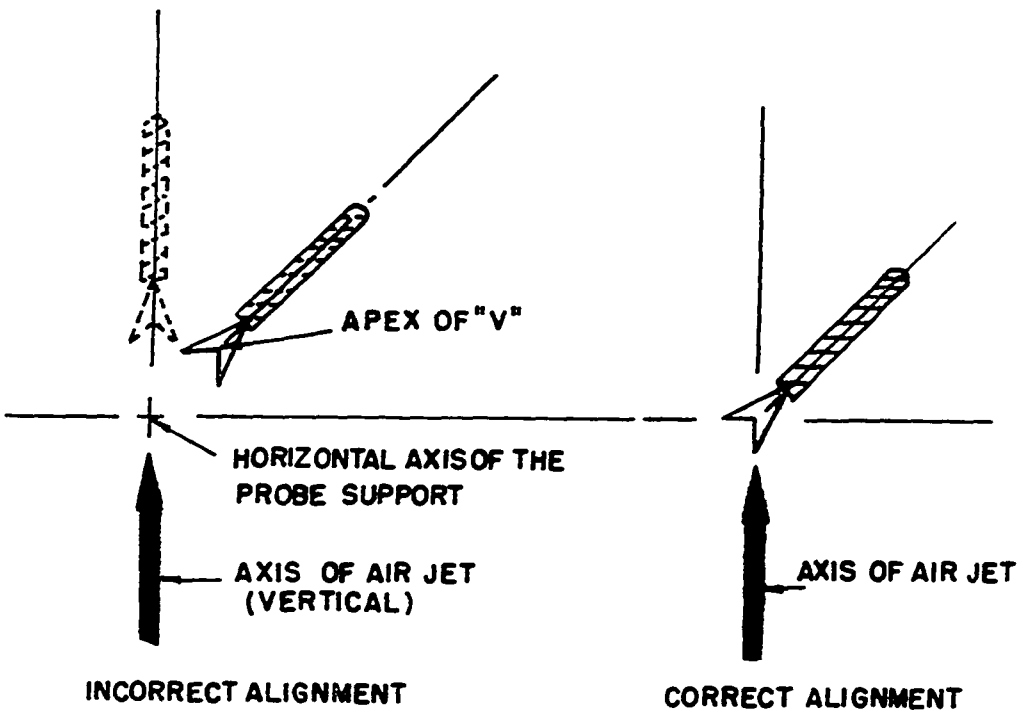

Figure 36b. Comparison of probe alignments

a Gaertner microscope was incorporated in the calibration tunnel as shown in Figure 36a. Sighting through the microscope one could observe if the apex of the sensor "V" remained at the same point as the sensor yaw angle with respect to the air jet was changed. A schematic of an incorrect alignment as viewed in the Gaertner microscope is shown on the left side of Figure 36b. By adjusting the probe within the holder, the probe could be aligned such that the apex of the "V" remained at the same point during the calibration procedure (see the right side of Figure 36b). Once the alignment was satisfactory, the calibration for magnitude and direction could commence. The calibration for magnitude and direction was executed by recording the inclination angle for each sensing element at inclination angles of 15° to 90° (at 15° intervals) together with the corresponding voltage reading for each wire at a given Pitot-static tube reading. Then the air jet velocity was increased and the process repeated.

The calibration theory for a hot wire inclined at an angle of 90° to the air jet will now be discussed. It has been shown by Sandborn (1966) that the velocity magnitude calibration data of a sensor perpendicular to the flow best fits the equation below:

$$\frac{i^2 R_h}{(R_h/R_c - 1)} = A + BQ^n \qquad (78)$$

where

i = sensor current, amps

R_h = sensor hot resistance, ohms

R_c = sensor cold resistance, ohms

A = a constant

B = a constant

Q = magnitude of the velocity vector (ft/sec)

n = exponent which depends on velocity

The ratio R_h/R_c is frequently called the overheat ratio (R_{oh}). Most testing was done with an overheat ratio of 1.5.

A constant temperature hot-wire anemometer has a constant total resistance across the portion of the bridge which includes the hot wire sensor. Thus, the sensor current can readily be expressed in terms of the bridge voltage, E_b, (the variable read on the anemometer) and the total resistance, R_t,

$$i = \frac{E_b}{R_t}$$

where

R_t = sum of sensor resistance + probe resistance + probe holder resistance + cable resistance + bridge leg resistance

A modified expression for the calibration is

$$\frac{E_b^2 R_h}{R_t^2 (R_{oh}-1)} = A + BQ^n \tag{79}$$

The air jet magnitude can be determined, independently, using the Pitot-static tube reading by the equation

$$Q = \left(\frac{2g_c \gamma_m \Delta h}{\rho}\right)^{1/2} \tag{80}$$

where

g_c = Newton's constant, 32.174 $lb_m ft/lb_f sec^2$

γ_m = specific weight of the manometer fluid lb_f/ft^3

Δh = differential height of the manometer fluid due to the dynamic pressure, feet of manometer fluid

ρ = density of the air in the test, lb_m/ft^3

It was permissible to neglect compressibility since the test Mach number was less than 0.12 (as recommended by Shapiro (1953) and Dean (1953)).

The theory of magnitude and direction calibration of the "V" probe will now be discussed. An orthogonal coordinate system like the one shown in Figure 37 will be useful in describing this procedure. It has been shown by Hinze (1959), Champagne and Sleicher (1967) that a hot wire is sensitive not only to the magnitudes of the velocity vector perpendicular to it, but also to the component parallel to the wire. The equation reflecting this influence is

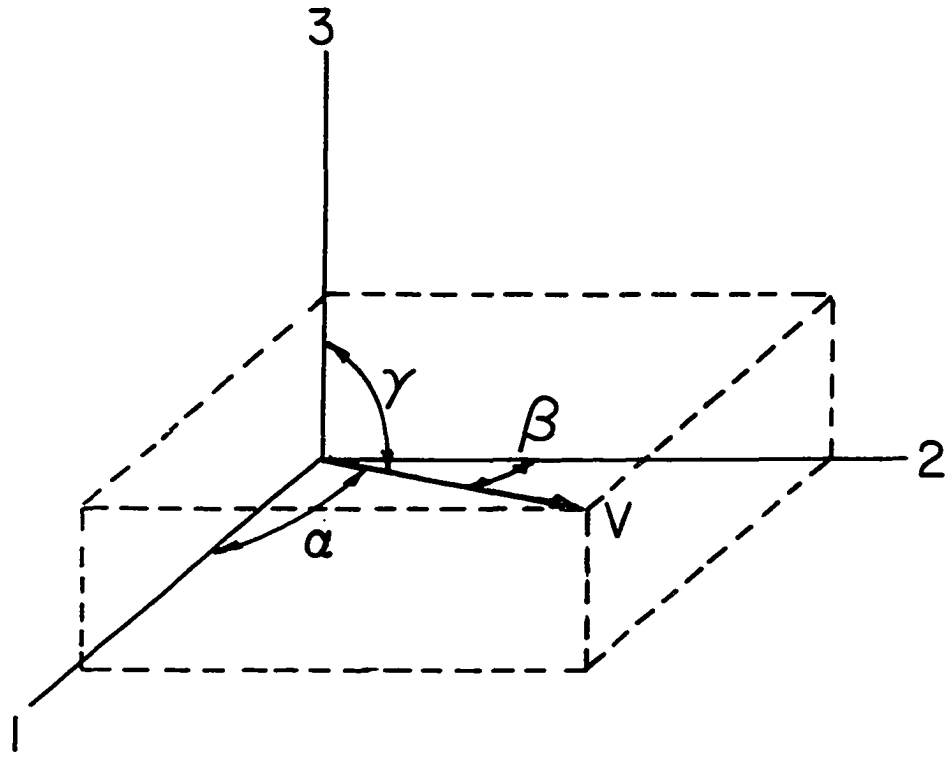

Figure 37. Polar coordinate system

$$Q_{eff}^2 = Q^2(\sin^2\alpha + k^2 \cos^2\alpha) \tag{81}$$

where

Q_{eff} = the velocity effectively sensed by the inclined wire

Q = actual velocity

α = inclination angle

k = "crossflow adjustment" factor

Writing the above equation for the three components of velocity (Figure 37) yields:

$$Q_{eff)_A}^2 = Q^2(\sin^2\alpha + k_a^2 \cos^2\alpha) \tag{82}$$

$$Q_{eff)_B}^2 = Q^2(\sin^2\beta + k_b^2 \cos^2\beta) \tag{83}$$

$$Q_{eff)_C}^2 = Q^2(\sin^2\gamma + k_c^2 \cos^2\gamma) \tag{84}$$

If the "crossflow adjustment" factor is a constant and if $k_a = k_b = k_c$, the above equations may be added to yield

$$Q_{eff)_A}^2 + Q_{eff)_B}^2 + Q_{eff)_C}^2 =$$

$$Q^2[\sin^2\alpha+\sin^2\beta+\sin^2\gamma+k^2(\cos^2\alpha+\cos^2\beta+\cos^2\gamma)] \tag{85}$$

which simplifies to

$$Q_{eff)_A}^2 + Q_{eff)_B}^2 + Q_{eff)_C}^2 = Q^2(2 + k^2)$$

Solving for Q^2 the result is

$$Q^2 = \frac{Q^2_{eff)_A} + Q^2_{eff)_B} + Q^2_{eff)_C}}{2 + k^2}$$

The sensor used during these experiments consisted of two coplanar wires. Therefore, the above equation simplifies to

$$Q^2 = \frac{Q^2_{eff)_A} + Q^2_{eff)_B}}{1+k^2} \tag{88}$$

If the value of k^2 is known (or assumed) and the effective velocity sensed by each wire is approximated (assuming normal flow in each case) from the voltage reading of each wire, then a first approximation of the velocity Q can be determined. Knowing the velocity Q, $Q_{eff})A$ and k, the direction of the velocity vector with respect to the sensor can be determined

$$\alpha = \sin^{-1}\left[\left(\frac{Q_{eff)_A}}{Q^2} - k^2\right)/(1 - k^2)\right]^{1/2} \tag{89}$$

However, k is a function of the sensor length to diameter ratio, and also a weak function of the velocity and the angle (Friehe and Schwarz (1968)). The variation of k with length to diameter ratio is not important as long as the k is known for a given sensor. Variations of k with velocity and angle must be considered for a given sensor if accurate results are required.

In order to take these variations into consideration the actual calibration data was used as discussed below.

The final velocity calculated using the calibration data was within 5% of the value calculated theoretically. The calibration data for a sensor inclined to the velocity vector may be represented as a surface shown in Figure 38 (Sandborn (1966)). However, it was more convenient to use the modified power as expressed by

$$MP = \frac{E_b^2 R_h}{R_t^2 (R_{oh}-1)} \tag{90}$$

in the surface rather than the voltage. An equation for modified power and the normal velocity Q was written

$$MP_{90} = C_1 + C_2 Q + C_3 Q^2 \tag{91}$$

Further, the modified power at some angle α was normalized by the power at $\alpha = 90°$ (for the same air jet velocity). A modified power ratio was then calculated

$$MPR = \frac{MP_\alpha}{MP_{90}} = \left[\frac{E_b^2 R_h}{R_t^2 (R_{oh}-1)}\right]_\alpha \Big/ \left[\frac{E_b^2 R_h}{R_t^2 (R_{oh}-1)}\right]_{\alpha=90°}$$

A correlation between $(MPR)^{1/2}$ and $\sin^{1/2}\alpha$ is shown in Figure 39 (Smith 1970).

Utilizing the first approximation of the angle previously calculated one can use Figure 39 to calculate a new value of MP_α/MP_{90}. This quantity with the measured power yield the corresponding MP_{90},

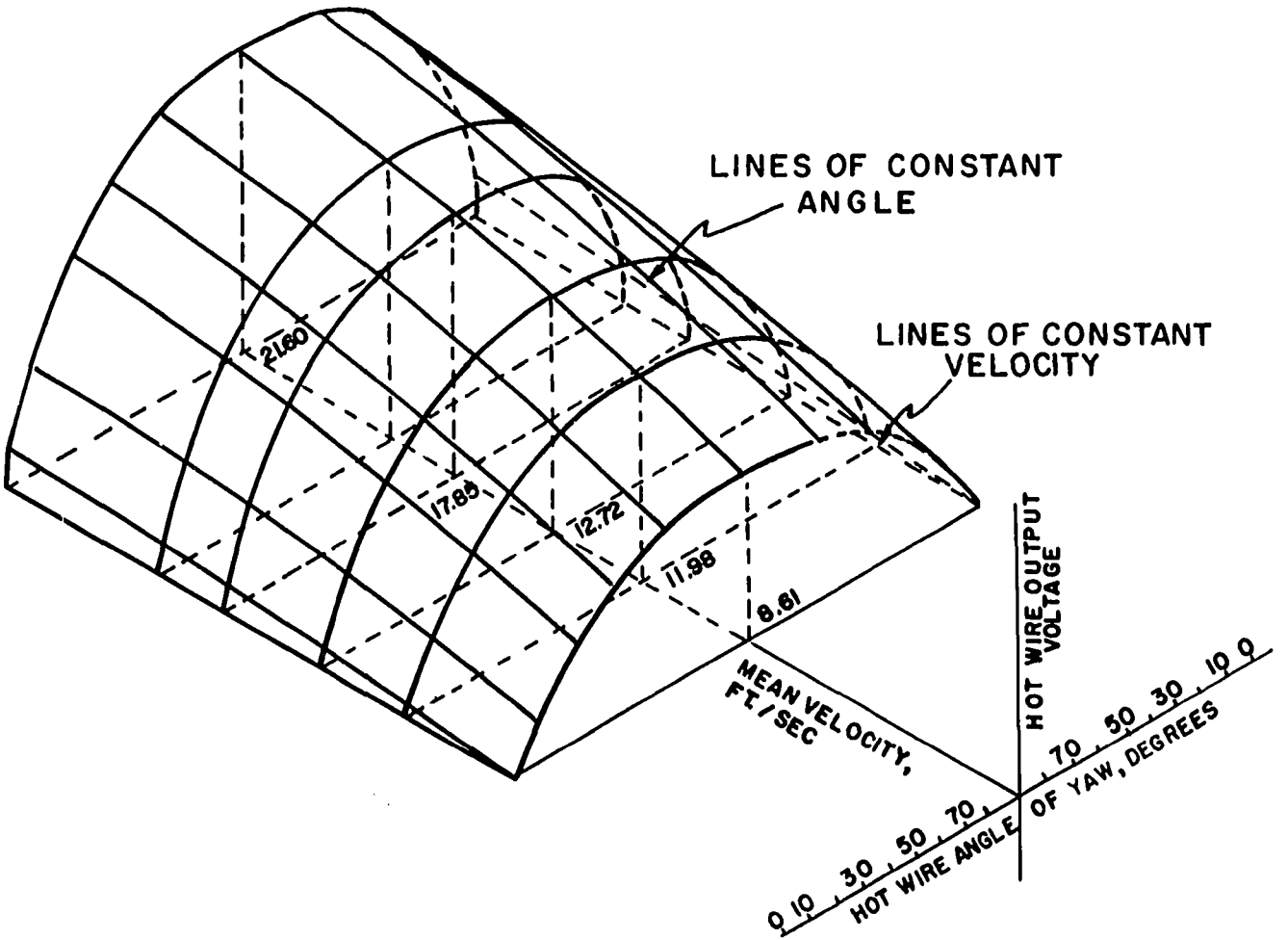

Figure 38. Hot wire calibration surface, Sandborn (1966)

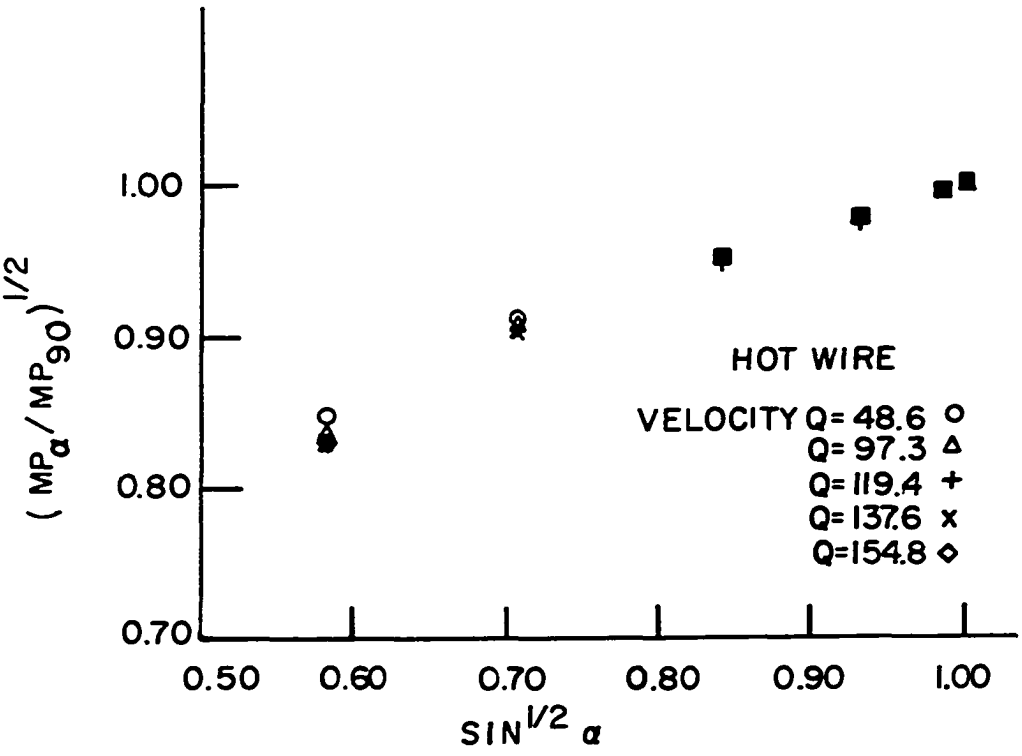

Figure 39. Hot wire correlation curves, Smith (1970)

$$MP_{90)_A} = MP_{\alpha)_{test}} \Big/ \left(\frac{MP_\alpha}{MP_{90}}\right)_{calibration} \tag{92}$$

Equation 91 can now be solved for Q using the value of MP_{90} calculated from Equation 92,

$$Q_A = -\frac{2C_2}{C_3} - \frac{1}{2}\left\{\left(\frac{C_2}{C_3}\right)^2 - \frac{4(C_1-[MP_{90}]_A}{C_3}\right\}^{1/2} \tag{93}$$

The same procedure was applied to the other sensor. If the two results were identical the solution was completed, if not, an average value of Q was calculated and the process repeated. The repetitive nature of the above operation was performed with an electronic computer IBM 360/65 at Iowa State University, (see Appendix E).

The data acquired had no utility unless the position of the probe was defined. The vertical position of the probe was established by observing the image of the sensor close to the wall with the Gaertner microscope. Position irregularities of the bottom wall and the positioner were measured by mounting a dial indicator to the arm of the traversing compound and used to correct raw probe position data. The horizontal reference position of the sensor in the throat cross-section plane was established by observing the sensor's position with respect to a reference line clearly etched on the top plate. The horizontal reference point at the exit was established by setting the Gaertner

microscope tangent to the sidewall, with the hair line parallel to the edge. Next, the sensor was brought into the proximity of the sidewall by using the South Bend rotary index table.

All throat measurements were made at a distance of 2.15 inches ($\frac{N}{D_h}$ = -.4) upstream from the actual throat. This was done to avoid the errors associated with measurements in the throat as discussed by Carlson et al. (1967) and Saqi and Johnston (1967).

Data Collection

Since the air supply system was a new installation, it had to be adjusted prior to actual data procurement. Preliminary testing revealed that the desired flow rate could be obtained if the Buffalo Forge Blower was operated at 1100 RPM. However, large fluctuations in the supply line accompanied this operating point. Changing the operating point by decreasing the resistance provided the first reduction in fluctuations. However, the remaining fluctuations of the system flow were still high. Familiarity with controls helped to minimize the remaining fluctuations. The Regutron II control system consisted of a potentiometer which was used to set the desired speed and four rheostats which allowed for adjustment of the minimum speed, maximum speed, the anti-hunt characteristics of the speed control and the rate of

speed change. Since the flow rate was established at this point, the controls were adjusted and the fluctuations noted. After considerable trial and error the settings of the Regutron II were optimized and this resulted in a substantial reduction of the flow system velocity fluctuations, down to a value of $\pm$ 3%.

Consultation with the manufacturer of the Regutron II, Electric Machinery Company, Minneapolis, Minnesota, revealed that this model will control within $\pm$ 2% of a setting depending upon load and voltage conditions. However, the Iowa State University unit was mounted on the outside wall which might affect the Zener diodes, which are not temperature compensated. It is believed that the remaining fluctuations were due to large eddies. Since the fluctuation level in the test section was still not satisfactory, a series flow resistance was installed in the small plenum chamber as described previously. The screens reduced the velocity fluctuations to about $\pm$ 1%. At this point it finally appeared that the test section could yield useful data. A further reduction of the test section velocity fluctuations was provided by the seven screens in the plenum chamber. Now the fluctuations were down to a fraction of a per cent which was considered satisfactory. It is encouraging to note that Hussain and Reynolds (1970) utilized a similar approach to minimize fluctuations in their test facility.

The only further unsteady flow difficulty encountered involved a slight drift in the system flow rate, the cause of which could not be isolated. However, by constantly monitoring the reference manometer readings it was possible to note the drift which was corrected by using the bypass valve.

Normally, the blower produced excessive flow immediately after start up. However, after an hour or two of warm up time the flow rate dropped off. If the system stabilized at a slightly different setting, the bypass valve was adjusted. Another one-half hour was allowed for the system to stabilize. In the meantime the instrumentation was also allowed to achieve steady state conditions. Normally, three hours would suffice for the blower and the instrumentation to reach stable states. One other difficulty encountered was associated with temperature change of the air stream. This effect was minimized by running early in the morning when the outside air was still cool enough to be used to keep the warmer laboratory air temperature fairly constant.

Once a stable state was reached, the hot wire standby voltage was reset to the value used during calibration and the barometer and reference velocity and pressures were recorded. The hot wire sensor was then brought into position and a reading taken. After each traverse was made measurement repeatability was checked. This permitted one to judge

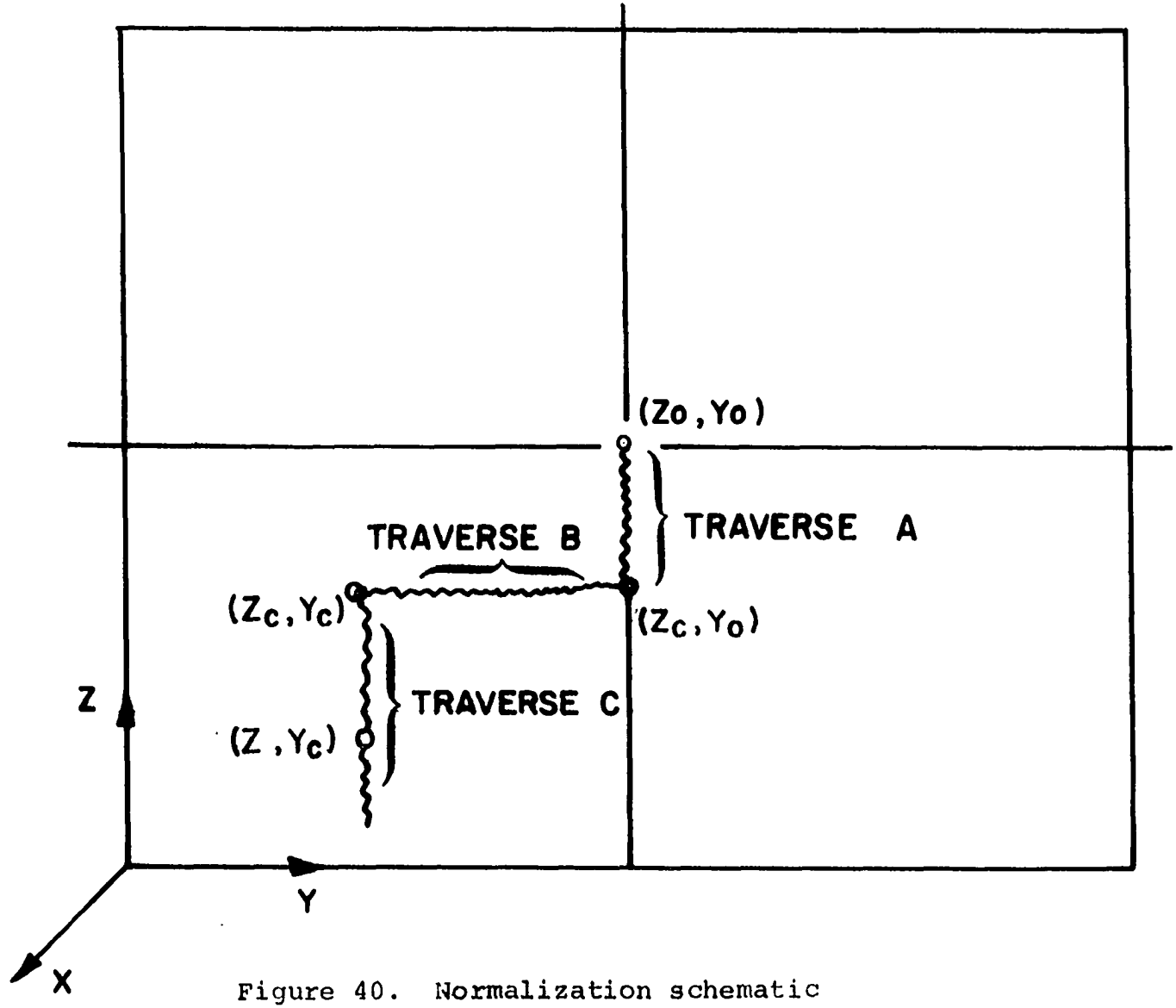

Figure 40. Normalization schematic

immediately if any serious changes of the instrumentation, ambient condition or flow occurred during the traverse. Three values of all the hot wire signals were recorded in time sequence for a given traverse point. These were later averaged to yield a more precise value. The coordinates and signal of each sensor were recorded directly on Fortran coding forms. Once the data was punched out on cards the flow variables such as velocity and direction were obtained from a data reduction program (Appendix E). There were two programs for this purpose. One was designed for the single sensor, the other for the double sensor.

Since the data were taken over a time period extending from April 10, 1970 to July 11, 1970, it was considered important to produce a composite set of data which would nearly represent a consistent set of results.

In order to accomplish this objective velocity traverses were linked as follows (Figure 40):

$$\frac{Q(z,y_c)}{Q\ (z_0,y_0)} = \left[\frac{Q(z,y_c)}{\overline{Q}(z_c,y_c)}\right]_c \cdot \left[\frac{Q(z_c,y_c)}{\overline{Q}(z_c,y_0)}\right]_b \cdot \left[\frac{Q(z_c,y_0)}{Q\ (z_0,y_0)}\right]_a \tag{94}$$

where

$\left[\frac{Q(z,y_c)}{\overline{Q}(z_c,y_c)_c}\right]$ pertains to traverse c

$Q(z,y_c)$ is the velocity at any point of traverse c

$\bar{Q}(z_c,y_c)$ is the average velocity for traverse c

and

$$\bar{Q}(z_c,y_0)_b = Q(z_c,y_0)_a \tag{95}$$

$$\bar{Q}(z_c,y_c)_c = Q(z_c,y_c)_b \tag{96}$$

Each term in the brackets was evaluated from the values contained in the array for that traverse. It was then possible to obtain velocity references to the velocity at the reference point (the center of the passage).

A similar procedure was utilized to reference the angles yielding the equation

$$\begin{aligned}\alpha(z,y_c) = \bar{\alpha}(z_0,y_0) + \{&[\alpha(z,y_c)-\bar{\alpha}(z_c,y_c)]_c \\ &+ [\alpha(z_c,y_c)-\bar{\alpha}(z_c,y_0)]_b \\ &+ [\alpha(z_c,y_0)-\bar{\alpha}(z_0,y_0)]_a\}\end{aligned} \tag{97}$$

Here again each term in the bracket could be evaluated from values contained in the array for the given traverse. Thus, all of the data was consistent within itself and variations due to changes in the reference conditions, calibration, and the like were eliminated.

The traverses were designated in the following manner:

SPTXXa = traverse number

S = series 1 or 2

P = position throat 1, exit plane 2

T = traverse type vertical V, horizontal H, tangential T

XX = if vertical traverse, y, distance in tenth of an inch, if horizontal traverse, z, distance in tenth of an inch

a = if more than one traverse with same designation letters a, b or c, included as necessary

For example 11V25 is a series 1 vertical traverse at the throat with y = 2.5 inches.

A summary of traverses taken is shown in Tables 1a, 1b, 2a and 2b. The data itself is presented in Appendix C.

Propagation of Uncertainty

It is known that a true value of a variable can be estimated whenever a large number of observations are available. One cannot utilize the same approach on single-sample investigations. Even though in this case there were three samples at each point, this is not really sufficient for a good statistical analysis. Thus, the three values were averaged and subsequently treated as single values. Kline and McClintock (1953) have studied this problem and recommend that the experimenter estimate the reliability of a given variable and report that observation in terms of an uncertainty interval for chosen odds. The mathematical expression for the above is

Table 1a. Series 1 throat traverse (velocity measurements only)

Traverse number	Coordinates and range (inches) x	y	z
11V03	-2.15	0.3	0.0,1.8
11V05	-2.15	0.5	0.0,1.8
11V08	-2.15	0.8	0.0,1.8
11V10	-2.15	1.0	0.0,1.8
11V20a	-2.15	2.0	0.0,1.8
11V20b	-2.15	2.0	1.5,3.4
11V25	-2.15	2.5	0.0,1.8
11V30	-2.15	3.0	0.0,1.8
11V40	-2.15	4.0	0.0,1.8
11V42	-2.15	4.2	0.0,1.8
11V45	-2.15	4.5	0.0,1.8
11V48	-2.15	4.8	0.0,1.8
11H18	-2.15	0.5,4.5	1.8
11H25	-2.15	2.5,5.0	2.5
11H32a	-2.15	0.0,2.5	3.2
11H32b	-2.15	0.5,4.5	3.2

Table 1b. Series 1 exit plane traverse (velocity and direction measurements)

Traverse number	Coordinates and range (inches) x	y	z
12V10	15.0	1.0	0.0,1.3
12V30a	15.0	3.0	0.0,1.8
12V30b	15.0	3.0	1.8,3.5
12V45	15.0	4.5	0.0,1.3
12H25a	15.0	0.0,3.0	2.5
12H25b	15.0	3.0,5.9	2.5
12H25c	15.0	1.6,5.4	2.5
12H13	15.0	1.0,4.8	1.3
10T00	0,45°		

Table 2a. Series 2 throat traverse (velocity measurements only)

Traverse number	Coordinates and range (inches) x	y	z
21V05	-2.15	0.5	0.0,1.8
21V15	-2.15	1.5	0.0,1.8
21V25a	-2.15	2.5	0.0,1.8
21V25b	-2.15	2.5	1.8,3.4
21V35	-2.15	3.5	0.0,2.5
21V45	-2.15	4.5	0.0,1.8
21H18a	-2.15	0.0,2.5	1.8
21H18b	-2.15	2.5,5.0	1.8
21H18c	-2.15	0.4,4.8	1.8
21H25a	-2.15	0.4,3.8	2.5
21H25b	-2.15	2.5,4.8	2.5

Table 2b. Series 2 exit plane traverse (velocity and direction measurements)

Traverse number	Coordinates and range (inches) x	y	z
22V20	15.0	2.0	0.0,1.5
22V30a	15.0	3.0	0.0,1.5
22V30b	15.0	3.0	1.3,2.5
22H13a	15.0	0.0,5.3	1.3
22H13b	15.0	3.0,6.0	1.3
22H13c	15.0	0.0,3.0	1.3
22H25	15.0	0.3,5.3	2.5

$$V_T = V_{ob} \pm E_v(\eta \text{ to } 1) \tag{98}$$

where

V_t = the true value

V_{ob} = observed or mean value

E_v = uncertainty interval

$(\eta$ to 1) = the odds given that V_t is within $\pm E_v$ of V_{ob}

The uncertainty interval E, can be estimated by using the following relationship suggested by Kline and McClintock (1953)

$$E_Q = \left[\left(\frac{\partial Q}{\partial a_1}\delta a_1\right)^2 + \left(\frac{\partial Q}{\partial a_2}\delta a_2\right)^2 + \ldots \left(\frac{\partial Q}{\partial a_n}\delta a_n\right)^2\right]^{1/2} \tag{99}$$

where Q is the dependent variable under consideration which is a function of the independent variables a_n. It is stipulated that each of the independent variables has a normal

distribution and Q is a function of the form $Q = Q(a_1, a_2, a_3, \ldots a_n)$. If the same odds are used for all of the independent variable uncertainties, then the calculated uncertainty of the dependent variable will have the same odds.

Independent variables and their uncertainties

Variable	Typical value	Uncertainty
Width	5.000 inches	0.003 inches
Height	5.000 inches	0.003 inches
Radius of Centerline	19.0985	0.003 inches
Angle	(0.00 - 45.00) deg.	2 min
Temperature		
mercury thermometer	(75-90) deg F.	0.5 deg. F.
thermocouple	(75-90) deg F.	1.0 deg. F.
Pressure		
barometer	28.900 - 30.000 in Hg	0.006 in Hg
manometers	(-1.00 - 4.00) in H_2O	0.01 in H_2O
Resistance	(3.00 - 10.00 ohms	0.01 ohms
Voltage	(2.000 - 3.000) volts	0.003 volts (Repeatability value)

A summary of typical values of dependent variables and their uncertainty values with 20 to 1 odds are shown below:

Static pressure

$$P_s = 0.390 \pm 0.0019 \text{ inches of water}$$

Density

$$P = 0.071 \pm 0.00013 \text{ lb}_m/\text{ft}^3$$

Velocity (Pitot-static tube measurement)

$$V = 118 \pm 0.6 \text{ ft/sec.}$$

Velocity (hot wire measurement)

$$V = 118 \pm 1.2 \text{ ft/sec. repeatability}$$

Angle

$$= 10° \pm 0.5° \text{ repeatability}$$

Effectiveness

$$= 0.435 \pm 0.002 \text{ dimensionless}$$

The calculations themselves are shown in Appendix D.

During the experiment a serious effort was made to insure a hot wire repeatability of 0.5 degrees and 1.2 ft/sec. From the practical viewpoint, this required maintaining temperature limits of $\pm$ 3° F during the test program.

In general the last reading during a traverse was within 1% of the first reading. A slightly greater deviation of each traverse from the calibration data was allowed. It is believed that this is satisfactory as long as the first and last points agree closely. Smith (1970) compared normalized data from two different traverses and the data were nearly identical. Unpublished data taken by the author showed that in spite of all the difficulties with absolute velocity

measurements the angle measured agreed closely from one calibration to another. This seems reasonable, if one assumes both wires age or corrode at a similar rate which apparently has been the case during these experiments.

DISCUSSION OF RESULTS

It has been shown by Sprenger (1959), Reneau, Johnston and Kline (1967), Sovran and Klomp (1967), Wolf and Johnston (1969), Runstadler and Dean (1969) and others that the effectiveness of a diffuser depends on a number of variables. Some are the area ratio, normalized length, turning angle, surface curvature, Reynolds number, inlet boundary layer thickness, inlet Mach number, inlet turbulence level and shape of the inlet velocity profile.

For practical reasons any research on diffuser flow must be sufficiently simplified so that meaningful results can be obtained and analyzed. The inlet velocity profile was chosen as the primary variable to be studied during the present experiment. It was varied significantly by changing the flow development lengths preceding the test diffuser. A development length of 5.5 hydraulic diameters was used in the first series of tests, while a length of 24.9 hydraulic diameters was used for the second series of tests.

Preliminary tests revealed that the flow at the diffuser throat or inlet and exit was nearly symmetrical about the horizontal centerline (midway between top and bottom walls). Thus bottom wall measurements were used to represent the flow over the top surface as well.

The shape of the velocity profile in the core near the diffuser inlet is shown in Figures 41 and 42, and in Figures 43 and 44 for the first and second series of tests. Examination of the figures reveals that there is a uniform core in both series of tests, but that the size of the core is reduced and the size of the boundary layer increased as the development section was made longer. It is pertinent to note that the core occupied only about 50% of the passage height and width in the second series of tests, considerably less than in the Series 1 tests as intended.

A comparison of the measured boundary layer profiles, such as shown in Figures 45 through 50 with $u = U(y/\delta)^{1/7}$ showed good agreement suggesting that the inlet boundary layer flow was turbulent during all of the tests.

The displacement thickness on the pressure wall is slightly larger than on the suction wall. However, the average of pressure and suction sidewalls displacement thickness measured in a plane midway between the top and bottom walls was 0.057 inches which corresponds closely to the value of 0.059 inches observed midway between vertical surfaces on the bottom wall of the Series 1 tests. The average sidewall displacement thickness for Series 2 tests was 0.225 inches and the bottom wall displacement thickness was 0.210 inches. A comparison of these profiles is shown in Figures 51a and 51b. The slight deviation is probably an upstream effect of the

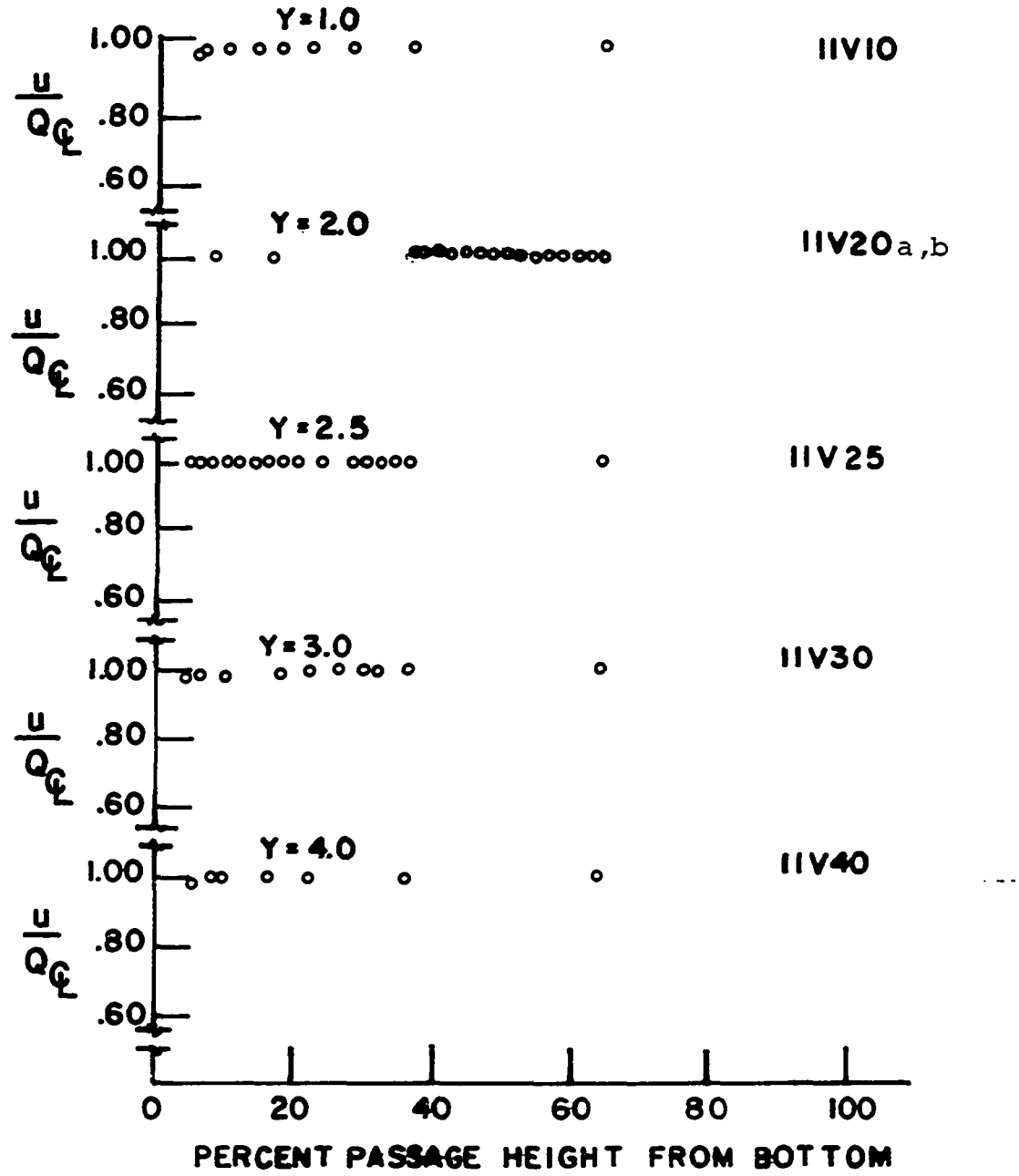

Figure 41. Vertical velocity profiles, core, Series 1

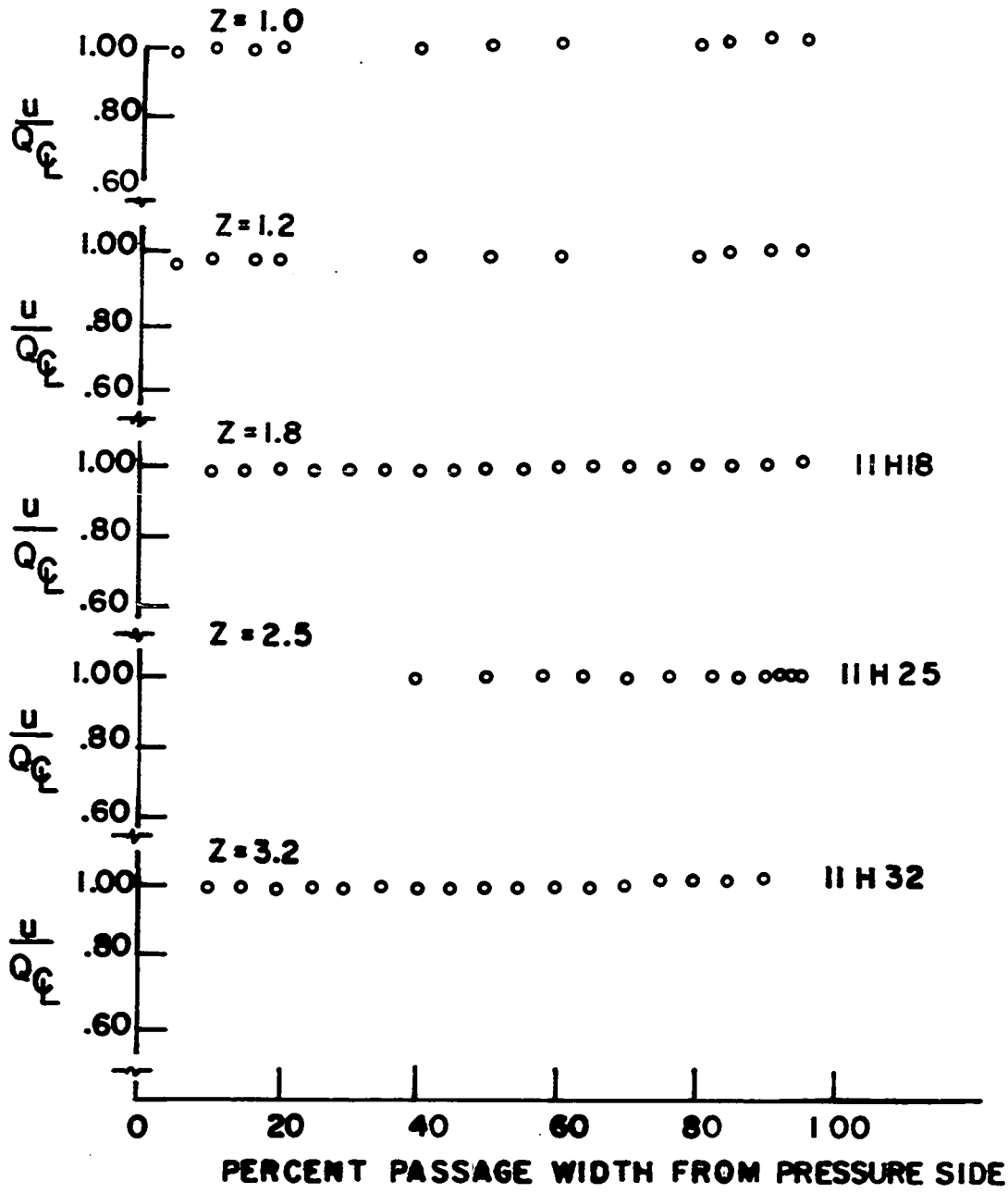

Figure 42. Horizontal velocity profiles, core, Series 1 (points at z=1.0 and 1.2 are cross plotted)

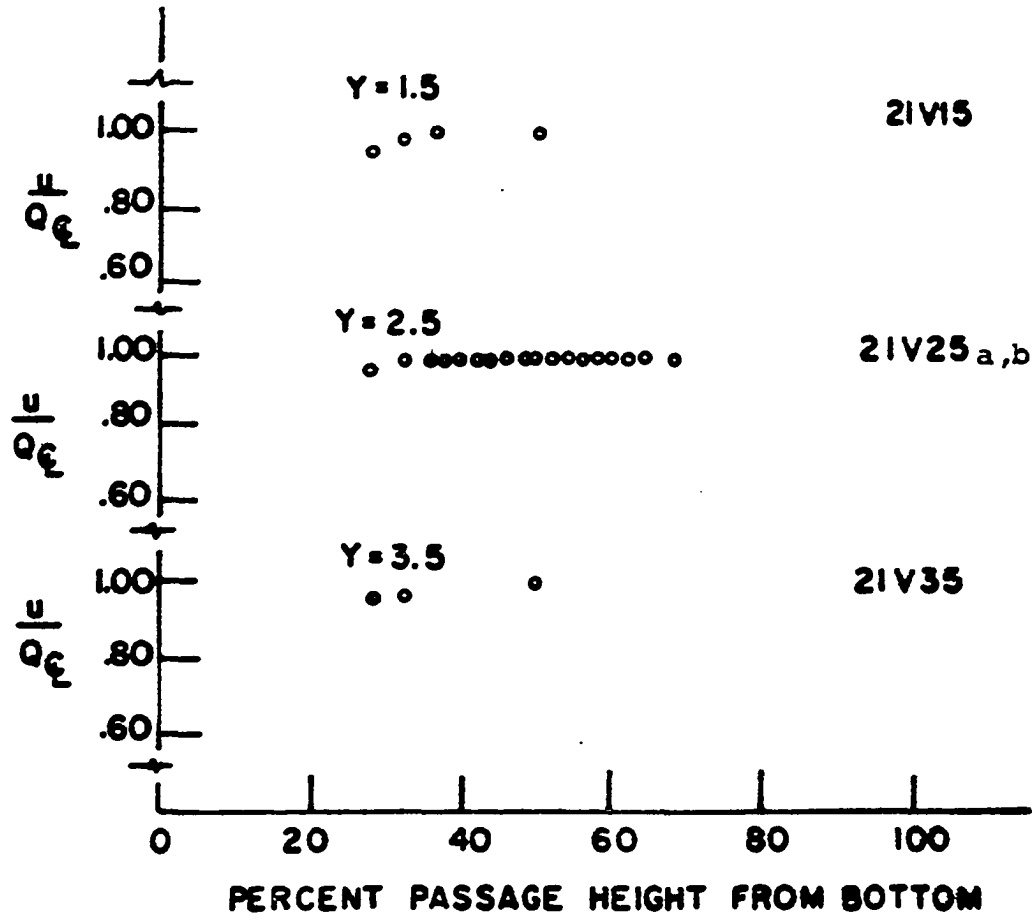

Figure 43. Vertical velocity profiles, core, Series 2

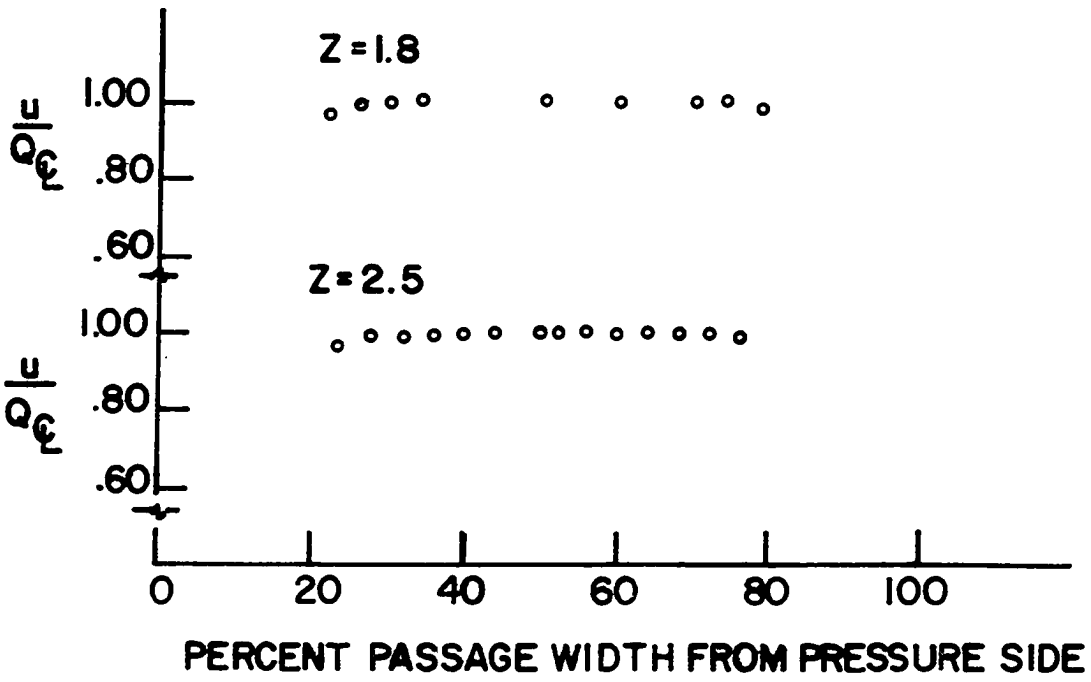

Figure 44. Horizontal velocity profiles, core, Series 2

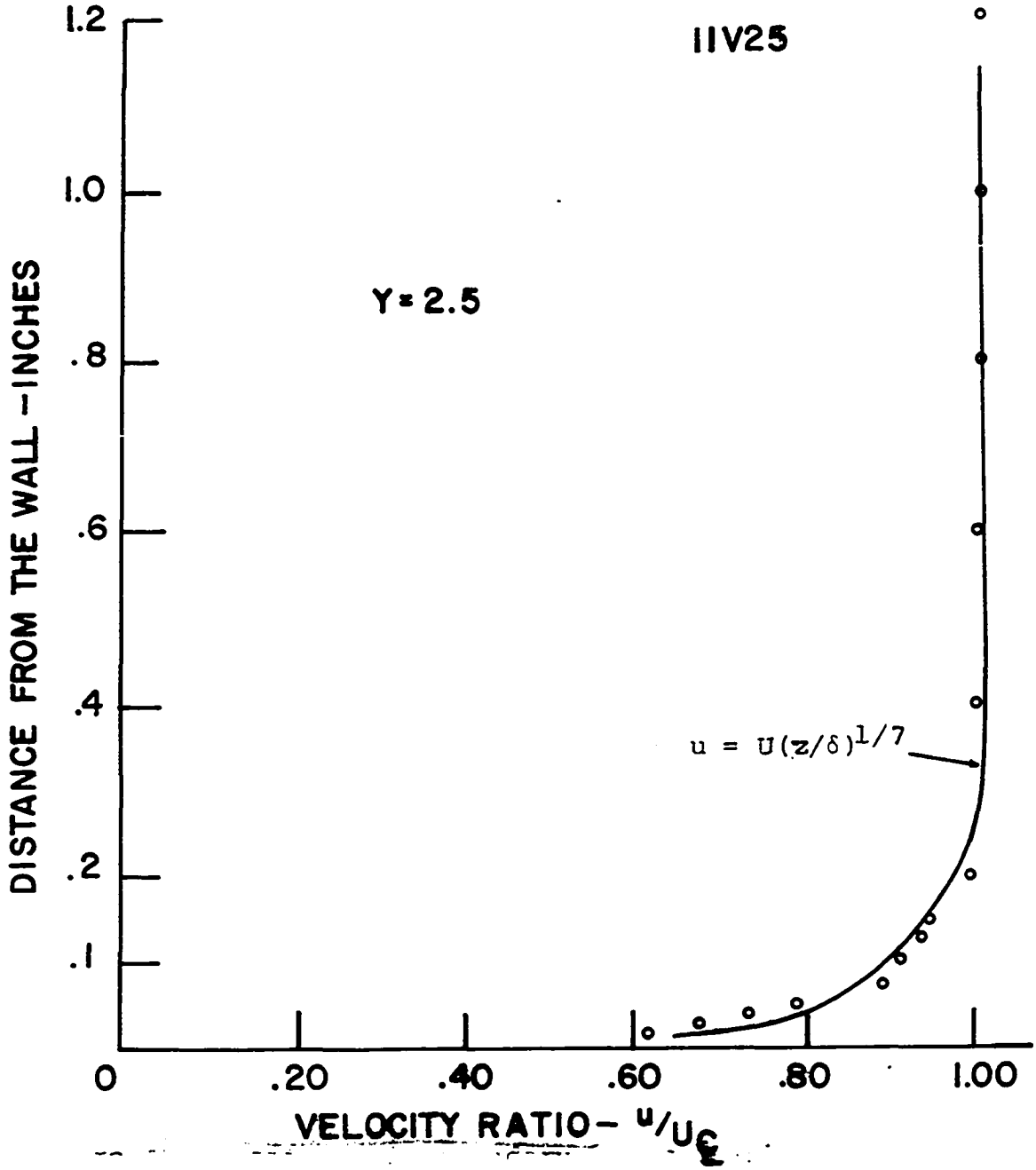

Figure 45. Bottom wall boundary layer, Series 1

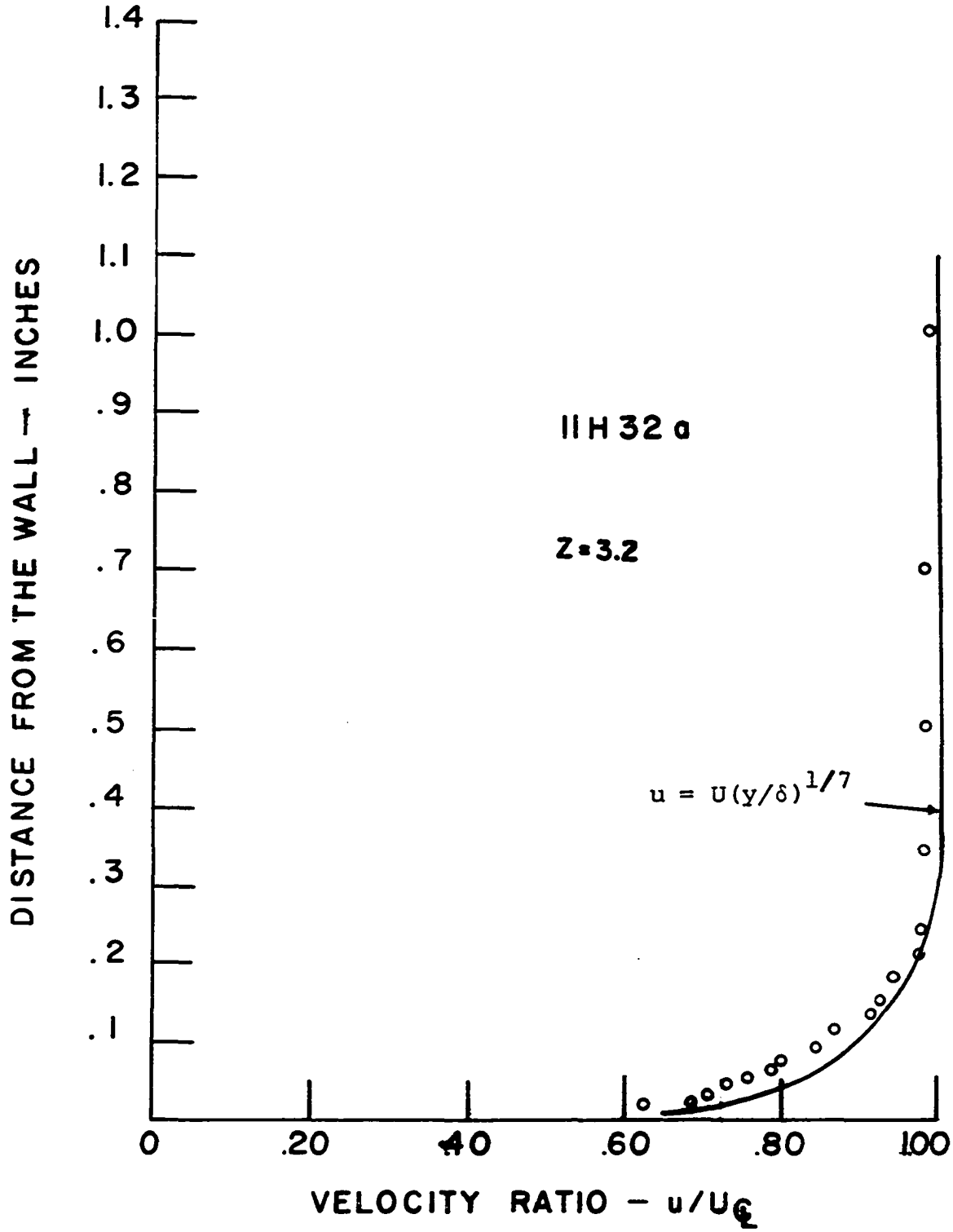

Figure 46. Pressure wall boundary layer, Series 1

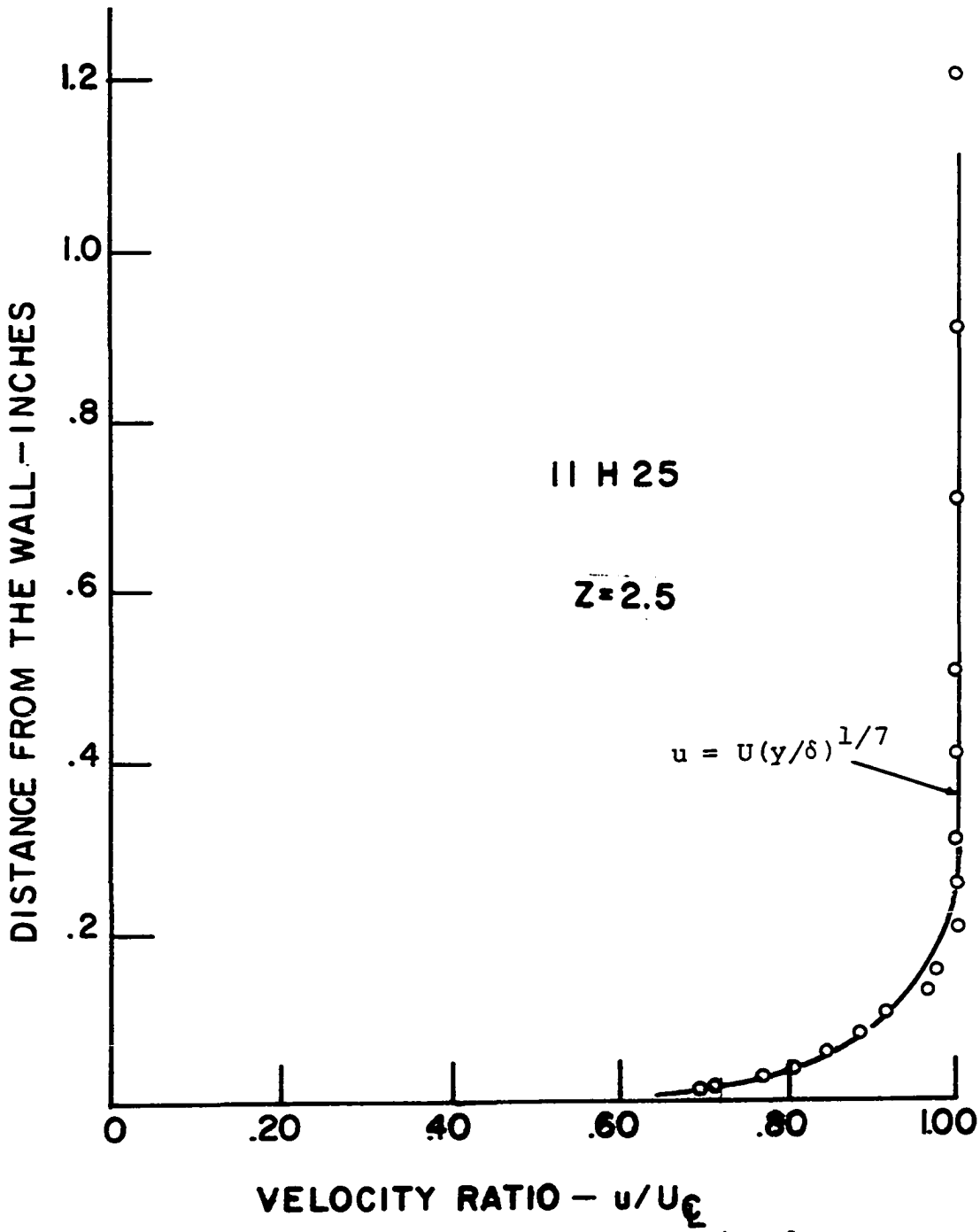

Figure 47. Suction wall boundary layer, Series 1

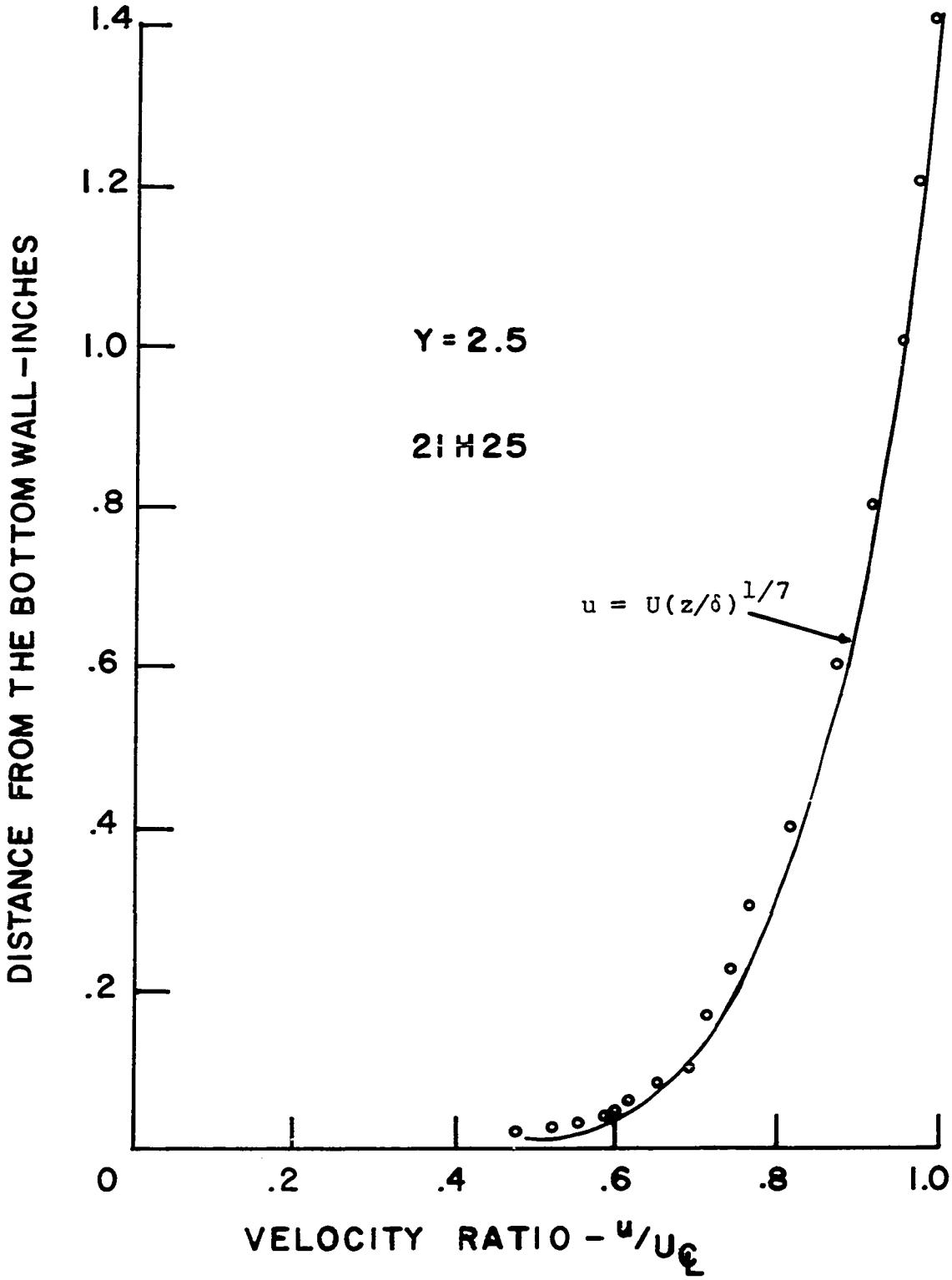

Figure 48. Bottom wall boundary layer, Series 2

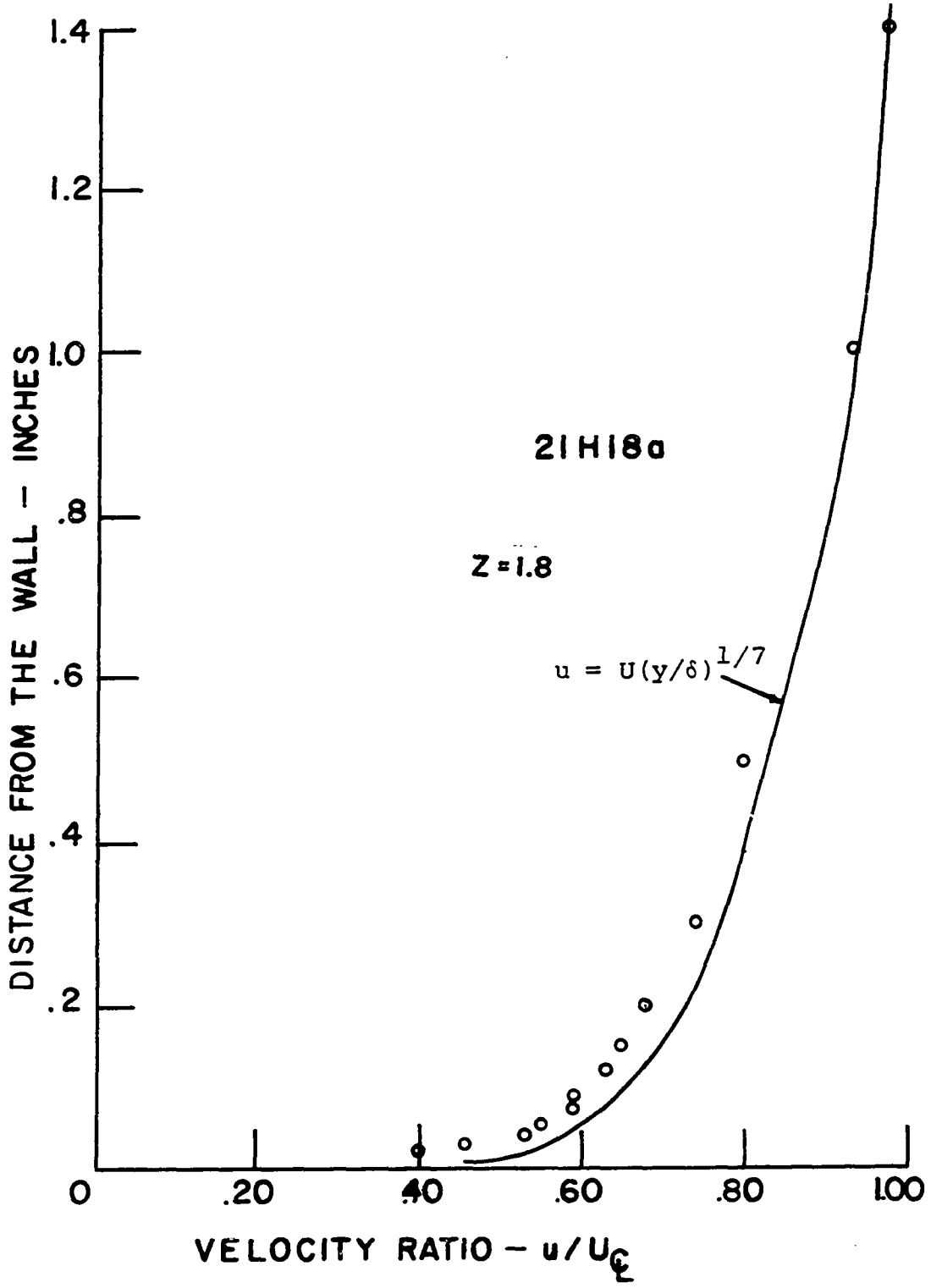

Figure 49. Pressure wall boundary layer, Series 2

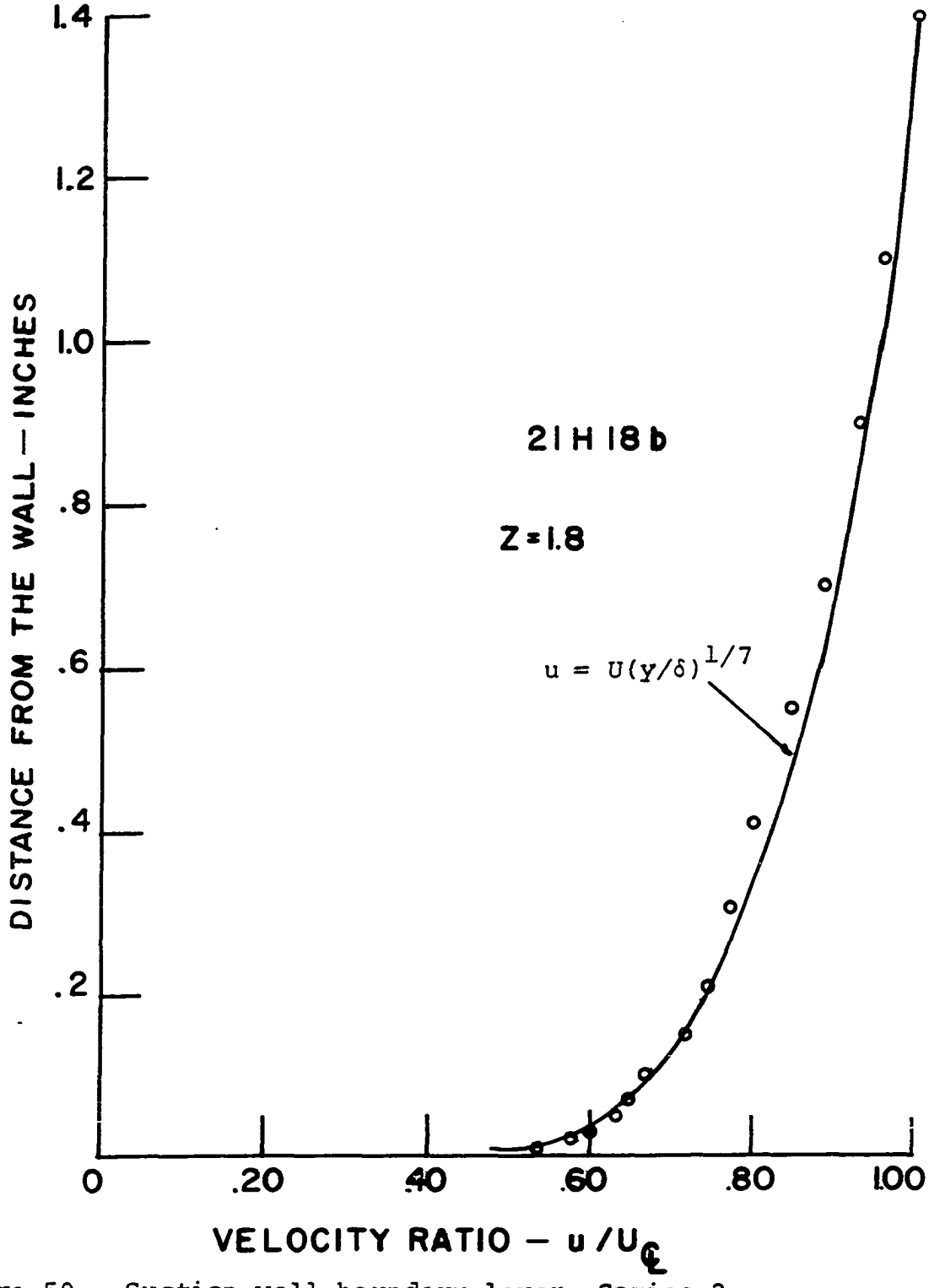

Figure 50. Suction wall boundary layer, Series 2

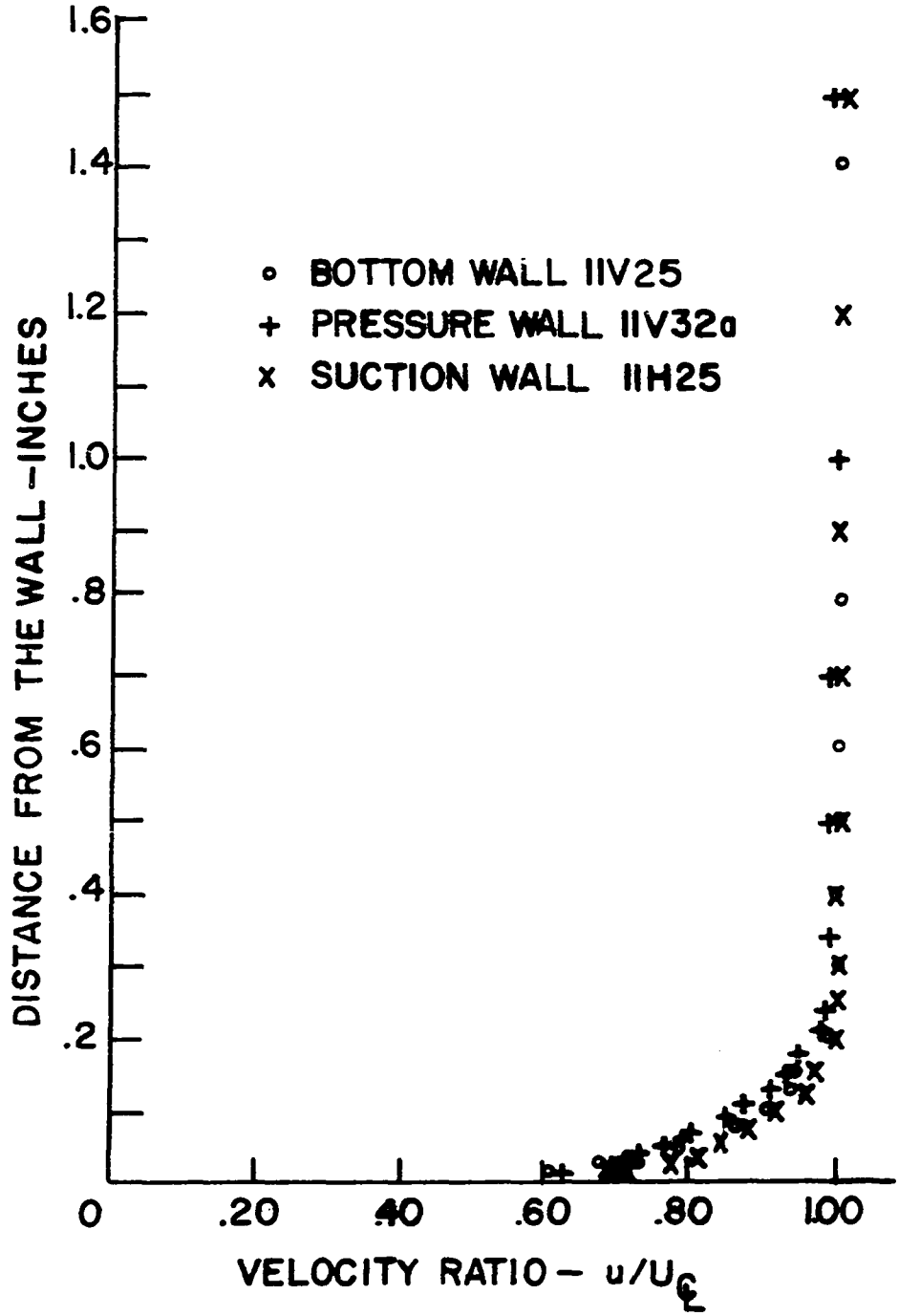

Figure 51a. Boundary layer composite, Series 1

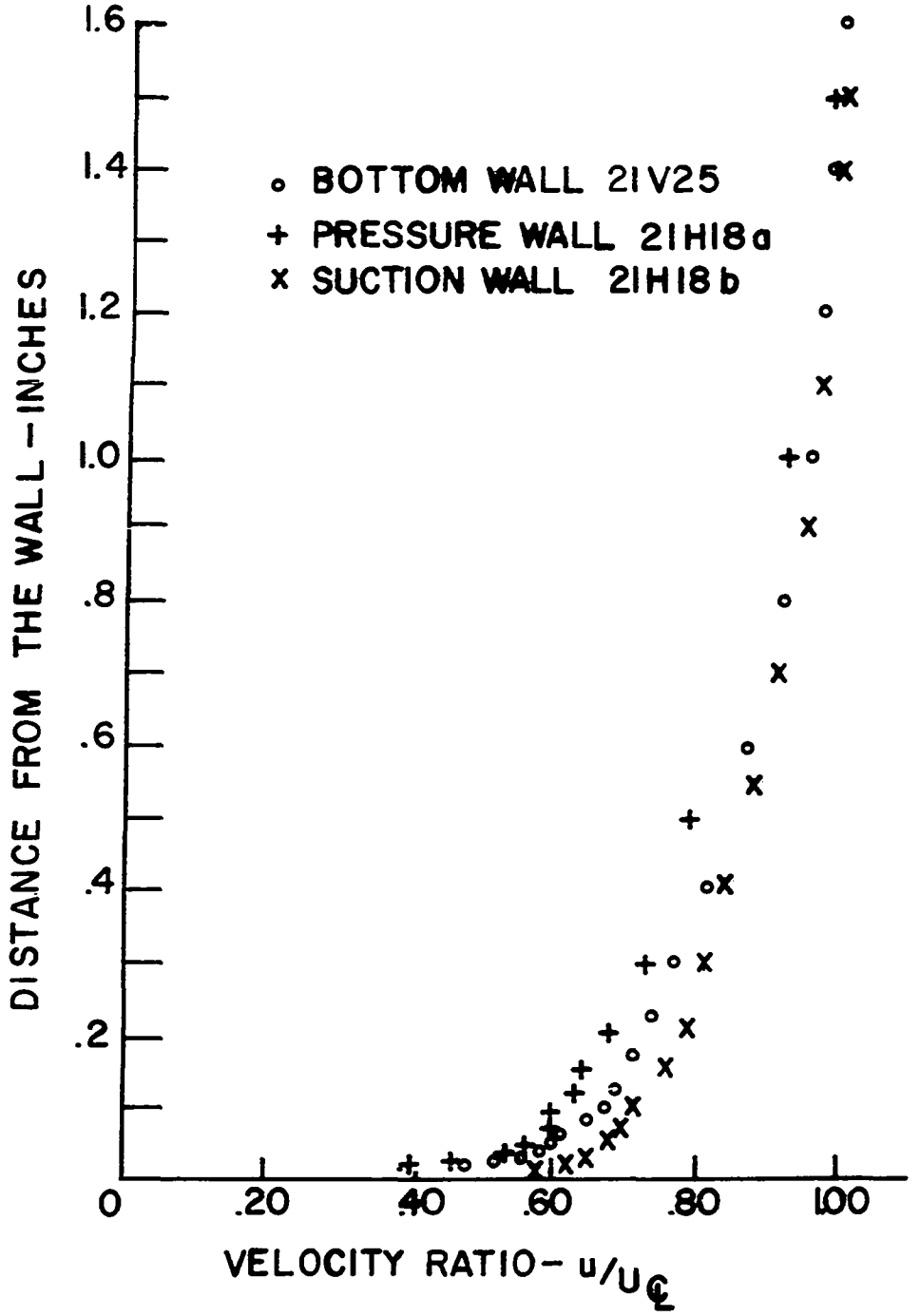

Figure 51b. Boundary layer composite, Series 2

curvature of the sidewalls in the diffuser. In attempting to avoid this influence, measurements were actually taken upstream of the diffuser throat plane after Carlson et al. (1967). The actual position at which the measurements were taken had to be a compromise between two conflicting requirements. One, moving upstream of the geometrical throat to avoid the curvature effects felt upstream and the other, measuring as close to the throat as possible in order to avoid including too much of the straight development section as part of the diffuser.

The blockage factor B as defined by Sovran and Klomp (1967) is:

$$B = \frac{1}{A}\int_A \left(1 - \frac{Q}{Q_{\mathfrak{C}}}\right) dA \qquad (100)$$

The procedure of calculating the blockage factors associated with this experiment consisted of calculating first the mid-plane displacement thickness on each wall, then the "blocked area" for each wall (displacement thickness times the equivalent width of that wall) and finally blockage factor B. This procedure is comparable to that used by Johnston and Powars (1969).

The diffuser inlet blockage was 4.5% for the Series 1 tests and 13.9% for the Series 2 tests. Estimated blockage

for fully developed inlet flow is 18%. This implies that there is a slight reduction of the flow through the diffuser with the long development section since the maximum velocity was the same (within 1/2%) for both series of tests.

As expected the diffuser effectiveness decreased significantly when the blockage factor was increased. The effectiveness of the diffuser tested here was 51% for the blockage factor of 4.5% and 43.5% for the blockage factor of 13.9%. It was evaluated using Equation 1. Figure 52 shows a comparison of the effectiveness of this diffuser and those circular arc ones designed and tested by Sagi et al. (1965). The reason for the greater performance of the diffuser tested here as compared to Sagi's (1965) is primarily due to its lower area ratio and smaller turning angle. There was also a difference in the turbulence intensity between the two experiments. Sagi and Johnston (1967) reported turbulence intensity of 1%, whereas the turbulence intensity was only 0.5% in this experiment.

An understanding of the rise in static pressure throughout the diffuser can be obtained by a study of the static pressure rise along the wall. Variation of pressure along the suction and pressure walls is shown in Figures 53 and 54. The normalized static pressure was obtained by dividing the

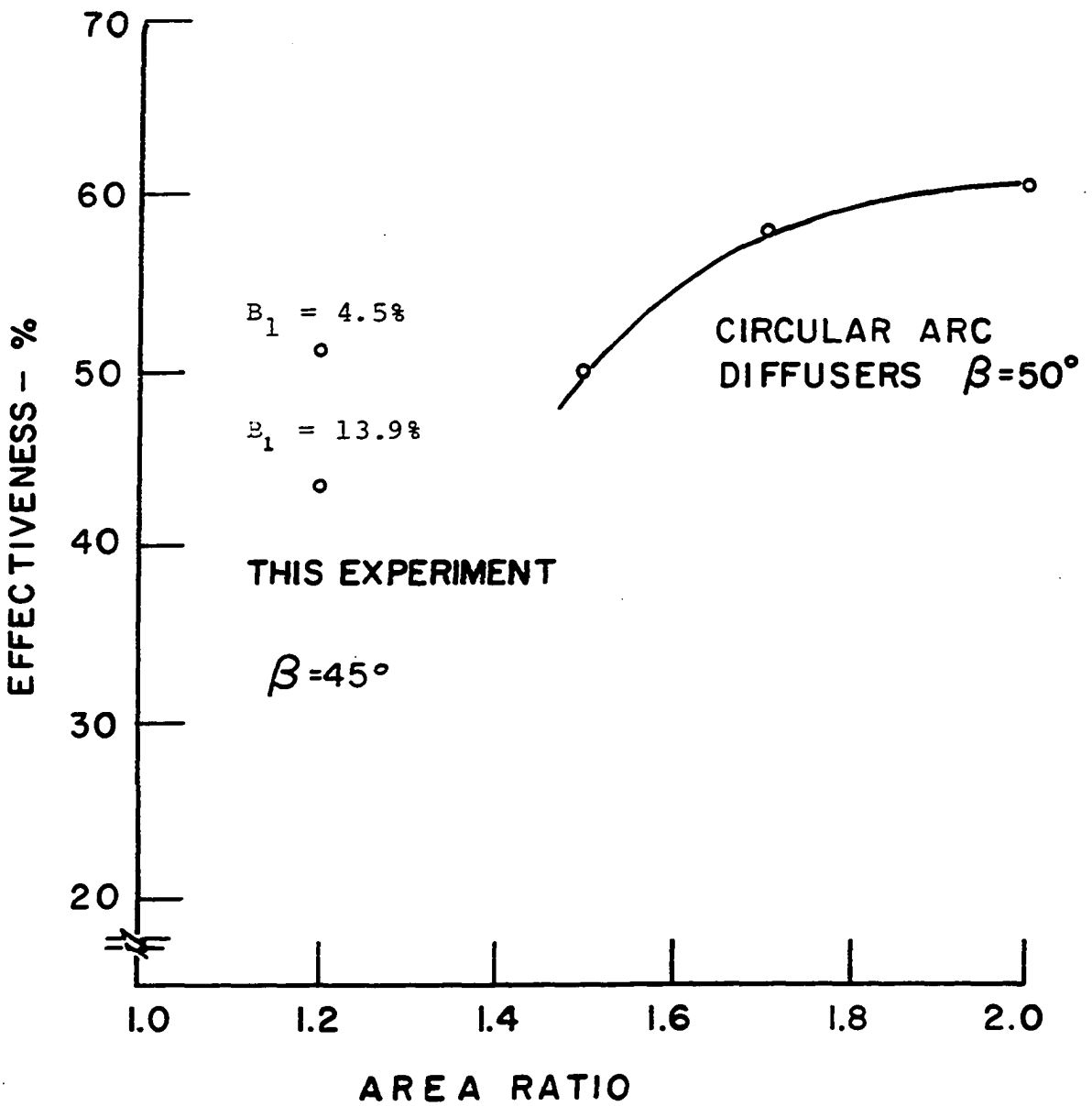

Figure 52. Effectiveness comparison with data from Sagi et al. (1965)

gauge pressure by the inlet dynamic head $\frac{1}{2}\rho\bar{Q}_1^2$ following the example of Sprenger (1959) and Norbury (1969).

These curves are similar in shape because the basic phenomena areidentical in both series of tests. The differences that exist are due to the differences in the effectiveness rather than due to a change in the basic flow pattern. Inspection of the suction wall normalized pressure reveals that there is a continual pressure rise. Since stall is denoted by the local absence of pressure rise, the above data indicates that the diffuser is well behaved.

Thus, the design objective has been reached and the stall regime of Fox and Kline (1962) proved to be a satisfactory guide for this purpose.

The pressure wall exhibits a continual rise in the normalized wall pressure initially. However, since its pressure is higher than the suction wall pressure, it must have a reduction of pressure as the exit is approached. This behavior verifies that the static pressure is uniform at the exit plane of the diffuser. The use of an average static pressure at the exit plane for effectiveness calculations is therefore justified in these experiments.

The radial pressure gradient can be approximated from the wall static pressure measurements if it is assumed that the

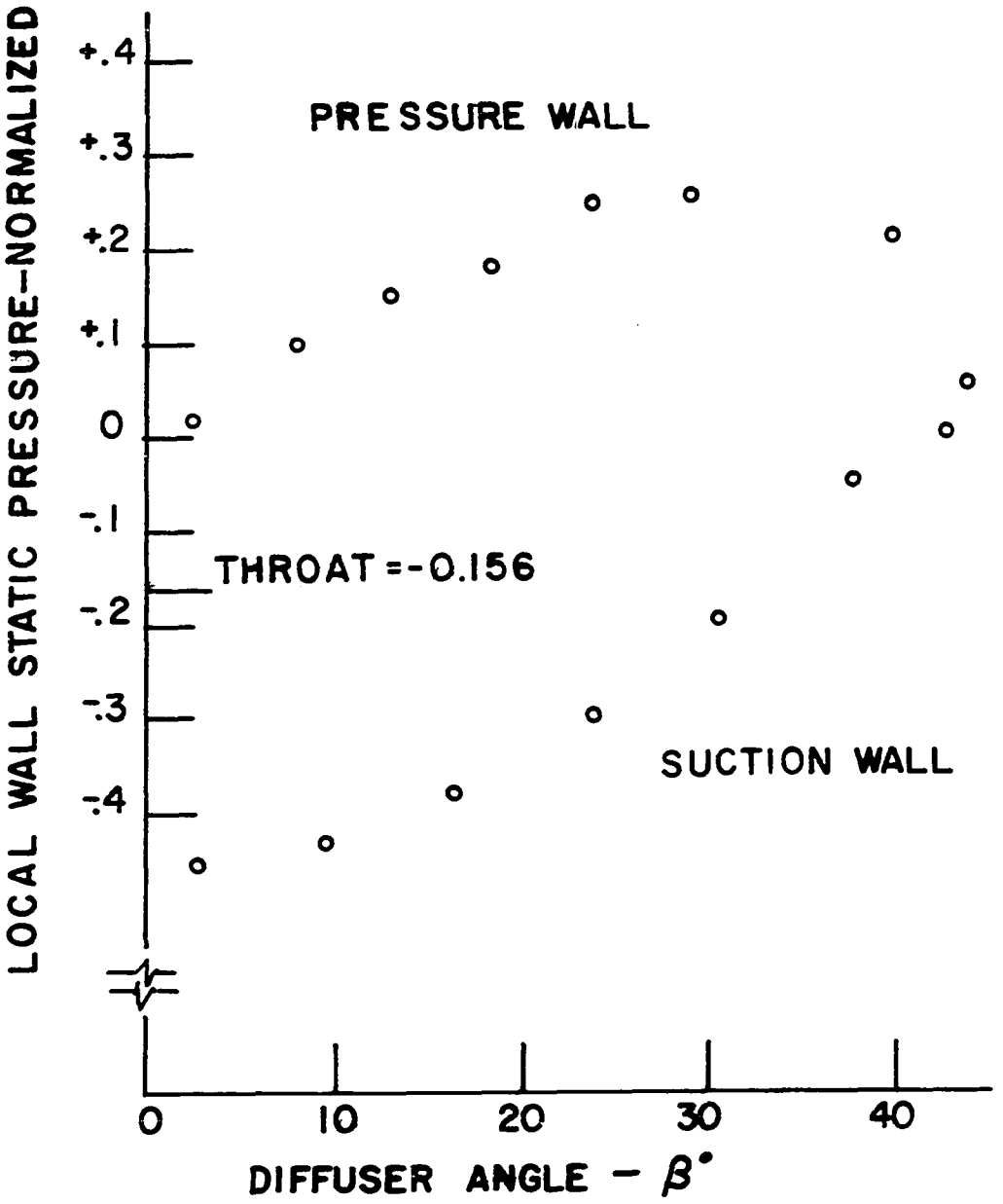

Figure 53. Wall static pressures, Series 1

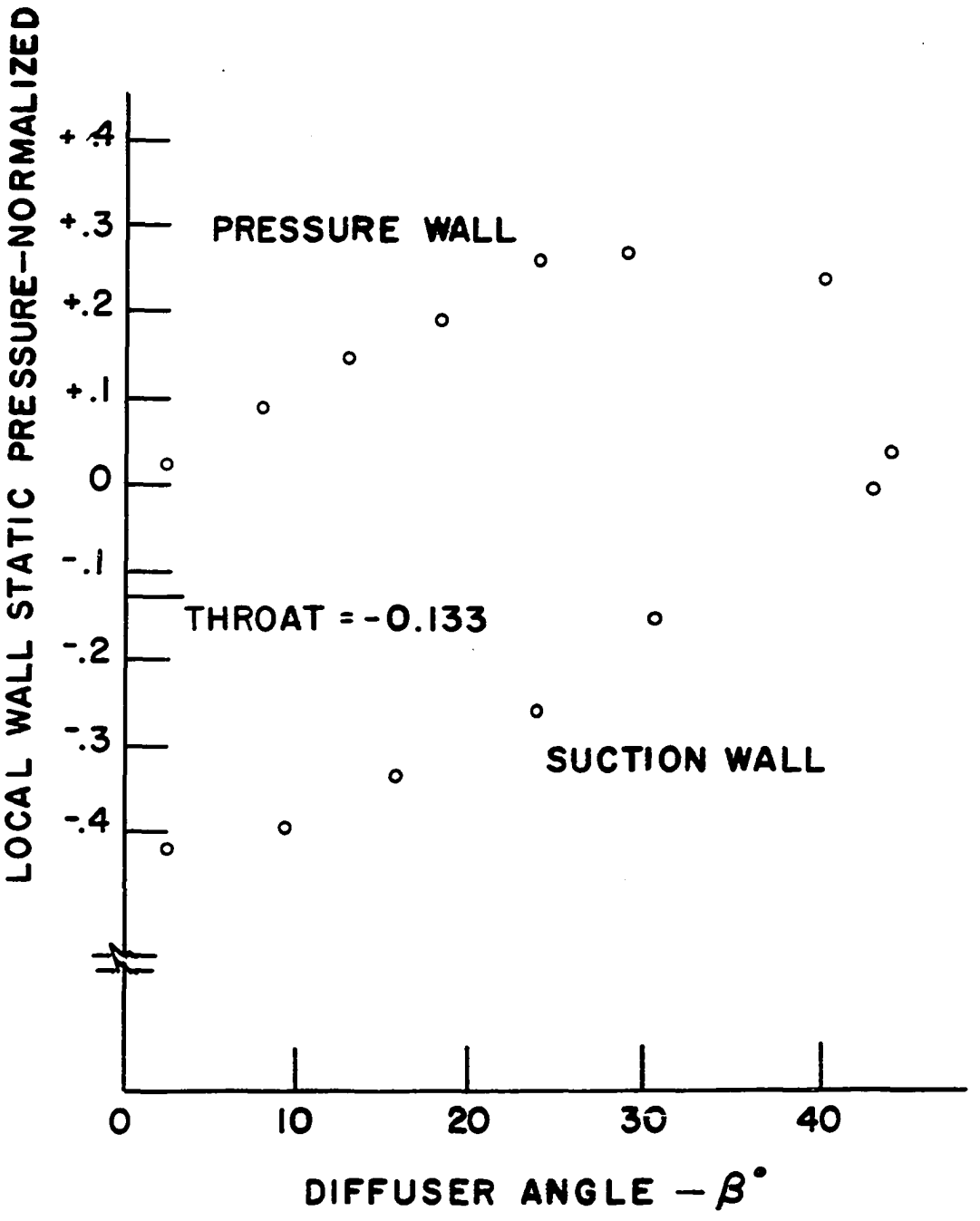

Figure 54. Wall static pressures, Series 2

variation is linear with radius. Taking the difference of pressures between the pressure side and the suction side at a given angle, β, dividing by the radial distance between these two positions, finally dividing by the throat dynamic head $\frac{1}{2} \rho \bar{Q}_1^2$ yields the normalized radial pressure gradient. The parameter $\frac{1}{2} \rho \bar{Q}_1^2$ is chosen since it performs the same normalizing function here as it did in the wall static pressure plots. Inspection of Figure 55 reveals that the radial pressure gradient is high during the first portion (first 22.5°) of the diffuser, and drops off in the second portion, going to zero at the exit plane. The maximum skewing angle (limiting streamline skewing angle) in the boundary layer, as measured by Smith (1970) in a curved passage goes up to a maximum value and then decays as shown in Figure 56. This behavior prompted the author to investigate Smith's (1970) data further to see if there was any correlation between the radial pressure gradient and the skewing angle. A plot of the radial pressure gradient for Smith's experiment is shown in Figure 57. Comparing Figures 56 and 57 it is noted that the value of β/β_{max} where the maximum skewing angle is reached is approximately equal to the value of β/β_{max} where the radial pressure gradient drops off toward zero at the exit of the diffuser. It is difficult to say whether this correlation is very strong due to the fact that this geometry had high area ratio ($\frac{A_2}{A_1} = 1.56$) with

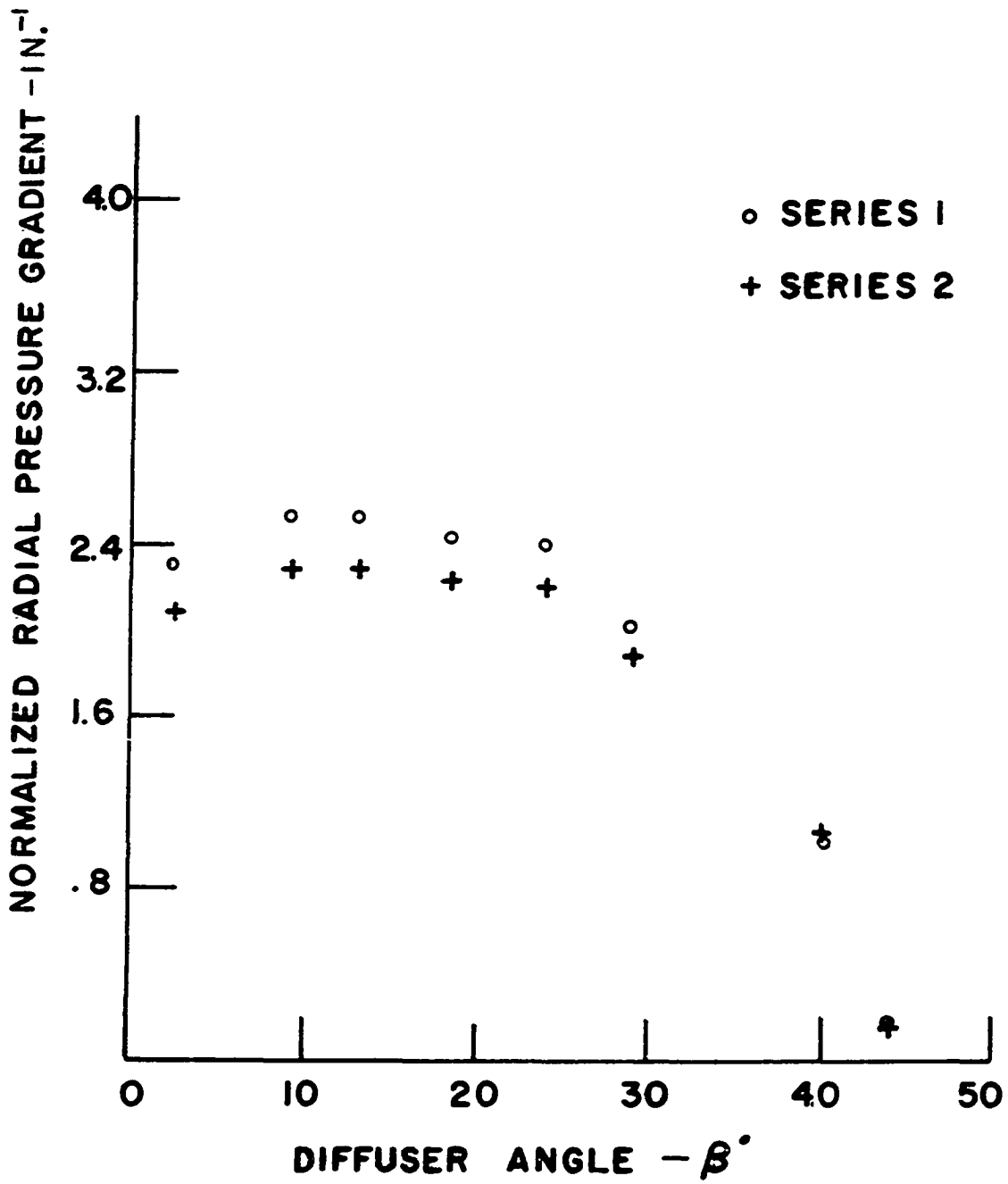

Figure 55. Radial pressure gradient, author's data

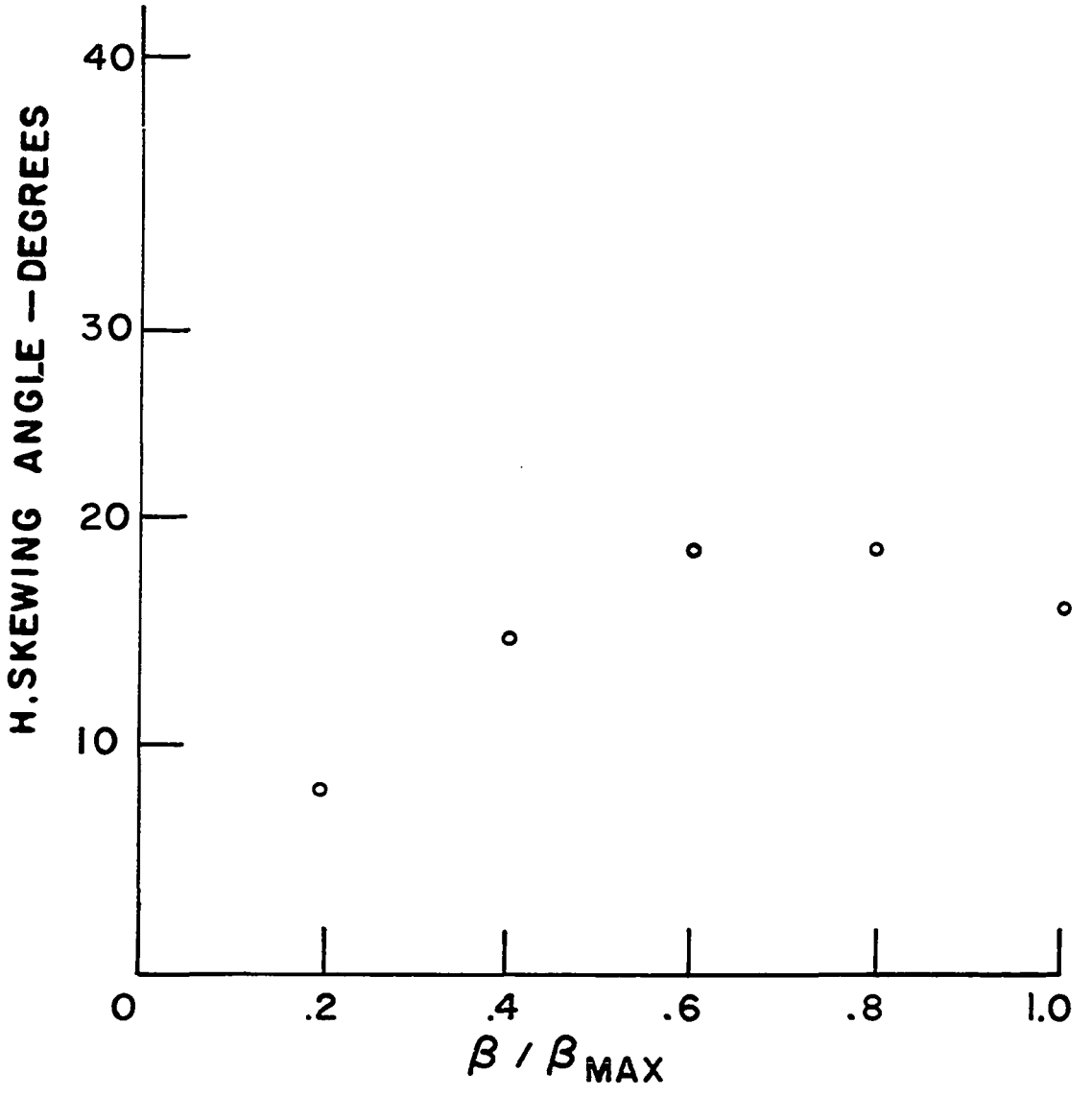

Figure 56. Limiting streamline skewing, Smith (1970)

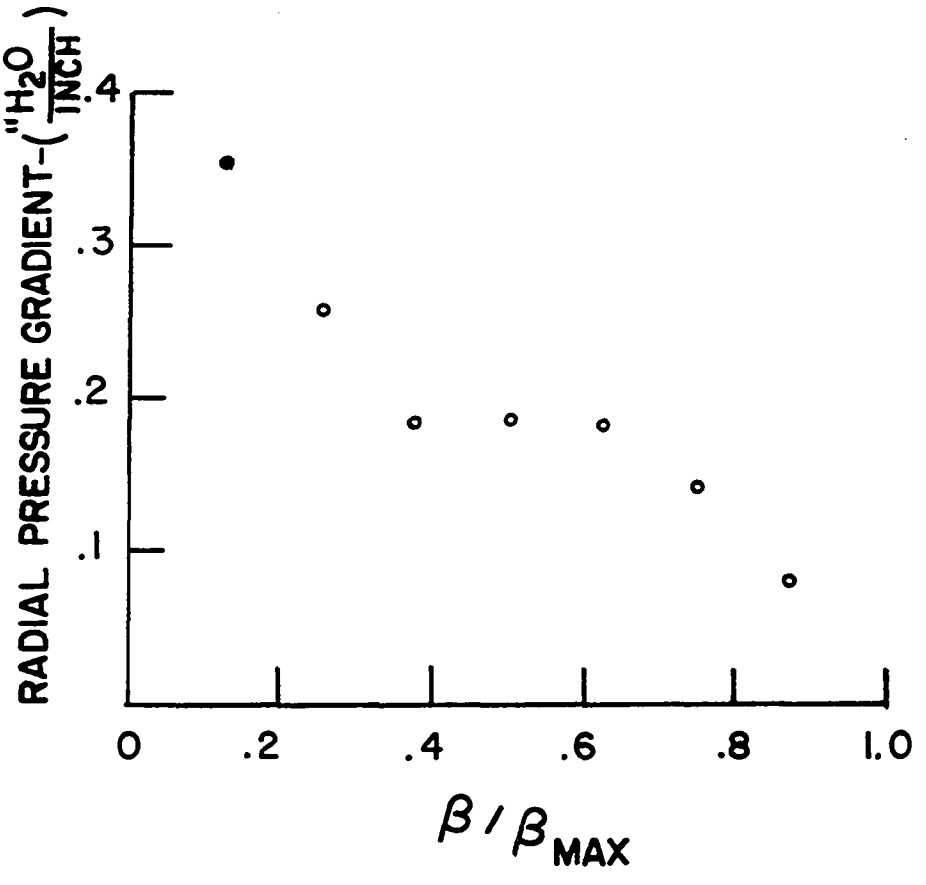

Figure 57. Radial pressure gradient (Smith 1970)

a normalized length N/W_1=3.15, thus being much closer to stall than the geometry tested by the author ($\frac{A_2}{A_1}$ = 1.2, $\frac{N}{W_1}$ = 3).

The primary purpose of a diffuser is efficient deceleration of moving fluid. It follows that the change in the velocity is an important parameter. In the past traversing mechanisms were seldom designed so that traversing along the meanline of the diffuser would be possible. This capability was present here and was utilized to determine the change in velocity magnitude and direction along the meanline of the diffuser. The meanline velocity ratio, is plotted against diffuser angle β in Figure 58. Inspection of the curve indicates that there is more diffusion in Series 1 than in Series 2. This observation is consistent with the higher effectiveness measured for Series 1 tests also. It can also be seen that the diffusion process is approximately linear for the first 30° of turning, consistent with the linear area increase in the diffuser. In the last 15° of turning the diffusion drops off toward zero. This is probably due to the fact that the flow senses the region of constant pressure downstream and begins to flow accordingly. The radial pressure gradient going to zero as the exit plane is reached is further manifestation of the effect of the imposed uniform static pressure condition at the diffuser exit on the upstream flow.

Smith (1970) noted that in his passage the shape factor, H_1, for bottom wall boundary layer, increased initially but

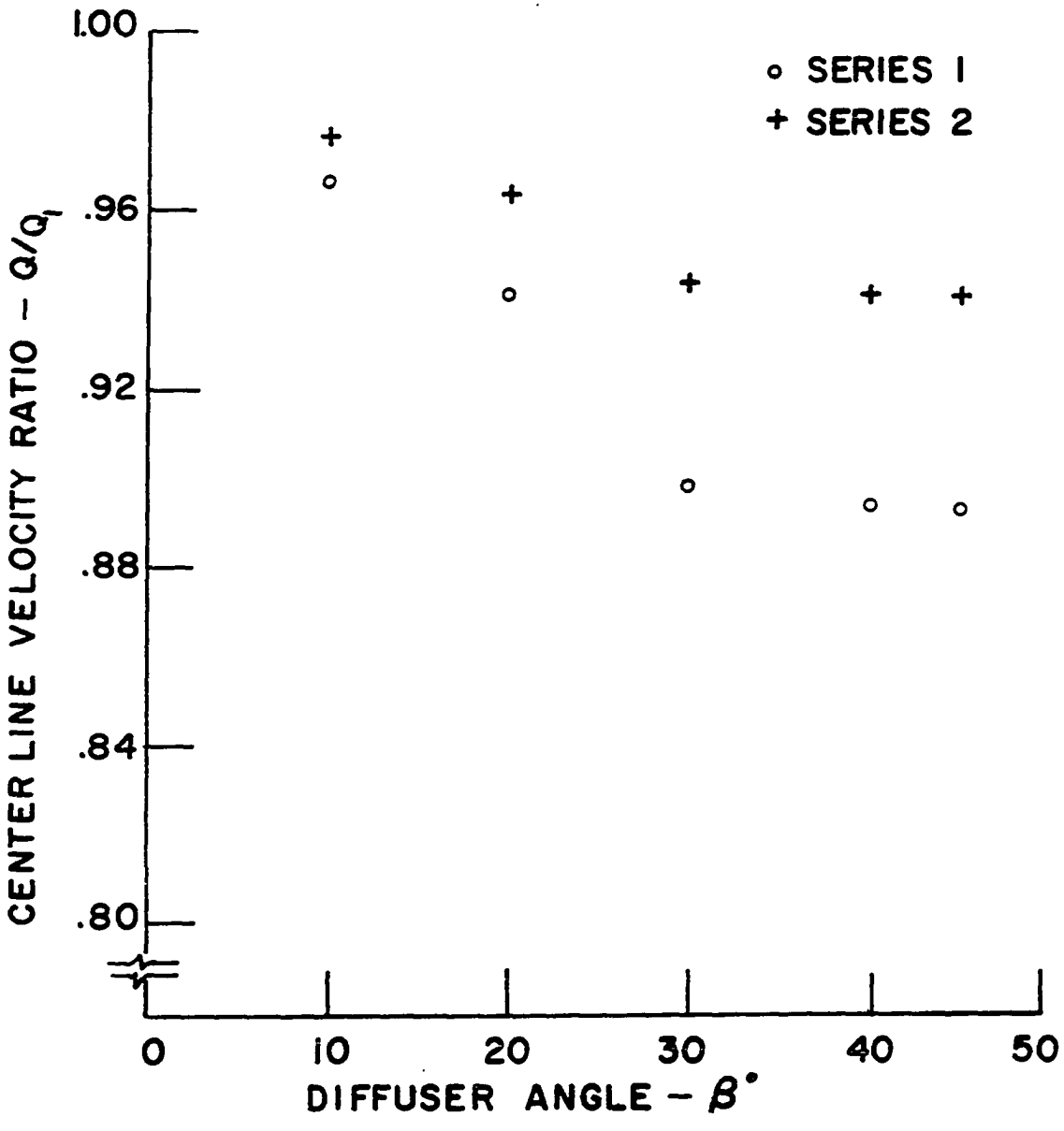

Figure 58. Meanline velocity ratio

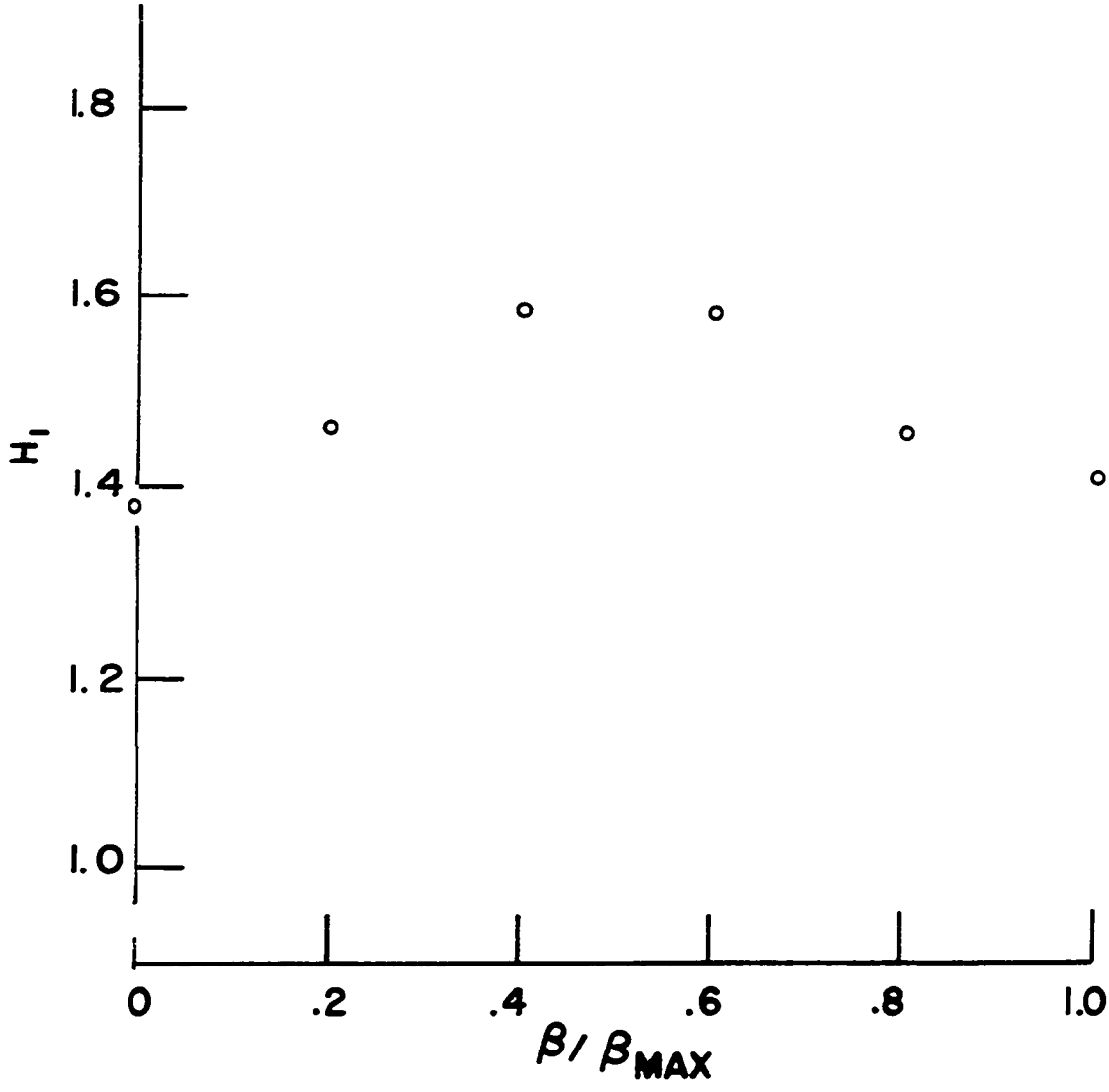

Figure 59. Streamwise shape factor, Smith (1970)

decreased as the exit plane was approached as shown in Figure 59. An explanation for this behavior was required. Using the expression due to van Doenhoff and Tetervin (1943) it is noted that shape factor depends on the momentum thickness, Reynolds number based on momentum thickness, the shape factor and the velocity head, thus

$$\frac{dH}{dx} = e^{4.68(H-2.995)}\left\{-\frac{\theta d(\frac{1}{2}\rho Q^2)}{(\frac{1}{2}\rho Q^2)\,dx} E - 2.035(H-1.286)\right\}\frac{1}{\theta}$$

where

$e = 2.7183$, base of natural logarithm

$E = [2.558 \ln(4.075\ Re_\theta)]^2$

Re_θ = Reynolds number based on momentum thickness

The sign (positive or negative) of the right hand side is dependent upon the quantity in the brackets. Note that for large E and a value of H greater than 1.286, the sign of the quantity within the brackets depends on first term in the brackets. Since the low velocity in this experiment permits the incompressibility assumption, the sign of first term depends on the velocity gradient, $\frac{dQ}{dx}$. Unfortunately, Smith (1970) did not have this data. There is considerable geometrical similarity between the author's experiment and Smith's (1970). In the first portion of the author's diffuser

$\frac{dQ}{dx}$ was negative (see Figure 58) which indicates an increase in the shape factor (Figure 59). It is likely that in the remainder of Smith's passage the velocity either remained constant or increased slightly. The shape factor would accordingly remain constant or decrease.

The core skewing angle along the meanline is plotted in Figure 60. There is no significant skewing along the meanline in the first series of tests. However, the skewing is very significant in the second series of tests, reaching a value of 8.3° at the exit of the diffuser.

Although no direct comparison could be made with any diffuser literature, since no comparable data exists in the open literature at this time, comparison was made with preliminary tests conducted by Francis (1965) on a constant area curved channel followed by a straight duct. Francis (1965) reported that the centerline velocity vector was tangent to the geometrical passage centerline. The blockage factor for the two geometries (Francis and Series I) were probably of about the same order of magnitude since the flow development lengths were similar, being four hydraulic diameters in Francis's test section, and 5.5 in this author's test section. However, there are two fundamental differences between these geometries. Francis had a constant area passage that was followed by a straight constant area discharge section. These differences are significant because diffusing flows behave substantially

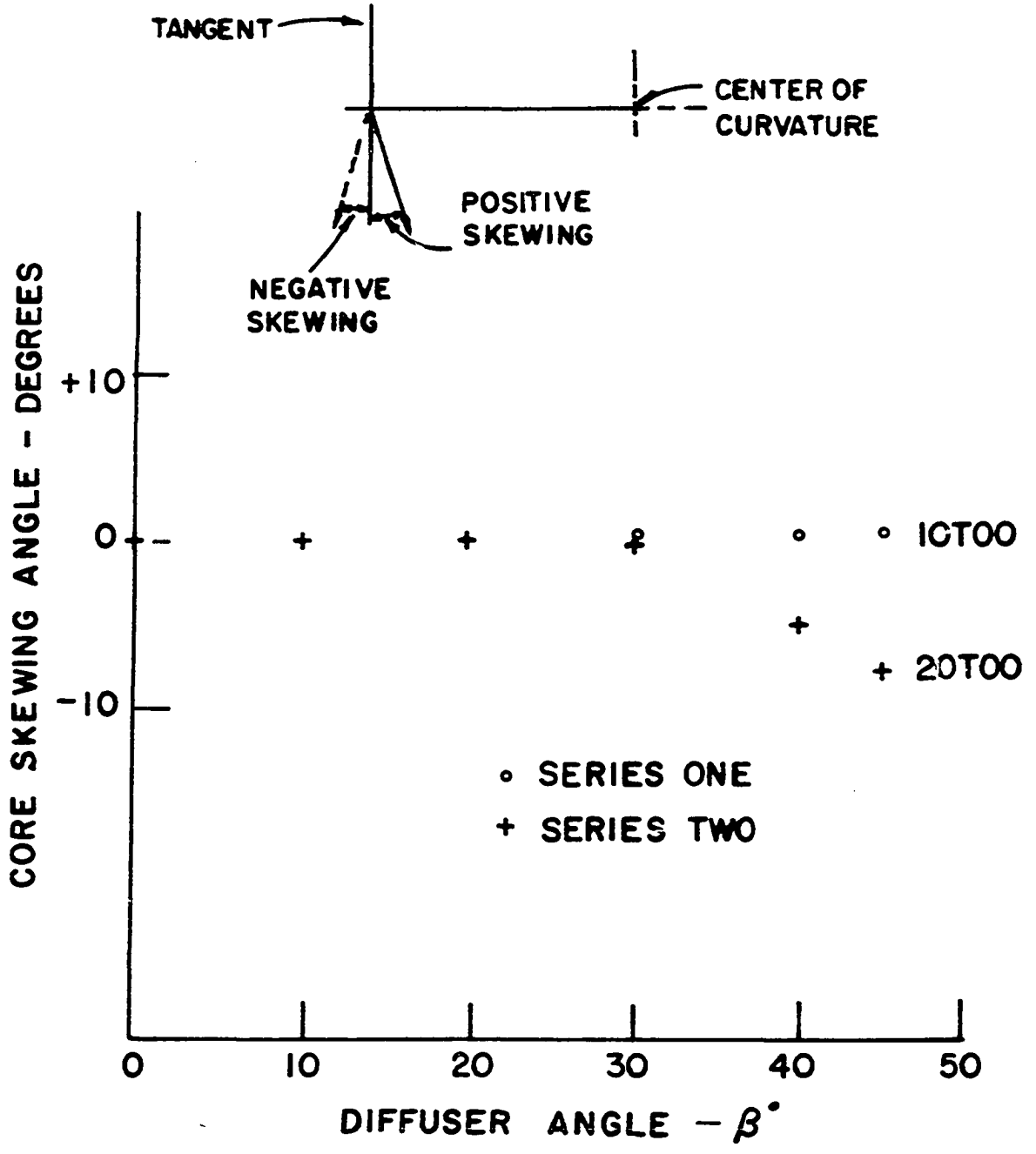

Figure 60. Core horizontal skewing

differently from constant area flows. Further, the influence of a downstream duct has a significant influence on diffuser performance as shown by Sovran and Klomp (1967). The data obtained here thus fills a void in the literature.

In an effort to obtain a more complete understanding of the diffuser tested a study of the flow behavior at the exit of the diffuser was conducted. Since the fluid flow phenomena is fundamentally different in the core and in the boundary layer, it is important to establish if there is a core at the exit of the diffuser. Core flow is characterized by uniform velocity. Inspection of the velocity profiles plotted in Figures 61a and 61b reveal that there is a sizeable core at the exit of the diffuser in the Series 1 tests. It is also useful to know the variation of the skewing angle. Figure 62 shows that the skewing angle lies within a band plus or minus $\frac{1}{2}$ degree of zero skewing angle in the core, but becomes much larger in the boundary layer. The relatively large skewing angle scatter observed here is due to incipient (and unknown) hot film sensor failure. The hot film was abandoned at this point. Figures 63, 64 and 65 show that the skewing in a constant in the core within the accuracy of the equipment.

The wall skewing angle reversal shown in Figure 64 suggests that a collateral boundary layer might not really exist there as might have been expected. A collateral layer

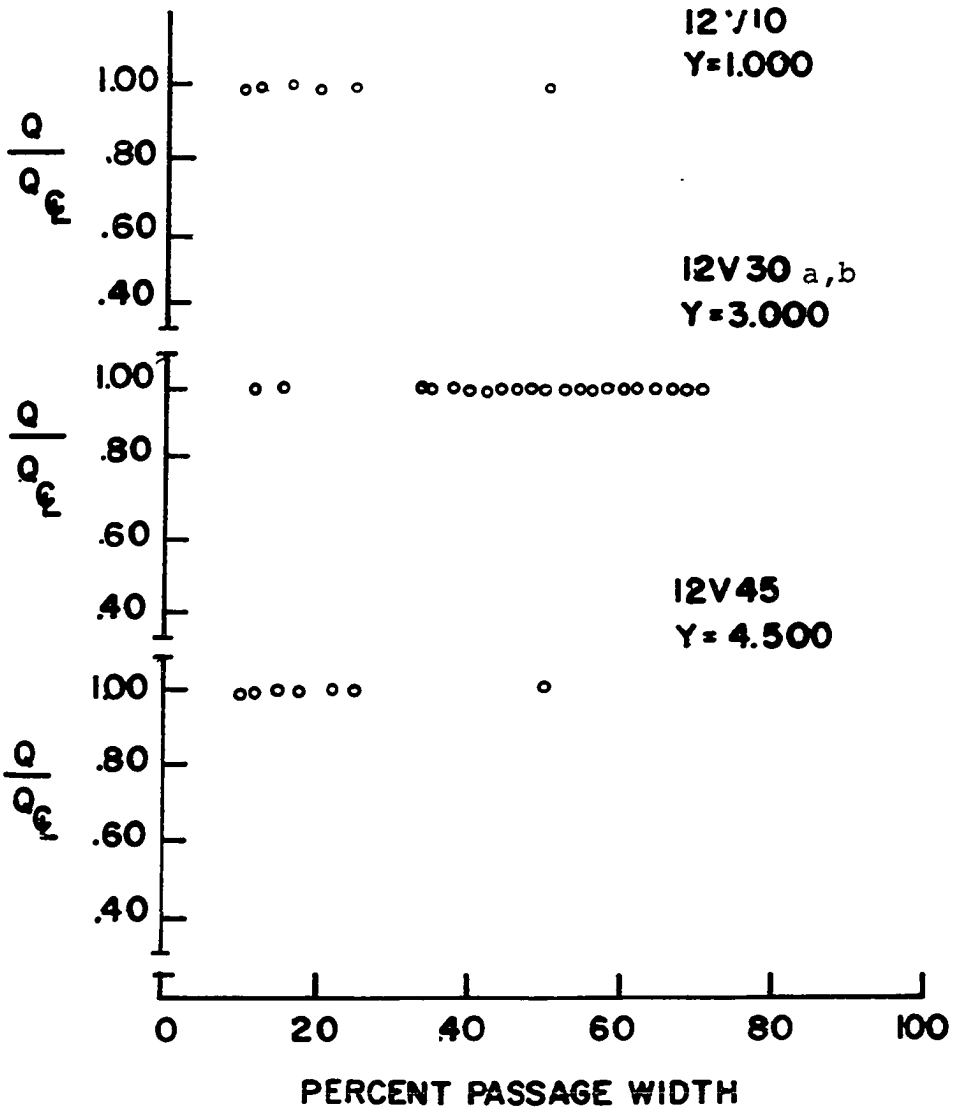

Figure 61a. Exit core velocity profile, Series 1

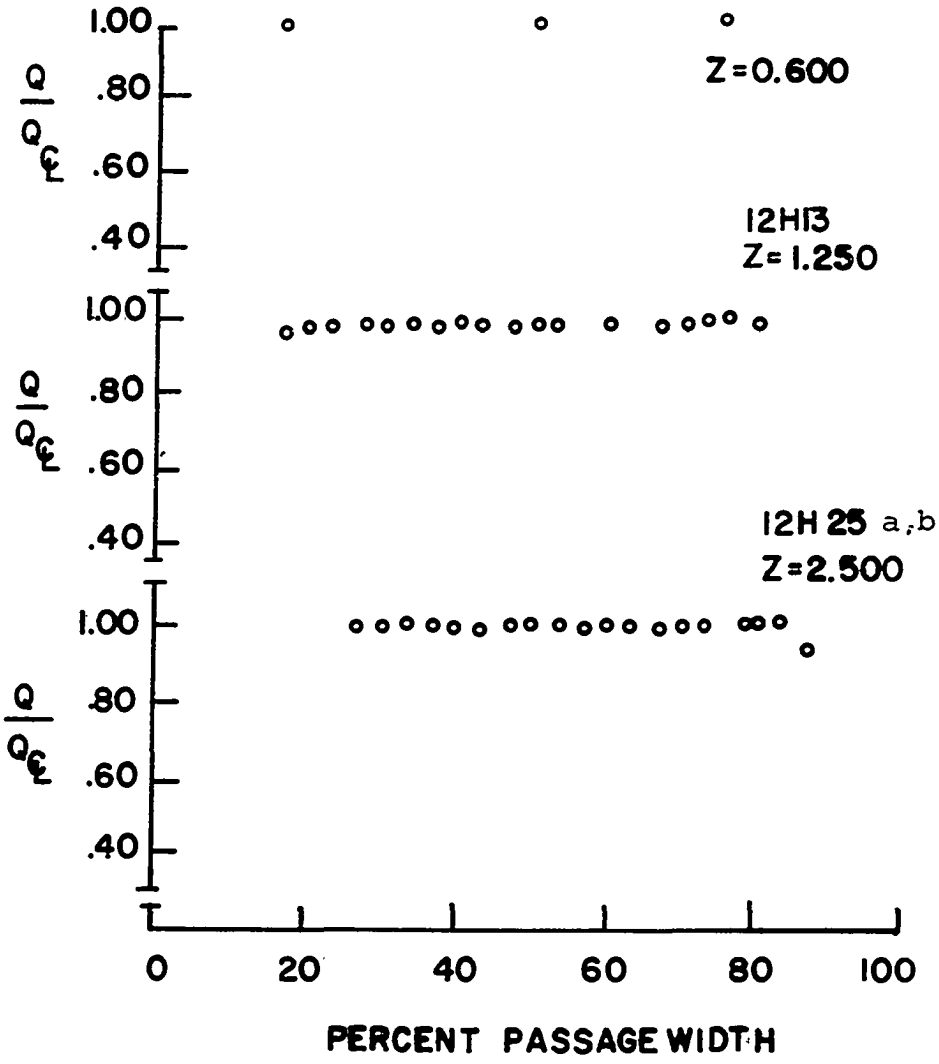

Figure 61b. Exit core velocity profiles, Series 1 (points at z=0.6 are cross plotted)

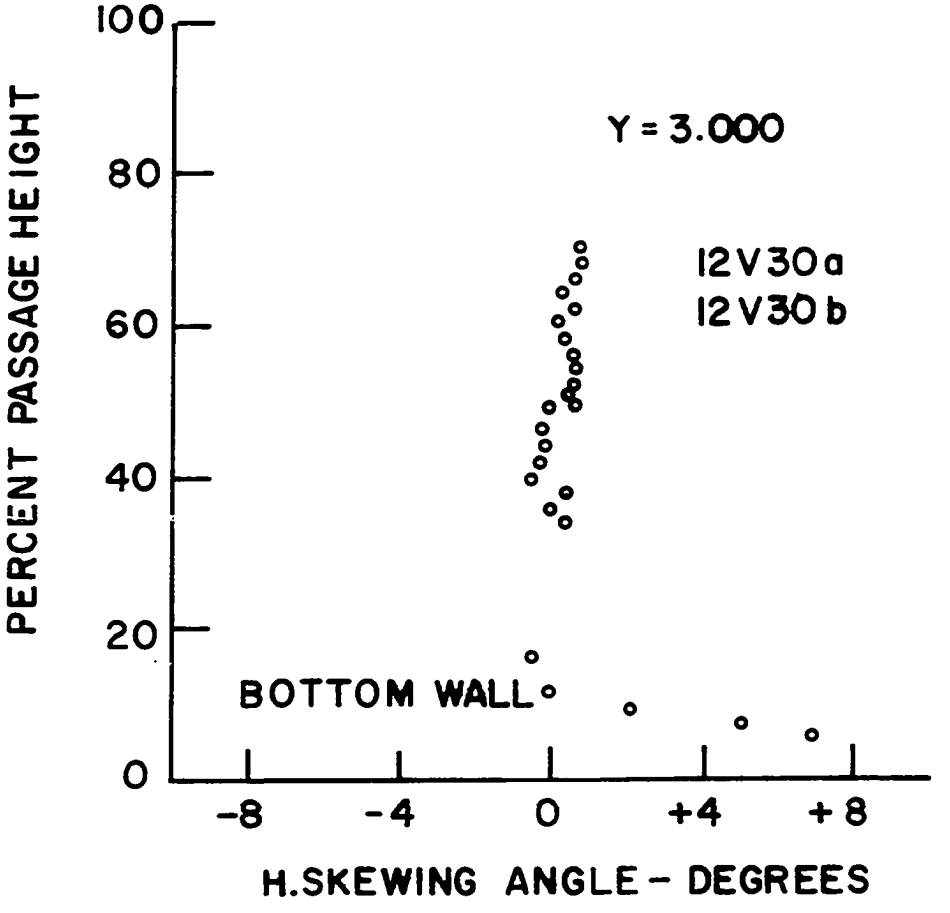

Figure 62. Horizontal skewing angle, Series 1

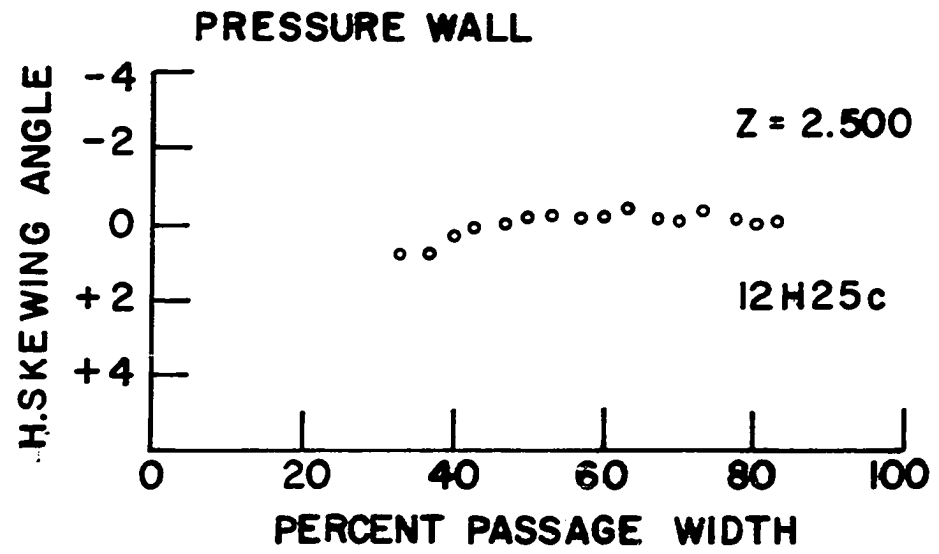

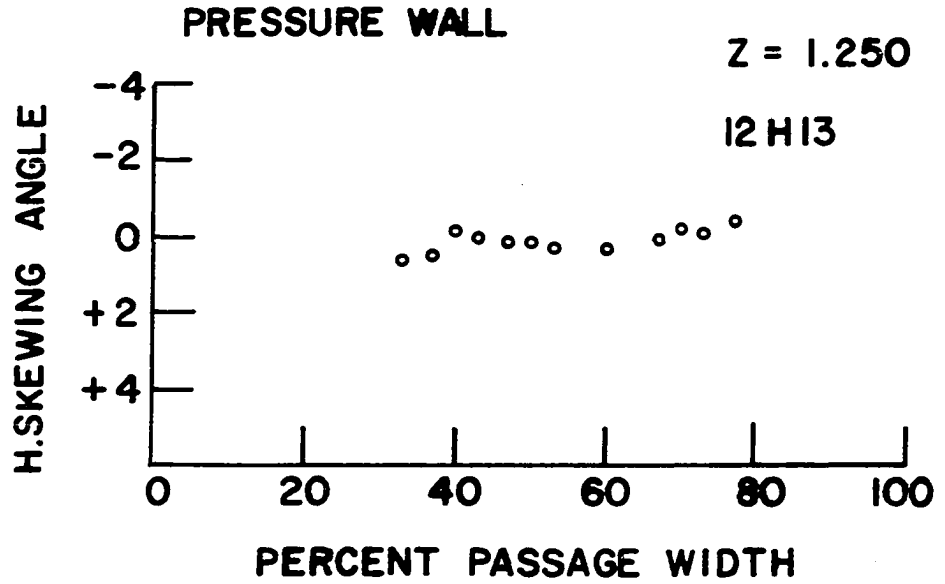

Figure 63. Horizontal skewing angle, Series 1

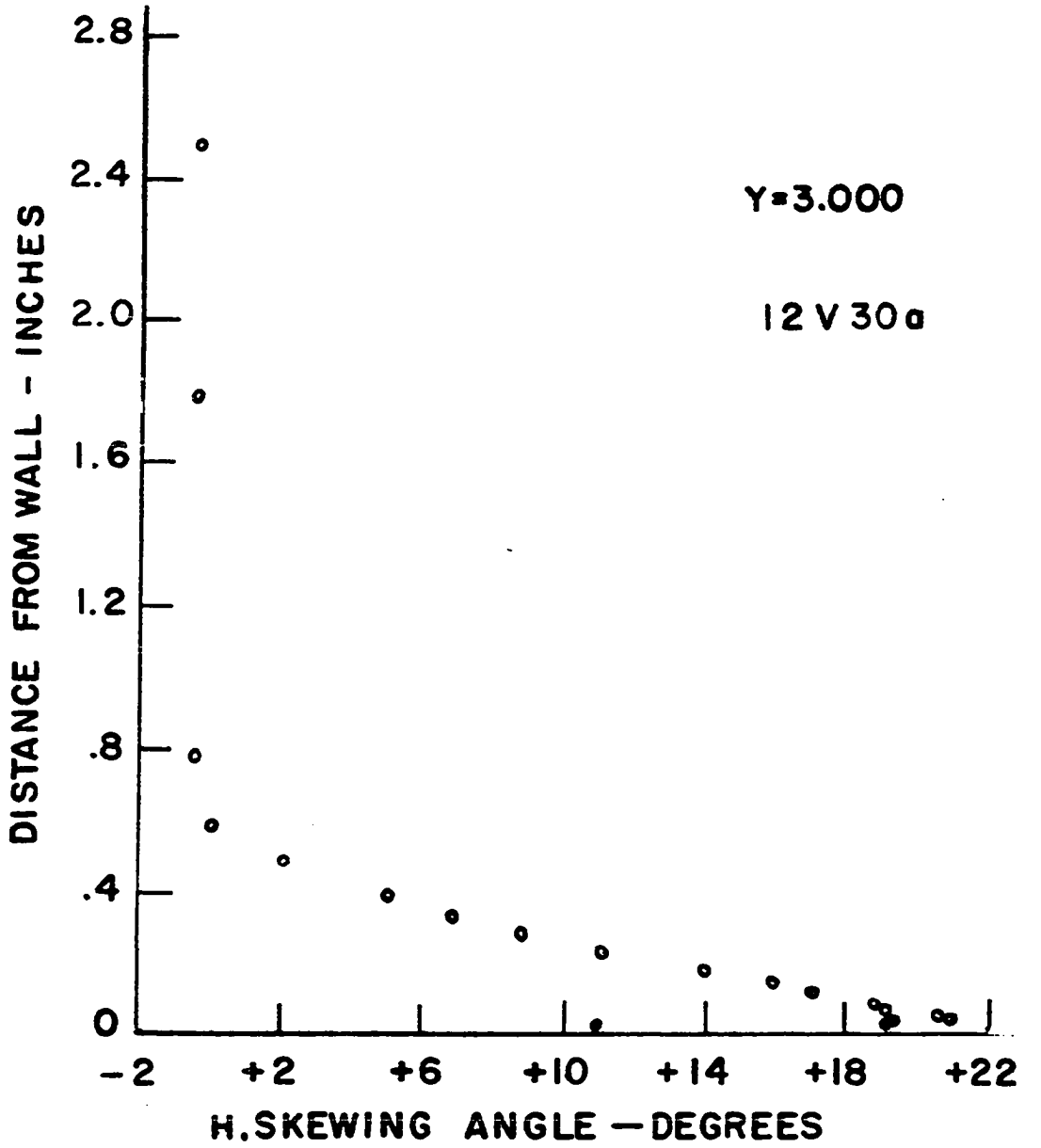

Figure 64. Horizontal skewing angle (boundary layer) Series 1

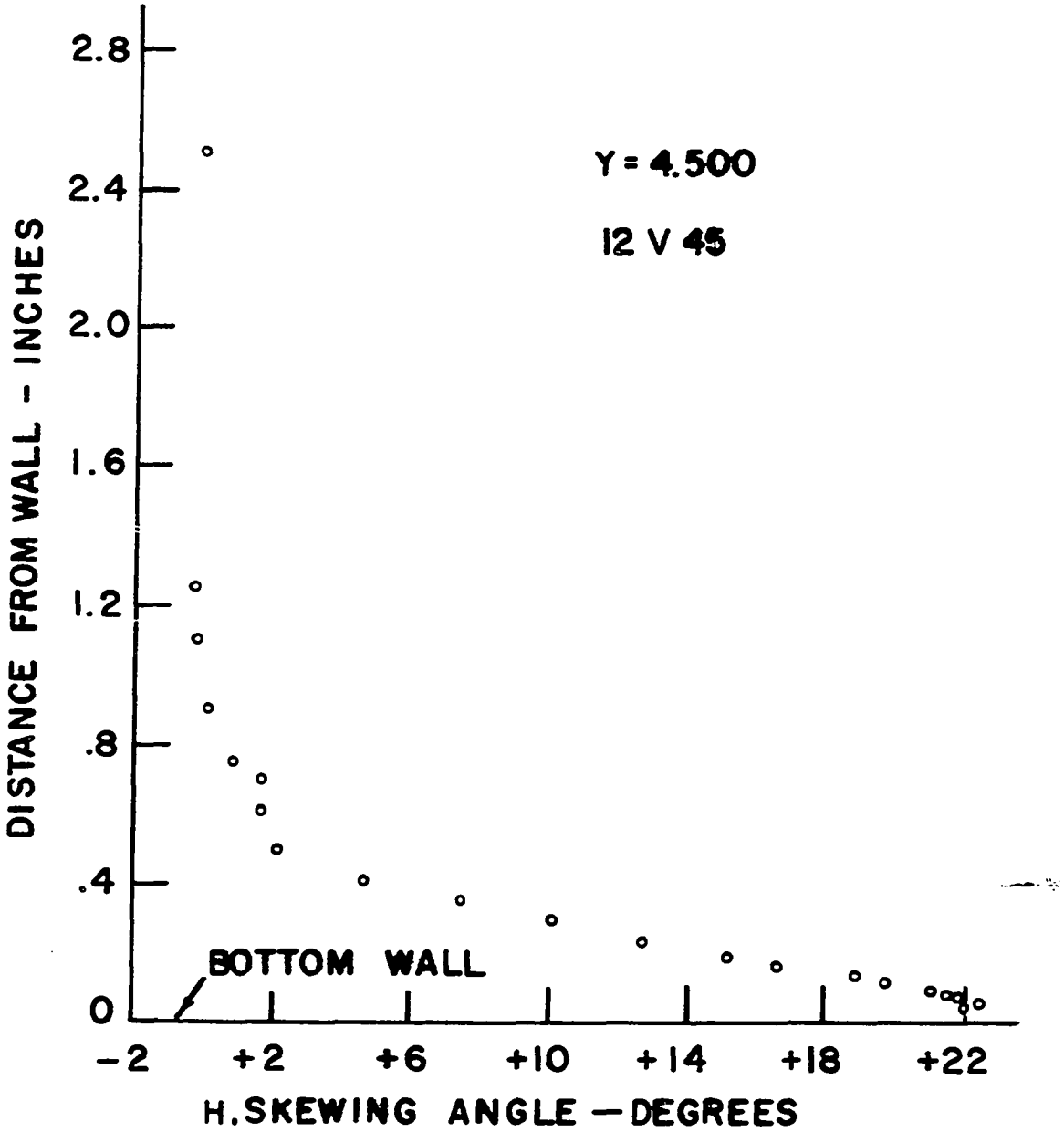

Figure 65. Horizontal skewing angle (boundary layer), Series 1

has a skewing angle which does not vary in a direction normal to the wall, Smith (1970). The obvious contradiction should be checked further experimentally. The inflection in the skewing angle curved observed close to the corner of the diffuser shown in Figure 66 is not considered representative of the general diffuser behavior, but rather the behavior encountered in the corner of the channel. The boundary layer velocity profiles along the bottom wall at the exit of the series one diffuser are shown in Figures 67, 68 and 69 for a value of Y (the distance from the pressure wall) of 1.0, 3.0 and 4.50 inches respectively. Here again it will be observed that the boundary layer close to the corner (at Y = 1.000) is of a slightly different nature than that in the core, represented by Figures 68 and 69.

A comparison of the boundary layer on the pressure surface, Figure 70, and that on the suction surface, Figure 71, shows that the boundary layer on the suction surface is substantially greater.

Summarizing it can be stated that there is a uniform core at the exit of the Series 1 diffuser. This core has negligible skewing. The core is surrounded by a boundary layer that is somewhat different on the pressure, bottom

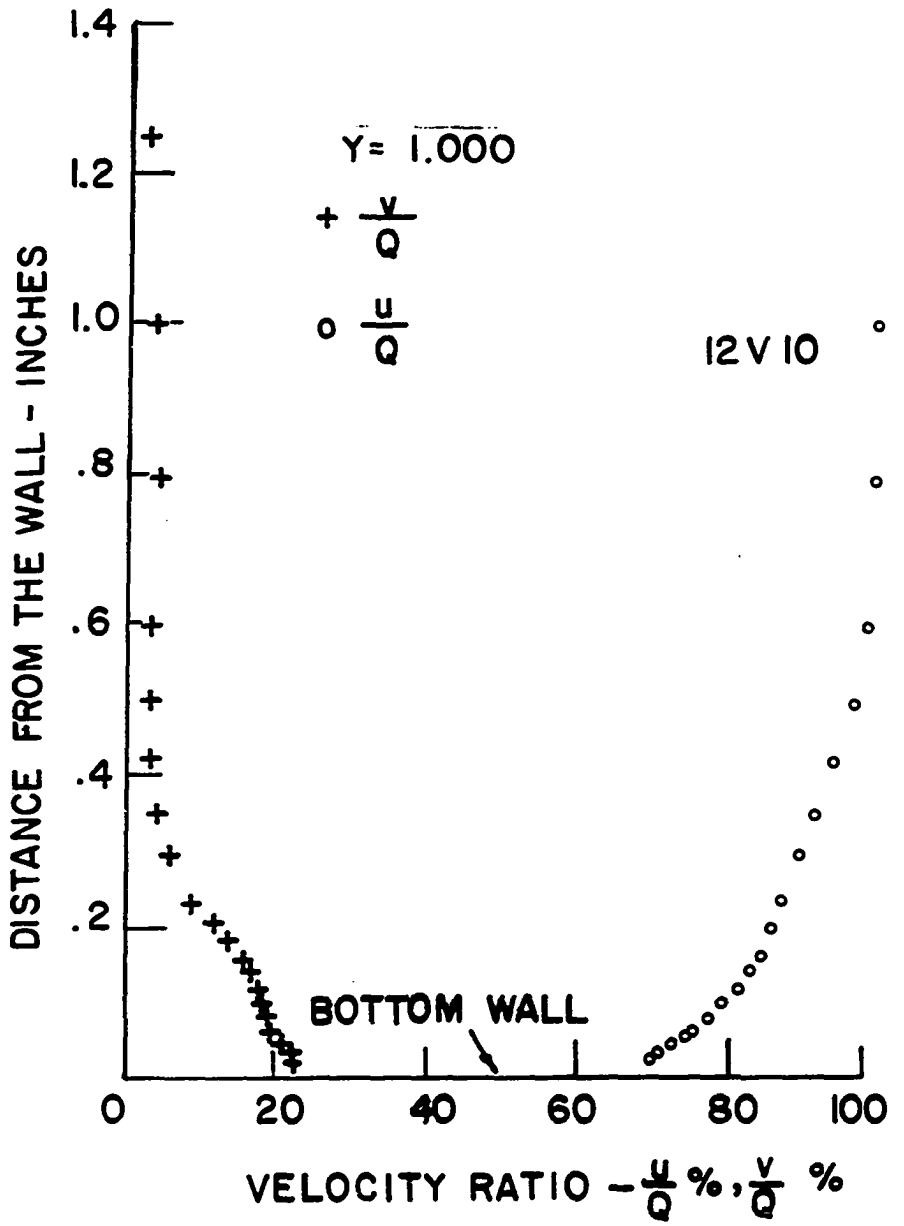

Figure 67. Velocity components (boundary layer) Series 1

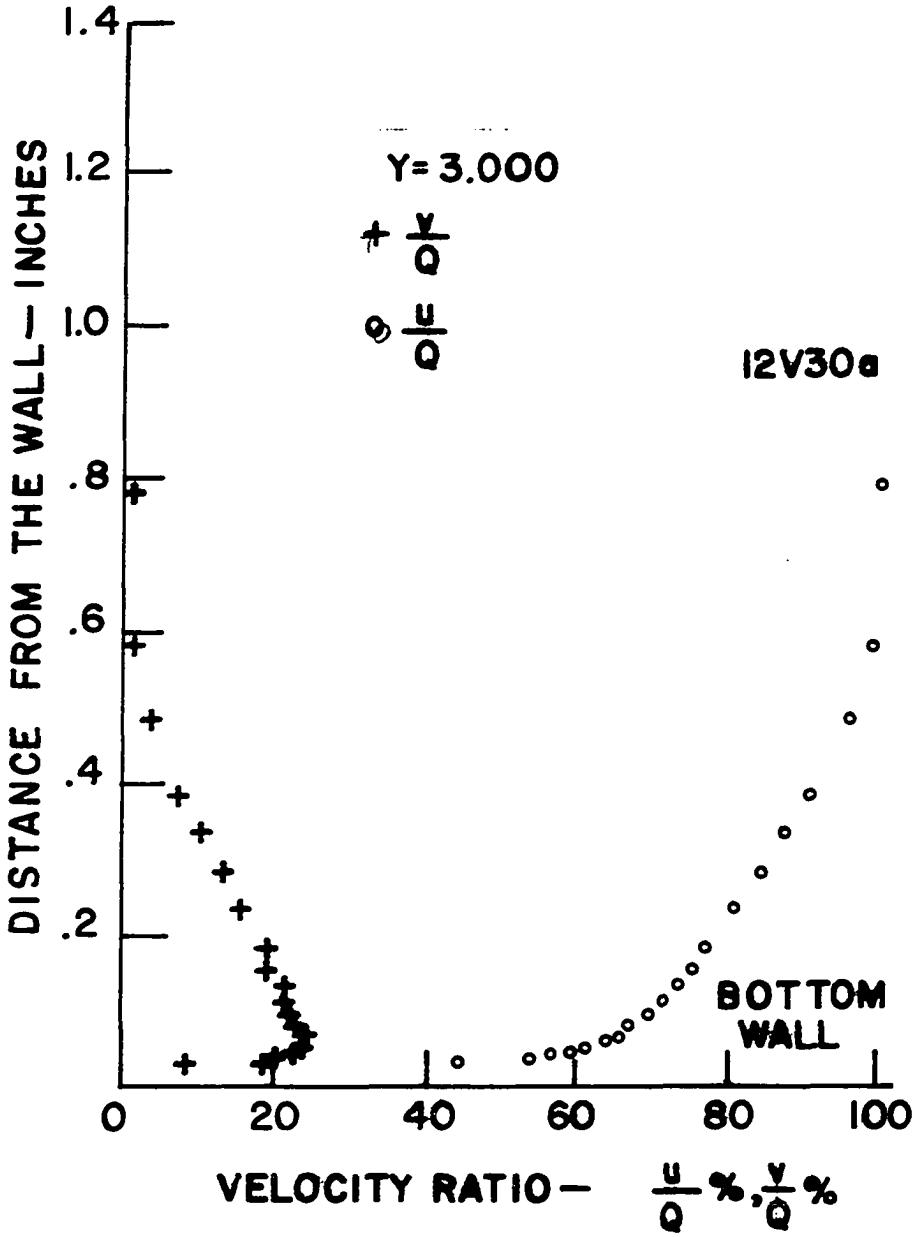

Figure 68. Velocity components (boundary layer) Series 1

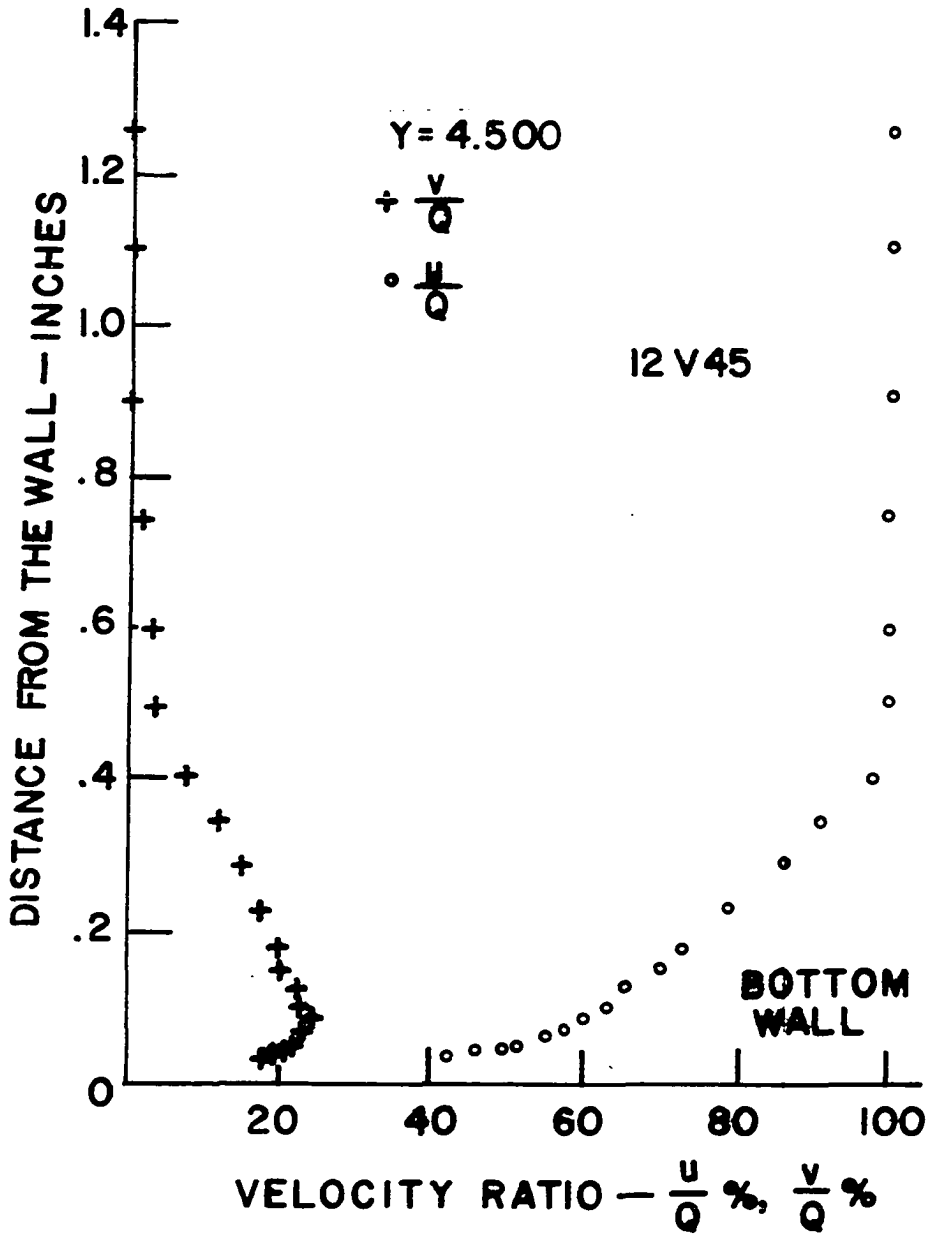

Figure 69. Velocity components (boundary layer), Series 1

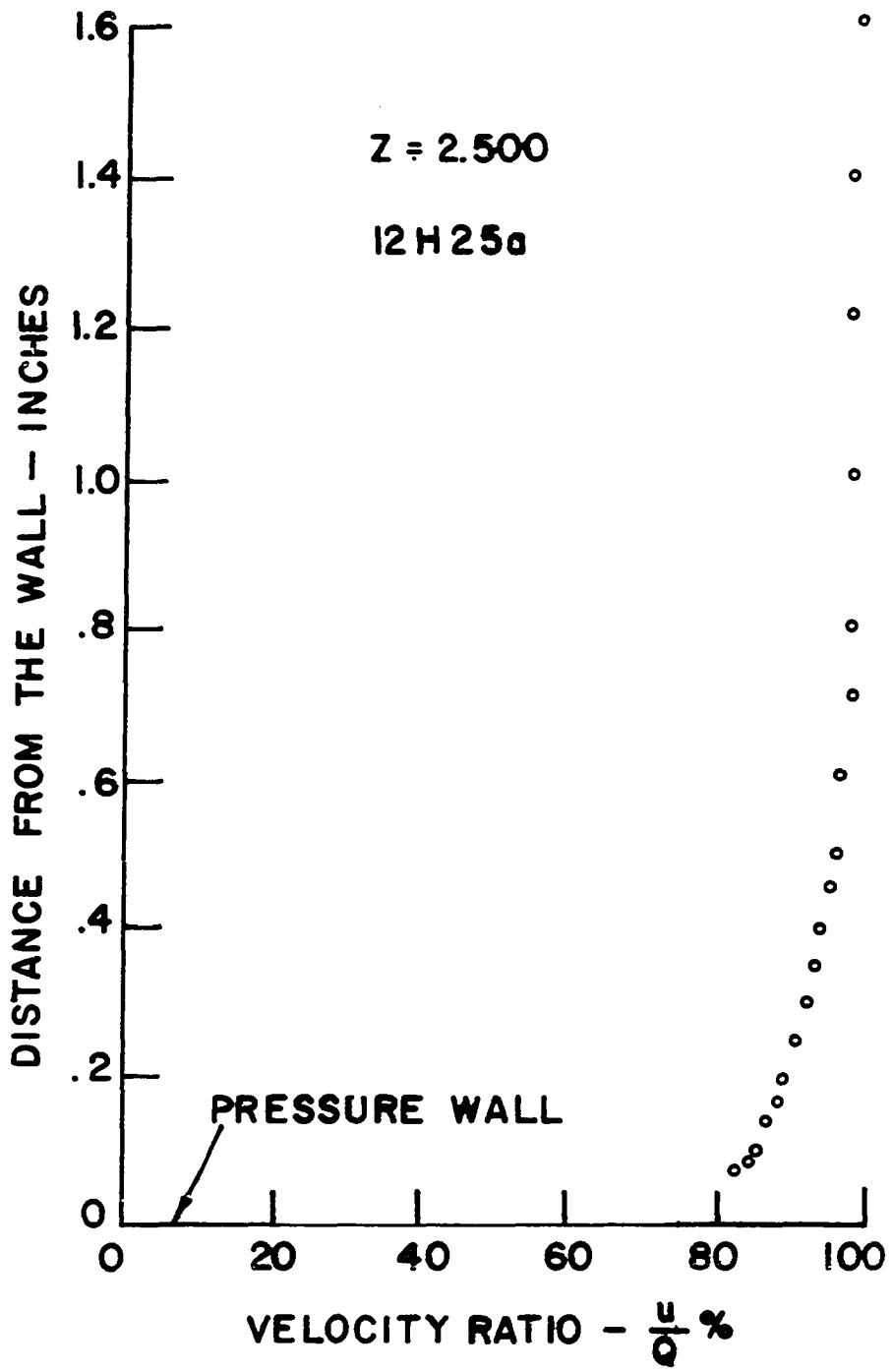

Figure 70. Pressure wall velocity profile, Series 1

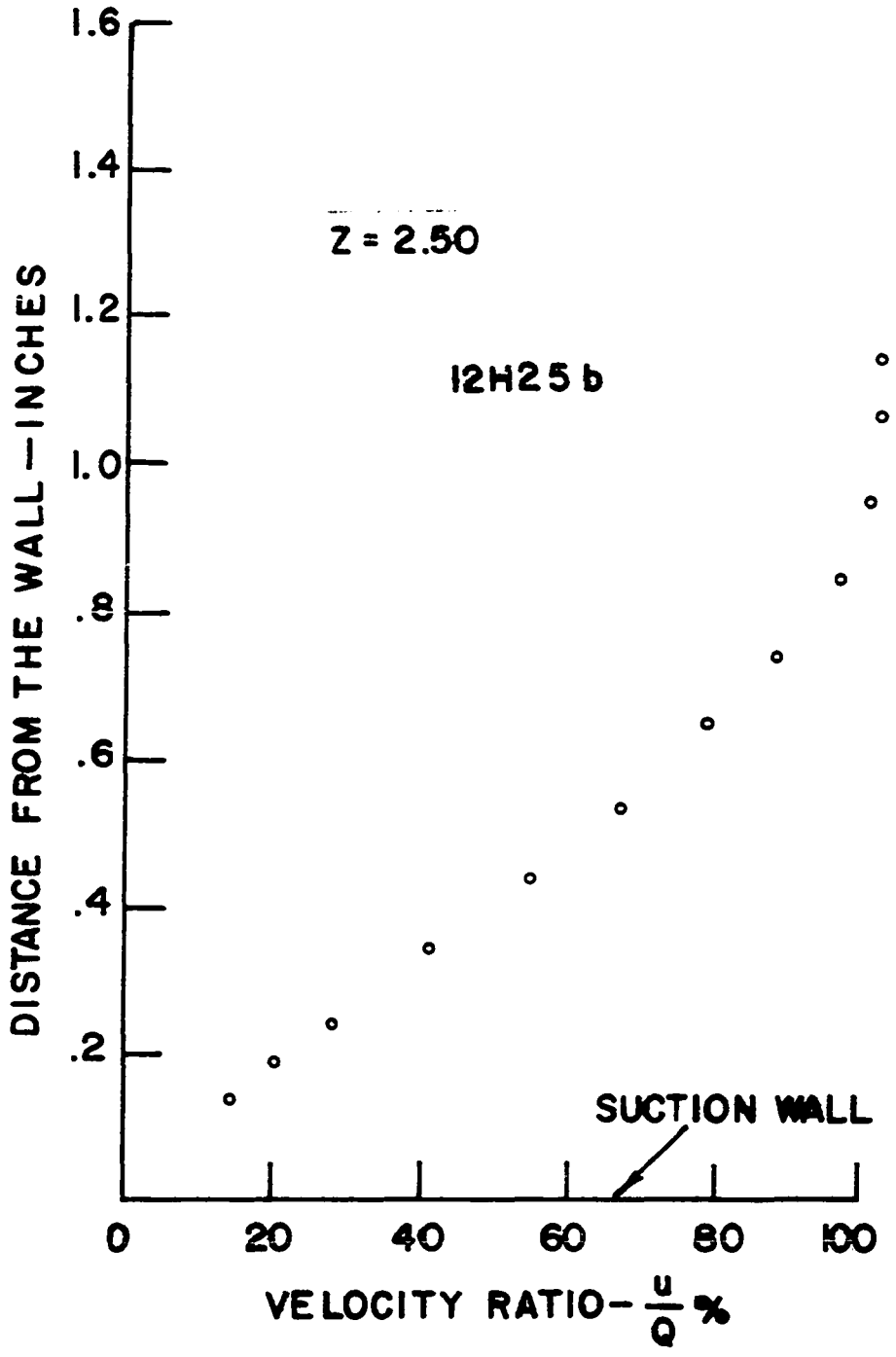

Figure 71. Suction wall velocity profile, Series 1

and suction walls. The boundary layer along the pressure wall does not exhibit as great a velocity defect as that on the suction wall.

Discussion of the exit plane behavior in Series 2 tests is now undertaken. The core is nearly absent in this series of tests as can be verified by examining Figures 72 and 73. The skewing in the core is nevertheless uniform along one given value of Y (the distance from the pressure wall), namely, 3 inches, Figure 74. The skewing angle is about -8.3°, which indicates that the mid-passage core flow is toward the pressure surface. The magnitude of the skewing angle across the width of the core is shown in Figure 75 for a value of z = 2.50 inches (the mid-plane) and z = 1.25 inches. The top graph shows that the skewing tends to become slightly smaller as the pressure wall is approached. This is reasonable, since the skewing angle must go to zero at the wall, since there is no blowing or suction at the wall. Inspection of Figures 76 and 77 reveals that the skewing angle is large in the boundary layer and decreases until a constant value is reached as the core is approached.

The velocity profiles along the bottom wall are plotted in Figures 78 and 79. The similarity of these profiles indicates that they are taken sufficiently far from the corner, thus avoiding corner effects. The velocity profiles along the pressure wall and the suction wall are shown in Figures 80

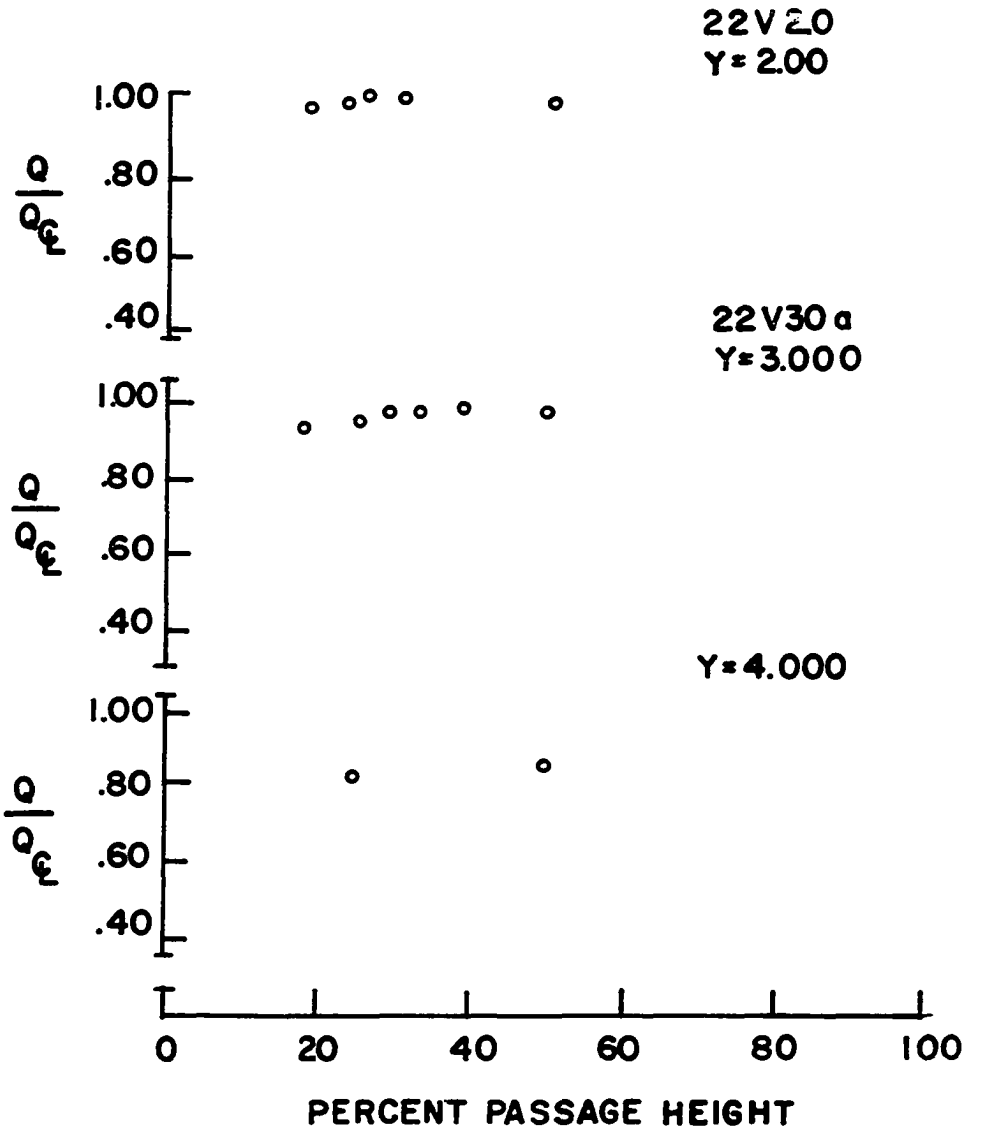

Figure 72. Vertical velocity profiles, core, Series 2 (points at y = 4.0 are cross plotted)

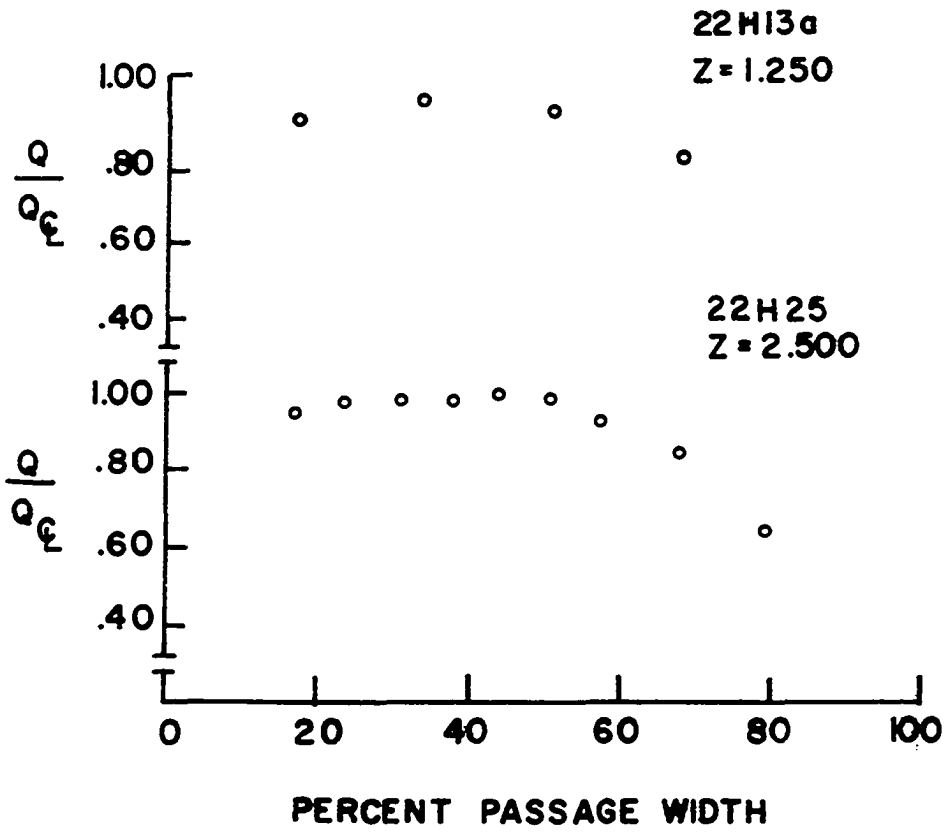

Figure 73. Horizontal velocity profiles, core Series 2

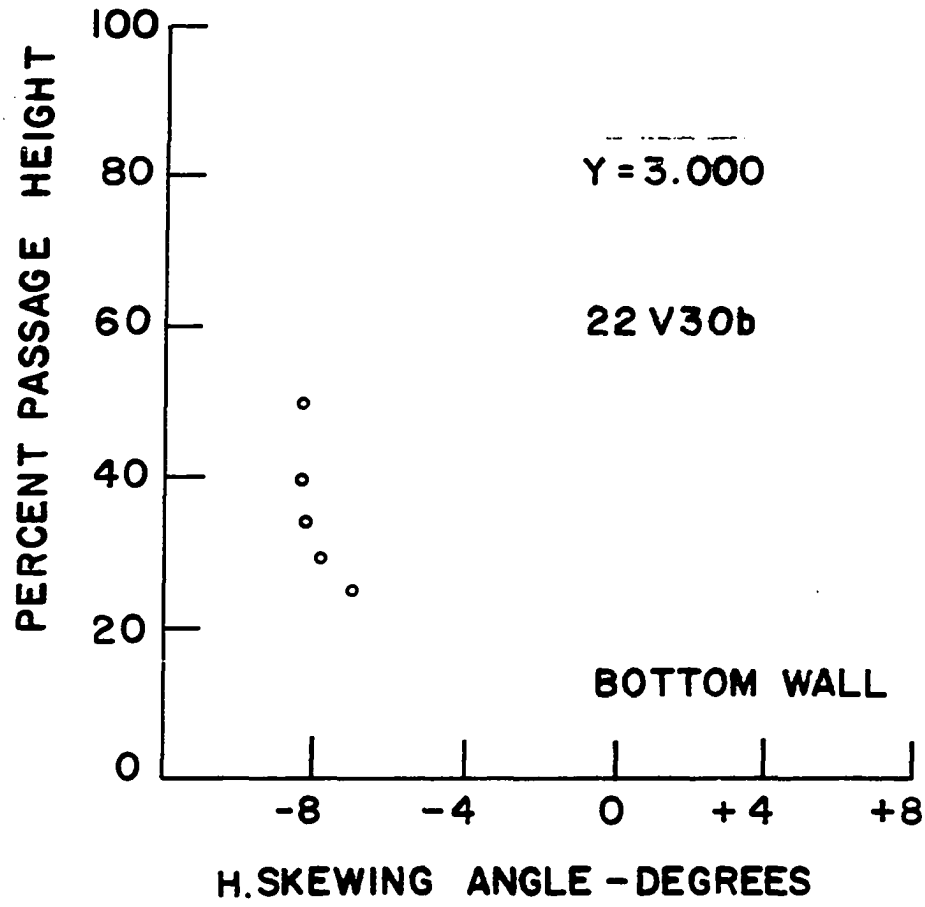

Figure 74. Horizontal skewing, Series 2

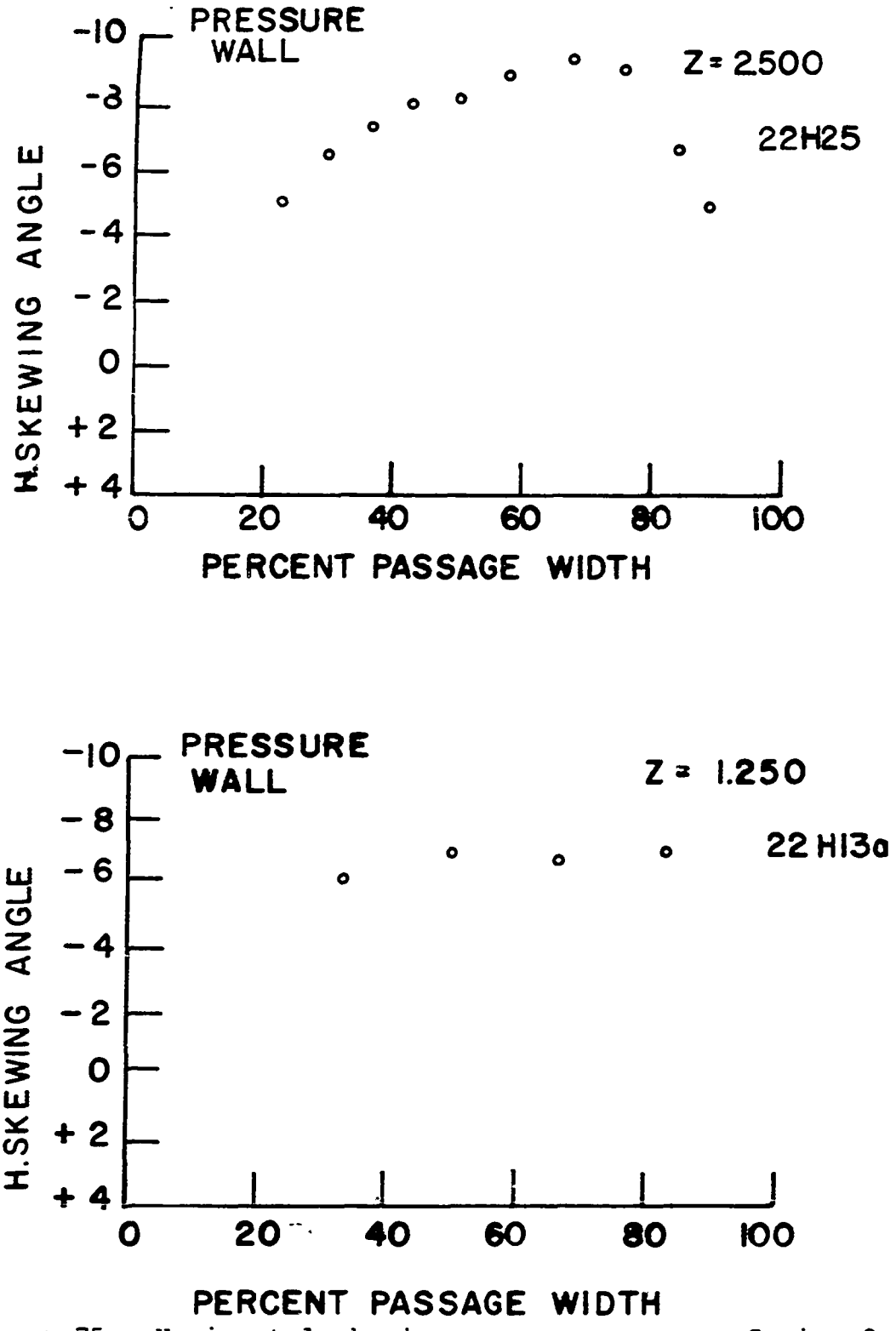

Figure 75. Horizontal skewing, across passage, Series 2

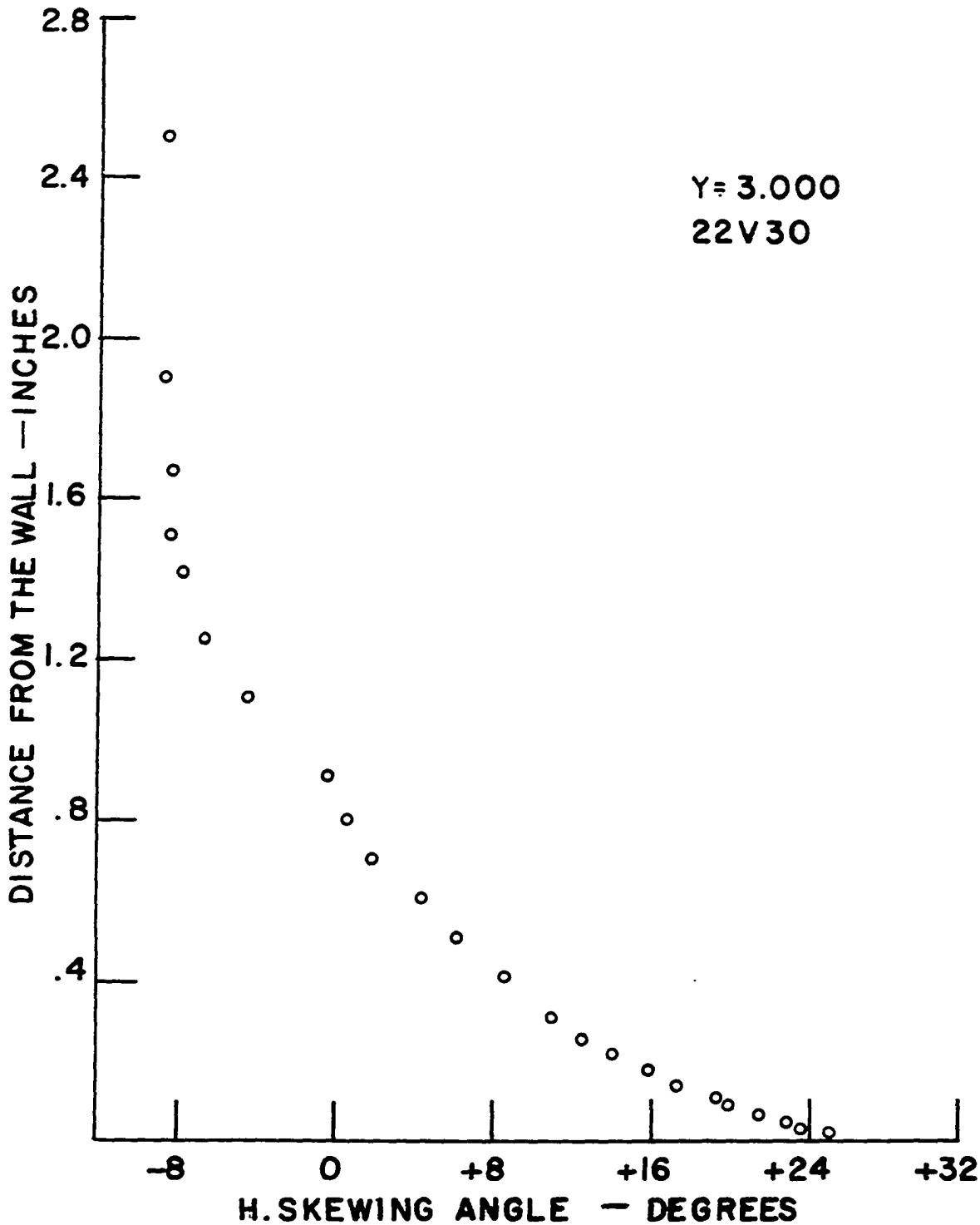

Figure 76. Horizontal skewing (boundary layer), Series 2

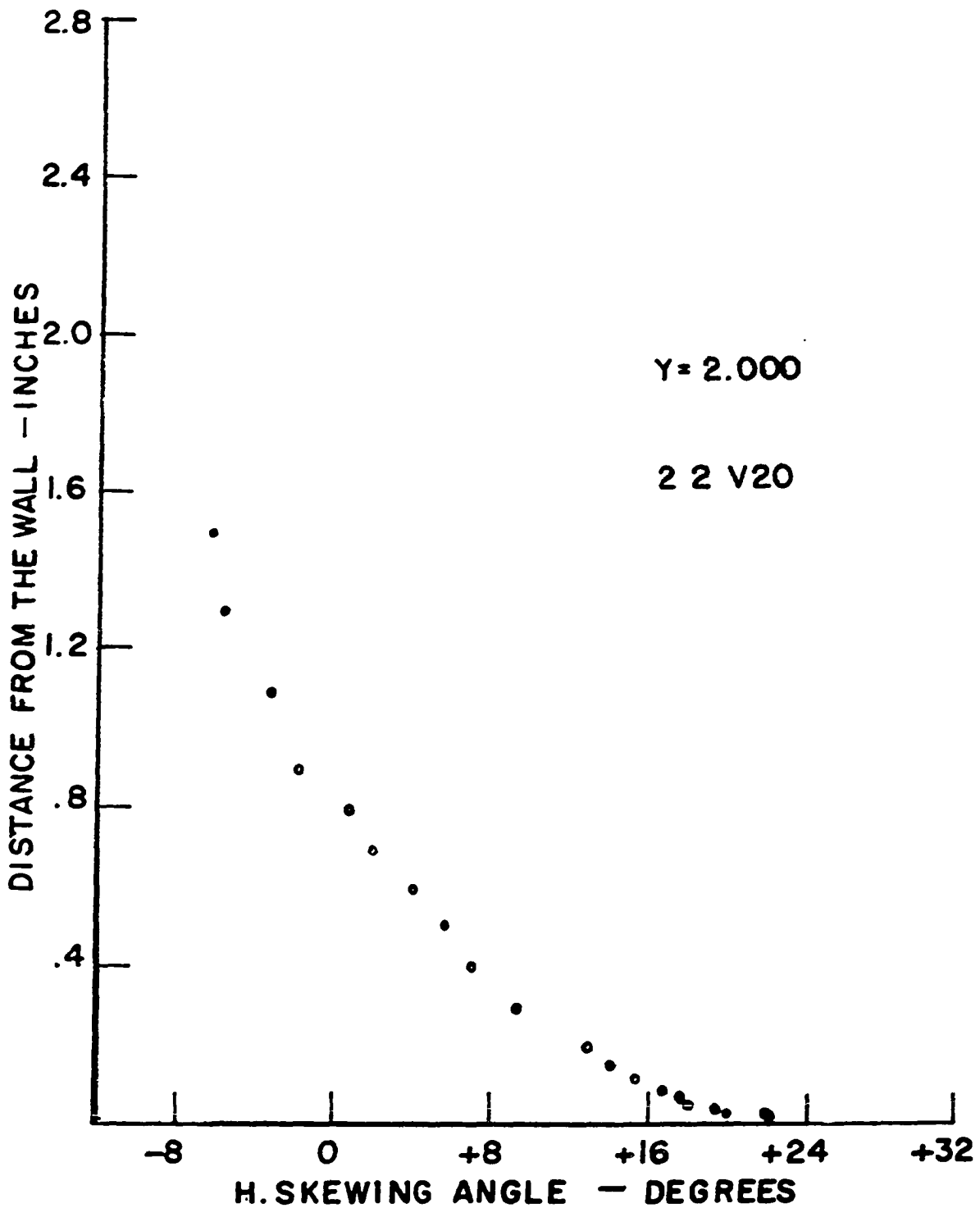

Figure 77. Horizontal skewing (boundary layer), Series 2

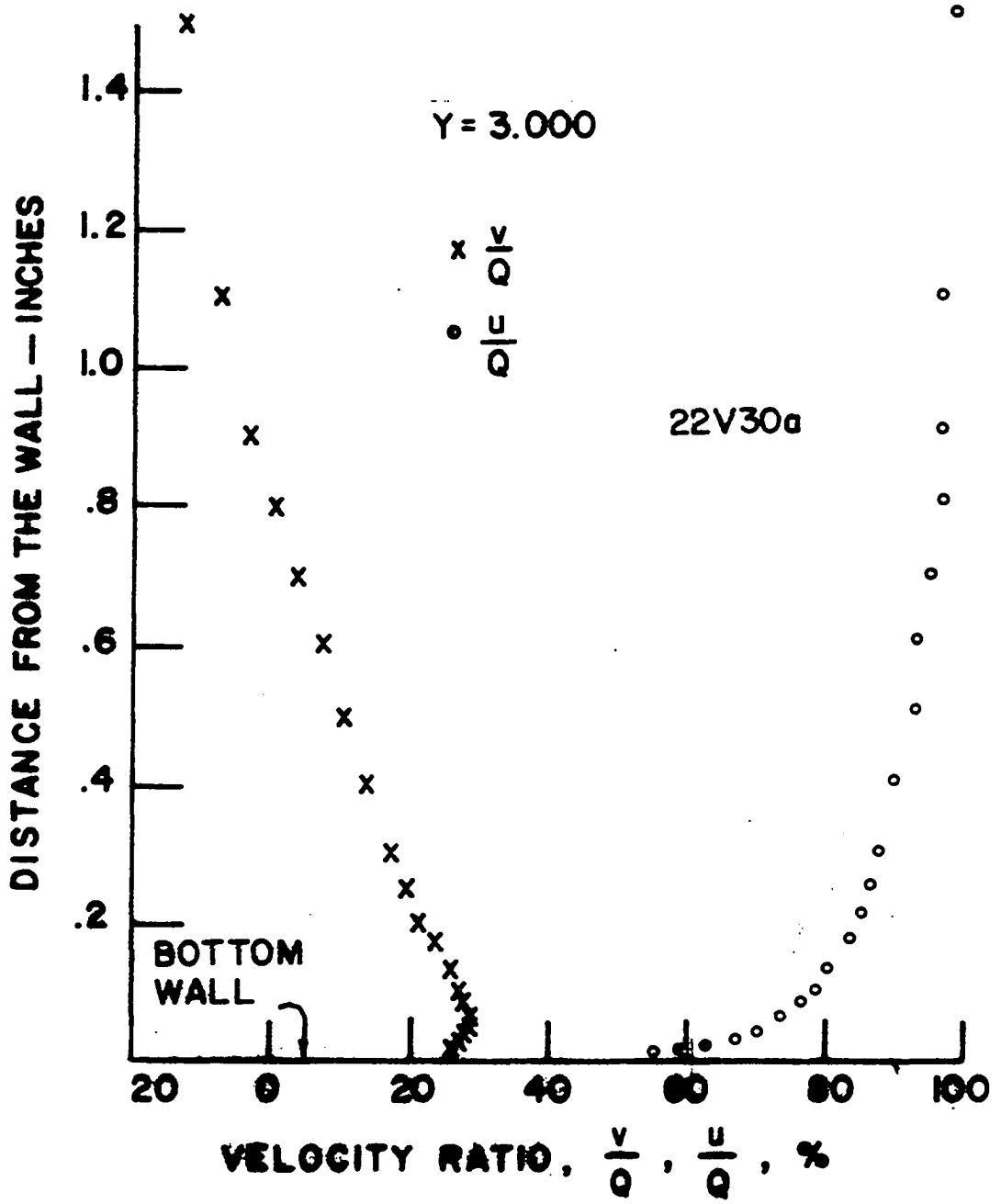

Figure 78. Velocity components (boundary layer), Series 2

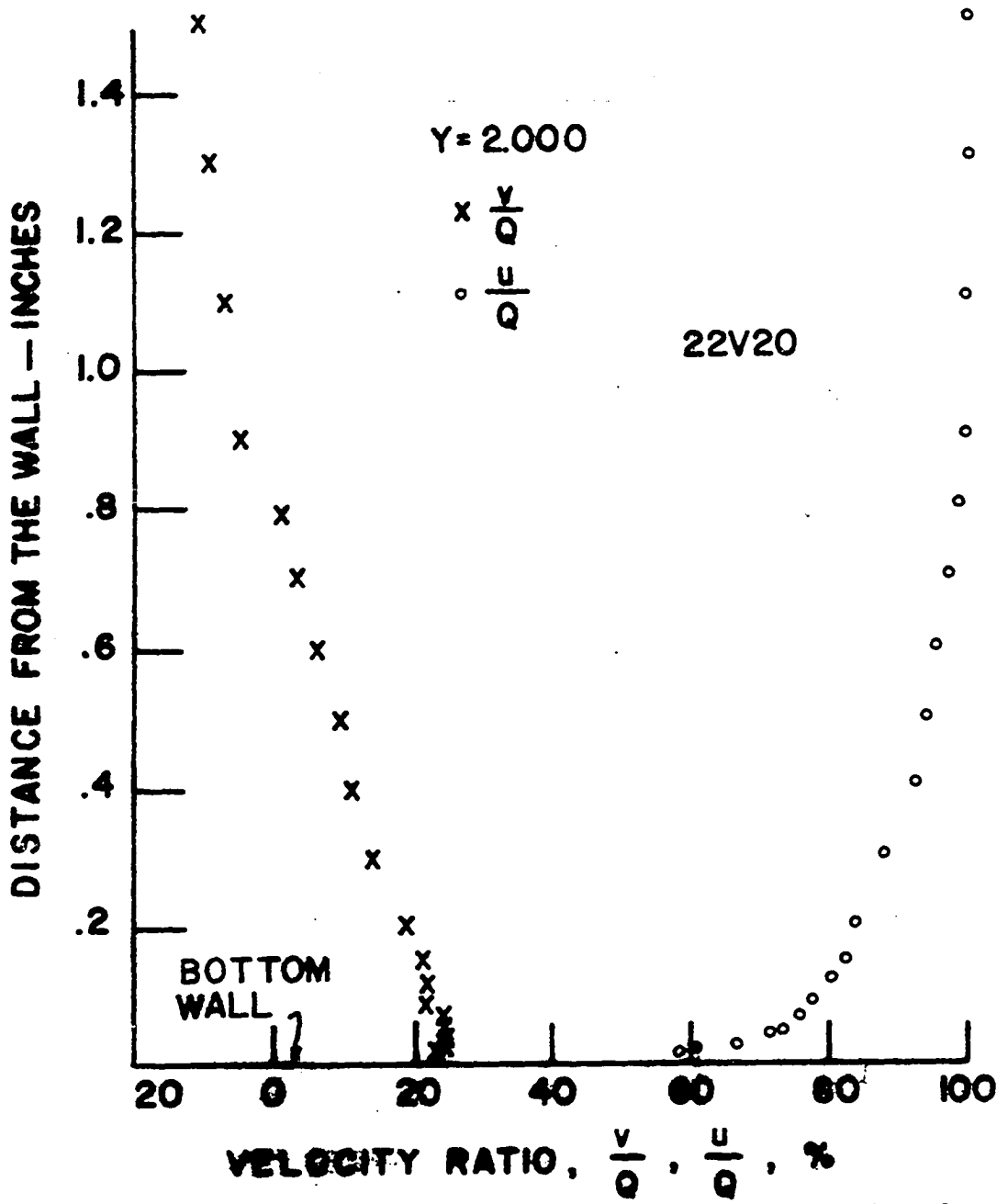

Figure 79. Velocity components (boundary layer), Series 2

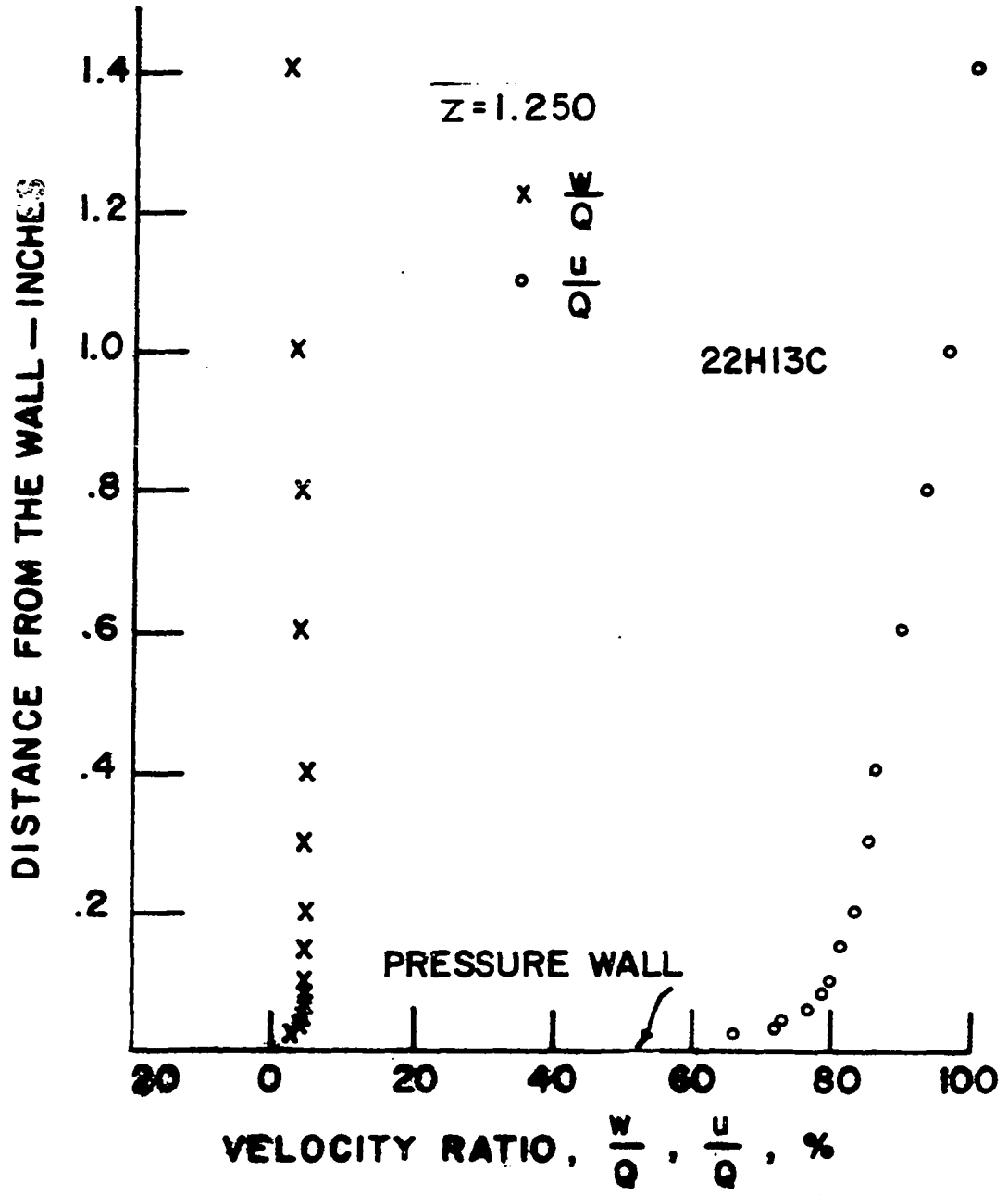

Figure 80. Pressure wall velocity components, Series 2

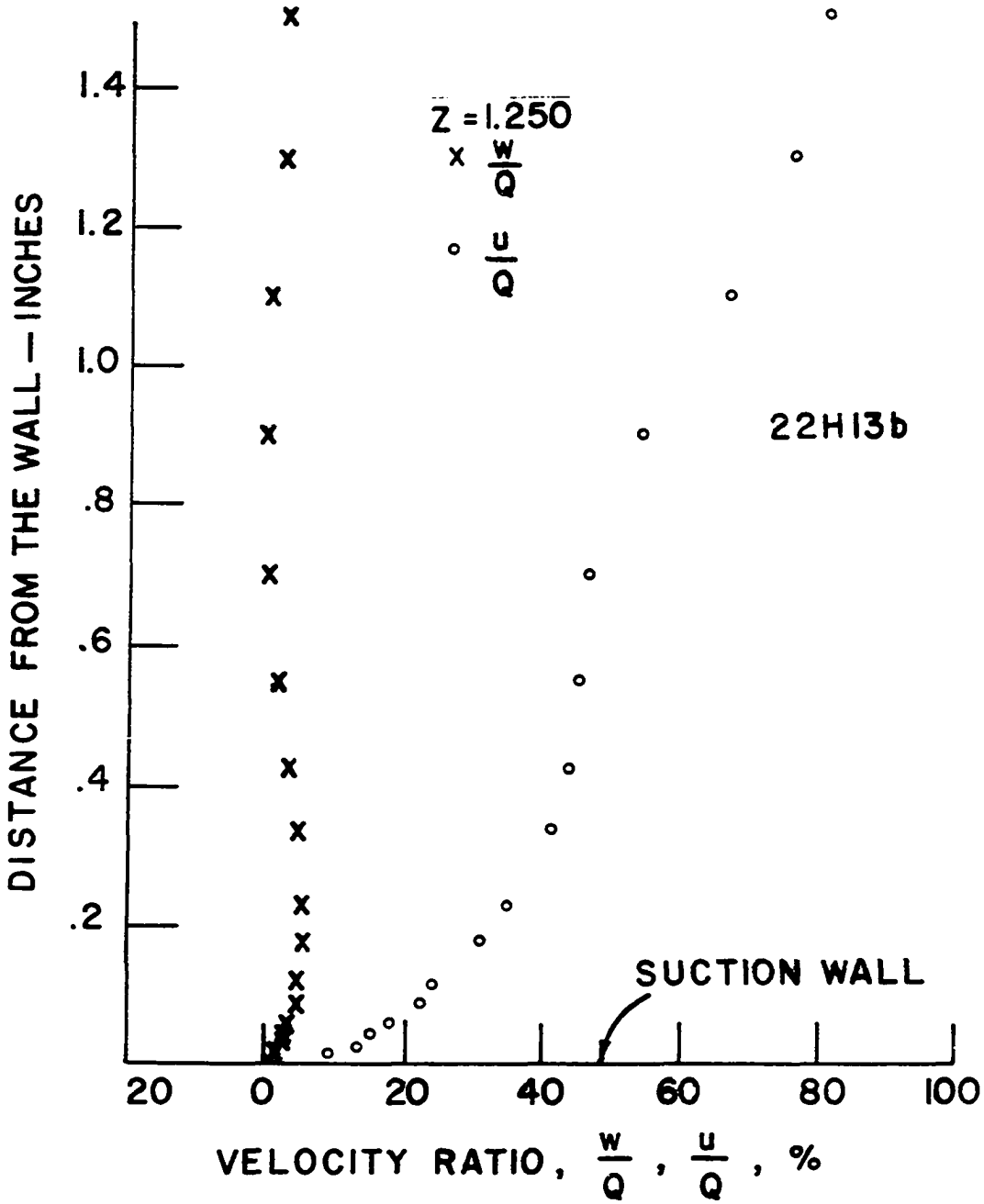

Figure 81. Suction wall velocity components, Series 2

and 81. The profile of the suction wall is substantially different from the pressure wall. It can be seen that stall is absent on the suction wall as indicated by the velocity profile shown in Figure 81.

The centerline skewing angle in the Series 2 tests was -8.3°. Because of this large value, it was decided that vertical skewing on the pressure and suction surfaces should be investigated. The vertical skewing angle is defined as the skewing angle in the vertical plane through the center of the passage. Positive vertical skewing along the pressure wall indicates the presence of a component of velocity downward, towards the bottom wall. The vertical skewing angle is less than 4° close to the wall and drops off towards zero as the center of the passage is reached (Figure 82).

The vertical skewing angle on the suction surface was also measured. On the suction surface, positive skewing indicates upward component of velocity, with flow away from the bottom wall. This vertical skewing angle is plotted in Figure 83. It is interesting to note that the vertical skewing angle has a larger value closer to the suction wall than the pressure wall. Further, it drops off much faster than that on the pressure wall. It is then followed by an increase in vertical skewing angle, then remains constant until the center of the passage is reached when it goes to zero again.

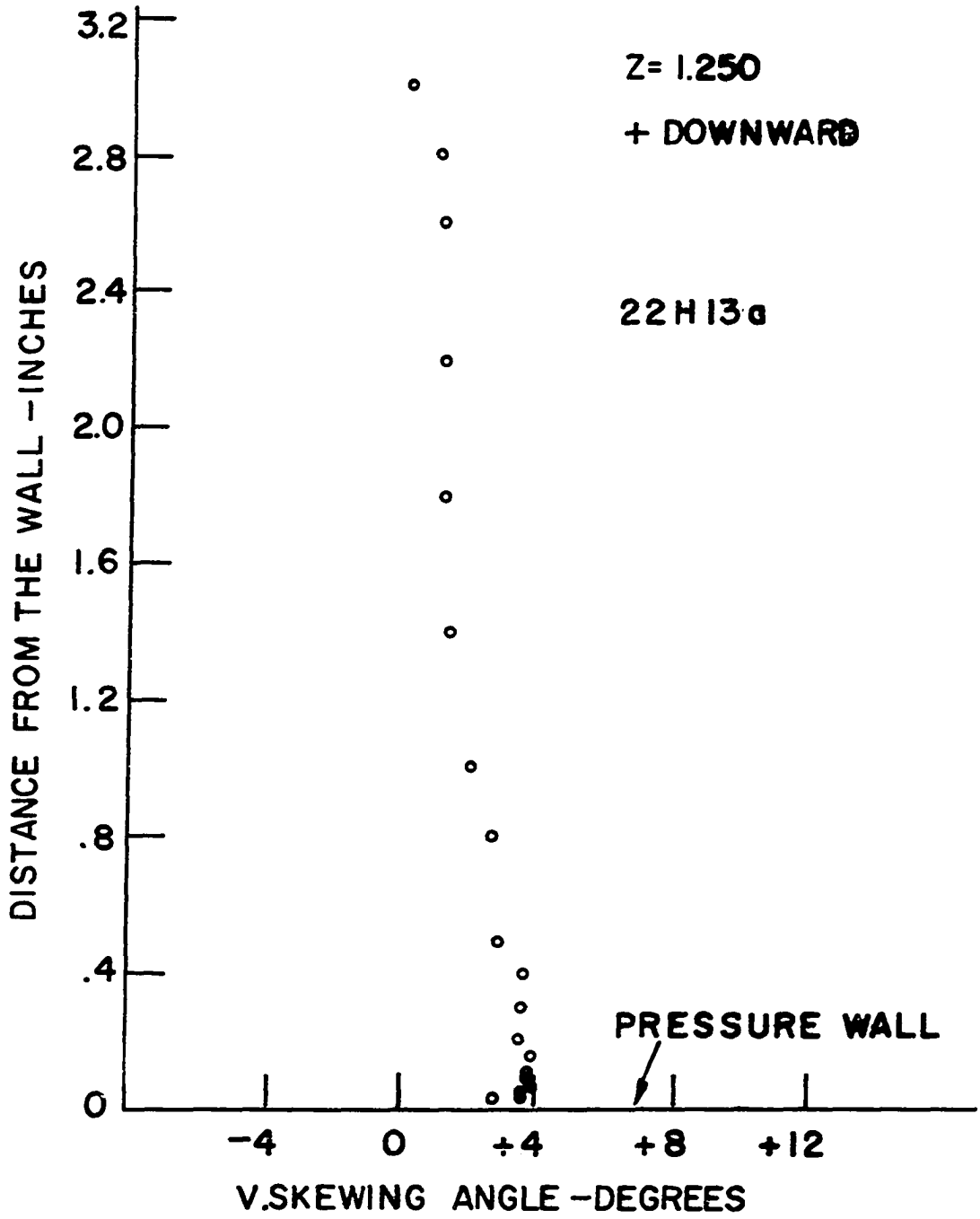

Figure 82. Pressure wall vertical skewing, Series 2

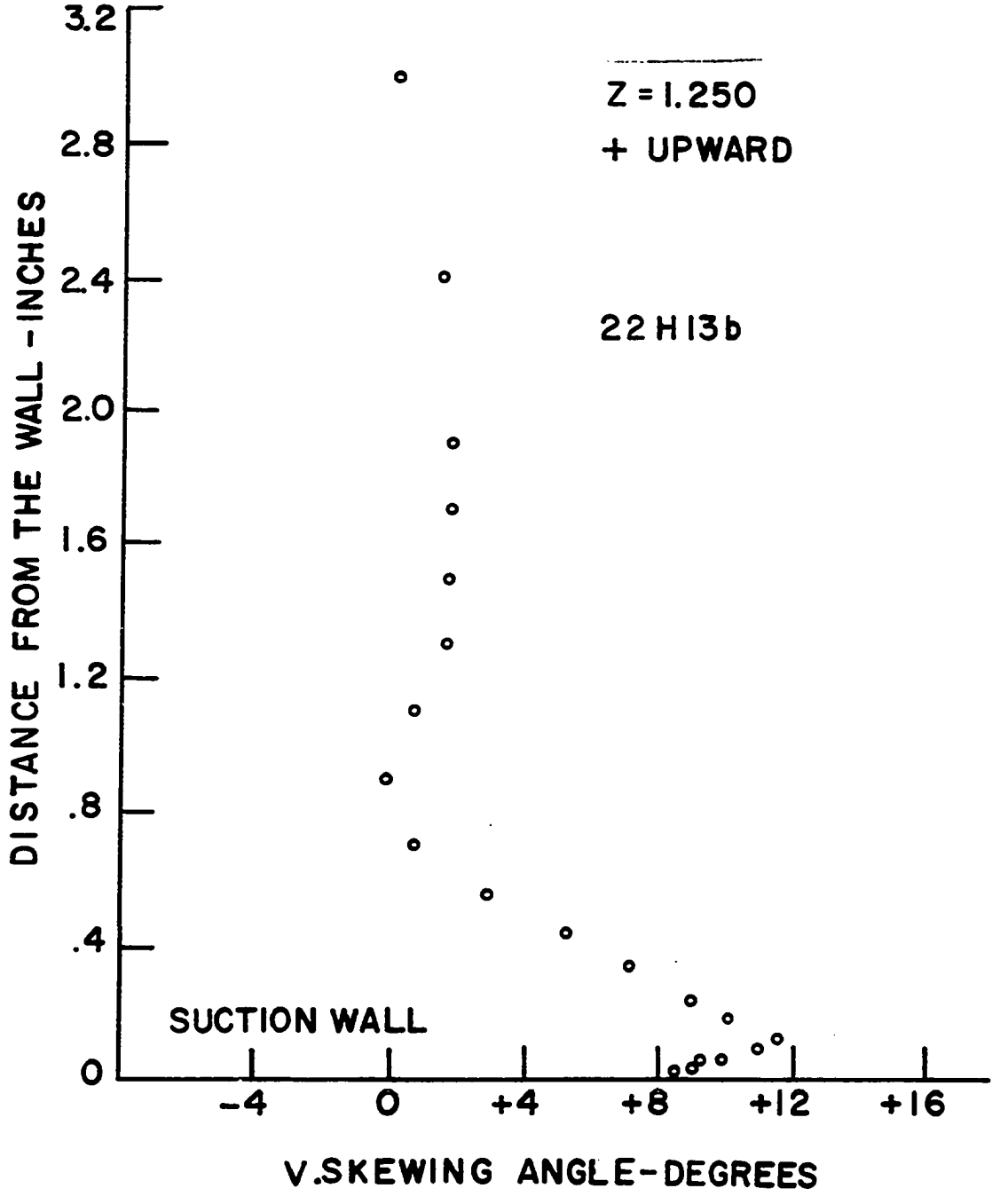

Figure 83. Suction wall vertical skewing, Series 2

The polar plots utilized in three-dimensional boundary layer analysis have been plotted in Figures 84, 85 and 86 for completeness. Inspection of Figures 84 and 85 reveals that three-dimensional boundary layer varies appreciably as one proceeds along the bottom from the pressure side to the suction side. The side-wall boundary layer polar plots for Series 2 tests show a marked difference.

The skewing angle behavior together with the velocity profile measurements indicate that the suction wall flow is rather complex as compared to the pressure wall.

The observations concerning the Series 2 tests are now summarized. There is an indication that some core is still present at the exit of the diffuser. There is uniform skewing in the vertical plane mid-way between the two vertical walls of the diffuser. At the geometric center of the passage the collateral core skewing angle is -8.3°. The maximum skewing angle of -9.5° is observed at z = 2.50 and Y = 4.000. The skewing decreases as one proceeds from this point of the passage towards the sidewalls. The bottom wall boundary layer exhibits a larger skewing angle relative to the skewing angle at the geometric center of the passage than the first series of tests. There is a slight vertical skewing of the fluid along the pressure surface. The vertical skewing on the suction wall is more than double that on the pressure surface. However, the skewing in the core and on the pressure and

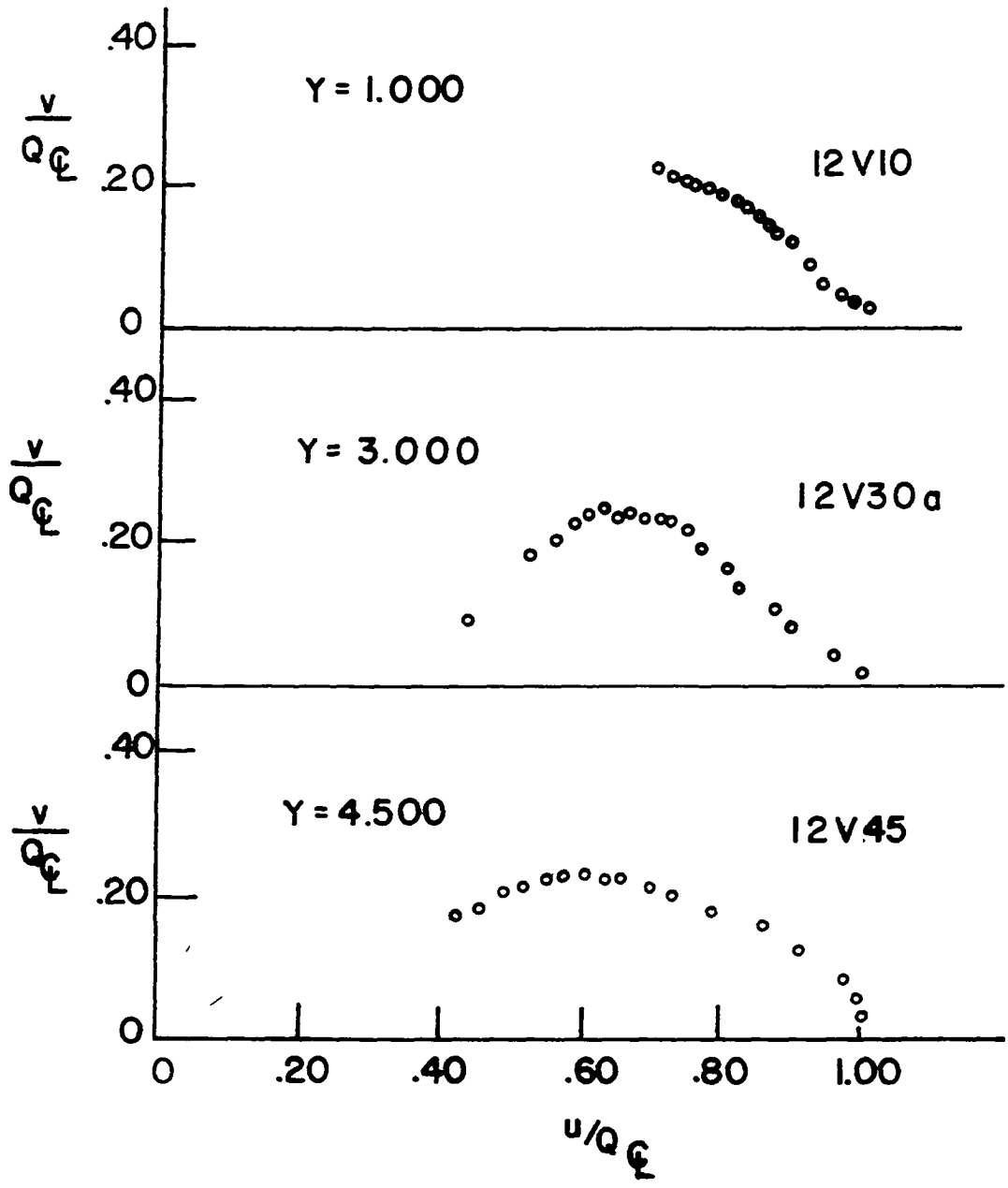

Figure 84. Bottom wall polar plots, Series 1

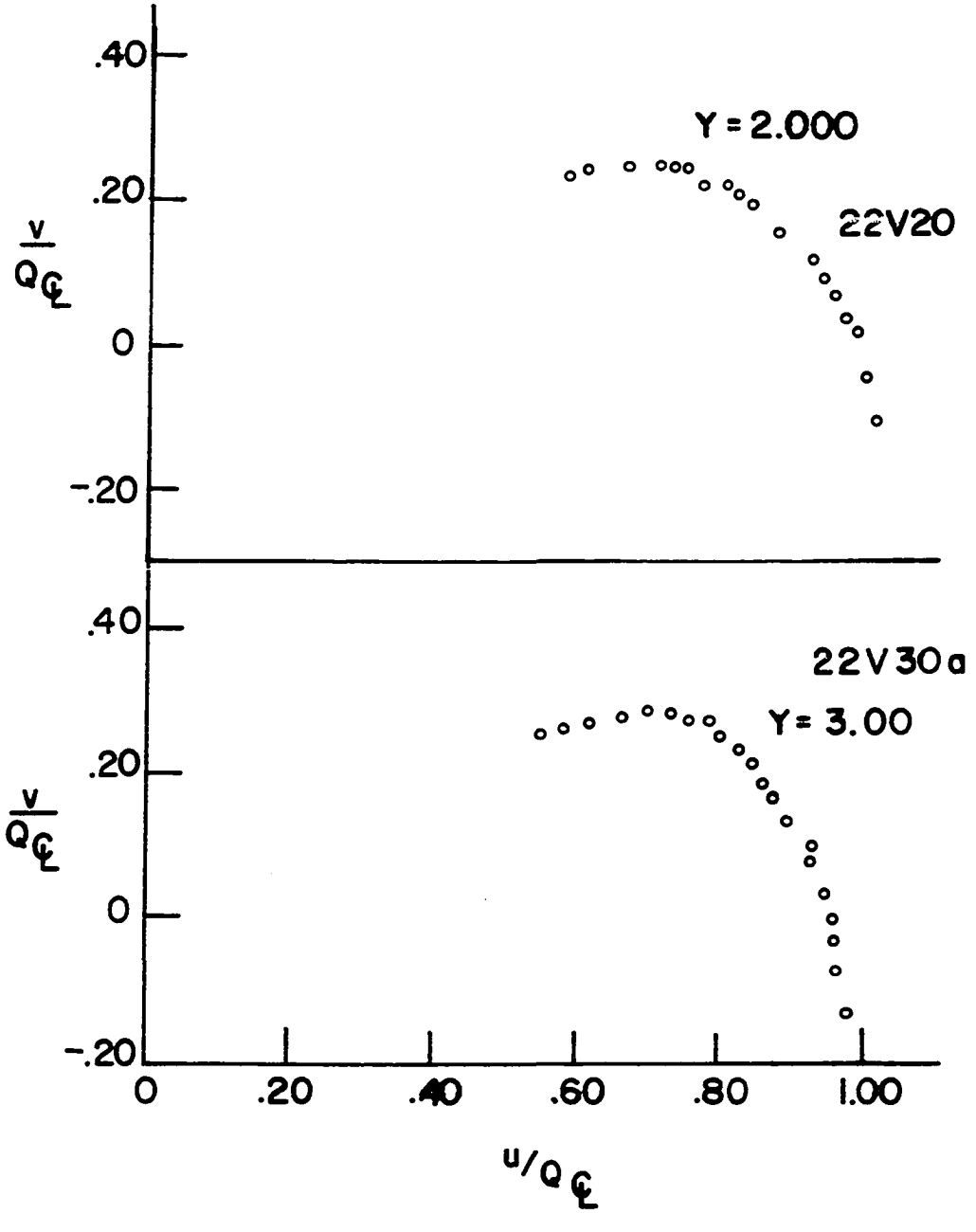

Figure 85. Bottom wall polar plots, Series 2

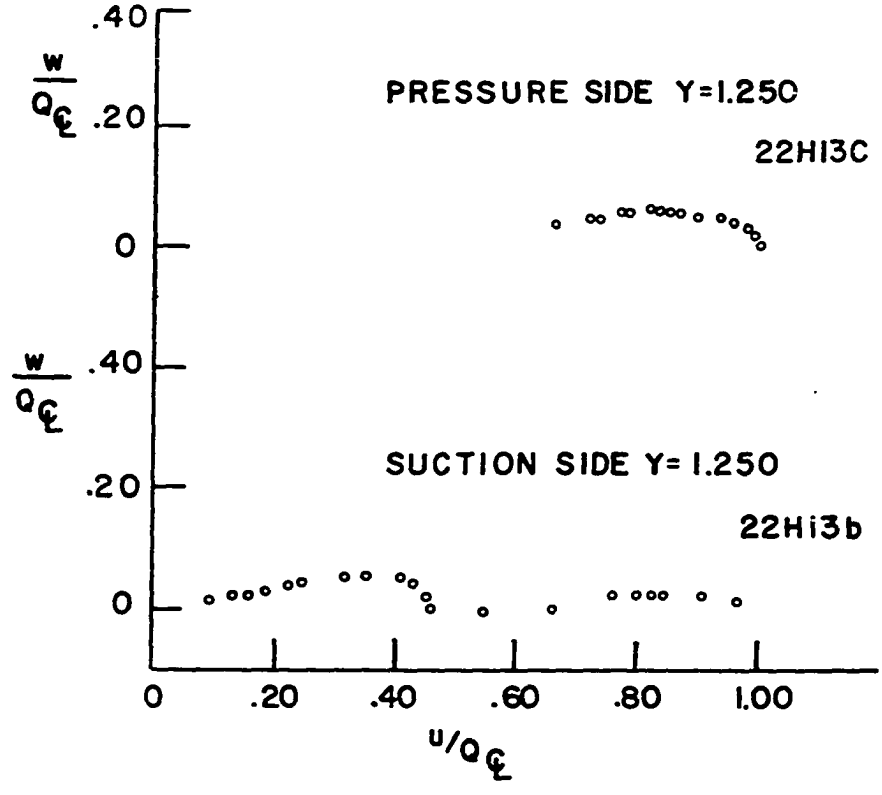

Figure 86. Sidewall polar plots Series 2

suction walls is rather small as compared to the skewing along the bottom wall.

It is believed that the first series of tests substantiates the observations reported by Fox and Kline (1962). They observed that there was no flow away from the suction surface in their curved diffuser study. Their conclusions were based on observations utilizing tufts. Gilman (1962) discussed this problem in the discussion following the above paper. He stated that "tired fluid will accumulate against the low pressure wall (suction wall) and no filament will be able to penetrate the higher pressure and higher energy layers radially outward from it." These observations together with the data obtained here in the first series of tests suggest the following model for the flow in a curved diffuser with small boundary layer (blockage factor less than 4.5%).

The flow model consists of a core region surrounded by boundary layer flow. Within the core the flow is irrotational and inviscid and there is no skewing anywhere within the core. The boundary layers surrounding the core will be the pressure wall, top and bottom wall and the suction wall boundary layer, Figure 87. The boundary layer on the pressure wall will be considered two-dimensional. This is justified on the basis of the experimental data obtained in the Series 2 tests. The pressure wall vertical skewing angle was only 3°, whereas, the core horizontal skewing angle was -8.3°.

Since the core skewing angle was negligible in the Series 1 tests, it follows that the vertical skewing along the pressure wall will probably also be negligible. The boundary layer on the top and bottom walls will be three-dimensional and there will be cross flow from the top and bottom walls towards the suction wall. The suction wall boundary layer is not two-dimensional due to the cross flow from the bottom and top walls. Further, it will be converging cross flow. This can be seen if it is assumed that the cross flow momentum is conserved as an element of fluid negotiates the corner and proceeds along the suction wall.

REMARKS

Based on the theoretical analysis and the experimental evidence gathered during the course of this research it is suggested that the three-dimensional flow in a curved diffuser with uniform core inlet flow and an inlet boundary layer blockage less than 5% may be analyzed utilizing the schematic model of the flow shown in Figure 87.

This model is similar to the model used in the analysis of laminar flow through a curved pipe of circular cross section by Barua (1963). It is based on the concept that the low momentum fluid in the top and bottom wall boundary layers moves towards the suction wall. As a result, the boundary layer on the suction wall grows more rapidly than the one on the pressure wall. As the magnitude of cross flow towards the suction wall becomes large there is some uniform skewing of the core flow away from the suction wall. In the Series 1 tests considered presently the uniform skewing of the core was less than one-half of a degree and can be considered negligible in the analysis of the flow in the core.

Any boundary layer analysis requires a knowledge of the core flow. A curvilinear coordinate system can be set up as shown in Figure A1 and derived in Appendix A. If $(\frac{Y}{R})^2$ is small, core flow can be represented by

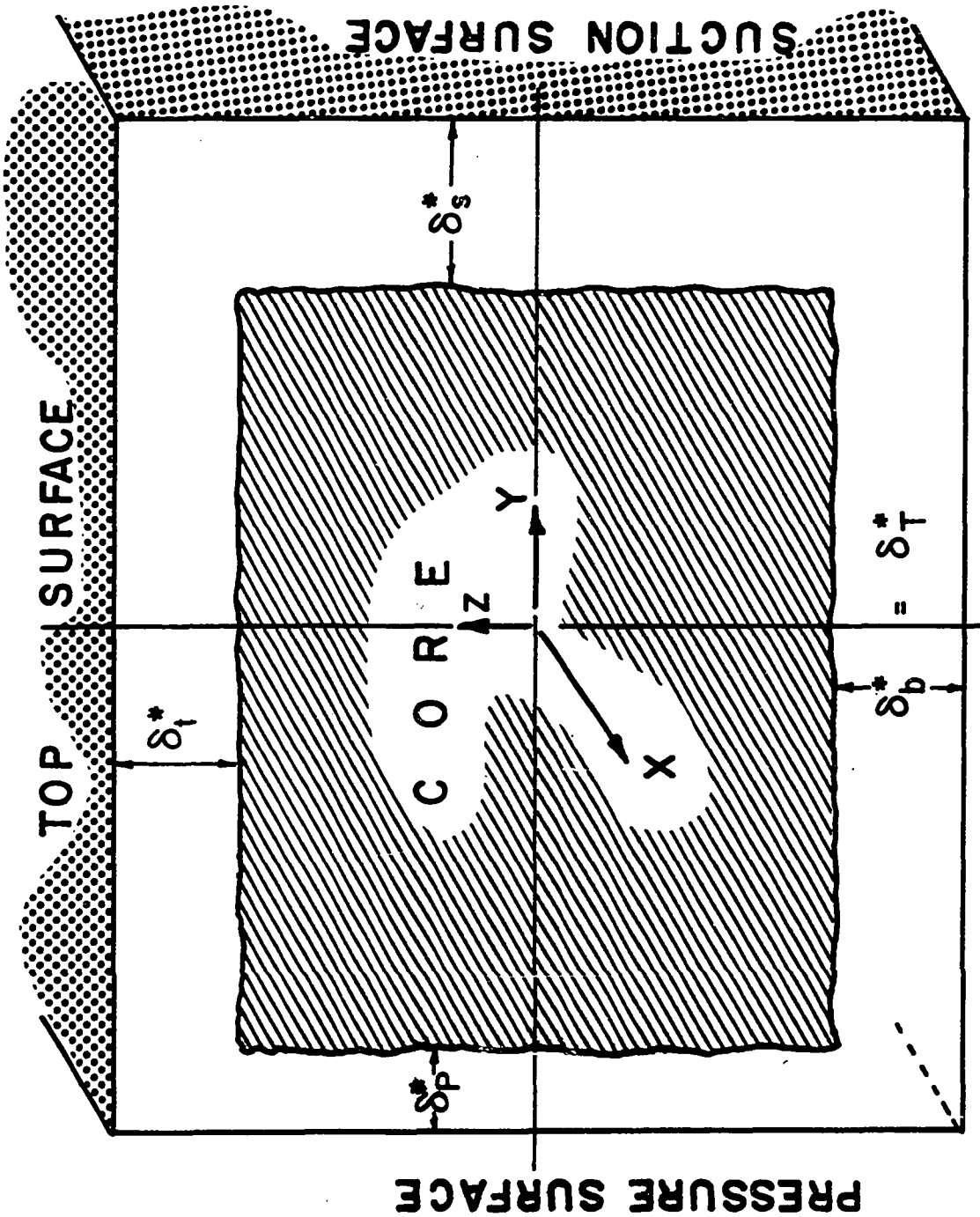

Figure 87. Flow development model

$$U = U_c \frac{R_c}{(R_c+y)} \tag{102}$$

as shown in Appendix B. However, this equation will not be valid throughout the diffuser, but rather for approximately the first half of the total length along the meanline. In the downstream portion of the diffuser the flow will be influenced by the uniform pressure distribution which exists in the exit cross section of the diffuser. The core flow in the second half of the diffuser can be approximated by Equation 102 but the value of $(\frac{R_c}{R_c+y})$ will be allowed to vary linearly until it reaches 0.99 at the exit.

The total flow rate, Q_f, is known from the conditions at the entrance. The entrance core velocity, U_c can be determined with

$$U_c = \frac{Q_f}{(b-\delta_t^* - \delta_b^*)(W - \delta_s^* - \delta_p^*)} \tag{103}$$

where

b = diffuser height (a constant for this geometry)

W = width (a function of meanline length)

δ_t^*, δ_b^*, δ_s^*, δ_p^* = the average displacement thickness on the top, bottom, suction and pressure walls respectively.

The iteration procedure is begun with the initial boundary layer conditions at the throat. A displacement thickness is chosen for all four walls some distance, dx, downstream. Then the continuity Equation 103 is used to calculate the new

core velocity U_c at the centerline. Equation 102 is used to calculate the local core velocity U. On the pressure wall, Truckenbrodt's (1955) Equations 15 and 16 can be used to calculate the momentum thickness and shape factor. Shear stress is found using Equation 14 as shown in Schlichting and Gersten (1962). Later refinements would include the cross flow influence, the curved wall shear correction effects as discussed by Ackeret (1967) and Cebeci (1969).

If it is now assumed that the top and bottom walls are identical for boundary layer calculation purposes, three-dimensional boundary layer equations from Francis and Pierce (1967) can be used

$$\frac{1}{h_1}\frac{\partial \theta_{11}}{\partial x_1} + \frac{1}{h_2 U}(2\theta_{11}+\delta_1^*)\frac{\partial U}{\partial x_1} + \frac{1}{h_1 h_2}(2\theta_{12}+\delta_2^*)\frac{\partial h_1}{\partial x_2}$$

$$+ \frac{1}{h_1 h_2}(\theta_{11}-\theta_{22})\frac{\partial h_2}{\partial x_1} + \frac{1}{h_2 U}(2\theta_{12}+\delta_2^*)\frac{\partial U}{\partial x_2}$$

$$+ \frac{1}{h_2}\frac{\partial \theta_{12}}{\partial x_2} = \frac{\tau_{0x_1}}{\rho U^2}$$

$$\frac{1}{h_2}\frac{\partial\theta_{22}}{\partial x_2} + \frac{2\theta_{22}}{h_2 U}\frac{\partial U}{\partial x_2} + \frac{2}{h_1 h_2}(\theta_{12}+\delta_2^*)\frac{\partial h_2}{\partial x_1}$$

$$+ \frac{1}{h_1 h_2}\frac{\partial h_1}{\partial x_2}(\theta_{22}-\delta_1^*-\theta_{11}) + \frac{2}{h_1 U}(\theta_{12}+\delta_2^*)\frac{\partial U}{\partial x_1}$$

$$+ \frac{1}{h_1}\frac{\partial}{\partial x_1}(\theta_{12}+\delta_2^*) = \frac{\tau_{0x_2}}{\rho U^2}$$

There are a total of seven unknowns in these equations, the streamwise and crossflow shear stresses, displacement thicknesses and momentum thicknesses plus an interaction momentum thickness. There are obviously more unknowns than equations, thus, auxiliary equations must be formulated using some of the three-dimensional models discussed previously. Mager (1952), Becker (1959), for example have formulated techniques for this purpose. Becker's (1959) approach suggests that cross flow momentum thickness and the interaction thickness may be neglected and that two-dimensional shear law and a two-dimensional shape parameter may be used. The above information together with Prandtl's (1946) three-dimensional boundary layer model are sufficient for a solution. Mager's (1952) technique is perhaps more general, but substantially similar to Becker's (1959).

A separate iteration scheme similar to the Schlichting and Gersten (1962) approach will no doubt be required for the three-dimensional boundary layer calculation. After

this portion of solution converges, the suction surface boundary layer will be analyzed. It will be assumed that a collateral three-dimensional boundary layer analysis such as used by Reneau and Johnston (1967) is an adequate first approximation. However, the boundary layer will not be diverging as in Reneau and Johnston's (1967) original analysis. Rather, the collateral layer will probably be converging due to the cross flow. Thus it will be necessary to calculate the $\frac{1}{a}$ parameter of Reneau and Johnston's Equation 7 as a function of the crossflow rather than the geometry. Smith's (1970) data indicates that the crossflow boundary layer tends to increase up to about the first one-half of the meanline length, and decays in the second half. It is probable that the decay is exponential as is the decay of swirl in a circular duct according to Wolf et al. (1969).

The utility of this approach might be limited by the appearance of stall on the suction surface. It will therefore, be necessary to use the method that was proposed by Moses and Chappell (1967) to extend the solution further.

The actual use of this method is presently hampered by limitation of the three-dimensional boundary layer theory.

CONCLUSIONS

Based on the experimental evidence reported in this dissertation, it is concluded that the diffuser exit core flow was collateral. The horizontal skewing angle (0.5°) was nearly uniform horizontally with small inlet blockage but non-uniform horizontally with larger inlet blockage. The meanline core horizontal skewing angle was -8.3° with the larger inlet blockage.

In view of this result, an outline of a method of analysis of the flow was prepared for the low inlet blockage case only. The basic approach consists of a curvilinear core flow coupled with a boundary layer analysis on each wall.

An increase in the blockage at the diffuser throat resulted in a reduction in the effectiveness of the diffuser from 51% to 43% for blockage factors of 4.5% and 13.9% respectively.

Stall was not observed in the present set of tests.

The uniform static pressure of the room into which the exit flow discharges was probably felt some distance upstream of the exit plane as indicated by the tangential traverse along the diffuser meanline, and the radial pressure gradient. The tangential traverse showed that most of the diffusion occurred in the first part of the diffuser. The

radial pressure gradient approached zero as the exit plane was reached.

Smith (1970) observed that the streamwise shape factor was increasing during the first part of the diffuser and later decreased. Such shape factor behavior might be partially explained by the streamwise velocity gradient obtained in this dissertation.

A comparison of the end wall polar plots indicated a significant difference between the polar plots for velocities near the pressure wall as compared to those near the suction wall.

The horizontal skewing angle reversal adjacent to the wall measured at the exit plane midway between the sidewalls (Figure 64) suggests that a collateral wall boundary layer might not really exist there as might have been expected. However, more extensive experimental work is required before a definite conclusion can be made.

REFERENCES

Ackeret, J. 1967. Aspects of internal flow. In Sovran, G., editor. Fluid mechanics of internal flow. Pp. 1-26. New York, New York, Elsevier Publishing Company.

Barua, S. N. 1963. On secondary flow in stationary curved pipes. Quarterly Mechanics and Applied Mathematics 16, Part 1: 62-67.

Bazin, H. 1865. Recherches hydrauliques. Memoires presentes par divers savants. Science mathematiques et physiques, Academie des Sciences, Paris, France, Series 2: 19.

Becker, E. 1959. Berechnung von reibungsschiehten mit schwacher sekundarstromung nach dem impulseverfahren. Zeitschrift fur Flugwissenschaften 7: 163-175.

Belik, L. 1968. An approximae solution for kinetic energy of secondary flow in blade cascades. International Journal of Mechanical Sciences 10, No. 10: 765-782.

Blechinger, Chester J. 1966. The effect of an exhaust diffuser on the performance of a gas turbine. Unpublished M.S. thesis. Madison, Wisconsin, Library, University of Wisconsin.

Bradshaw, P. 1967. The turbulence structure of equilibrium boundary layers. Journal of Fluid Mechanics 29: 625-645.

Brundrett, E. and Baines, W. D. 1964. The production and diffusion of vorticity in duct flow. Journal of Fluid Mechanics 19: 375-394.

Carlson, J. J., Johnston, J. P. and Sagi, C. J. 1967. Effects of wall shape on flow regimes and performance in straight two-dimensional diffusers. Journal of Basic Engineering 89: 151-160.

Cebeci, T. 1969. Laminar and turbulent incompressible boundary layers on slender bodies of revolution in axial flow. American Society of Mechanical Engineers Paper 69 WA/FE-2.

Champagne, F. H. and Sleicher, C. A. 1967. Turbulence measurements with inclined hot-wires. Part 2. Hot-wire response equations. Journal of Fluid Mechanics 28: 177-182.

Chandrasekhar, S. 1962. Hydrodynamic stability and hydromagnetic stability. Oxford, England, Oxford University Press. 1962.

Chiu, C. L. 1967. Factors determining the strength of secondary flow. American Society Civil Engineers Proceedings, Journal of Engineering Mechanics 93: 69-77.

Cockrell, D. J. and Markland, E. 1963. A review of incompressible diffusers flow. Aircraft Engineering 35: 286-292.

Coles, D. 1956. The law of the wake in the turbulent boundary layer. Journal of Fluid Mechanics 1: 191-226.

Cooke, J. C. 1961. Three-dimensional turbulent boundary layers. Great Britain Aeronautical Research Council Current Paper No. 625.

Dean, R. C. Jr. 1953. Aerodynamic measurements. Massachusetts Institute of Technology Gas Turbine Laboratory Report.

Detra, R. W. 1953. Secondary flow through curved pipes. Mitteilungen aus dum Institut fur Aerodynamic No. 20. Zurich, Switzerland, Eidgenossichen Technischlen Hochschule.

Eichelbrenner, E. A. and Peube, J. L. 1966. The role of S-shaped cross flow profiles in three-dimensional boundary layer theory. U.S. Navy European Research Contracts, ONR Contract NG2558-4460. Defense Documentation Center, Defense Supply Agency, AD 650-953.

Einstein, H. A. and Li, H. 1958. Secondary currents in straight channels. American Geophysical Union Transactions 30N06: 1085-1088.

Eskinazi, S. and Yeh, H. 1956. An investigation of fully developed turbulent flows in a curved channel. Journal of Aeronautical Sciences 23: 23-24.

Fox, R. W. and Kline, S. J. 1962. Flow regimes in curved subsonic diffusers. Journal of Basic Engineering 84: 303-316.

Francis, G. P. 1965. Incompressible flow of the three-dimensional turbulent boundary layer on the floor of curved channels. Unpublished Ph.D. thesis. Ithaca, New York, Library, Cornell University.

Francis, G. P. and Pierce, F. J. 1967. An experimental study of skewed turbulent boundary layers in low speed flows. Journal of Basic Engineering 89: 597-608.

Friehe, C. A. and Schwarz, W. H. 1968. Deviations from the cosine law for yawed cylindrical anemometer sensors. American Society of Mechanical Engineers Transactions, Series E, Journal of Applied Mechanics 35: 655-662.

Froberg, Carl-Erik. 1969. Introduction to numerical analysis. Second edition. Reading, Massachusetts, Addison-Wesley Publishing Company.

Gessner, F. B. and Jones, J. B. 1965. On some aspects of fully developed turbulent flow in rectangular channels. Journal of Fluid Mechanics 23: 683-713.

Gilman, F. 1962. Discussion. American Society of Mechanical Engineers Transactions, Series D, Journal of Basic Engineering 84: 315.

Gomi, M. 1967. Theory of secondary flows through cascades. Japan Society Mechanical Engineers Bulletin 10, No. 37: 86-99.

Görtler, H. 1955. Dreidimensionales zur stabilitastheorie grenzschlichten. Zeitschrift fur angewandte Mathematik und Mechanik 35: 326-364.

Gruschwitz, E. 1935. Turbulence reibungsschiehten mit sekundarstromung. Ingenieur-Archiv 6: 355-365.

Hawthorne, W. R. 1951. Secondary circulation in fluid flow. Royal Society Proceedings A206: 374-387.

Hawthorne, W. R. 1955. Some formulas for the calculation of secondary flows in cascades. Aeronautical Research Council Report 17,519.

Hawthorne, W. R. 1967. The Applicability of Secondary Flow Analyses to the Solution of Internal Flow Problems. In Sovran, G. (Ed.) Fluid Mechanics of Internal Flow, Elsevier Publishing Co., New York, N.Y.

Hawthorne, W. R. and Novak, R. A. 1970. The aerodynamics of turbomachinery. In Sears, W. R. and VanDyke, M., editors. Annual Review of Fluid Mechanics. Pp. 341-366. Palo Alto, California, Annual Reviews Inc.

Hinze, J. O. 1959. Turbulence. New York, New York, McGraw-Hill Book Co., Inc.

Hinze, J. O. 1967. Secondary currents in wall turbulence. The Physics of Fluid 10: S122-125.

Horlock, J. H., Louis, J. F., Percival, P. M. E. and Lakshminarayana, B. 1966. Wall Stall in Compressor Cascade. Journal of Basic Engineering 88: 637-648.

Hornung, H. G. and Joubert, P. N. 1963. The mean velocity profile in three-dimensional turbulent boundary layers. Journal of Fluid Mechanics, Part 3, 15: 368-384.

Hribar, A. E. and Purdy, K. R. 1969. On the interaction of intense acoustic fields and viscous fluid flows. Journal of Basic Engineering 91: 74-80.

Hussain, A. K. M. F. and Reynolds, W. C. 1970. The mechanics of an organized wave in turbulent shear flow. Journal of Fluid Mechanics 41: 241-258.

Johnston, J. P. 1957. On the three-dimensional turbulent boundary layer generated by secondary flow. Journal of Basic Engineering 82: 233-246. 1960. Also available as Three-dimensional turbulent boundary layer. Massachusetts Institute of Technology Gas Turbine Laboratory Report No. 39.

Johnston, J. P. and Powars, C. A. 1969. Some effects of inlet blockage and aspect ratio on diffuser performance. Journal of Basic Engineering 91: 551-553.

Joubert, P. N., Perry, A. E. and Brown, K. C. 1967. Critical review and current developments in three-dimensional turbulent boundary layers. In Sovran, G., editor. Fluid Mechanics of internal flow. Pp. 210-237. New York, New York, Elsevier Publishing Company.

Kline, S. J. and McClintock, F. A. 1953. Describing uncertainties in single sample experiments. Mechanical Engineering 75: 3-8.

Kuethe, A. M., McKee, P. G. and Curry, W. H. 1949. Measurements in the boundary layer of a yawed wing. U.S. National Advisory Committee for Aeronautics Technical Note 1946.

Lakshminarayana, B. and Horlock, J. H. 1967. Effect of shear flows on the outlet angle in axial compressor cascades. Journal of Basic Engineering 89: 191-200.

Laufer, J. 1954. The structure of turbulence in fully developed pipe flow. NACA Report 1174.

Liggett, J. A., Chiu, C. L. and Maio, L. S. 1968. Secondary currents in a corner. American Society of Civil Engineering Proceedings, Journal of Hydraulics Division 91: 99-117.

Livesey, J. L., Turner, J. T. and Grasspole, W. T. 1965. The decay of turbulent velocity profiles. Proceedings Institute of Mechanical Engineers 180, Pt. 3F: 127-136.

Loos, H. G. 1953. Analysis of secondary flow in the stator of an axial turbomachine. California Institute of Technology Technical Report No. 3.

Louis, J. F. 1960. Secondary flow in compressor cascades. Aeronautical Research Council Reports and Memoranda No. 3136.

Ludwieg, H. and Tillman, W. 1949. Untersuchen uber die wandschubspannung in turbulenten reibungsschiehten. Ingenieur Archiv 17: 288-299.

Mager, A. 1952. Generalization of boundary layer momentum integral equations to three-dimensional flows including those of a rotating system. U.S. National Adivsory Committee for Aeronautics Report 1067.

Masuda, K. and Otsuka, S. 1966. On the application limit of the inviscid small perturbation theory to the secondary flows in cascades. Nagoya University Faculty of Engineering Memoirs 18: 63-78.

Moffatt, H. K. 1964. Viscous and resistive eddies near a sharp corner. Journal of Fluid Mechanics 18: 1-18.

Moore, C. A. and Kline, S. J. 1958. Some effects of vanes and of turbulence on two-dimensional wide angle subsonic diffusers. U.S. National Advisory Committee for Aeronautics TN 4080.

Moses, H. L. and Chappell, J. R. 1967. Turbulent boundary layers in diffusers exhibiting partial stall. Journal of Basic Engineering 89: 655-665.

Norbury, J. F. 1959. Some measurements of boundary-layer growth in two-dimensional diffusers. Journal of Basic Engineering 81: 285-296. 1959.

Okiishi, Theodore and Serovy, George K. 1967. An experimental study of the turbulent-flow boundary-layer development in smooth annuli. Journal of Basic Engineering 89: 823-836.

Oswatitsch, K. 1959. Physikalische grundlagen der stromungs lehre. In Flugge, S., editor. Handbuch der Physik. Vol. 8. Part 1. P. 39. Gottingen, Springer-Verlag.

Patterson, G. N. 1937. Modern diffuser design. Aircraft Engineering 10: 267-273.

Perry, A. E. and Joubert, P. N. 1965. A three-dimensional turbulent boundary layer. Journal of Fluid Mechanics 22: 285-304.

Pletcher, R. H. 1962. An investigation of secondary flow in the entrance section of a straight rectangular duct. Unpublished M.S. thesis. Ithaca, New York, Library, Cornell University.

Prandtl, L. 1946. On boundary layers in three-dimensional flow. British Ministry of Aircraft Production Volkenrode R and T 64.

Prandtl, L. and Tietjens, O. G. 1934. Applied Hydro- and Aeromechanics. New York, New York, Dover Publications, Inc.

Puzyrewski, R. 1964. Description of the phenomenon of secondary flows in curved channels by means of convection of rotation lines. Archivum Mechaniki Stosowanes 1: 737-744.

Rayleigh , J. W. S. 1916. The dynamics of revolving fluids. Royal Society Proceedings 6A: 149-153.

Reneau, L. R. and Johnston, J. P. 1967. A performance prediction method for unstalled, two-dimensional diffusers. Journal of Basic Engineering 89: 643-654.

Reneau, L. R., Johnston, J. P. and Kline, S. J. 1967. Performances and design of straight two-dimensional diffuser. Journal of Basic Engineering 89: 141-150. 1967.

Rouse, H. and Hassan, M. M. 1949. Cavitation-free inlets and contractions. Mechanical Engineering 71: 213-218.

Runstadler, P. W. and Dean, R. C. 1968. Straight channel diffuser performance at high inlet mach numbers. American Society of Mechanical Engineers Paper 68-WA/FE-19.

Sagi, C. S. and Johnston, J. P. 1967. The design and performance of two-dimensional diffusers. Journal of Basic Engineering 89: 715-731.

Sagi, C. J., Johnston, J. P. and Kline, S. J. 1965. The design and performance of two-dimensional curved subsonic diffusers. Stanford University Report PD-9.

Sandborn, V. A. 1966. Metrology of fluid mechanics. Colorado State University Report CER66VAS32.

Scarborough, J. B. 1962. Numerical mathematical analysis. Fifth edition. Baltimore, Maryland, The Johns Hopkins Press.

Schlichting, H. 1968. Boundary layer theory. 6th edition. New York, New York, McGraw-Hill Book Company, Inc.

Schlichting, H. and Gersten, K. 1961. Berechnung der stromung in rotationsymetrischen diffusoren mit helfe der grenzschicht-theorie. Zeitschrift fur Flugwissenschaften (ZFW) 4/5: 135-140.

Schubauer, G. B. and Spangenberg, W. G. 1960. Forced mixing in boundary layers. Journal of Fluid Mechanics 8: 10-32.

Shapiro, A. H. 1953. The dynamics and thermodynamics of compressible fluid flow. New York, New York, The Ronald Press Company.

Smith, L. H. 1955. Secondary flow in axial turbomachinery. Journal of Basic Engineering 77: 1065-1076.

Smith, M. D. 1970. Incompressible skewed turbulent boundary layer on an end wall of a curved two-dimensional diffuser. Unpublished Ph.D. thesis. Ames, Iowa, Library, Iowa State University.

Smith, P. D. 1968. Calculation methods for three-dimensional turbulent boundary layers. Aeronautical Research Council Report and Memoranda No. 3523.

Soderberg, O. E. 1958. Secondary flow and losses in a compressor cascade. Massachusetts Institute of Technology Gas Turbine Laboratory Report No. 46.

Sovran, G. and Klomp, E. D. 1967. Experimentally determined optimum geometries for retilinear diffusers with rectangular, conical or annular cross-section. In Sovran, G., editor. Fluid mechanics of internal flow. Pp. 270-319. New York, New York, Elsevier Publishing Company.

Sprenger, H. 1959. Experimental investigation of straight and curved diffusers. Mitteilungen aus dem Institut fur Aerodynamik No. 27.

Squire, H. B. and Winter, K. C. 1951. Secondary flow in a cascade of airfoils in a non-uniform stream. Journal of Aeronautical Sciences 18: 271-277.

Stratford, B. S. 1959. Prediction of separation of the turbulent boundary layer. Journal of Fluid Mechanics 5: 1-35.

Truckenbrodt, E. 1955. A Method of Quadrature for Calculation of the Laminar and Turbulent Boundary Layers in Case of Plane and Rotationally Symmetric Flow. NACA TM1379.

Van Doenhoff, A. E. and Tetervin, N. 1943. Determination of general relations for the behavior of turbulent boundary layers. NACA Report 772.

Wattendorf, F. L. 1935. A study of the effect of curvature on fully developed turbulent flow. Royal Society of London Proceedings 148: 565-598.

Wolf, L. Jr., Lavan, A. and Fejer, A. A. 1969. Measurements of the decay of swirl in turbulent flow. American Institute of Aeronautics and Astronautics Journal 7: 971-973.

Wolf, S., and Johnston, J. P. 1966. Effects of Non-uniform Inlet Velocity Profiles on Flow Regimes and Performance in Two-Dimensional Diffusers. Stanford University Report PD-12.

Wolf, S. F. and Johnston, J. P. 1969. Effects on non-uniform inlet velocity profiles on flow regimes and performance in two-dimensional diffuser. American Society of Mechanical Engineers Paper 68-WA/FE-25.

ACKNOWLEDGMENTS

Thanks are due to the members of the author's graduate study committee, Professor Robert C. Fellinger, Dr. Kenneth A. Heimes, Dr. Patrick Kavanaugh, Dr. Gundo A. Nariboli, Dr. George K. Serovy and Dr. Donald F. Young.

Financial assistance received from the Iowa State University Engineering Research Institute and the Iowa State University Mechanical Engineering Department is acknowledged.

The author is especially grateful to Dr. Theodore Okiishi who provided useful guidance frequently throughout the author's research program of study.

The author is also grateful to various other faculty, as well as Mr. Girard together with his machinists, Mr. John Siegfried and Mr. Clifford Osam in particular, who were most helpful during the experimental phase of this dissertation.

Special thanks are expressed to the author's wife who so willingly shouldered the domestic responsibility and also found time to sew the flexible connection by the large plenum chamber and did much typing.

This dissertation was typed by Mrs. Pat Gunnells. Ink drawings were done by Mr. Tom Kelly.

APPENDIX A: CURVILINEAR COORDINATE SYSTEM

The curvilinear coordinate system valid for a curved passage will be derived in this Appendix. The configuration under discussion is shown in Figure A1.

It is desired to calculate the scale factors, h_1, h_2, and h_3. From the figure, note that the distance between two points P and Q, not on the surface is,

$$(PQ)^2 = (PR)^2 + (RQ)^2$$

Note that QR = Δn, the normal distance from the surface. The distance from the center of curvature C, to point A on the surface is CA. CA is local radius R, thus, the distance along the arc from P to R can be calculated from

$$PR = CP(\Delta\phi)$$

And the distance along the surface is

$$AB = CA\Delta\phi = \Delta S$$

where S is the distance along the surface. Solving for

$$\Delta\phi = \frac{\Delta S}{R}$$

Substituting for $\Delta\phi$ in the PR expression yields

$$PR = (R + n)\frac{\Delta S}{R} = (1 + \frac{n}{R})\Delta S$$

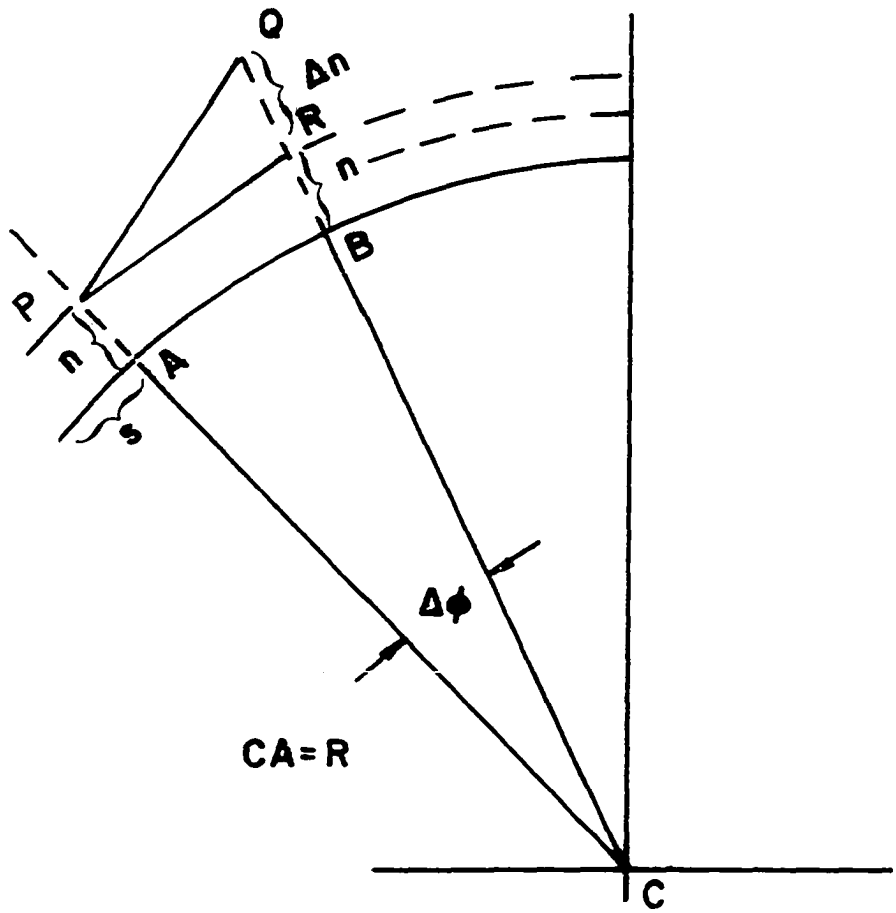

Figure A1. Curvilinear coordinate system

The expression for the distance between PQ becomes

$$= (PQ)^2 = (1 + \frac{n}{R})\ \Delta S^2 + \Delta n^2$$

$$= h_1^2 (\Delta S)^2 + h_2^2 (\Delta n)^2$$

$$h_1 = (1 + \frac{n}{R}), \quad h_2 = 1 = h_3$$

APPENDIX B: LOCAL VELOCITY EQUATION

The equation for the local velocity in the curved diffuser with inviscid irrotational incompressible flow will be derived in this appendix.

The assumption of incompressible irrotational flow can be written in curvilinear coordinates, thus

$$\nabla \times \bar{U} = 0 \tag{B1}$$

$$\nabla \times \bar{U} = \frac{1}{h_1 h_2 h_3} \{h_1 [\frac{\partial}{\partial x_2} (h_3 u_3) - \frac{\partial}{\partial x_3} (h_2 u_2)] i_1$$

$$+ h_2 [\frac{\partial}{\partial x_3} (h_1 u_1) - \frac{\partial}{\partial x_1} (h_3 u_3)] i_2$$

$$+ h_3 [\frac{\partial}{\partial x_1} (h_2 u_2) - \frac{\partial}{\partial x_2} (h_1 u_1)] i_3\} \tag{B2}$$

Since the top and bottom walls are straight and parallel the component of velocity $U_3 = 0$, and derivatives in x_3 direction are zero, thus, Equation B2 becomes

$$\nabla \times \bar{U} = \frac{i_3 h_3}{h_1 h_2 h_3} (\frac{\partial}{\partial x_1} (h_2 u_2) - \frac{\partial}{\partial x_2} (h_1 u_1)) = 0 \tag{B3}$$

Using the coordinate system derived in Appendix A gives

$$\frac{1}{(1 + \frac{x_2}{R})} [\frac{\partial u_2}{\partial x_1} - \frac{\partial}{\partial x_2} (u_1 (1 + \frac{x_2}{R}))] = 0$$

Expanding the above equation and simplifying results in the following

$$\frac{u_1}{R+x_2} + \frac{\partial u_1}{\partial x_2} - \frac{R}{R+x_2}\left(\frac{\partial u_2}{\partial x_1}\right) = 0 \qquad \text{(B5)}$$

Patel (1968) has examined this equation by reviewing experimental data and shows that the last term is negligible provided

$$\left(\frac{x_2}{R}\right)^2 << 1$$

This condition is satisfied for the geometry under consideration, $\left(\left(\frac{x_2}{R_c}\right)^2 = 0.024\right)$ thus, the equation becomes

$$\frac{u_1}{R+x_2} + \frac{\partial u_1}{\partial x_2} = 0 \qquad \text{(B6)}$$

If R is replaced by the radius at the centerline R_c, and u_1 by the centerline velocity u_c, and x_2 by the perpendicular distance y from the centerline the expression for the local velocity in terms of the centerline velocity becomes

$$u = u_c\left(1 + \frac{y}{R_c}\right) \qquad \text{(B7)}$$

APPENDIX C: DIFFUSER EXPERIMENTAL DATA

Series 1, throat traverse number 11V03:

Z	Y	U/UCL	U-FT/SEC
1.800	0.250	0.995	116.660
0.015	0.250	0.473	55.467
0.020	0.250	0.535	62.726
0.025	0.250	0.555	65.044
0.030	0.250	0.566	66.397
0.040	0.250	0.584	68.520
0.050	0.250	0.604	70.836
0.060	0.250	0.630	73.928
0.075	0.250	0.644	75.497
0.090	0.250	0.682	79.949
0.115	0.250	0.717	84.090
0.140	0.250	0.748	87.708
0.175	0.250	0.772	90.498
0.250	0.250	0.793	92.951
0.350	0.250	0.793	92.951
0.450	0.250	0.834	97.778
0.600	0.250	0.870	101.967
0.800	0.250	0.949	111.298
1.000	0.250	0.980	114.922
1.200	0.250	0.981	115.048
1.500	0.250	0.986	115.609
1.800	0.250	0.986	115.671

Series 1, throat traverse number 11V05:

Z	Y	U/UCL	U-FT/SEC
1.800	0.500	0.993	116.473
0.025	0.500	0.572	67.097
0.030	0.500	0.617	72.361
0.035	0.500	0.632	74.082
0.040	0.500	0.639	74.959
0.045	0.500	0.648	76.025
0.055	0.500	0.660	77.336
0.065	0.500	0.672	78.747
0.080	0.500	0.697	81.728
0.095	0.500	0.718	84.244
0.110	0.500	0.743	87.161
0.130	0.500	0.769	90.207
0.160	0.500	0.796	93.331
0.200	0.500	0.834	97.828
0.250	0.500	0.884	103.662
0.300	0.500	0.917	107.571
0.450	0.500	0.943	110.589
0.650	0.500	0.950	111.438
0.900	0.500	0.988	115.858
1.200	0.500	0.988	115.858
1.500	0.500	0.988	115.858
1.800	0.500	0.988	115.858

Series 1, throat traverse number 11V08:

Z	Y	U/UCL	U-FT/SEC
1.800	0.800	1.001	117.349
0.010	0.800	0.497	58.260
0.015	0.800	0.565	66.240
0.020	0.800	0.586	68.678
0.025	0.800	0.595	69.818
0.035	0.800	0.636	74.529
0.045	0.800	0.656	76.979
0.060	0.800	0.695	81.488
0.075	0.800	0.732	85.863
0.100	0.800	0.765	89.667
0.125	0.800	0.808	94.756
0.150	0.800	0.848	99.422
0.175	0.800	0.877	102.791
0.225	0.800	0.910	106.721
0.275	0.800	0.955	111.949
0.375	0.800	0.971	113.838
0.600	0.800	0.976	114.457
0.800	0.800	0.976	114.457
1.000	0.800	0.978	114.653
1.200	0.800	0.978	114.653
1.400	0.800	0.978	114.653
1.800	0.800	0.978	114.653

Series 1, throat traverse number 11V10:

Z	Y	U/UCL	U-FT/SEC
1.800	1.000	0.992	116.347
0.020	1.000	0.520	60.976
0.025	1.000	0.532	62.376
0.030	1.000	0.553	64.852
0.035	1.000	0.577	67.618
0.045	1.000	0.585	68.621
0.055	1.000	0.638	74.757
0.065	1.000	0.664	77.914
0.080	1.000	0.678	79.558
0.100	1.000	0.734	86.120
0.125	1.000	0.754	88.447
0.150	1.000	0.810	95.003
0.175	1.000	0.877	102.812
0.225	1.000	0.940	110.266
0.275	1.000	0.976	114.491
0.325	1.000	0.987	115.725
0.500	1.000	0.987	115.725
0.700	1.000	0.987	115.725
0.900	1.000	0.987	115.725
1.100	1.000	0.987	115.725
1.400	1.000	0.987	115.725
1.800	1.000	0.987	115.725

Series 1, throat traverse number 11V20a:

Z	Y	U/UCL	U-FT/SEC
1.800	2.000	0.988	115.848
0.025	2.000	0.676	79.261
0.030	2.000	0.709	83.106
0.035	2.000	0.731	85.657
0.040	2.000	0.739	86.599
0.045	2.000	0.761	89.242
0.050	2.000	0.783	91.760
0.055	2.000	0.795	93.201
0.065	2.000	0.823	96.544
0.075	2.000	0.846	99.217
0.085	2.000	0.873	102.351
0.095	2.000	0.889	104.283
0.105	2.000	0.911	106.871
0.115	2.000	0.923	108.267
0.125	2.000	0.931	109.126
0.140	2.000	0.944	110.671
0.165	2.000	0.954	111.915
0.200	2.000	0.981	115.082
0.250	2.000	0.988	115.848
0.400	2.000	0.988	115.848
0.800	2.000	0.988	115.848
1.800	2.000	0.988	115.848

Series 1, throat traverse number 11V20b:

Z	Y	U/UCL	U-FT/SEC
1.800	2.000	0.999	117.134
1.500	2.000	0.997	116.948
1.600	2.000	0.993	116.450
1.700	2.000	0.993	116.387
1.800	2.000	0.993	116.387
1.900	2.000	0.993	116.387
2.000	2.000	0.993	116.450
2.100	2.000	0.997	116.948
2.200	2.000	1.000	117.258
2.300	2.000	1.002	117.506
2.400	2.000	0.997	116.886
2.500	2.000	0.998	117.072
2.600	2.000	1.006	118.016
2.700	2.000	1.006	117.906
2.800	2.000	1.005	117.798
2.900	2.000	1.008	118.239
3.000	2.000	1.009	118.353
3.100	2.000	1.007	118.127
3.200	2.000	1.007	118.127
3.300	2.000	1.006	118.016
3.400	2.000	1.004	117.691
1.800	2.000	1.001	117.382

Series 1, throat traverse number 11V25:

Z	Y	U/UCL	U-FT/SEC
1.800	2.500	1.001	117.434
0.015	2.500	0.610	71.495
0.025	2.500	0.677	79.380
0.035	2.500	0.734	86.103
0.050	2.500	0.790	92.674
0.075	2.500	0.865	101.411
0.100	2.500	0.912	106.978
0.125	2.500	0.938	110.006
0.150	2.500	0.943	110.545
0.200	2.500	0.999	117.153
0.250	2.500	1.001	117.363
0.300	2.500	1.001	117.363
0.400	2.500	1.001	117.363
0.500	2.500	1.001	117.363
0.600	2.500	1.001	117.363
0.700	2.500	1.001	117.363
0.800	2.500	1.001	117.363
0.900	2.500	1.001	117.363
1.000	2.500	1.001	117.434
1.200	2.500	1.001	117.434
1.400	2.500	1.001	117.434
1.800	2.500	1.001	117.434

Series 1, throat traverse number 11V30:

Z	Y	U/UCL	U-FT/SEC
1.800	3.000	0.997	116.917
0.015	3.000	0.632	74.148
0.020	3.000	0.670	78.610
0.025	3.000	0.711	83.333
0.030	3.000	0.728	85.380
0.035	3.000	0.734	86.075
0.045	3.000	0.776	91.050
0.060	3.000	0.818	95.961
0.080	3.000	0.864	101.264
0.100	3.000	0.898	105.278
0.125	3.000	0.925	108.495
0.175	3.000	0.941	110.327
0.225	3.000	0.976	114.414
0.325	3.000	0.976	114.414
0.500	3.000	0.976	114.414
0.700	3.000	0.976	114.414
0.900	3.000	0.988	115.869
1.100	3.000	0.992	116.288
1.300	3.000	0.997	116.917
1.500	3.000	0.997	116.917
1.600	3.000	0.997	116.917
1.800	3.000	0.997	116.917

Series 1, throat traverse number 11V40:

Z	Y	U/UCL	U-FT/SEC
1.800	4.000	1.006	117.939
0.015	4.000	0.593	69.577
0.020	4.000	0.641	75.196
0.025	4.000	0.654	76.728
0.030	4.000	0.681	79.826
0.035	4.000	0.697	81.772
0.040	4.000	0.712	83.438
0.050	4.000	0.722	84.628
0.060	4.000	0.728	85.366
0.070	4.000	0.752	88.190
0.085	4.000	0.777	91.126
0.100	4.000	0.787	92.270
0.120	4.000	0.838	98.261
0.140	4.000	0.862	101.062
0.165	4.000	0.885	103.756
0.190	4.000	0.922	108.129
0.265	4.000	0.981	114.987
0.365	4.000	1.003	117.592
0.500	4.000	1.006	117.939
0.800	4.000	1.006	117.939
1.100	4.000	1.006	117.939
1.800	4.000	1.006	117.939

Series 1, throat traverse number 11V42:

Z	Y	U/UCL	U-FT/SEC
1.800	4.200	1.005	117.835
0.010	4.200	0.577	67.665
0.015	4.200	0.620	72.720
0.020	4.200	0.637	74.729
0.030	4.200	0.687	80.598
0.040	4.200	0.711	83.354
0.055	4.200	0.735	86.164
0.070	4.200	0.764	89.598
0.085	4.200	0.786	92.136
0.100	4.200	0.823	96.452
0.120	4.200	0.853	99.964
0.160	4.200	0.880	103.194
0.200	4.200	0.926	108.609
0.250	4.200	0.967	113.364
0.300	4.200	0.990	116.142
0.400	4.200	1.011	118.494
0.500	4.200	1.012	118.629
0.600	4.200	1.012	118.629
0.800	4.200	1.012	118.629
1.000	4.200	1.012	118.629
1.400	4.200	1.012	118.629
1.800	4.200	1.012	118.629

Series 1, throat traverse number 11V45:

Z	Y	U/UCL	U-FT/SEC
1.800	4.500	1.015	119.066
0.015	4.500	0.554	65.001
0.020	4.500	0.615	72.158
0.025	4.500	0.629	73.746
0.030	4.500	0.643	75.431
0.040	4.500	0.649	76.140
0.050	4.500	0.669	78.499
0.060	4.500	0.698	81.833
0.070	4.500	0.715	83.857
0.085	4.500	0.725	85.014
0.100	4.500	0.753	88.299
0.125	4.500	0.768	89.999
0.150	4.500	0.798	93.571
0.175	4.500	0.844	98.915
0.210	4.500	0.857	100.494
0.250	4.500	0.900	105.583
0.300	4.500	0.916	107.464
0.400	4.500	0.956	112.121
0.600	4.500	0.980	114.864
0.800	4.500	1.015	119.066
1.300	4.500	1.015	119.066
1.800	4.500	1.015	119.066

Series 1, throat traverse number 11V48:

Z	Y	U/UCL	U-FT/SEC
1.800	4.750	1.029	120.706
0.013	4.750	0.574	67.321
0.018	4.750	0.587	68.850
0.023	4.750	0.608	71.298
0.028	4.750	0.628	73.617
0.035	4.750	0.642	75.305
0.045	4.750	0.653	76.566
0.055	4.750	0.689	80.738
0.070	4.750	0.720	84.462
0.090	4.750	0.748	87.673
0.110	4.750	0.763	89.503
0.135	4.750	0.800	93.749
0.170	4.750	0.840	98.530
0.225	4.750	0.868	101.775
0.300	4.750	0.914	107.192
0.400	4.750	0.933	109.432
0.625	4.750	0.986	115.600
0.900	4.750	0.987	115.726
1.100	4.750	0.913	107.075
1.300	4.750	1.005	117.836
1.500	4.750	1.012	118.644
1.800	4.750	1.013	118.764

Series 1, throat traverse number 11H18:

Z	Y	U/UCL	U-FT/SEC
1.800	2.500	0.996	116.743
1.800	0.500	0.989	115.993
1.800	0.750	0.988	115.809
1.800	1.000	0.988	115.871
1.800	1.250	0.988	115.809
1.800	1.500	0.991	116.177
1.800	1.750	0.987	115.748
1.800	2.000	0.987	115.686
1.800	2.250	0.987	115.748
1.800	2.500	0.987	115.748
1.800	2.750	0.995	116.634
1.800	3.000	0.996	116.743
1.800	3.250	0.998	117.076
1.800	3.500	0.997	116.964
1.800	3.750	0.999	117.189
1.800	4.000	1.004	117.773
1.800	4.250	1.007	118.137
1.800	4.500	1.014	118.897
1.800	4.750	1.020	119.562
1.800	3.000	1.002	117.536
1.800	2.000	0.997	116.853
1.800	2.500	1.004	117.773

Series 1, throat traverse number 11H25:

Z	Y_s	U/UCL	U-FT/SEC
2.500	2.500	1.000	117.258
2.500	0.010	0.694	81.381
2.500	0.015	0.716	83.985
2.500	0.025	0.770	90.338
2.500	0.035	0.808	94.707
2.500	0.055	0.843	98.827
2.500	0.075	0.883	103.594
2.500	0.100	0.918	107.621
2.500	0.125	0.963	112.921
2.500	0.150	0.972	114.008
2.500	0.200	1.000	117.258
2.500	0.250	1.000	117.258
2.500	0.300	1.000	117.258
2.500	0.400	1.006	117.908
2.500	0.500	1.000	117.258
2.500	0.700	1.000	117.258
2.500	0.900	1.000	117.258
2.500	1.200	1.000	117.258
2.500	1.500	1.000	117.258
2.500	1.800	1.000	117.258
2.500	2.100	1.000	117.258
2.500	2.500	1.000	117.258

Series 1, throat traverse number 11H32a:

Z	Y	U/UCL	U-FT/SEC
3.200	2.500	1.022	119.878
3.200	0.015	0.624	73.116
3.200	0.020	0.684	80.198
3.200	0.030	0.709	83.189
3.200	0.040	0.732	85.788
3.200	0.050	0.759	89.023
3.200	0.060	0.788	92.401
3.200	0.070	0.798	93.524
3.200	0.090	0.846	99.212
3.200	0.110	0.869	101.846
3.200	0.130	0.913	107.039
3.200	0.150	0.929	108.918
3.200	0.180	0.946	110.942
3.200	0.210	0.975	114.312
3.200	0.240	0.976	114.396
3.200	0.340	0.977	114.565
3.200	0.500	0.978	114.650
3.200	0.700	0.979	114.822
3.200	1.000	0.979	114.822
3.200	1.500	0.979	114.822
3.200	2.000	0.979	114.822
3.200	2.500	0.996	116.748

Series 1, throat traverse number 11H32b:

Z	Y	U/UCL	U-FT/SEC
3.200	2.000	1.003	117.586
3.200	1.750	1.000	117.208
3.200	1.500	0.998	117.018
3.200	1.250	0.999	117.144
3.200	1.000	1.000	117.208
3.200	0.750	1.001	117.397
3.200	0.500	1.001	117.334
3.200	2.000	1.001	117.397
3.200	2.250	1.001	117.397
3.200	2.500	1.002	117.460
3.200	2.750	1.002	117.523
3.200	3.000	1.003	117.586
3.200	3.250	1.006	117.963
3.200	3.500	1.012	118.712
3.200	3.750	1.017	119.265
3.200	4.000	1.018	119.380
3.200	4.250	1.027	120.462
3.200	4.500	1.039	121.777
3.200	3.000	1.021	119.730
3.200	3.000	1.021	119.730
3.200	3.000	1.021	119.730
3.200	2.000	1.015	119.040

Series 1, exit plane traverse number 12V10:

Z	Y	U/UCL	U-FT/SEC	ALPHA
1.250	1.000	0.991	104.160	2.515
0.026	1.000	0.736	77.429	17.632
0.032	1.000	0.742	77.993	17.107
0.042	1.000	0.752	79.081	16.014
0.052	1.000	0.769	80.848	15.299
0.062	1.000	0.776	81.587	14.676
0.082	1.000	0.801	84.232	14.130
0.100	1.000	0.816	85.794	12.899
0.120	1.000	0.832	87.508	12.027
0.145	1.000	0.844	88.762	11.109
0.160	1.000	0.856	90.008	10.323
0.185	1.000	0.869	91.393	9.321
0.210	1.000	0.880	92.543	8.529
0.235	1.000	0.897	94.355	7.345
0.295	1.000	0.916	96.377	5.332
0.350	1.000	0.938	98.664	3.413
0.425	1.000	0.966	101.620	2.768
0.500	1.000	0.983	103.416	1.926
0.600	1.000	0.994	104.492	1.884
0.800	1.000	0.995	104.676	2.785
1.000	1.000	0.986	103.658	3.284
1.250	1.000	0.991	104.223	2.526

Series 1, exit plane traverse number 12V30a:

Z	Y	U/UCL	U-FT/SEC	ALPHA
1.786	3.000	0.998	104.961	0.598
0.031	3.000	0.451	47.473	10.966
0.036	3.000	0.565	59.449	19.129
0.041	3.000	0.599	63.039	19.495
0.046	3.000	0.633	66.564	20.951
0.051	3.000	0.653	68.709	20.991
0.061	3.000	0.678	71.268	20.848
0.071	3.000	0.698	73.388	20.246
0.081	3.000	0.709	74.579	19.026
0.096	3.000	0.733	77.122	18.925
0.111	3.000	0.746	78.481	17.530
0.131	3.000	0.769	80.823	17.149
0.156	3.000	0.784	82.404	15.878
0.186	3.000	0.796	83.701	14.072
0.236	3.000	0.826	86.850	11.125
0.286	3.000	0.853	89.708	8.822
0.336	3.000	0.879	92.387	6.848
0.386	3.000	0.908	95.486	4.992
0.486	3.000	0.963	101.255	2.029
0.586	3.000	1.002	105.356	0.029
0.786	3.000	1.007	105.913	-0.559
1.786	3.000	1.008	105.988	-0.598

Series 1, exit plane traverse number 12V30b:

Z	Y	U/UCL	U-FT/SEC	ALPHA
1.786	3.000	1.000	105.153	-0.009
1.686	3.000	0.995	104.622	0.353
1.886	3.000	0.995	104.635	0.372
1.986	3.000	1.005	105.688	-0.610
2.086	3.000	1.005	105.651	-0.353
2.186	3.000	1.005	105.714	-0.259
2.286	3.000	1.007	105.900	-0.293
2.386	3.000	1.006	105.803	-0.129
2.486	3.000	0.997	104.820	0.635
2.500	3.000	0.996	104.780	0.579
2.600	3.000	0.997	104.833	0.579
2.700	3.000	0.998	104.951	0.600
2.800	3.000	1.002	105.386	0.550
2.900	3.000	1.001	105.307	0.289
3.000	3.000	1.005	105.732	0.147
3.100	3.000	0.998	104.964	0.544
3.200	3.000	1.003	105.466	0.218
3.300	3.000	1.001	105.215	0.529
3.400	3.000	0.998	104.992	0.730
3.500	3.000	0.999	105.032	0.712
2.500	3.000	1.003	105.482	-0.448
1.786	3.000	1.000	105.165	0.009

Series 1, exit plane traverse number 12V45:

Z	Y	U/UCL	U-FT/SEC	ALPHA
1.250	4.500	1.020	107.297	-0.381
0.036	4.500	0.460	48.404	22.050
0.040	4.500	0.496	52.184	22.047
0.045	4.500	0.534	56.131	22.335
0.050	4.500	0.556	58.446	22.471
0.060	4.500	0.592	62.203	21.801
0.070	4.500	0.613	64.461	21.646
0.085	4.500	0.648	68.097	21.096
0.100	4.500	0.672	70.708	19.758
0.120	4.500	0.696	73.152	18.867
0.150	4.500	0.729	76.608	16.644
0.180	4.500	0.759	79.773	15.292
0.230	4.500	0.810	85.189	12.746
0.290	4.500	0.871	91.575	10.069
0.350	4.500	0.928	97.598	7.477
0.410	4.500	0.979	102.926	4.590
0.500	4.500	1.007	105.884	2.207
0.600	4.500	1.013	106.565	1.656
0.750	4.500	1.014	106.660	0.938
0.900	4.500	1.015	106.717	0.052
1.100	4.500	1.020	107.228	-0.371
1.250	4.500	1.020	107.228	-0.371

Series 1, exit plane traverse number 12H25a:

Z	Y	U/UCL	U-FT/SEC	ALPHA
2.500	3.000	1.004	105.560	-0.166
2.500	0.075	0.825	86.742	10.133
2.500	0.085	0.844	88.724	9.599
2.500	0.101	0.849	89.319	9.164
2.500	0.113	0.858	90.238	8.821
2.500	0.140	0.869	91.373	8.279
2.500	0.168	0.882	92.783	7.700
2.500	0.201	0.890	93.640	7.319
2.500	0.254	0.906	95.313	7.094
2.500	0.304	0.921	96.815	6.827
2.500	0.353	0.929	97.728	6.477
2.500	0.401	0.941	98.977	5.790
2.500	0.455	0.954	100.373	5.689
2.500	0.506	0.961	101.065	5.287
2.500	0.607	0.969	101.942	4.814
2.500	0.710	0.975	102.531	3.564
2.500	0.807	0.968	101.813	3.303
2.500	1.009	0.974	102.430	2.801
2.500	1.220	0.975	102.549	2.586
2.500	1.417	0.974	102.431	2.170
2.500	1.611	0.977	102.738	1.842
2.500	3.000	0.996	104.758	0.166

Series 1, exit plane traverse number 12H25b:

Z	Y	U/UCL	U-FT/SEC	ALPHA
2.500	3.000	0.988	103.899	0.450
2.500	5.860	0.146	15.382	-4.364
2.500	5.811	0.206	21.635	-2.646
2.500	5.756	0.283	29.796	-3.313
2.500	5.660	0.417	43.879	-2.437
2.500	5.564	0.549	57.743	-2.594
2.500	5.465	0.672	70.640	-1.899
2.500	5.353	0.787	82.749	-2.485
2.500	5.260	0.882	92.728	-2.163
2.500	5.156	0.972	102.199	-1.530
2.500	5.055	1.010	106.176	-0.893
2.500	4.959	1.029	108.158	-0.417
2.500	4.859	1.030	108.300	-0.338
2.500	4.660	1.036	108.959	-0.642
2.500	4.460	1.038	109.106	-0.710
2.500	4.209	1.037	109.102	-0.687
2.500	4.009	1.038	109.143	-0.664
2.500	3.810	1.028	108.105	-0.372
2.500	3.615	1.025	107.813	-0.484
2.500	3.410	1.023	107.561	-0.677
2.500	3.216	1.024	107.641	-0.631
2.500	3.000	1.012	106.419	-0.450

Series 1, exit plane traverse number 12H25c:

Z	Y	U/UCL	U-FT/SEC	ALPHA
2.500	3.000	1.003	105.516	-0.166
2.500	1.611	0.985	103.568	1.511
2.500	1.800	0.987	103.767	1.286
2.500	2.000	0.995	104.628	0.971
2.500	2.200	0.995	104.612	0.938
2.500	2.400	0.992	104.331	0.389
2.500	2.600	0.995	104.668	0.188
2.500	2.800	0.998	104.968	0.089
2.500	3.000	1.003	105.516	-0.166
2.500	3.200	1.003	105.516	-0.166
2.500	3.400	1.008	105.951	-0.042
2.500	3.600	1.005	105.730	-0.143
2.500	3.800	1.008	105.974	-0.376
2.500	4.000	1.014	106.638	-0.073
2.500	4.200	1.014	106.622	0.016
2.500	4.400	1.015	106.722	-0.272
2.500	4.600	1.019	107.145	-0.060
2.500	4.800	1.022	107.508	0.141
2.500	5.000	1.022	107.520	0.075
2.500	5.200	0.934	98.221	-1.290
2.500	5.400	0.741	77.878	-1.963
2.500	3.000	0.997	104.802	0.166

Series 1, exit plane traverse number 12H13:

Z	Y	U/UCL	U-FT/SEC	ALPHA
1.250	3.000	1.003	105.443	-0.438
1.250	3.000	1.003	105.443	-0.438
1.250	1.000	0.992	104.284	2.520
1.250	1.200	0.989	103.985	2.499
1.250	1.400	0.986	103.648	1.558
1.250	1.600	0.990	104.109	1.255
1.250	1.800	0.993	104.447	1.054
1.250	2.000	1.000	105.119	0.722
1.250	2.200	0.999	105.018	0.587
1.250	2.400	1.000	105.156	0.085
1.250	2.600	1.000	105.113	-0.173
1.250	2.800	0.999	105.063	-0.229
1.250	3.000	1.001	105.229	-0.205
1.250	3.200	1.004	105.548	-0.426
1.250	3.600	1.004	105.548	-0.426
1.250	4.000	1.012	106.431	0.128
1.250	4.200	1.018	107.007	-0.067
1.250	4.400	1.018	107.032	-0.078
1.250	4.600	1.024	107.689	-0.305
1.250	4.800	1.005	105.732	-0.993
1.250	3.800	1.014	106.582	-0.038
1.250	3.000	1.001	105.254	-0.216

Series 1, tangential centerline traverse 10T00:

BETA	Q/Q1	Q-FT/SEC	ALPHA
0.000	1.000	117.258	0.000
10.000	0.967	113.338	0.000
20.000	0.941	110.340	0.000
30.000	0.898	105.230	0.000
40.000	0.893	104.711	0.000
45.000	0.893	104.711	0.000

Series 2, throat traverse number 21V05:

Z	Y	U/UCL	U-FT/SEC
1.800	0.500	0.778	91.796
0.020	0.500	0.277	32.691
0.025	0.500	0.407	47.960
0.030	0.500	0.449	52.908
0.035	0.500	0.467	55.119
0.045	0.500	0.498	58.748
0.055	0.500	0.513	60.560
0.070	0.500	0.538	63.442
0.090	0.500	0.560	66.023
0.125	0.500	0.597	70.375
0.175	0.500	0.629	74.197
0.225	0.500	0.648	76.446
0.300	0.500	0.677	79.914
0.400	0.500	0.697	82.247
0.600	0.500	0.715	84.335
0.800	0.500	0.734	86.525
1.000	0.500	0.754	88.950
1.200	0.500	0.769	90.681
1.400	0.500	0.767	90.459
1.800	0.500	0.786	92.734
1.600	0.500	0.785	92.600
1.800	0.500	0.786	92.734

Series 2, throat traverse number 21V15:

Z	Y	U/UCL	U-FT/SEC
1.800	1.500	1.009	118.977
0.015	1.500	0.431	50.873
0.020	1.500	0.488	57.596
0.025	1.500	0.506	59.664
0.035	1.500	0.526	62.000
0.045	1.500	0.553	65.212
0.060	1.500	0.580	68.393
0.080	1.500	0.596	70.277
0.100	1.500	0.616	72.720
0.150	1.500	0.661	77.964
0.200	1.500	0.688	81.212
0.250	1.500	0.708	83.539
0.350	1.500	0.729	86.003
0.500	1.500	0.783	92.382
0.650	1.500	0.831	98.073
0.800	1.500	0.866	102.201
1.000	1.500	0.911	107.463
1.200	1.500	0.939	110.806
1.400	1.500	0.946	111.650
1.600	1.500	0.984	116.110
1.800	1.500	1.002	118.218
1.800	1.500	1.002	118.218

Series 2, throat traverse number 21V25a:

Z	Y	U/UCL	U-FT/SEC
1.800	2.500	1.002	118.139
0.020	2.500	0.477	56.296
0.025	2.500	0.519	61.215
0.030	2.500	0.554	65.370
0.040	2.500	0.582	68.662
0.050	2.500	0.600	70.803
0.060	2.500	0.613	72.265
0.080	2.500	0.649	76.574
0.100	2.500	0.666	78.560
0.125	2.500	0.688	81.203
0.175	2.500	0.709	83.624
0.225	2.500	0.741	87.373
0.300	2.500	0.765	90.298
0.400	2.500	0.817	96.328
0.600	2.500	0.867	102.231
0.800	2.500	0.916	108.094
1.000	2.500	0.954	112.563
1.200	2.500	0.967	114.051
1.400	2.500	0.988	116.593
1.600	2.500	1.000	117.996
1.800	2.500	1.000	117.996
1.800	2.500	0.998	117.712

Series 2, throat traverse number 21V25b:

Z	Y	U/UCL	U-FT/SEC
1.872	2.500	1.000	117.960
1.972	2.500	1.001	118.031
2.072	2.500	1.001	118.031
2.172	2.500	1.002	118.171
2.272	2.500	1.002	118.242
2.372	2.500	1.001	118.101
2.500	2.500	1.002	118.242
2.600	2.500	0.999	117.821
2.700	2.500	0.998	117.751
2.800	2.500	0.996	117.473
2.900	2.500	0.997	117.612
3.000	2.500	0.999	117.821
3.100	2.500	0.997	117.612
3.200	0.0	0.999	117.821
3.200	2.500	0.999	117.821
3.200	2.500	0.999	117.821
3.200	2.500	0.999	117.821
3.200	2.500	0.999	117.821
3.400	2.500	0.998	117.681
2.500	2.500	0.999	117.891
2.500	2.500	0.999	117.891
2.500	2.500	0.999	117.891

Series 2, throat traverse number 21V25b:

Z	Y	U/UCL	U-FT/SEC
1.872	2.500	1.000	117.960
1.972	2.500	1.001	118.031
2.072	2.500	1.001	118.031
2.172	2.500	1.002	118.171
2.272	2.500	1.002	118.242
2.372	2.500	1.001	118.101
2.500	2.500	1.002	118.242
2.600	2.500	0.999	117.821
2.700	2.500	0.998	117.751
2.800	2.500	0.996	117.473
2.900	2.500	0.997	117.612
3.000	2.500	0.999	117.821
3.100	2.500	0.997	117.612
3.200	0.0	0.999	117.821
3.200	2.500	0.999	117.821
3.200	2.500	0.999	117.821
3.200	2.500	0.999	117.821
3.200	2.500	0.999	117.821
3.400	2.500	0.998	117.681
2.500	2.500	0.999	117.891
2.500	2.500	0.999	117.891
2.500	2.500	0.999	117.891

Series 2, throat traverse number 21V35:

Z	Y	U/UCL	U-FT/SEC
1.800	3.500	1.000	118.968
0.015	3.500	0.485	57.252
0.020	3.500	0.526	62.015
0.025	3.500	0.541	63.854
0.040	3.500	0.579	68.201
0.060	3.500	0.605	71.340
0.080	3.500	0.621	73.199
0.120	3.500	0.648	76.461
0.160	3.500	0.679	80.062
0.220	3.500	0.712	83.969
0.300	3.500	0.732	86.319
0.400	3.500	0.757	89.242
0.600	3.500	0.799	94.289
0.800	3.500	0.857	101.121
1.000	3.500	0.897	105.881
1.200	3.500	0.940	110.828
1.400	3.500	0.962	113.509
1.600	3.500	0.964	113.693
1.800	3.500	0.964	113.683
1.800	3.500	0.964	113.683
1.800	3.500	1.008	118.963
1.800	3.500	1.008	118.963

Series 2, throat traverse number 21V45:

Z	Y	U/UCL	U-FT/SEC
1.800	4.500	0.851	100.394
0.020	4.500	0.531	62.691
0.025	4.500	0.567	66.885
0.030	4.500	0.597	70.439
0.040	4.500	0.621	73.197
0.060	4.500	0.647	76.378
0.080	4.500	0.671	79.187
0.120	4.500	0.702	82.834
0.200	4.500	0.754	88.911
0.300	4.500	0.785	92.573
0.400	4.500	0.808	95.286
0.500	4.500	0.829	97.831
0.600	4.500	0.834	98.399
0.700	4.500	0.837	98.778
0.900	4.500	0.837	98.683
1.100	4.500	0.837	98.683
1.300	4.500	0.837	98.683
1.500	4.500	0.837	98.683
1.600	4.500	0.837	98.683
1.700	4.500	0.837	98.778
1.800	4.500	0.843	99.490
1.800	4.500	0.843	99.490

Series 2, throat traverse number 21H18A:

Z	Y	U/UCL	U-FT/SEC
1.800	2.500	1.005	118.542
1.800	0.020	0.397	46.814
1.800	0.030	0.457	53.955
1.800	0.040	0.529	62.400
1.800	0.050	0.544	64.151
1.800	0.070	0.587	69.298
1.800	0.090	0.589	69.426
1.800	0.120	0.623	73.481
1.800	0.150	0.641	75.575
1.800	0.200	0.675	79.582
1.800	0.300	0.732	86.326
1.800	0.500	0.792	93.417
1.800	1.000	0.920	108.580
1.800	1.500	0.979	115.430
1.800	2.500	0.994	117.309
1.800	2.500	0.994	117.309
1.800	2.500	0.994	117.309
1.800	2.500	0.994	117.309
1.800	2.500	0.994	117.309
1.800	2.500	0.994	117.309
1.800	2.500	0.994	117.309
1.800	2.500	0.994	117.309

Series 2, throat traverse number 21H18b:

Z	Y	U/UCL	U-FT/SEC
1.800	2.500	1.000	117.926
1.800	0.010	0.582	68.608
1.800	0.020	0.621	73.247
1.800	0.030	0.649	76.515
1.800	0.050	0.683	80.610
1.800	0.070	0.696	82.158
1.800	0.100	0.716	84.471
1.800	0.150	0.764	90.102
1.800	0.210	0.788	92.904
1.800	0.310	0.812	95.727
1.800	0.410	0.839	98.967
1.800	0.550	0.876	103.332
1.800	0.700	0.908	107.143
1.800	0.900	0.947	111.757
1.800	1.100	0.970	114.366
1.800	1.400	1.000	117.926
1.800	1.500	1.000	117.926
1.800	1.700	1.000	117.926
1.800	1.900	1.000	117.926
1.800	2.100	1.000	117.926
1.800	2.300	1.000	117.926
1.800	2.500	1.000	117.926

Series 2, throat traverse number 21H18c:

Z	Y	U/UCL	U-FT/SEC
1.800	2.500	0.994	117.253
1.800	0.386	0.782	92.271
1.800	0.500	0.822	96.915
1.800	0.600	0.848	100.050
1.800	0.700	0.870	102.679
1.800	0.900	0.922	108.720
1.800	1.100	0.968	114.170
1.800	1.300	0.989	116.700
1.800	1.500	1.005	118.598
1.800	1.700	1.007	118.813
1.800	2.500	1.011	119.229
1.800	4.800	0.751	88.552
1.800	4.700	0.788	92.952
1.800	4.600	0.825	97.292
1.800	4.500	0.847	99.945
1.800	4.300	0.891	105.115
1.800	4.100	0.938	110.666
1.800	3.900	0.981	115.682
1.800	3.700	1.006	118.669
1.800	3.500	1.008	118.958
1.800	3.000	1.008	118.958
1.800	2.500	1.005	118.598

Series 2, throat traverse number 21H25a:

Z	Y	U/UCL	U-FT/SEC
2.500	2.500	1.000	117.926
2.500	0.378	0.790	93.135
2.500	0.500	0.824	97.223
2.500	0.600	0.852	100.545
2.500	0.700	0.866	102.119
2.500	0.800	0.898	105.889
2.500	0.900	0.905	106.777
2.500	1.000	0.934	110.216
2.500	1.200	0.966	113.917
2.500	1.400	0.985	116.218
2.500	1.600	0.985	116.218
2.500	1.800	0.996	117.509
2.500	2.000	0.997	117.578
2.500	2.200	1.001	118.065
2.500	2.600	0.999	117.856
2.500	2.800	0.997	117.648
2.500	3.000	0.999	117.856
2.500	3.200	0.999	117.787
2.500	3.400	1.000	117.995
2.500	3.600	1.005	118.558
2.500	3.800	0.984	116.018
2.500	2.500	1.000	117.926

Series 2, throat traverse number 21H25b:

Z	Y	U/UCL	U-FT/SEC
2.500	2.500	0.994	117.230
2.500	4.800	0.739	87.140
2.500	4.700	0.790	93.240
2.500	4.600	0.821	96.853
2.500	4.500	0.845	99.701
2.500	4.400	0.857	101.082
2.500	4.300	0.880	103.840
2.500	4.200	0.907	106.980
2.500	4.100	0.949	111.995
2.500	4.000	0.969	114.246
2.500	3.900	0.978	115.423
2.500	3.800	0.998	117.712
2.500	3.600	1.007	118.834
2.500	3.400	1.007	118.763
2.500	3.200	1.006	118.692
2.500	3.000	1.007	118.763
2.500	2.800	1.006	118.692
2.500	2.700	1.006	118.622
2.500	2.600	1.006	118.622
2.500	2.500	1.006	118.622
2.500	2.500	1.006	118.622
2.500	2.500	1.006	118.622

Series 2, exit plane traverse number 22V20:

Z	Y	U/UCL	U-FT/SEC	ALPHA
1.500	2.000	1.041	115.901	-6.347
1.500	2.000	1.041	115.901	-6.347
0.015	2.000	0.632	70.399	21.666
0.020	2.000	0.651	72.541	21.721
0.030	2.000	0.711	79.174	20.307
0.040	2.000	0.751	83.688	19.260
0.050	2.000	0.767	85.454	18.786
0.070	2.000	0.791	88.041	18.114
0.090	2.000	0.809	90.140	16.843
0.120	2.000	0.831	92.579	15.639
0.150	2.000	0.847	94.311	14.360
0.200	2.000	0.862	95.965	12.868
0.300	2.000	0.896	99.839	9.534
0.400	2.000	0.924	102.888	7.149
0.500	2.000	0.944	105.179	5.507
0.600	2.000	0.957	106.527	4.069
0.700	2.000	0.972	108.251	2.018
0.800	2.000	0.986	109.770	0.784
0.900	2.000	1.012	112.752	-2.632
1.100	2.000	1.021	113.705	-3.825
1.300	2.000	1.035	115.234	-5.840
1.500	2.000	1.036	115.390	-5.992

Series 2, exit plane traverse number 22V30a:

Z	Y	U/UCL	U-FT/SEC	ALPHA
1.500	3.000	0.987	109.901	-8.272
0.010	3.000	0.607	67.611	24.970
0.015	3.000	0.644	71.696	24.311
0.020	3.000	0.681	75.790	23.709
0.030	3.000	0.722	80.368	22.688
0.040	3.000	0.755	84.129	22.558
0.060	3.000	0.788	87.763	21.419
0.080	3.000	0.806	89.786	20.033
0.100	3.000	0.830	92.481	19.484
0.130	3.000	0.838	93.279	17.505
0.170	3.000	0.863	96.143	16.056
0.210	3.000	0.873	97.206	14.257
0.250	3.000	0.881	98.168	12.539
0.300	3.000	0.890	99.172	11.175
0.400	3.000	0.908	101.138	8.731
0.500	3.000	0.930	103.562	6.383
0.600	3.000	0.930	103.531	4.577
0.700	3.000	0.949	105.679	2.115
0.800	3.000	0.959	106.829	0.644
0.900	3.000	0.963	107.245	-1.717
1.100	3.000	0.967	107.726	-4.401
1.500	3.000	0.986	109.852	-7.548

Series 2, exit plane traverse number 22V30b:

Z	Y	U/UCL	U-FT/SEC	ALPHA
2.500	3.000	1.000	111.374	-8.316
2.500	3.000	1.000	111.374	-8.316
2.500	3.000	1.000	111.374	-8.316
2.500	3.000	1.000	111.374	-8.316
1.950	3.000	1.000	111.423	-8.349
1.950	3.000	1.000	111.423	-8.349
1.950	3.000	1.000	111.423	-8.349
1.950	3.000	1.000	111.423	-8.349
1.650	3.000	0.990	110.266	-8.198
1.650	3.000	0.990	110.266	-8.198
1.650	3.000	0.990	110.266	-8.198
1.650	3.000	0.990	110.266	-8.198
1.250	3.000	0.965	107.460	-6.918
1.250	3.000	0.965	107.460	-6.918
1.250	3.000	0.965	107.460	-6.918
1.400	3.000	0.981	109.279	-7.823
1.400	3.000	0.981	109.279	-7.823
1.650	3.000	0.990	110.266	-8.198
1.650	3.000	0.990	110.266	-8.198
1.950	3.000	1.000	111.423	-8.349
1.950	3.000	1.000	111.423	-8.349
2.500	3.000	1.000	111.374	-8.316

Series 2, exit plane traverse number 22H13a:

Z	Y	U/UCL	U-FT/SEC	ALPHA
1.250	3.000	0.964	107.393	-6.900
1.250	3.000	0.963	107.252	-6.966
1.250	0.250	0.811	90.301	2.295
1.250	0.500	0.854	95.070	-0.246
1.250	1.000	0.940	104.738	-2.594
1.250	2.000	0.994	110.740	-6.240
1.250	3.000	0.962	107.181	-6.953
1.250	4.000	0.845	94.151	-6.729
1.250	5.000	0.602	67.037	-7.009
1.250	5.250	0.436	48.588	-6.243
1.250	3.000	0.964	107.383	-6.866
1.250	3.500	0.914	101.768	-7.215
1.250	4.500	0.795	88.492	-6.541
1.250	3.000	0.964	107.393	-6.900
1.250	3.000	0.964	107.393	-6.900
1.250	3.000	0.964	107.393	-6.900
1.250	3.000	0.964	107.393	-6.900
1.250	3.000	0.964	107.393	-6.900
1.250	3.000	0.964	107.393	-6.900
1.250	3.000	0.964	107.393	-6.900
1.250	3.000	0.964	107.393	-6.900
1.250	3.000	0.964	107.393	-6.900

Series 2, exit plane traverse number 22H13b:

Z	Y	U/UCL	U-FT/SEC	ALPHA
1.250	3.000	0.965	107.423	-0.202
1.250	3.000	0.965	107.423	-0.202
1.250	5.989	0.093	10.329	8.316
1.250	5.979	0.134	14.913	8.808
1.250	5.960	0.157	17.495	9.051
1.250	5.943	0.184	20.532	9.851
1.250	5.914	0.231	25.781	10.719
1.250	5.885	0.251	27.974	10.398
1.250	5.825	0.321	35.703	9.903
1.250	5.775	0.360	40.129	8.833
1.250	5.665	0.416	46.369	6.914
1.250	5.575	0.436	48.592	5.063
1.250	5.450	0.454	50.539	2.684
1.250	5.300	0.465	51.830	0.518
1.250	5.100	0.542	60.411	-0.242
1.250	4.900	0.665	74.113	0.468
1.250	4.700	0.760	84.678	1.543
1.250	4.500	0.804	89.525	1.664
1.250	4.300	0.827	92.052	1.658
1.250	4.100	0.841	93.666	1.604
1.250	3.600	0.903	100.584	1.405
1.250	3.000	0.964	107.364	0.202

Series 2, exit plane traverse number 22H13C:

Z	Y	U/UCL	U-FT/SEC	ALPHA
1.250	3.000	0.963	107.209	-0.110
1.250	0.025	0.666	74.153	2.768
1.250	0.025	0.666	74.153	2.768
1.250	0.035	0.726	80.815	3.695
1.250	0.045	0.734	81.743	3.598
1.250	0.060	0.774	86.242	3.893
1.250	0.080	0.794	88.382	3.765
1.250	0.100	0.804	89.507	3.792
1.250	0.150	0.822	91.520	3.940
1.250	0.200	0.835	92.986	3.580
1.250	0.300	0.852	94.910	3.629
1.250	0.400	0.869	96.798	3.638
1.250	0.600	0.902	100.423	2.869
1.250	0.800	0.936	104.246	2.689
1.250	1.000	0.961	107.056	2.037
1.250	1.400	1.001	111.500	1.408
1.250	1.800	1.008	112.259	1.171
1.250	2.200	1.010	112.502	1.187
1.250	2.600	1.007	112.200	1.119
1.250	2.800	0.989	110.118	0.956
1.250	3.000	0.966	107.577	0.110
1.250	3.000	0.966	107.577	0.110

Series 2, exit plane traverse number 22H25:

Z	Y	U/UCL	U-FT/SEC	ALPHA
2.500	3.000	0.999	111.292	-8.359
2.500	0.200	0.825	91.890	2.034
2.500	0.300	0.837	93.255	0.793
2.500	0.500	0.868	96.614	-0.586
2.500	0.700	0.909	101.200	-2.110
2.500	1.000	0.961	106.996	-3.210
2.500	1.400	0.994	110.729	-4.997
2.500	1.800	0.999	111.216	-6.477
2.500	2.200	1.008	112.239	-7.423
2.500	2.600	1.014	112.959	-7.984
2.500	3.000	1.003	111.707	-8.308
2.500	3.500	0.948	105.532	-9.008
2.500	4.000	0.863	96.166	-9.497
2.500	4.500	0.756	84.144	-9.131
2.500	5.000	0.523	58.282	-6.711
2.500	5.250	0.374	41.613	-4.770
2.500	3.000	1.000	111.374	-8.316
1.250	3.000	0.965	107.460	-6.918
1.450	3.000	0.981	109.279	-7.828
1.650	3.000	0.990	110.266	-8.198
1.950	3.000	1.000	111.423	-8.349
2.500	3.000	1.001	111.446	-8.241

Series 2, exit plane traverse number 20T00:

BETA	Q/Q1	Q-FT/SEC	ALPHA
0.000	1.000	117.961	0.000
10.000	0.977	115.248	0.000
20.000	0.964	113.714	0.000
30.000	0.945	111.473	0.500
40.000	0.941	111.001	5.300
45.000	0.941	111.001	8.300

APPENDIX D: UNCERTAINTY CALCULATIONS

$$\rho = \frac{P}{RT}$$

$$\frac{\partial \rho}{\partial P} = \frac{1}{RT}, \quad \frac{\partial \rho}{\partial T} = -\frac{P}{RT^2}$$

$$\frac{\delta \rho}{\rho} = \left[\left(\frac{\partial \rho}{\partial P} \frac{\delta P}{\rho} \right)^2 + \left(\frac{\partial \rho}{\partial T} \frac{\delta T}{\rho} \right)^2 \right]^{1/2}$$

$$= \left[\left(\frac{\delta P}{P} \right)^2 + \left(-\frac{\delta T}{T} \right)^2 \right]^{1/2}$$

$$P = 29.071 \pm 0.005$$

$$T = 75°F \pm 1°F$$

$$\frac{\delta \rho}{\rho} = \left[\left(\frac{0.005}{29.071} \right)^2 + \left(-\frac{1}{535} \right)^2 \right]^{1/2}$$

$$\frac{\delta \rho}{\rho} = \left[354.10^{-8} \right]^{1/2} = 18.8 \cdot 10^{-4}$$

$$\rho = 0.071 \pm 0.00013 \ \frac{lb_m}{ft^3}$$

Static pressure for performance measurements

0.10 reading + fluctuation accuracy

Reading ≈ 22" H_2O

Velocity measurement - Pitot tube

$$V = \left(\frac{2g_c \gamma \Delta h}{\rho}\right)^{1/2}$$

$$= (\text{constant} \quad \frac{\Delta h}{\rho})^{1/2}$$

$$\Delta h = 1.95 \pm 0.01$$

$$\rho = 0.071 \pm 0.00013$$

$$\frac{\partial V}{\partial \Delta h} = \frac{1}{2} \rho^{-1/2} \Delta h^{-1/2}$$

$$\frac{\partial V}{\partial \rho} = - \frac{1}{2} \Delta h^{1/2} \rho^{-3/2}$$

$$\frac{\Delta V}{V} = \left[\left(\frac{\partial V}{\partial (\Delta h)} \frac{\delta (\Delta h)}{V}\right)^2 + \left(\frac{\partial V}{\partial \rho} \frac{\partial \rho}{V}\right)^2\right]^{1/2}$$

$$\frac{\Delta V}{V} = \frac{1}{2}\left[\left(\frac{\delta (\Delta h)}{\Delta h}\right)^2 + \left(\frac{\delta \rho}{\rho}\right)^2\right]$$

$$= \frac{1}{2}\left[\left(\frac{0.01}{1.95}\right)^2 + (18.8 \cdot 10^{-4})^2\right]^{1/2} = .105 \cdot 10^{-2}$$

Effectiveness, Error:

$$\eta = \frac{C_p}{C_p'},$$

$$\ln \eta = \ln C_p - \ln C_p'$$

$$\frac{\delta \eta}{\eta} = \frac{\delta C_p}{C_p} - \frac{\delta C_p'}{C_p'}$$

But

$$\frac{\delta_\eta}{\eta} = \left[\left(\frac{\partial_\eta}{\partial C_p}\frac{\delta C_p}{\eta}\right)^2 + \left(\frac{\partial \eta}{\partial C_p}\frac{\partial C_p'^2}{\eta}\right)\right]^{1/2}$$

$$\frac{\partial \eta}{\partial C_p} = \frac{1}{C_p'}$$

$$\frac{\partial \eta}{\partial C_p'} = -\frac{C_p}{(C_p')^2}$$

$$\frac{\delta \eta}{\eta} = \left[\left(\frac{1}{C_p}^2\frac{\delta C_p}{C_p}\right)^2 + \left(-\frac{C_p}{(C_p')}\frac{\delta C_p'^2}{C_p}\right)^{1/2}\right]$$

$$= \left[\left(\frac{\delta C_p}{C_p}\right)^2 + \left(\frac{\delta C_p'^2}{C_p'}\right)\right]$$

$$\frac{\delta C_p'}{C_p'} = ?$$

$$C_p' = 1 - \frac{1}{AR^2} = 1 - \frac{1}{\left(\frac{z_2y_2}{z_1y_1}\right)^2} = 1 - \left(\frac{z_1y_1}{z_2y_2}\right)^2$$

$$= \frac{(z_2y_2)^2-(z_1y_1)^2}{(z_2y_2)^2}$$

$$\frac{\partial C_p'}{C_p'} = \left[\left(\frac{\partial C_p'}{\partial z_1}\frac{\delta z_1}{C_p'}\right)^2 + \left(\frac{\partial C_p'}{\partial y_1}\frac{\delta y_1}{C_p'}\right)^2 +\right.$$

$$\left. \cdot \left(\frac{\partial C_p'}{\partial z_2}\frac{\delta z_2}{C_p'}\right)^2 + \left(\frac{\partial C_p'}{\partial y_2}\frac{\delta y_2}{C_p'}\right)^2\right]^{1/2}$$

$$\frac{\partial C_p'}{\partial z_2} = -(x_1y_1)^2(-2x_2^{-3}y_2^{-2}); \quad \frac{\partial C_p'}{\partial y_2} = \frac{-(x_1y_1)^2}{-2x_2^2y_2^3}$$

$$\left(\frac{\partial C_p'}{C_p'}\right)^2 = \left[\left(\frac{-2z_1y_1^2}{(x_2y_2)^2}\frac{z_1}{z_1}\frac{\delta z_1}{C_p'}\right)^2 + \left(\frac{-2z_1^2y_1}{(z_2y_2)^2}\frac{\delta y_1 y_1}{C_p' y_1}\right)^2 + \left(\frac{-(z_1y_1)^2\,\delta z_2 z_2}{(z_2^3y_2^2)\,C_{p_1} z_2}\right) + \left(\frac{(z_1y_1)^2\,\delta y_2 y_2}{-z_2^2y_2^3\,C_p'\,y_2}\right)\right]$$

$$= \left(\frac{2}{\frac{(z_2y_2)^2-(z_1y_1)^2}{(z_1y_1)^2}}\right)^2\left[\left(\frac{\delta z_1}{z_1}\right)^2+\left(\frac{\delta y_1}{y_1}\right)^2+\left(\frac{\delta z_2}{z_2}\right)^2+\left(\frac{\delta y_2}{y_2}\right)^2\right]$$

$$\left(\frac{\delta C_p'}{C_p'}\right)^2 = \left[\frac{2}{\left(\frac{A_2}{A_1}\right)^2-1}\right]^2\left[\left(\frac{\delta z_1}{z_1}\right)^2+\left(\frac{\delta y_1}{y_1}\right)^2+\left(\frac{\delta z_2}{z_2}\right)^2+\left(\frac{\delta y_3}{y_2}\right)^2\right]$$

$$= \left(\frac{2}{1.44-1}\right)^2\left[\left(\frac{\delta z_1}{z_1}\right)^2+\left(\frac{\delta y_1}{y_1}\right)^2+\left(\frac{\delta z_2}{z_2}\right)^2+\left(\frac{\delta y_2}{y_2}\right)\right]$$

$z_1 = 4.991 \pm 0.003$

$y_1 = 4.992 \pm 0.003$

$z_2 = 5.002 \pm 0.005$

$y_2 = 6.015 \pm 0.005$

$$\frac{\delta C_p'}{C_p'} = .0016 = .16\%$$

Recall from page 262 that

$$\frac{\delta\eta}{\eta} = \left[\left(\frac{\partial\eta}{\partial C_p}\frac{\delta C_p}{\eta}\right)^2 + \left(\frac{\partial\eta}{\partial C_p'}\frac{\delta C_p'}{\eta}\right)^2\right]^{1/2}$$

and

$$\frac{\delta\eta}{\eta} = \left[\left(\frac{\delta C_p}{C_p}\right)^2 + \left(\frac{\delta C_p'}{C_p'}\right)^2\right]$$

$$\frac{\delta C_p'}{C_p'} = 15.53\cdot10^{-4} = 1.55\cdot10^{-3}$$

$$\frac{\delta C_p}{C_p} = 5.9\cdot10^{-3}$$

$$\frac{\delta\eta}{\eta} = \left[(5.9)^2 + (1.55)^2\right]^{1/2}\cdot10^{-3}$$

$$\frac{\delta\eta}{\eta} = [37.2]^{1/2}\cdot10^{-3} = 6.08\cdot10^{-3}$$

$$\simeq 0.6\%$$

APPENDIX E: MAJOR PROGRAM VARIABLES AND PROGRAM

CFMH (LL,MM)	two-dimensional array for barometer correction
TCM (LL)	a one-dimensional array of tabulated temperatures for barometer correction table
CCMH (MM)	one-dimensional array of barometer correction
CHWALA (II)	one-dimensional array of Standard static pressure readings on reference manometer
CHWALL (II,JJ)	a two-dimensional array of pressures on manometer bank being calibrated
ICALIB	control card answers question calibration data? yes = 1, no = 2
IDATA	control card answers question test data? yes = 1, no = 2
IWALLP	control card answers question wall static pressure? yes = 1, no = 2
IPTOT	control card answers question total pressure? yes = 1, no = 2
BMH	barometer reading
TBA	temperature near barometer
ATMT	atmospheric temperature in test room
ST	air stream temperature
HSTAT	dynamic pressure
RCLDUI	cold resistance of U
RCBLUI	cable resistance of U wire
RCLDVI	cold resistance of V sensor
RCBLVI	cable resistance of V wire
JCMAX	number of angle calibration
KCMAX	max number of vel in hot wire calibration

PHIUI (IC)	angle of U wire
CEBRUI (IC)	U sensor calibration
PHIVI (IC)	angle of V wire
CEBRVI (IC)	V sensor calibration voltage
HVEL (IC)	velocity head in calibration
KCMAX	maximum number of velocity point
RADCTR	radius of centerline
RADSUC	radius of suction wall
RADPRS	radius of pressure wall
WIDTH	width
HEIGHT	height
ARARTO	area ratio
IMAX	number of Z values
JMAX	number of R values
KMAX	number of X values
MMAX	number of times references data recorded
ZI (L)	Z coordinate (vertical)
RI (L)	R coordinate
THETAI (L)	X coordinate (or Beta)
EBARUI (L)	U sensor reading (mean)
EBARVI (L)	V sensor reading (mean)
ERMSUI (L)	U sensor turbulence reading
ERMSVI (L)	V sensor turbulence reading
ESUMI (L)	sum of U and V turbulence reading

EDIFFI (L)	difference of U and V turbulence reading
Z (I,J,K)	averaged Z coordinate
RAD (I,J,K)	averaged R coordinate
THETA (I,J,K)	averaged X coordinate (or Beta)
EBARU (I,J,K)	averaged U sensor
EBARV (I,J,K)	averaged V sensor
ERMSU (I,J,K)	averaged U turbulence
ERMSV (I,J,K)	averaged V turbulence
ESUM (I,J,K)	averaged sum of U and V turbulence
EDIFF (I,J,K)	averaged difference of U and V turbulence
RCLDU	cold resistance U sensor
RCBLU	cable resistance U sensor
RCLDV	cold resistance V sensor
RCBLV	cable resistance V sensor
ROVHT	overheat ratio
IMAX	number of Z values
JMAX	number of R values
KMAX	number of X values
TOL	tolerance on velocity
CK	k in "cosine law"
IWIRE	number of wires 1 or 2
RDELH	dynamic pressure
RSTAT	static pressure
TATM	atmospheric temperature

TSTAG	plenum temperature
HTOT	plenum pressure
BRD	barometer reading
TBR	temperature near barometer
ICALCG	control card if 1 another set of calibration data is read, if 2 does not read another set
IDFOLO	control card, if 1 goes to statement 14, if 2 goes to end

```
//C338B   JOB   'I4020,TIME=3,SIZE=128K',BLECHINGER
//STEP1  EXEC  WATFIV                                                    02
//GO.SYSIN  DD  *                                                        03
/JOB          I4020BLECHINGER,TIME=180,PAGES=40
      DIMENSION FPRIMU(15),XPONU(15), AEBSQU(15)
      DIMENSION UBAR(25),DPDU(25)
      DIMENSION  CFMH(20,5),TCM(20), CCMH(5), CHWALA(6),  CHWALL(6,24)
      DIMENSION  CEBRUI(3),  HVEL(3),   VELCAL(15), PVEL(15), ECALIB(15)
     1          ,CEB2KU(15)
      DIMENSION    ZI(3),     YI(3),    EBARU(3), ERMSU(3),
     1             Y(22,22), Z(22,22), EBAR(22,22),   ERMS(22,22)
      DIMENSION  ZA(22),   EBARA(22),     ERMSA(22),SWATM(10),
     1           ERMSSU(22), CAPPAU(22),  QSTURB(22),  TURB(22)
      DIMENSION  RDELH(10), RSTAT(10), TATM(10), TS(10), HTOT(10),
     1           BRD(10), TBR(10),PATM(10), SWMF(10),RSPRES(10),RHO(10),
     2          RVEL(10), PTOT(10)
      DIMENSION  HWALL(10,24),  HWALLA(24), PWALL(24)
C     REFERENCE VELOCITY,PLENUM CHAMBER PRESSURE,ETC IS CALCULATED  HERE
  100 FORMAT (10F8.3)
 3000 FORMAT (F12.4)
  141 FORMAT (3F8.3)
  101 FORMAT (5F8.3)
  102  FORMAT (6F8.3)
  105 FORMAT (7F8.3,16X,F8.3)
  107 FORMAT (4X,I4)
  108 FORMAT (8X,F8.3,16X,F8.3)
  109 FORMAT (10X,'CALIBRATION RUN')
  110 FORMAT (5X,'VOLTS',5X,'FT/SEC')
  111 FORMAT (2F10.5)
  112 FORMAT (5X,'HOT WIRE DESCRIPTION')
  113 FORMAT(5X,'RES.COLD',5X,'RES.CABLE',5X,'OVERHEAT',5X,'RES.HOT')
  114 FORMAT (4F15.4)
  115 FORMAT (I4)
  116 FORMAT (2I4)
```

```
  117 FORMAT (2F8.3,8X,F8.3,8X,F8.3)
  125 FORMAT (8X,'Z-IN',8X,'VEL-FT/SEC',7X,'TURB-(')
  118 FORMAT (3F15.5)
  121 FORMAT (12X,F15.4)
  120 FORMAT (10X,'THE Y CO-ORDINATE')
  334 FORMAT (I4)
 9001 FORMAT (I4)
C     SEMIPERMANENT DATA FOR BAROMETER AND INCLINED MANOMETER IS READ.
      READ (1,100) ((CFMH(LL,MM),LL=1,20),MM=1,5)
      READ (1,100) (TCM(LL),LL=1,20)
      MM=1
      READ (1,101) (CCMH(MM),MM=1,5)
      READ (1,102)  (CHWALA(II),II=1,6)
      READ (1,102)((CHWALL(II,JJ),II=1,6),JJ=1,24)
C      THE REFERENCE BAROMETRIC PRESSURE STREAM TEMPERATURE ETC ARE CAL
      READ (1,105) BMH,TBA,ATMT,ST,HSTAT,RCLDUI,RCBLUI,ROVHT
      CALL FIT2D (BMH,CMH,TBA,CCMH,CFMH,TCM)
      ATMP = (BMH-CMH-0.009)*0.4912
      ATMPF= ATMP*144.0
C     ATMP IS BAR.PRESSURE IN PSIA, ATMPF IS IN LBF/(FT*FT)
      SWATMC= ATMPF/(53.36*(ATMT+459.688))
      SWMFC= (ATMT-80.0)*(ATMT-100.0)*62.344/800.0
     1   +(ATMT-60.0)*(ATMT-100.0)*62.189/(-400.0)
     2   +(ATMT-60.0)*(ATMT-80.0)*61.996/800.0
      WRITE (3,3000) SWMFC
      PSTAT = ATMPF +( HSTAT/12.0)*(SWMFC-SWATMC)
      WRITE (3,3000) PSTAT
      DEN = PSTAT/ (53.36*(ST +459.668))
      WRITE (3,3000) DEN
C     HOT WIRE CHARACTERISTICS ARE READ AND CALCULATED
      RSENSU =RCLDUI-RCBLUI
      RSNOPU =ROVHT*RSENSU
      ROPU   =RCBLUI+RSNOPU
      RU= RSNOPU/((ROPU+40.0)*(ROPU+40.0)*(ROVHT-1.0))
      COEFEU =RSNOPU/((ROPU+40.0)*(ROPU+40.0)*(ROVHT-1.0))
C     READ  CALIBRATION DATA
      READ (1,107) KCMAX
```

```
      DO 10 K=1,KCMAX
      READ (1,108) (CEBRUI(L),HVEL(L),L=1,3)
      PVEL(K) =(HVEL(1)+HVEL(2)+HVEL(3))/3.0
      WRITE (3,3000) PVEL(K)
      VELCAL(K)= SQRT(2.0*32.174*(SWMFC-DEN)*PVEL(K)/(12.0*DEN))
      ECALIB(K) = (CEBRUI(1)+CEBRUI(2)+CEBRUI(3))/3.0
      CEB2KU(K) = ECALIB(K)*ECALIB(K)*COEFEU
   10 CONTINUE
      CALL XPN (VELCAL,CEB2KU,FPRIMU,XPONU,KCMAX,AEBSQU,COFAAU,
     1    COFBBU,COFCCU)
      WRITE (3,109)
      WRITE (3,110)
      DO 15 K=1,KCMAX
      WRITE (3,111) ECALIB(K),VELCAL(K)
   15 CONTINUE
      WRITE (3,112)
      WRITE (3,113)
      WRITE (3,114) RSENSU,RCBLUI,ROVHT,ROPU
C     NOW DATA FROM THE TEST IS READ IN.
      READ (1,115) IDATA
      GO TO (1000,2000),IDATA
 1000 READ (1,116) IMAX,JMAX
      DO 20 J=1,JMAX
      WRITE (3,120)
      DO 20 I=1,IMAX
      READ (1,117) (ZI(L),YI(L),EBARU(L),ERMSU(L),L=1,3)
      Y(I,J)= (YI(1)+YI(2)+YI(3))/3.0
      Z(I,J)= (ZI(1)+ZI(2)+ZI(3))/3.0
      EBAR(I,J)=(EBARU(1)+EBARU(2)+EBARU(3))/3.0
      ERMS(I,J)=(ERMSU(1)+ERMSU(2)+ERMSU(3))/3.0
   20 CONTINUE
      DO 50 J=1,JMAX
      WRITE (3,121) Y(1,J)
      WRITE (3,125)
      DO 50 II=1,IMAX
      DO 30 N=1,IMAX
      ZA(N)=Z(N,J)
```

```
      EBARA(N)=EBAR(N,J)
      ERMSA(N)=ERMS(N,J)
   30 CONTINUE
      DO 40 ITB=3,KCMAX
      IF (EBARA(II)-ECALIB(ITB))        42,42,40
   40 CONTINUE
   42 ETB0= ECALIB(ITB-2)
      ETB1= ECALIB(ITB-1)
      ETB2= ECALIB(ITB)
      UBAR(II)= (EBARA(II)-ETB1)*(EBARA(II)-ETB2)*VELCAL(ITB-2)/
     1     ((ETB0-ETB1)*(ETB0-ETB2))+(EBARA(II)-ETB0)* (EBARA(II)-ETB2)*
     2     VELCAL(ITB-1)/((ETB1-ETB0)*(ETB1-ETB2)) +(EBARA(II)-ETB0)*
     3     (EBARA(II)-ETB1)*VELCAL(ITB)/((ETB2-ETB0)*(ETB2-ETB1))
      DPDU(II) = COFBBU+2.0*COFCCU*UBAR(II)
      CAPPAU(II)= 0.5*DPDU(II)/(RU*EBARA(II))
      ERMSSU(II)=ERMSA(II)
      QSTURB(II)= SQRT(ERMSSU(II)/CAPPAU(II))
      TURB(II)  =(QSTURB(II)/UBAR(II))*100.0
      WRITE (3,118) ZA(II),UBAR(II),TURB(II)
   50 CONTINUE
      MMAX =3
      READ (1,333) (RDELH(M),RSTAT(M),TATM(M),TS(M),HTOT(M),
     1     BRD(M),TBR(M), M=1,MMAX)
  333 FORMAT (7F8.4)
      DO 830 M=1,MMAX
      TBA=TBR(M)
      BMH=BRD(M)
      CALL FIT2D (BMH,CMH,TBA,CCMH,CFMH,TCM)
      BRD(M)=BMH
      PATM(M)=(BRD(M)-CMH-0.009)*0.4912
      SWMF(M) =(TATM(M)-80.0)*(TATM(M)-100.0)*62.344/800.0
     1     +(TATM(M)-60.0)*(TATM(M)-100.0)*62.189/(-400.0)
     2     +(TATM(M)-60.0)*(TATM(M)-80.0)*61.996/800.0
      SWATM(M) =PATM(M)*144.0/(53.36*(TATM(M)+459.688))
      RSPRES(M)= PATM(M)*144.0+((RSTAT(M)/12.0)*(SWMF(M)-SWATM(M)))
      RHO(M)   =  RSPRES(M)/(53.36*(TS(M)+459.688))
      RVEL(M)  =  SQRT(2.0*32.174*(SWMF(M)-RHO(M)) *RDELH(M)/
     1    (12.0*RHO(M)))
```

```
      PTOT(M)  =  PATM(M) *144.0+((HTOT(M)/12.0) *(SWMF(M)-SWATM(M)))
C     RVEL IS THE REFERENCE VELOCITY                                  (FT/SEC
C     RSPRES IS THE REFERENCE STATIC PRESSURE FROM THE PITOT TUBE (PSFA)
C     RHO  IS THE REFERENCE DENSITY                                   LBM/FT3
  830 ARVELX=0.0
      SWATMX = 0.00
      ARSPRX=0.0
      APTOTX=0.0
      APATX=0.0
      ATATX=0.0
      ARHOX=0.0
      SWMFX = 0.000
      DO 840 I=1,MMAX
      SWATMX = SWATMX + SWATM(I)
      ARVELX= ARVELX+ RVEL(I)
      ARSPRX= RSPRES(I) +ARSPRX
      APTOTX= APTOTX + PTOT(I)
      APATX = APATX  + PATM(I)
      ATATX = ATATX  + TATM(I)
      ARHOX = ARHOX  + RHO(I)
      SWMFX = SWMFX + SWMF(I)
  840 CONTINUE
      AVSWAT = SWATMX/MMAX
      ARVEL = ARVELX/MMAX
      ARSPR = ARSPRX/MMAX
      APTOT = APTOTX/MMAX
      APATM = APATX /MMAX
      ARHO  = ARHOX /MMAX
      SWMFA= SWMFX/MMAX
      WRITE (3,841)
  841 FORMAT (10X,'REF-VEL',5X,'REF-PSTAT',5X,'REF-PT',5X,'BAR-PR',5X,
```

```
     1    'DENSITY')
          WRITE (3,842) ARVEL,ARSPR,        APTOT,APATM,ARHO
  842 FORMAT(5X,5F10.3)
 2000 READ (1,334) IWLPR
      GO TO (2001,9000),IWLPR
 2001 READ (1,930) KPMAX,JPMAX
C     THE SUBSECTION  CALCULATES  STATIC PRESSURES.
  930 FORMAT (2I4)
      READ (1,141) ((HWALL(KP,JP),KP=1,KPMAX),JP=1,JPMAX)
      DO 410 JP=1,JPMAX
      HWALLA(JP)=0.0
      DO 410 KP=1,KPMAX
      HWALLA(JP)=HWALLA(JP)+HWALL(KP,JP)
  410 CONTINUE
      DO 411 JP=1,JPMAX
      HWALLA(JP)=HWALLA(JP)/KPMAX
  411 CONTINUE
      DO 430 JP=1,JPMAX
      DO 428 IP=1,KPMAX
      IF (CHWALL(IP,JP)-HWALLA(JP)) 428,429,429
  428 CONTINUE
  429 HWALLA(JP) = CHWALA(IP-1)+(CHWALA(IP)-CHWALA(IP-1)*HWALLA(JP)-
     1    CHWALL(IP-1,JP))/(CHWALL(IP,JP)-CHWALL(IP-1,JP))
  430 CONTINUE
      DO 31 JP=1,JPMAX
      HWALLA(JP)=HWALLA(JP)-HWALLA(JPMAX)
      PWALL(JP) = SWMFA *HWALLA(JP)/12.0
   31 CONTINUE
C     PWALL IS THE WALL STATIC  PRESSURE IN LBF/FT**2
C     PS IS THE AVERAGE THROAT STATIC PRESSURE
      PSTATA=(HWALLA(1)+HWALLA(1)+HWALLA(3)+HWALLA(4)+HWALLA(5)+
     1    HWALLA(6)+HWALLA(7)+HWALLA(8))/8.0
      PSTATL=(HWALLA(1)+HWALLA(2)+HWALLA(3)+HWALLA(4))/4.0
      PSTATR=(HWALLA(5)+HWALLA(6)+HWALLA(7)+HWALLA(8))/4.0
      PS   = APATM*144.0+((PSTATA /12.0)*(SWMFA-AVSWAT))
      PSPRES=APATM*144.0+((PSTATL/12.0)*(SWMFA-AVSWAT))
      PSSUCT = APATM *144.0 + ((PSTATR/12.0)* (SWMFA-AVSWAT))
```

```
      WRITE (3,131)
  131 FORMAT (5X,'PS-AVG',10X,'PS-PRES',10X,'PS-SUCT')
      WRITE (3,132) PS,PSPRES,PSSUCT
  132 FORMAT (3F15.4)
      WRITE(3,133)
  133 FORMAT (4X,'WALL STATIC')
      DO 140 I =1,JPMAX
      WRITE (3,134) PWALL(I)
  134 FORMAT (F12.3)
  140 CONTINUE
 9000 READ (1,9001) KMORE
      GO TO (1000,9999),KMORE
 9999 STOP
      END
      SUBROUTINE FIT2D(X,Y,Z,XB,YB,ZB)
      DIMENSION  XB(5),YB(20,5),ZB(20),YST(3)
      DO 1 I=3,5
      IF (X-XB(I))2,2,1
    1 CONTINUE
    2 DO 3 J=3,20
      IF (Z-ZB(J))4,4,3
    3 CONTINUE
    4 X0=ZB(J-2)
      X1=ZB(J-1)
      X2=ZB(J)
      DO 5 K=1,3
      L= I+K
      Y0=YB(J-2,L-3)
      Y1=YB(J-1,L-3)
      Y2=YB(J,L-3)
    5 YST(K)=(Z-X1)*(Z-X2)*Y0/((X0-X1)*(X0-X2))
     1  + (Z-X2)*(Z-X0)*Y1/((X1-X2)*(X1-X0))
     2  + (Z-X0)*(Z-X1)*Y2/((X2-X0)*(X2-X1))
      X0=XB(I-2)
      X1=XB(I-1)
      X2=XB(I)
```

```
      Y=(X-X1)*(X-X2)*YST(1)/((X0-X1)*(X0-X2))
     1  +(X-X2)*(X-X0)*YST(2)/((X1-X2)*(X1-X0))
     2  +(X-X0)*(X-X1)*YST(3)/((X2-X0)*(X2-X1))
      RETURN
      END
      SUBROUTINE XPN(X,Y,DYDX,XPON,MMAX,YY,AA,BB,CC)
      DIMENSION X(15),Y(15),DYDX(15),XPON(15),B(3),A(9),YY(15)
      DO 1 I=1,3
      B(I)=0.0
    1  CONTINUE
      DO 2 J=1,9
      A(J)=0.0
    2 CONTINUE
      DO 3 M=1,MMAX
      B(1)=Y(M)+B(1)
      B(2)=Y(M)*X(M)+B(2)
      B(3)=Y(M)*X(M)*X(M)+B(3)
      A(2)=X(M)+A(2)
      A(3)=X(M)*X(M)+A(3)
      A(6)=X(M)*X(M)*X(M)+A(6)
      A(9)=X(M)*X(M)*X(M)*X(M)+A(9)
    3 CONTINUE
      A(1)=MMAX
      A(4)=A(2)
      A(5)=A(3)
      A(7)=A(3)
      A(8)=A(6)
      COFDET = A(1)*(A(5)*A(9)-A(6)*A(8))-A(4)*(A(2)*A(9)-A(3)*A(8))
     1  +A(7)*(A(2)*A(6)-A(3)*A(5))
      AA=((B(1)*(A(5)*A(9)-A(6)*A(8))-B(2)*(A(2)*
     1  A(9)-A(3)*A(8))+B(3)*(A(2)*A(6)-A(3)*A(5)))/COFDET)
      BB=((A(1)*(B(2)*A(9)-A(6)*B(3))-A(4)*(B(1)*
     1  A(9)-A(3)*B(3))+A(7)*(B(1)*A(6)-A(3)*B(2)))/COFDET)
      CC=  ((A(1)*(A(5)*B(3)-B(2)*A(8))-A(4)*(A(2)*
     1  B(3)-B(1)*A(8))+A(7)*(A(2)*B(2)-B(1)*A(5)))/COFDET)
```

```
      DO 4 M=1,MMAX
      YY(M)=AA+BB*X(M)+CC*X(M)*X(M)
      DYDX(M)=BB+2.0*CC*X(M)
    4 CONTINUE
      DO 5 M=2,MMAX
      XPON(M)= (X(M)*DYDX(M) -X(M-1)*DYDX(M-1))/(Y(M)-Y(M-1))
    5 CONTINUE
      RETURN
```

```
      DIMENSION CFMH(20,5),TCM(20),CCMH(5),CHWALA(6),CHWALL(6,24),
     1   PHIUI(3),PHIVI(3),CEBRUI(3),CEBRVI(3),HVELI(3),PHIU(6,15)
     2  ,PHIV(6,15),CEBARU(6,15),CEBARV(6,15),HVEL(6,15),
     3   CEB2KU(6,15),CEB2KV(6,15),VEL(6,15),XPONU(15),XPONV(15)
     4  ,VEL1(15),EB2KU1(15),EB2KV1(15),BUTHRY(15),BVTHRY(15),
     5   AU(15),BU(15),AV(15),BV(15),VEL2(15),ZI(3),RI(3),SINUPL(6)
      DIMENSION THETAI(3),A(9),B(3),EUE90P(6,15),EVE90P(6,15),
     1   EBARUI(3),EBARVI(3),ERMSUI(3),ERMSVI(3),ESUMI(3),SINVPL(6),
     2   EDIFFI(3),Z(22,5,2),RAD(22,5,2),THETA(22,5,2)
      DIMENSION EBARU(22,5,2),EBARV(22,5,2),ERMSSS(3),ESMDIF(3),
     1   ERMSUU(3),ERMSVV(3),ERMSSU(22,5,2),ERMSSV(22,5,2),ESUMS1
     2   (3),EDIFS1(3),EDIFFS(22,5,2),ESUMS(22,5,2),UBAR(22,5,2),
     3   VBAR(22,5,2),QSBAR(22,5,2),ALPHA(22,5,2),BETA(22,5,2),
     4   CKU2(22,5,2),CKV2(22,5,2),QSTURB(22,5,2),
     5   QTTURB(22,5,2),QSQTIN(22,5,2),RDELH(6)
      DIMENSION RSTAT(6)
     1   ,TATM(6),TS(6),HTOT(6),BRD(6),TBR(6),PATM(6),RSPRES(6),
     2   RHO(6),RVEL(6),PTOT(6),HWALL(6,24),HWALLA(24)
      DIMENSION PWALL(24),HTOTKP(5,2),PTOTKP(5,2),PSTATC(5,2),
     1   PSTATG(5,2),FPRIMU(6,15),FPRIMV(6,15),
     2   UVPHIP(6,15),VVPHIP(6,15),SINUP(6,15),SINVP(6,15)
      DIMENSION AEBSQU(15),AEBSQV(15)
  100 FORMAT (10F8.3)
  101 FORMAT (5F8.3)
  102 FORMAT (6F8.3)
  103 FORMAT (4I4)
  104 FORMAT (6F10.6)
  105 FORMAT (9F8.3)
  106 FORMAT (2F8.3)
  107 FORMAT (7F8.3)
  108 FORMAT (I4)
  109 FORMAT (3F8.3)
  110 FORMAT (7F8.3)
  111 FORMAT ('1',6X,'CALIBRATION DATA')
  112 FORMAT ('0',10X,'PHI-U',6X,'CEBAR-U',5X,'CEB2K-U',5X,
     1  'VELOCITY',4X,'CEB2K-V',5X,'CEBAR-V',6X,'PHI-V')
```

```
113 FORMAT (F16.4,F13.4,F12.5,F13.4,F11.5,2F12.4)
114 FORMAT (10X,'FP(U)',2X,'SR(UE2K/UE2K-P)',2X,'SR(SIN)',6X,
   1  'FP(V)',2X,'SR(VE2K/VE2K-P)',2X,'SR(SIN)')
115 FORMAT (F17.7,2F12.4,F12.7,2F12.4)
116 FORMAT ('0',10X,'AU',5X,'BU(THRY)',6X,'BU',3X,'U-(EB)(EB)K'
   1,3X,'VEL-90',3X,'V-(EB)(EB)K',5X,'BV',6X,'BV(THRY)',5X,'AV')
117 FORMAT (F15.4,8F11.4)
118 FORMAT (10X,'N(U)',7X,'N(V)')
119 FORMAT (F15.4,F11.4)
120 FORMAT (9X,'VEL2',5X,'BU(THRY)',3X,'BV(THRY)')
121 FORMAT (F15.4,2F11.4)
122 FORMAT (9X,'RAD=',F7.3,6X,'THETA=',F7.3)
123 FORMAT (11X,'Z',6X,'EBARU',5X,'ERMSSU',5X,'UBAR',8X,'EBARV'
   1  ,5X,'ERMSSV',5X,'VBAR',8X,'ESUMS',6X,'EDIFFS')
124 FORMAT (F15.3,8F11.5)
125 FORMAT (11X,'Z',5X,'QSBAR',6X,'QSTURB',5X,'QTTURB',5X,'QSQTIN'
   1  ,6X,'CKU2',7X,'CKV2',7X,'ALPHA',7X,'BETA')
126 FORMAT (7X,'REF-VEL',2X,'REF-ST-PRES',2X,'PTOT-PLEN',4X,
   1  'PATM',7X,'TATM',7X,'RHO')
127 FORMAT (F15.3,5F11.3)
128 FORMAT (6X,'HWALLA-1',5X,'-2',6X,'-3',6X,'-4',6X,'-5',6X,
   1  '-6',6X,'-7',6X,'-8',6X,'-9',5X,'-10',5X,'-11',5X,'-12')
129 FORMAT (7X,'PWALL-1',5X,'-2',6X,'-3',6X,'-4',6X,'-5',6X,
   1  '-6',6X,'-7',6X,'-8',6X,'-9',5X,'-10',5X,'-11',5X,'-12')
130 FORMAT (F15.3,11F8.3)
131 FORMAT (11X,'Z',9X,'HTOT-KP',5X,'PTOT-KP',4X,'PSTAT-GA')
132 FORMAT (F15.3,3F12.3)
133 FORMAT (7X,'XPONUL=',F7.4)
134 FORMAT (7X,'XPONUH=',F7.4)
135 FORMAT (7X,'XPONVL=',F7.4)
136 FORMAT (7X,'XPONVH=',F7.4)
137 FORMAT (7X,'CENTERLINE RADIUS        =',F6.3,'INCHES')
138 FORMAT (7X,'SUCTION WALL RADIUS      =',F6.3,'INCHES')
139 FORMAT (7X,'PRESSURE WALL RADIUS     =',F6.3,'INCHES')
140 FORMAT (7X,'PASSAGE WIDTH AT ENTR.   =',F6.3,'INCHES')
141 FORMAT (7X,'PASSAGE HEIGHT AT ENTR.  =',F6.3,'INCHES')
142 FORMAT (7X,'AREA RATIO(EXIT TO ENTR)=',F6.3)
```

```
143 FORMAT ('0',' COFAAU=',F10.7,6X,'COFAAV=',F10.7,
   1          /,' COFBBU=',F10.7,6X,'COFBBV=',F10.7,
   2          /,' COFCCU=',F10.7,6X,'COFCCV=',F10.7)
144 FORMAT ('0',4X,'SECOND ORDER LEAST SQUARES FIT',/,12X,'VALUES'
   1   ,'  FOR',/,6X,'U=(EB)(EB)K',2X,'V=(EB)(EB)K')
145 FORMAT(3X,'DUBIOUS VALUE')
146 FORMAT(8F8.4)
    READ (1,100) ((CFMH(LL,MM),LL=1,20),MM=1,5)
    READ (1,100) (TCM(LL),LL=1,20)
    MM=1
    READ (1,101) (CCMH(MM),MM=1,5)
    READ (1,102) (CHWALA(II),II=1,6)
    READ (1,102) ((CHWALL(II,JJ),II=1,6),JJ=1,24)
 17 READ (1,103) ICALIB,IDATA,IWALLP,IPTOT
    GO TO (1,1000),ICALIB
  1 READ (1,100) BMH,TBA,ATMT,ST,HSTAT,RCLDUI,RCBLUI,RCLDVI,
   1  RCBLVI,ROVHT
    RSENSU=RCLDUI-RCBLUI
    RSNOPU=ROVHT*RSENSU
    ROPU=RSNOPU+RCBLUI
    COEFEU=RSNOPU/((ROPU+40.0)*(ROPU+40.0)*(ROVHT-1.0))
    RSENSV=RCLDVI-RCBLVI
    RSNOPV=ROVHT*RSENSV
    ROPV=RSNOPV+RCBLVI
    COEFEV=RSNOPV/((ROPV+40.0)*(ROPV+40.0)*(ROVHT-1.0))
    READ(1,103) JCMAX,KCMAX
    DO 2 KC=1,KCMAX
    DO 2 JC=1,JCMAX
    IF(JC-2) 200,199,199
199 IF(CEBRUI(1)) 4000,201,200
200 READ (1,101) ( PHIUI(IC),CEBRUI(IC),PHIVI(IC),CEBRVI(IC),
   1  HVELI(IC), IC=1,3)
201 PHIU(JC,KC)= PHIUI(1)
    CEBARU(JC,KC)= (CEBRUI(1)+CEBRUI(2)+CEBRUI(3))/3.0
    PHIV(JC,KC)= PHIVI(1)
    CEBARV(JC,KC)= (CEBRVI(1)+CEBRVI(2)+CEBRVI(3))/3.0
    HVEL(JC,KC)= (HVELI(1)+HVELI(2)+HVELI(3))/3.0
```

```
2 CONTINUE
  DO 3 KC=1,KCMAX
  DO 3 JC=1,JCMAX
  CEB2KU(JC,KC)= CEBARU(JC,KC)*CEBARU(JC,KC)* COEFEU
  CEB2KV(JC,KC)= CEBARV(JC,KC)*CEBARV(JC,KC)* COEFEV
3 CONTINUE
  CALL FIT2D (BMH,CMH,TBA,CCMH,CFMH,TCM)
  ATMP = (BMH-CMH-0.009)*0.4912
  SWMF = (ATMT-80.0)*(ATMT-100.0)*62.344/800.0
 1  +(ATMT-60.0)*(ATMT-100.0)*62.189/(-400.0)
 2  +(ATMT-60.0)*(ATMT-80.0)*61.996/800.0
  SWATM= ATMP*144./(53.36*(ATMT+459.688))
  PSTAT= ATMP*144.+((HSTAT/12.)*(SWMF-SWATM))
  DEN  = PSTAT/(53.36*(ST+459.688))
  DO 4 KC=1,KCMAX
  DO 4 JC=1,JCMAX
  VEL(JC,KC)=SQRT(2.*32.174*(SWMF-DEN)*HVEL(JC,KC)/
 1  (12.*DEN))
4 CONTINUE
  CALL XPNKGS (VEL,CEB2KU,FPRIMU,XPONU,KCMAX,AEBSQU,
 1   COFAAU,COFBBU,COFCCU)
  XPUAVE =0.0
  DO 5  KC=2,5
  XPUAVE =XPONU(KC)+XPUAVE
5 CONTINUE
  XPONUL= 0.25*XPUAVE
  XPUAVE = 0.0
  DO 6  KC=6,KCMAX
  XPUAVE = XPONU(KC)+XPUAVE
6 CONTINUE
  XPONUH = XPUAVE/(KCMAX-5)
  CALL XPNKGS (VEL,CEB2KV,FPRIMV,XPONV,KCMAX,AEBSQV,
 1   COFAAV,COFBBV,COFCCV)
  XPVAVE =0.0
  DO 7  KC=2,5
  XPVAVE= XPONV(KC)+XPVAVE
7 CONTINUE
```

```
      XPONVL=0.25*XPVAVE
      XPVAVE=0.0
      DO 8  KC=6,KCMAX
      XPVAVE= XPONV(KC)+XPVAVE
    8 CONTINUE
      XPONVH = XPVAVE/(KCMAX-5)
      DO 9 KC=1,KCMAX
      VEL1(KC)= VEL(1,KC)
      EB2KU1(KC)= CEB2KU(1,KC)
      EB2KV1(KC)= CEB2KV(1,KC)
    9 CONTINUE
      GO TO 14
      CALL SLOPE (CEB2KU,PHIU,VEL1,UVPHIP,SINUP,BU,AU,JCMAX,KCMAX,
     1   EB2KU1)
      CALL SLOPE (CEB2KV,PHIV,VEL1,VVPHIP,SINVP,BV,AV,JCMAX,KCMAX,
     1   EB2KV1)
      WRITE (3,111)
      DO 500 KC=1,KCMAX
      BUTHRY(KC)=1.0 + BU(KC)
      BVTHRY(KC)=1.0 + BV(KC)
      WRITE (3,112)
      WRITE (3,113) (PHIU(JC,KC),CEBARU(JC,KC),CEB2KU(JC,KC),VEL
     1  (JC,KC),CEB2KV(JC,KC),CEBARV(JC,KC),PHIV(JC,KC),JC=1,JCMAX)
      WRITE (3,114)
      WRITE (3,115) (FPRIMU(JC,KC),UVPHIP(JC,KC),SINUP(JC,KC),
     1  FPRIMV(JC,KC),VVPHIP(JC,KC),SINVP(JC,KC),JC=1,JCMAX)
  500 CONTINUE
      WRITE (3,116)
      WRITE (3,117) (AU(KC),BUTHRY(KC),BU(KC),EB2KU1(KC),VEL1(KC)
     1  ,EB2KV1(KC),BV(KC),BVTHRY(KC),AV(KC),KC=1,KCMAX)
      WRITE (3,118)
      WRITE (3,119) (XPONU(KC),XPONV(KC),KC=1,KCMAX)
      WRITE (3,133) XPONUL
      WRITE (3,134) XPONUH
      WRITE (3,135) XPONVL
      WRITE (3,136) XPONVH
      WRITE (3,143) COFAAU,COFAAV,COFBBU,COFBBV,COFCCU,COFCCV
```

```
      WRITE (3,144)
      WRITE (3,119) (AEBSQU(KC),AEBSQV(KC),KC=1,KCMAX)
      GO TO (11,2000),IDATA
 1000 GO TO (10,2000),IDATA
   10 READ (1,103) KCMAX
      READ (1,104) (VEL1(KC),KC=1,KCMAX)
      READ (1,104) (EB2KV1(KC),KC=1,KCMAX)
      READ (1,104) (EB2KU1(KC),KC=1,KCMAX)
      READ (1,104) (BUTHRY(KC),KC=1,KCMAX)
      READ (1,104) (BVTHRY(KC),KC=1,KCMAX)
      READ (1,104) COFAAU,COFAAV,COFBBU,COFBBV,COFCCU,COFCCV
   11 LC=1
      DO 13 KC=1,KCMAX
      IF (BUTHRY(KC)-1.0)12,13,12
   12 BUTHRY(LC)= BUTHRY(KC)
      BVTHRY(LC)= BVTHRY(KC)
      VEL2(LC)= VEL1(KC)
      AU(LC)=AU(KC)
      AV(LC)=AV(KC)
      BU(LC)=BU(KC)
      BV(LC)=BV(KC)
      DO 1012 JC=1,JCMAX
      EUE90P(JC,LC)=UVPHIP(JC,KC)
      SINUPL(JC)=SINUP(JC,KC)
      EVE90P(JC,LC)=VVPHIP(JC,KC)
      SINVPL(JC)=SINVP(JC,KC)
 1012 CONTINUE
      LC=LC+1
   13 CONTINUE
      LCMAX=LC-1
   14 READ (1,104) RADCTR,RADSUC,RADPRS,WIDTH,HEIGHT,ARARTO
      READ (1,103) IMAX,JMAX,KMAX,MMAX
      DO 18  K=1,KMAX
      DO 18  J=1,JMAX
      DO 18  I=1,IMAX
      READ (1,105)  (ZI(L),RI(L),THETAI(L),EBARUI(L),EBARVI(L),
     1  ERMSUI(L),ERMSVI(L),ESUMI(L),EDIFFI(L),L=1,3)
```

```
      Z(I,J,K)= ZI(1)
      RAD(I,J,K)= RI(1)
      THETA(I,J,K)= THETAI(1)
      EBARU(I,J,K)= (EBARUI(1)+EBARUI(2)+EBARUI(3))/3.0
      EBARV(I,J,K)= (EBARVI(1)+EBARVI(2)+EBARVI(3))/3.0
      DO 15 L=1,3
      ESMDIF(L)= ESUMI(L)*ESUMI(L)- EDIFFI(L)*EDIFFI(L)
   15 CONTINUE
      ESMDFA=(ESMDIF(1)+ESMDIF(2)+ESMDIF(3))/3.0
      DO 16 L=1,3
      ERMSUU(L)= ERMSUI(L)*ERMSUI(L)
      ERMSVV(L)= ERMSVI(L)*ERMSVI(L)
      ESUMS1(L)= ESUMI(L)*ESUMI(L)
      EDIFS1(L)= EDIFFI(L)*EDIFFI(L)
   16 CONTINUE
      EDIFFS(I,J,K)=(EDIFS1(1)+EDIFS1(2)+EDIFS1(3))/3.0
      ESUMS(I,J,K)=ESMDFA+EDIFFS(I,J,K)
      ERMUAV=(ERMSUU(1)+ERMSUU(2)+ERMSUU(3))/3.0
      ERMVAV=(ERMSVV(1)+ERMSVV(2)+ERMSVV(3))/3.0
      SUMEAV=EDIFFS(I,J,K)+ESMDFA/2.0
      AVEEMS=SUMEAV-ERMVAV
      ERMSSU(I,J,K)=(AVEEMS+ERMUAV)/2.0
      ERMSSV(I,J,K)=SUMEAV-ERMSSU(I,J,K)
   18 CONTINUE
      READ (1,101) RCLDU,RCBLU,RCLDV,RCBLV,ROVHT
      READ (1,103) IMAX,JMAX,KMAX,KCMAX
      READ (1,106) TOL,CK
      READ (1,108) IWIRE
      RSENSU=RCLDU-RCBLU
      RSNOPU=ROVHT*RSENSU
      ROPU=RSNOPU + RCBLU
      RU= RSNOPU/((ROPU+40.0)*(ROPU+40.0)*(ROVHT-1.0))
      RSENSV=RCLDV-RCBLV
      RSNOPV=ROVHT*RSENSV
      ROPV=RSNOPV + RCBLV
      RV= RSNOPV/((ROPV+40.0)*(ROPV+40.0)*(ROVHT-1.0))
      DO 22 K=1,KMAX
      DO 22 J=1,JMAX
```

```
      DO 22 I=1,IMAX
      CALL EQVEL (EBARU,UBAR,EB2KU1,VEL1,RU,I,J,K,KCMAX,EB2KU)
      UBARS = UBAR(I,J,K)*UBAR(I,J,K)
      GO TO (1011,1010),IWIRE
 1010 CALL EQVEL (EBARV,VBAR,EB2KV1,VEL1,RV,I,J,K,KCMAX,EB2KV)
      VBARS = VBAR(I,J,K)*VBAR(I,J,K)
      QTOT= SQRT((UBARS+VBARS)/(1.0+CK*CK))
      SINA1=SQRT((UBARS/(QTOT*QTOT)-CK*CK)/(1.0-CK*CK))
      SINB1=SQRT(1.0-SINA1*SINA1)
      ITER=1
      QTOT1=QTOT
      QUTOT=0.0
      QVTOT=0.0
      IF (SINA1-SINB1) 1021,1021,1020
   19 CALL CAL2D (SINA2,EUEPER,QTOT,SINUPL,EUE90P,VEL2,JCMAX,LCMAX)
      CALL CAL2D (SINB2,EVEPER,QTOT,SINVPL,EVE90P,VEL2,JCMAX,LCMAX)
      PU90=EB2KU/EUEPER/EUEPER
      PV90=EB2KV/EVEPER/EVEPER
      QUTOT=-COFBBU/COFCCU/2.0-0.5*SQRT((COFBBU/COFCCU)*(COFBBU
     1    /COFCCU)-4.0*(COFAAU-PU90)/COFCCU)
      QVTOT=-COFBBV/COFCCV/2.0-0.5*SQRT((COFBBV/COFCCV)*(COFBBV
     1    /COFCCV)-4.0*(COFAAV-PV90)/COFCCV)
      QTOT=0.5*(QUTOT+QVTOT)
      IF(ABS(QTOT-QTOT1)-TOL) 21,21,20
   20 IF (5-ITER) 1018,1018,1019
 1018 WRITE (3,145)
 1019 ITER=ITER+1
      IF (SINA1-SINB1) 1021,1021,1020
 1020 CALL BFIT(QTOT,A2,VEL2,AV,LCMAX)
      CALL BFIT(QTOT,B2,VEL2,BV,LCMAX)
      PV90=COFAAV+COFBBV*QTOT+COFCCV*QTOT*QTOT
      SINB2=(SQRT(EB2KV/PV90)-A2)/B2
      SINB1=SINB2*SINB2
      SINA1=SQRT(1.0-SINB1*SINB1)
      SINA2=SQRT(SINA1)
      WRITE (3,108) ITER
```

```
      WRITE (3,110) SINA1,SINB1,SINA2,SINB2,QUTOT,QVTOT,QTOT
      QTOT1=QTOT
      GO TO 19
 1021 CALL BFIT(QTOT,A1,VEL2,AU,LCMAX)
      CALL BFIT(QTOT,B1,VEL2,BU,LCMAX)
      PU90=COFAAU+COFBBU*QTOT+COFCCU*QTOT*QTOT
      SINA2=(SQRT(EB2KU/PU90)-A1)/B1
      SINA1=SINA2*SINA2
      SINB1=SQRT(1.0-SINA1*SINA1)
      SINB2=SQRT(SINB1)
      WRITE (3,108) ITER
      WRITE (3,110) SINA1,SINB1,SINA2,SINB2,QUTOT,QVTOT,QTOT
      QTOT1=QTOT
      GO TO 19
   21 QSBAR(I,J,K)=QTOT
      CALL BFIT(QTOT,A1,VEL2,AU,LCMAX)
      CALL BFIT(QTOT,B1,VEL2,BU,LCMAX)
      CALL BFIT(QTOT,A2,VEL2,AV,LCMAX)
      CALL BFIT(QTOT,B2,VEL2,BV,LCMAX)
      ALPHA(I,J,K)=57.2958*ATAN(SINA1/SINB1)
      BETA(I,J,K)=90.0 - ALPHA(I,J,K)
      CKU2(I,J,K)= (1.0/SINB1/SINB1-1.0)*(((1.0-B1)/
     1       SINA2 +B1)**4-1.0)
C     THE FIRST BRACKETED TERM IN THE PREVIOUS EQUATION IS TANGENT
C     SQUARED ALPHA. SINB1 IS USED BECAUSE IT'S RELATIONSHIP WITH
C     TANGENT SQUARED ALPHA IS DIRECT,WHEREAS SINA1 IS NOT.
      CKV2(I,J,K)= (1.0/SINA1/SINA1-1.0)*(((1.0-B2)/
     1       SINB2 +B2)**4-1.0)
      DPDU = COFBBU + 2.0*COFCCU*UBAR(I,J,K)
      CAPPAU = 0.5*DPDU/(RU*EBARU(I,J,K))
      DPDV = COFBBV + 2.0*COFCCV*VBAR(I,J,K)
      CAPPAV = 0.5*DPDV/(RV*EBARV(I,J,K))
      COEFAU = 1.0 -(1.0-CKU2(I,J,K))*COS(ALPHA(I,J,K)/57.2958)
     1  *COS(ALPHA(I,J,K)/57.2958)
      COEFAV = 1.0 -(1.0-CKV2(I,J,K))*COS(BETA(I,J,K)/57.2958)
     1  *COS(BETA(I,J,K)/57.2958)
      GAMMAU = CAPPAU/SQRT(COEFAU)
```

```
      GAMMAV = CAPPAV/SQRT(COEFAV)
      COEFCU = (1.0+CKU2(I,J,K))*COS(ALPHA(I,J,K)
     1  /57.2958)*COS(BETA(I,J,K)/57.2958)
      COEFCV = (1.0+CKV2(I,J,K))*COS(ALPHA(I,J,K)
     1  /57.2958)*COS(BETA(I,J,K)/57.2958)
      B(1)= ERMSSU(I,J,K)/(GAMMAU*GAMMAU)
      B(2)= ERMSSV(I,J,K)/(GAMMAV*GAMMAV)
      B(3)= (ESUMS(I,J,K)-EDIFFS(I,J,K))/(4.0*GAMMAU*GAMMAV)
      A(1)= COEFAU*COEFAU
      A(2)= COEFCU*COEFCU
      A(3)= 2.0*COEFAU*COEFCU
      A(4)= COEFAV*COEFAV
      A(5)= COEFCV*COEFCV
      A(6)= -2.0*COEFAV*COEFCV
      A(7)= COEFAU*COEFAV
      A(8)= -COEFCU*COEFCV
      A(9)= -(COEFAU*COEFCV-COEFAV*COEFCU)
      COFDET = A(1)*(A(5)*A(9)-A(6)*A(8))-A(4)*(A(2)*A(9)-A(3)*A(8))
     1  +A(7)*(A(2)*A(6)-A(3)*A(5))
      QSTURB(I,J,K)= SQRT((B(1)*(A(5)*A(9)-A(6)*A(8))-B(2)*(A(2)*
     1  A(9)-A(3)*A(8))+B(3)*(A(2)*A(6)-A(3)*A(5)))/COFDET)
      QTTURB(I,J,K)= SQRT((A(1)*(B(2)*A(9)-A(6)*B(3))-A(4)*(B(1)*
     1  A(9)-A(3)*B(3))+A(7)*(B(1)*A(6)-A(3)*B(2)))/COFDET)
      QSQTIN(I,J,K) =  ((A(1)*(A(5)*B(3)-B(2)*A(8))-A(4)*(A(2)*
     1  B(3)-B(1)*A(8))+A(7)*(A(2)*B(2)-B(1)*A(5)))/COFDET)
      GO TO 22
1011  QSBAR(I,J,K)=UBAR(I,J,K)
      DPDU = COFBBU + 2.0*COFCCU*UBAR(I,J,K)
      CAPPAU = 0.5*DPDU/(RU*EBARU(I,J,K))
      QSTURB(I,J,K)=SQRT(ERMSSU(I,J,K))/CAPPAU
      QTTURB(I,J,K)=0.0
      QSQTIN(I,J,K)=0.0
      ALPHA(I,J,K)=90.0
      VBAR(I,J,K)=UBAR(I,J,K)
      BETA(I,J,K)=90.0
      CKU2(I,J,K)=0.0
      CKV2(I,J,K)=0.0
```

```
   42 QSBAR(I,J,K) = QTOT
      ALPHA(I,J,K)= 57.2958*ATAN(SINA1/SINB1)
      BETA(I,J,K) = 90.0 -ALPHA(I,J,K)
      CKU2(I,J,K) = 0.000
      CKV2(I,J,K) = 0.000
      QSTURB(I,J,K) = 0.000
      QSQTIN(I,J,K) = 0.000
   22 CONTINUE
      READ(1,107) (RDELH(M),RSTAT(M),TATM(M),TS(M),HTOT(M),
     1  BRD(M),TBR(M),M=1,MMAX)
      READ(1,108) IDFOLO
 1111 DO 23 M=1,MMAX
      TBA=TBR(M)
      BMH=BRD(M)
      CALL FIT2D (BMH,CMH,TBA,CCMH,CFMH,TCM)
      BRD(M)=BMH
      PATM(M)=(BRD(M)-CMH-0.009)*0.4912
      SWMF= (TATM(M)-80.0)*(TATM(M)-100.0)*62.344/800.0
     1  +(TATM(M)-60.0)*(TATM(M)-100.0)*62.189/(-400.0)
     2  +(TATM(M)-60.0)*(TATM(M)-80.0)*61.996/800.0
      SWATM= PATM(M)*144.0/(53.36*(TATM(M)+459.688))
      RSPRES(M)= PATM(M)*144.0 + ((RSTAT(M)/12.0)*(SWMF-SWATM))
      RHO(M)= RSPRES(M)/(53.36*(TS(M)+459.688))
      RVEL(M)= SQRT(2.*32.174*(SWMF-RHO(M))*RDELH(M)/(12.*RHO(M)))
      PTOT(M)= PATM(M)*144.0 + ((HTOT(M)/12.)*(SWMF-SWATM))
   23 CONTINUE
      IF(PTOT-3) 24,33,33
   24 WRITE (3,120)
      WRITE(3,121) (VEL2(LC),BUTHRY(LC),BVTHRY(LC), LC=1,LCMAX)
      WRITE(3,137) RADCTR
      WRITE (3,138) RADSUC
      WRITE (3,139) RADPRS
      WRITE (3,140) WIDTH
      WRITE (3,141) HEIGHT
      WRITE (3,142) ARARTO
      DO 501 K=1,KMAX
      DO 501 J=1,JMAX
```

```
      WRITE (3,122) RAD(1,J,K),THETA(1,J,K)
      WRITE (3,123)
      WRITE (3,124) (Z(I,J,K),EBARU(I,J,K),ERMSSU(I,J,K),UBAR(I,J,K)
     1  ,EBARV(I,J,K),ERMSSV(I,J,K),VBAR(I,J,K),ESUMS(I,J,K),
     2  EDIFFS(I,J,K),I=1,IMAX)
  501 CONTINUE
      DO 502 K=1,KMAX
      DO 502 J=1,JMAX
      WRITE (3,122) RAD(1,J,K),THETA(1,J,K)
      WRITE (3,125)
      WRITE (3,124) (Z(I,J,K),QSBAR(I,J,K),QSTURB(I,J,K),QTTURB
     1  (I,J,K),QSQTIN(I,J,K),CKU2(I,J,K),CKV2(I,J,K),ALPHA(I,J,K)
     2  ,BETA(I,J,K),I=1,IMAX)
      WRITE(2,146) (Z(I,J,K),RAD(I,J,K),THETA(I,J,K),QSBAR(I,J,K)
     1,QSTURB(I,J,K),QTTURB(I,J,K),QSQTIN(I,J,K),ALPHA(I,J,K)
     2,I=1,IMAX)
  502 CONTINUE
      WRITE (3,126)
      WRITE (3,127) (RVEL(M),RSPRES(M),PTOT(M),PATM(M),TATM(M),
     1  RHO(M),M=1,MMAX)
      GO TO (14,3000),IDFOLO
 2000 GO TO (25,3000),IWALLP
   25 READ (1,108) KKMAX
      GO TO (2223,2222),IDATA
 2222 READ (1,106) SWMF
 2223 READ (1,109)((HWALL(KK,JJ),KK=1,KKMAX),JJ=1,24)
      DO 26 JJ=1,24
      HWALLA(JJ)=0.0
      DO 26 KK=1,KKMAX
      HWALLA(JJ)=HWALLA(JJ)+HWALL(KK,JJ)
   26 CONTINUE
      DO 27 JJ=1,24
      HWALLA(JJ)=HWALLA(JJ)/KKMAX
   27 CONTINUE
      DO 30 JJ=1,24
      DO 28 II=1,6
      IF (CHWALL(II,JJ)-HWALLA(JJ)) 28,29,29
```

```
   28 CONTINUE
   29 HWALLA(JJ)= CHWALA(II-1)+ (CHWALA(II)-CHWALA(II-1))*(HWALLA
     1  (JJ)-CHWALL(II-1,JJ))/(CHWALL(II,JJ)-CHWALL(II-1,JJ))
   30 CONTINUE
      DO 31 JJ=1,24
      HWALLA(JJ)=HWALLA(JJ)-HWALLA(24)
      PWALL(JJ)= SWMF* HWALLA(JJ)/12.0
   31 CONTINUE
      WRITE (3,128)
      WRITE (3,130)(HWALLA(JJ),JJ=1,24)
      WRITE (3,129)
      WRITE (3,130)(PWALL(JJ),JJ=1,24)
 3000 GO TO (32,4000),IPTOT
   32 READ (1,103) IMAX,JMAX,KMAX,MMAX
      READ (1,107) (RDELH(M),RSTAT(M),TATM(M),TS(M),HTOT(M),
     1  BRD(M),TBR(M),M=1,MMAX)
      IPTOT=3
      GO TO 1111
   33 GO TO (35,34),IDATA
   34 READ (1,101)(((QSBAR(IMAX,J,K),J=1,JMAX),K=1,KMAX)
      READ (1,109) ((Z(IMAX,J,K),RAD(IMAX,J,K),THETA (IMAX,J,K),
     1  J=1,JMAX),K=1,KMAX)
      READ (1,104) RADCTR,RADSUC,RADPRS,WIDTH,HEIGHT,ARARTO
   35 READ (1,101)((HTOTKP(J,K),J=1,JMAX),K=1,KMAX)
      M=1
      DO 37 K=1,KMAX
      DO 36 J=1,JMAX
      PTOTKP(J,K)= (PATM(M)+PATM(M+1)+PATM(M+2))*48.0
     1  + (HTOTKP(J,K)/12.0)*(SWMF-SATM)
      PSTATC(J,K)= PTOTKP(J,K)- 0.5*(RHO(M)+RHO(M+1)
     1  +RHO(M+2))*QSBAR(IMAX,J,K)*QSBAR(IMAX,J,K)/(3.0*32.174)
      PSTATG(J,K)= PSTATC(J,K)-(PATM(M)+PATM(M+1)+
     1  PATM(M+2))/3.0
   36 CONTINUE
      M= M+3
   37 CONTINUE
      WRITE (3,137) RADCTR
```

```
      WRITE (3,138) RADSUC
      WRITE (3,139) RADPRS
      WRITE (3,140) WIDTH
      WRITE (3,141) HEIGHT
      WRITE (3,142) ARARTO
      DO 503 K=1,KMAX
      DO 503 J=1,JMAX
      WRITE (3,122) RAD(IMAX,J,K),THETA(IMAX,J,K)
      WRITE (3,131)
      WRITE (3,132) Z(IMAX,J,K),HTOTKP(J,K),PTOTKP(J,K)
     1  ,PSTATG(J,K)
  503 CONTINUE
 4000 READ(1,108) ICALCG
      GO TO (17,5000), ICALCG
 5000 STOP
      END
      SUBROUTINE FIT1(X,Y,XB,YB,M,NMAX,KMAX)
      DIMENSION  X(6,15),Y(6,15),XB(15),YB(15)
      DO 3 N=1,NMAX
      DO 1 K=3,KMAX
      IF (X(N,M)-XB(K))2,2,1
    1 CONTINUE
    2 X0=XB(K-2)
      X1=XB(K-1)
      X2=XB(K)
    3 Y(N,M)=(X(N,M)-X1)*(X(N,M)-X2)*YB(K-2)/((X0-X1)*(X0-X2))
     1  +(X(N,M)-X2)*(X(N,M)-X0)*YB(K-1)/((X1-X2)*(X1-X0))
     2  +(X(N,M)-X0)*(X(N,M)-X1)*YB(K)/((X2-X0)*(X2-X1))
      RETURN
      END
      SUBROUTINE FIT2D(X,Y,Z,XB,YB,ZB)
      DIMENSION  XB(5),YB(20,5),ZB(20),YST(3)
      DO 1 I=3,5
      IF (X-XB(I))2,2,1
    1 CONTINUE
    2 DO 3 J=3,20
      IF (Z-ZB(J))4,4,3
```

```
3 CONTINUE
4 X0=ZB(J-2)
  X1=ZB(J-1)
  X2=ZB(J)
  DO 5 K=1,3
  L= I+K
  Y0=YB(J-2,L-3)
  Y1=YB(J-1,L-3)
  Y2=YB(J,L-3)
5 YST(K)=(Z-X1)*(Z-X2)*Y0/((X0-X1)*(X0-X2))
 1  + (Z-X2)*(Z-X0)*Y1/((X1-X2)*(X1-X0))
 2  + (Z-X0)*(Z-X1)*Y2/((X2-X0)*(X2-X1))
  X0=XB(I-2)
  X1=XB(I-1)
  X2=XB(I)
  Y=(X-X1)*(X-X2)*YST(1)/((X0-X1)*(X0-X2))
 1  +(X-X2)*(X-X0)*YST(2)/((X1-X2)*(X1-X0))
 2  +(X-X0)*(X-X1)*YST(3)/((X2-X0)*(X2-X1))
  RETURN
  END
  SUBROUTINE CAL2D(X,Y,Z,XB,YB,ZB,IMAX,JMAX)
  DIMENSION XB(6),YB(6,15),ZB(15),YST(3)
  DO 1 I=3,IMAX
  IF (X-XB(IMAX-I+1))2,2,1
1 CONTINUE
2 DO 3 J=3,JMAX
  IF (Z-ZB(J))4,4,3
3 CONTINUE
4 X0=ZB(J-2)
  X1=ZB(J-1)
  X2=ZB(J)
  DO 5 K=1,3
  L=(IMAX-I+1)+K
  Y0=YB(L-1,J-2)
  Y1=YB(L-1,J-1)
  Y2=YB(L-1,J)
5 YST(K)=(Z-X1)*(Z-X2)*Y0/((X0-X1)*(X0-X2))
```

```
     1   + (Z-X2)*(Z-X0)*Y1/((X1-X2)*(X1-X0))
     2   + (Z-X0)*(Z-X1)*Y2/((X2-X0)*(X2-X1))
         X0=XB(IMAX-I+1)
         X1=XB(IMAX-I+2)
         X2=XB(IMAX-I+3)
         Y=(X-X1)*(X-X2)*YST(1)/((X0-X1)*(X0-X2))
     1   +(X-X2)*(X-X0)*YST(2)/((X1-X2)*(X1-X0))
     2   +(X-X0)*(X-X1)*YST(3)/((X2-X0)*(X2-X1))
         RETURN
         END
         SUBROUTINE XPNKGS (X,Y,DYDX,XPON, MMAX,YY,AA,BB,CC)
         DIMENSION  X(6,15),Y(6,15),DYDX(6,15),XPON(15),B(3),A(9),YY(15)
         DO 1 I=1,3
         B(I)=0.0
     1 CONTINUE
         DO 2 J=1,9
         A(J)=0.0
     2 CONTINUE
         DO 3 M=1,MMAX
         B(1)=Y(1,M)+B(1)
         B(2)=Y(1,M)*X(1,M)+B(2)
         B(3)=Y(1,M)*X(1,M)*X(1,M)+B(3)
         A(2)=X(1,M)+A(2)
         A(3)=X(1,M)*X(1,M)+A(3)
         A(6)=X(1,M)*X(1,M)*X(1,M)+A(6)
         A(9)=X(1,M)*X(1,M)*X(1,M)*X(1,M)+A(9)
     3 CONTINUE
         A(1)=MMAX
         A(4)=A(2)
         A(5)=A(3)
         A(7)=A(3)
         A(8)=A(6)
         COFDET = A(1)*(A(5)*A(9)-A(6)*A(8))-A(4)*(A(2)*A(9)-A(3)*A(8))
     1   +A(7)*(A(2)*A(6)-A(3)*A(5))
         AA=((B(1)*(A(5)*A(9)-A(6)*A(8))-B(2)*(A(2)*
     1   A(9)-A(3)*A(8))+B(3)*(A(2)*A(6)-A(3)*A(5)))/COFDET)
```

```
      BB=((A(1)*(B(2)*A(9)-A(6)*B(3))-A(4)*(B(1)*
     1  A(9)-A(3)*B(3))+A(7)*(B(1)*A(6)-A(3)*B(2)))/COFDET)
      CC=  ((A(1)*(A(5)*B(3)-B(2)*A(8))-A(4)*(A(2)*
     1  B(3)-B(1)*A(8))+A(7)*(A(2)*B(2)-B(1)*A(5)))/COFDET)
      DO 4 M=1,MMAX
      YY(M) =AA+BB*X(1,M)+CC*X(1,M)*X(1,M)
      DYDX(1,M)=BB+2.0*CC*X(1,M)
      DO 4 K=2,6
      DYDX(K,M)=0.0
    4 CONTINUE
      DO 5 M=2,MMAX
      XPON(M)=(X(1,M)*DYDX(1,M)-X(1,M-1)*DYDX(1,M-1))/
     1   (Y(1,M)-Y(1,M-1))
    5 CONTINUE
      RETURN
      END
      SUBROUTINE SLOPE (X,Y,Z,P1,P2,B,A,IMAX,JMAX,EBSQDK)
      DIMENSION  X(6,15),Y(6,15),Z(15),P1(6,15),P2(6,15)
     1  ,B(15),VBAR(6,15),A(15),EBSQDK(15)
      DO 6 J=1,JMAX
      IF (Y(2,J)) 4,4,1
    1 DO 2 I=1,IMAX
      P1(I,J)= SQRT(X(I,J)/EBSQDK(J))
      P2(I,J)= SQRT(SIN(Y(I,J)/57.2958))
    2 CONTINUE
      P1AVE=0.0
      P2AVE=0.0
      P1P2 =0.0
      P2P2 =0.0
      DO 3 I=4,IMAX
      P1AVE = P1AVE + P1(I,J)
      P2AVE = P2AVE + P2(I,J)
      P1P2  = P1P2 + P1(I,J)*P2(I,J)
      P2P2  = P2P2 + P2(I,J)*P2(I,J)
    3 CONTINUE
      P1AVE = P1AVE/(IMAX-3)
      P2AVE = P2AVE/(IMAX-3)
```

```
      P1P2  = P1P2/(IMAX-3)
      P2P2  = P2P2/(IMAX-3)
      B(J)=(P1AVE*P2AVE-P1P2)/(P2AVE*P2AVE-P2P2)
      A(J)= P1AVE-B(J)*P2AVE
      GO TO 6
    4 B(J)=0.0
      A(J)=0.0
      DO 5 I=1,IMAX
      P1(I,J)=0.0
      P2(I,J)=0.0
    5 CONTINUE
    6 CONTINUE
      RETURN
      END
      SUBROUTINE LSTSQR (X,Y,A,B)
      DIMENSION X(3),Y(3)
      XB= (X(1)+X(2)+X(3))/3.0
      YB= (Y(1)+Y(2)+Y(3))/3.0
      XY= (X(1)*Y(1)+X(2)*Y(2)+X(3)*Y(3))/3.0
      XX= (X(1)*X(1)+X(2)*X(2)+X(3)*X(3))/3.0
      IF (XB*XB-XX) 1,2,1
    1 B=(XB*YB-XY)/(XB*XB-XX)
      A= YB-B*XB
      GO TO 3
    2 B=0.0
      A=YB
    3 CONTINUE
      RETURN
      END
      SUBROUTINE EQVEL (X,Y,XB,YB,A,L,M,N,KMAX,X2A)
      DIMENSION  X(22,5,2),Y(22,5,2),XB(15),YB(15)
      X2A=X(L,M,N)*X(L,M,N)*A
      DO 1 K=3,KMAX
      IF (X2A-XB(K))2,2,1
    1 CONTINUE
    2 X0=XB(K-2)
      X1=XB(K-1)
```

```
      X2=XB(K)
      Y(L,M,N)=(X2A-X1)*(X2A-X2)*YB(K-2)/((X0-X1)*(X0-X2))
     1   +(X2A-X2)*(X2A-X0)*YB(K-1)/((X1-X2)*(X1-X0))
     2   +(X2A-X0)*(X2A-X1)*YB(K)/((X2-X0)*(X2-X1))
      RETURN
      END
      SUBROUTINE BFIT (X,Y,XB,YB,LMAX)
      DIMENSION  XB(15),YB(15)
      DO 1 L=3,LMAX
      IF (X-XB(L))2,2,1
    1 CONTINUE
    2 X0=XB(L-2)
      X1=XB(L-1)
      X2=XB(L)
      Y=(X-X1)*(X-X2)*YB(L-2)/((X0-X1)*(X0-X2))
     1   +(X-X2)*(X-X0)*YB(L-1)/((X1-X2)*(X1-X0))
     2   +(X-X0)*(X-X1)*YB(L)/((X2-X0)*(X2-X1))
      RETURN
```